



Doctoral Dissertation  
Doctoral Program in Science and Technology of Materials (32<sup>th</sup> Cycle)

# Nanocoatings based on graphene related materials for gas barrier and heat shielding applications

**Lorenza Maddalena**

\*\*\*\*\*

## Supervisors

Prof. A. Fina, Supervisor  
Prof. F. Carosio, Co-Supervisor

## Doctoral Examination Committee:

Prof. Jamie Grunlan, Referee, Texas A&M University  
Prof. Gaëlle Fontaine, Referee, Université de Lille  
Prof. Magnus Norgren, Mittuniversitet  
Prof. Alberto Frache, Politecnico di Torino  
Dr. Rossella Arrigo, Politecnico di Torino

This thesis is licensed under a Creative Commons License, Attribution - Non-commercial - No Derivative Works 4.0 International: see [www.creativecommons.org](http://www.creativecommons.org). The text may be reproduced for non-commercial purposes, provided that credit is given to the original author.

I hereby declare that, the contents and organisation of this dissertation constitute my own original work and does not compromise in any way the rights of third parties, including those relating to the security of personal data.

Lorenza Maddalena  
Turin, 2019

# Summary

The Layer by Layer (LbL) assembly was chosen to deposit graphene related material (GRM) based coatings capable of conferring gas barrier or flame retardancy to polymers. The term GRMs indicate every 2D material with high aspect ratio formed by graphene sheets stacked together by low interactions. Graphite nanoplatelets (GNP) and graphite oxide nanoplatelets (GO), which consist in GNP with oxygen functionalizations, are used more specifically for particles with thickness in the range of nanometers and variable lateral size. The recent literature shows that GO can be employed in the water-based deposition of gas barrier coatings. However, the intrinsic defectiveness and the high water sensitivity of this material, makes GO unsuitable for packaging applications that require very low oxygen transmission rates at high humidity. GNP may overcome this problem but their suspension in water is a challenge due to the low affinity of GNP towards water. In this thesis, different liquid exfoliation strategies for the production of water-based GNP suspensions were evaluated encompassing the use of a polyaromatic surfactant and polyelectrolytes as GNP dispersing/stabilizing agents. In a first attempt, GNP were tip-sonicated in presence of a perylene bis-imides derivative but, the obtained suspension was not sufficiently stable due to the self-stacking of employed molecules. In contrast, the presence of either positively or negatively charged polyelectrolytes yielded highly stable (up to 4-5 months) GNP suspensions. The so produced suspensions were employed in a LbL assembly, yielding thin coatings where GNPs are preferentially oriented parallel to the substrate surface and embedded within a polyelectrolyte assembly. The resulting “brick and mortar” morphology is able to increase the tortuosity path of permeating molecules thus enhancing the gas barrier properties of PET films and achieving below detection limits oxygen transmission rates. These results outclass other GNP-based systems reported in the literature with the additional advantage of being thinner. Similar coating structures were employed for flame retardant purposes

exploiting the high aspect ratio of GNP in order to prepare coatings able to act as a barrier to the release of volatiles released by the decomposition of substrates during combustion. To this aim, GO nanoplatelets were LbL assembled on open cell polyurethane foams (PU) employing either Chitosan (CHIT) or polydiallylammmoniumchloride (PDAC) as positive polyelectrolytes. The GO/polycations LbL depositions were able to penetrate inside the foam and homogenously coat every surface available with a nanostructured coating where GO nanoplatelets are embedded within a continuous polyelectrolyte matrix in a brick and mortar-like fashion. Both systems showed the suppression of melt-dripping phenomenon and retention of sample geometry during flammability tests. The effect of nanoplatelets aspect ratio was investigated in CHIT/GO assemblies showing that similar flame retardant performances can be obtained by depositing thinner and smaller nanoparticles, demonstrating the importance of the number of interfaces, with the advantage of reduced coating add-on. The effect of modified ionic strength was evaluated in PDAC/GO assemblies by the addition of a phosphate salt, which allows depositing thicker coatings. Samples prepared at modified ionic strength showed self-extinguishment in flammability test and no ignition at all when exposed to heat flux typical of developing fires ( $35\text{ kW/m}^2$ ). This is ascribed to the barrier effect of GO towards volatiles obtained from PU pyrolysis. To further improve the efficiency and performance of these GRM-based coatings, a new one-step approach, where the assembly of GRM is forced by the solvent removal, was developed. Microfluidized GNP water-based suspensions were employed, evaluating different grade of exfoliation. The one-step deposited coating yielded morphologies similar to LbL assembled coatings. Combustion behaviour was not affected by GNP dimensions; however, the addition of a phosphate salt to the GNP suspensions deposited on the foams allow to reach self-extinguishment. Concluding, GNP have a beneficial effect on the overall flame retardancy but a phosphate salt is needed for reaching superior performances.



# Acknowledgment

Now, at the end of this part of my professional carrier, I think that thanks people who worked or interacted with me is dutiful.

First, I would like to thank my supervisors Prof. Alberto Fina and Prof. Federico Carosio for their help and support to develop new research skills.

I would like to thank Dr. Mauro Tortello for the training on the scanning probe microscopy and in particular on Atomic Force Microscopy applications, which consisted in a new interesting and fascinating world for me.

During my PhD, I had the opportunity to visit the Karoliska Institute of technology in Stockholm and it is very important for me acknowledge Prof. Lars Wågberg. He hosted me in his group and gave to me all the possible support for the development of my research, ranging from discussions to technical advices and devices.

I would also thank all the people working in the Alessandria Polytechnic headquarters for the technical support and friendship. And last but not the least, my friends Ing. Chiara Paravidino and Dr. Ivana Miletto for their support, the scientific discussions during our travels and friendship.





*To my family.*

# Contents

1. State of the art .....	1
1.1 Production of graphene and related materials.....	2
1.1.1 Top-down approaches .....	2
1.1.2 Bottom-up approaches .....	9
1.1.3 Final remarks of different synthetic methods for graphene related material .....	13
1.2 Graphene and related materials: properties vs. defects .....	15
1.3 Graphene and graphene oxide barrier properties towards gasses.....	20
1.4 Gas barrier properties in nanocomposites containing graphene and related materials .....	22
1.4.1 Bulk nanocomposites .....	23
1.4.2 Gas barrier properties in polymer nanocomposites .....	25
1.4.3 Surface modification of polymers with graphene and related materials .....	28
1.5 Fire occurrence and Flame retardancy .....	34
1.6 Flame retardancy in polymer nanocomposites .....	37
1.6.1 Graphene related material bulk nanocomposites for flame retardancy .....	40
1.6.2 Layer by Layer coatings for flame retardancy .....	42
Scope of the thesis .....	44
2. Materials and methods .....	46
2.1 Materials .....	46
2.1.1 Materials adopted for sample preparation.....	46
2.1.2 Reduced graphite oxide synthesis.....	47
2.1.3 Graphite oxide synthesis.....	47

2.2 Procedure .....	49
2.2.1 Suspension preparation .....	49
2.2.2 Layer by layer deposition of PAA/GNP-PBI assembly.....	50
2.2.3 Layer by layer deposition of GBGP assembly.....	50
2.2.4 Layer by layer deposition of CHIT-GO assembly.....	51
2.2.5 Layer by layer deposition of PDAC-GO assembly.....	51
2.2.6 One-pot deposition on PU foams.....	52
2.3 Characterization.....	54
2.3.1 Nanoplatelets characterization .....	54
2.3.2 Layer by layer growth characterization .....	55
2.3.3 Fluorescence characterization of perylene bisimides based suspensions .....	55
2.3.4 Gas barrier properties characterization .....	55
2.3.5 Flame retardant characterization.....	56
2.3.6 Flame retardant residue characterization .....	56
3. GRMs for enhanced gas barrier .....	58
3.1 Water based suspension of graphite nanoplatelets stabilized in perylene bisimides solution for gas barrier application .....	60
3.1.1 Characterization of suspensions and Layer by layer growth .....	60
3.2 Multilayers of GNP-polymer based suspensions for the preparation of gas barrier membrane .....	66
3.2.1 Characterization of GNP-polymer suspensions .....	66
3.2.2 Coating growth by FT-IR, QCM-D and SPAR. ....	69
3.2.3 Morphology on PET thin film and Gas Barrier properties .....	74
4. GRMs for flame retardancy application .....	76
4.1 Multilayer of Chitosan and GO to reduce flame retardancy of PU-Foam .....	77
4.1.1 Layer by layer growth and characterization.....	78
4.1.2 Morphology of the coating on PU foams.....	80
4.1.3 Flammability tests.....	81
4.1.4 Forced combustion tests.....	83
4.1.5 Coating evolution during combustion and residue analysis .....	85
4.2 Effect of nanoparticles aspect ratio on flame retardant properties of GO-CHIT layer by layer treated PU foams.....	87

4.2.1 Nanoparticles characterization.....	88
4.2.2 Layer by layer growth and characterization.....	89
4.2.3 Morphology on PU foams.....	92
4.2.4 Flammability tests.....	93
4.2.5 Forced combustion test .....	95
<b>4.3 Polydiallyl ammonium-chloride and graphite oxide layer by layer treated PU foams: effect of ionic strength on the assembly and flame retardancy. ....</b>	<b>97</b>
4.3.1 Layer by layer growth and characterization.....	98
4.3.2 Morphology of the coating on PU foams.....	100
4.3.3 Flammability tests.....	101
4.3.4 Forced combustion tests.....	103
4.3.5 Coating evolution during combustion and residues analysis.....	104
4.3.6 Flame penetration tests .....	108
<b>4.4 Heat shielded PU foam obtained by one-pot deposition of high shear mixed graphite.....</b>	<b>109</b>
4.4.1 Morphology of the coating .....	110
4.4.2 Flammability tests.....	112
4.4.3 Forced combustion tests.....	113
4.4.4 Flame penetration test .....	116
<b>5. Conclusions.....</b>	<b>118</b>
<b>6. References.....</b>	<b>122</b>

# List of Tables

Table 1 LDA calculation of Energy barrier in graphene defects. ....	20
Table 2 LDA calculation of gas atoms and molecules kinetic diameter.....	21
Table 3 Oxygen permeability of GRMs bulk nanocomposites as function of process and quantities. ....	24
Table 4 GOA, GOB, GOC, characterization furnished by the producer. ....	49
Table 5 PU fomas weight gain after LbL GOX-CHIT deposition.....	51
Table 6 Mass add-on of LbL treated foams. ....	52
Table 7 Mass gain of one-pot caoted PU foams.....	53
Table 8 TGA residues of neat polymer and suspensions. ....	67
Table 9 Signal attribution of P and B. ....	70
Table 10 Comparison between BP and GBGP system permenability with literature. ....	75
Table 11 Attribution of CHIT and GO FT-IR signals.....	79
Table 12 Horizontal flammability test data of untreated and LbL treated foams.....	82
Table 13 Cone calorimetry data of untreated and LbL-treated PU foams. ....	84
Table 14 Comparison of pkHRR reduction between the CHIT/GO coatings reported in this paper and previously published Chitosan based LbL coatings on PU foams.....	85
Table 15 Thickness of 10 BL GOx/CHIT assemblies.....	92
Table 16 Horizontal flammability test data of untreated and LbL treated foams.....	95
Table 17 Cone calorimetry data of LbL-treated PU foams.....	96
Table 18 Signals and attribution of PDAC, Graphene Oxyde and APD.....	99
Table 19 Horizontal flame test data releated to untreated, 3 BL , 3BL and 6 BL treated PU Foam with unmodified and modified ionic strenght.....	103
Table 20 Cone calorimetry data of untreted and LbL-treated foams. ....	104

Table 21 Flammability test of x cycles treated PU foams.....	113
Table 22 Flammability test of x cycles_P treated PU foams. ....	113
Table 23 Cone calorimetry data of untreated and one pot treated PU foams. .....	115
Table 24 Cone calorimetry data of untreated and one pot treated PU foams with phosphate salt.....	116



# List of Figures

Figure 1 a) Micromechanical cleavage, b) anodic bonding, c) photoexfoliation of graphite. ....	3
Figure 2 Tip sonication scheme of graphite platelet in liquid media. ....	4
Figure 3 Scheme of an high shear mixer equipped with a rotor-stator system. ....	8
Figure 4 Scheme of a microfluidization system. ....	9
Figure 5 Graphene growth silicon carbide mechanism. ....	10
Figure 6 Thermal-CVD and Plasma Enhanced-CVD scheme. ....	11
Figure 7 Bottom-up fabrication of Graphene nanoribbon on surface starting from 10,109-dibromo-9,99-bianthryl monomers (1). Figure reprinted with the permission of Springer Nature from ref.[88]. ....	12
Figure 8 Fabrication of graphene from SAM deposition on surface. Reprinted with the permission of Wiley and Sons from ref [89]. ....	12
Figure 9 Atomic model of a) Stone-Wales defect and AC-TEM micrograph; c)-d) single vacancies, e)-f) di-vacancies, g)-h) multi-vacancies before and after reconstruction; Figure is adapted from [103] with permission from Elsevier. b) is adapted from [104] Copyright (2008) American Chemical Society.....	16
Figure 10 a) Configuration of a carbon ad-atom in different symmetry. Configuration of ad-atom adsorbed on b) single vacancies and c) double vacancies. Figure is adapted from [103] with permission from Elsevier. ....	16
Figure 11 Modelling of a dislocation a) before and b) after reconstruction along zig-zag direction. Example of a) symmetric grain boundary and b) closed flower-type grain loop defects. Figure adapted from [103] with permission from Elsevier. ....	17
Figure 12 Schematization of tortuosity model: a) neat polymer is permeable to a gas molecule, b) inclusion of nanoparticles is able to modify the gas molecule path in the polymer matrix; c) effect of highly oriented nanoparticles added to the polymer matrix.....	25

Figure 13 Scheme of LbL process with details about charge reversal. On the left right, nanostructured coating growth with attention on enthalpy (orange) and entropy (purple) contributions.....	30
Figure 14 Fires occurred in USA in 2017 .....	34
Figure 15 Polymer surface combustion cycle.....	37
Figure 16 FE-SEM micrograph of reduced graphite oxide.....	47
Figure 17 TEM micrographs of graphene oxide (GO) at different magnification.....	48
Figure 18 Raman Spectrum of prepared GO.....	49
Figure 19 One pot deposition operative scheme.....	53
Figure 20 Perylene bisimides derivative used in this work (named PBI) as an example of all perylene bisimides derivative solubilisation in water and stabilization effect.....	60
Figure 21 a) VIS spectra of PBI 1*10-4 M solution and b)VIS spectra of GNP-PBI (1*10-4 M) suspension.....	61
Figure 22 UV-VIS spectra of 10 <sup>-5</sup> M PBI solution in ultrapure water, ultrapure water at pH 2, ultrapure water at pH 8, PBS buffer pH 7.4 (a). Fluorescence spectra of 10 <sup>-5</sup> M PBI solution in ultrapure water, ultrapure water at pH 2, ultrapure water at pH 8, PBS buffer pH 7.4 (b).....	62
Figure 23 Fluorescence spectrum of GNP-PBI suspension A, and fluorescence spectrum of filtered GNP-PBI suspension named Af.....	63
Figure 24 VIS LbL growth of PBI-PAA system.....	64
Figure 25 LBL growth of PAA/GNP-BPI followed by a) VIS spectroscopy and b) FT-IR spectrometry.....	65
Figure 26 Digital image of a) neat PET 10 um thick and of b) the 10 BL PAA/GNP-PBI treated PET 10 um thick. c) Oxygen Transmission rate of LBL coated and untreated PET thin film.....	66
Figure 27 a) TGA in N <sub>2</sub> atmosphere of neat B, P, and GNP. B) TGA measurements of GB and GP in N <sub>2</sub> atmosphere.....	67
Figure 28 Raman spectra of GB, GP, and GNP.....	68
Figure 29 SEM micrographs of GB and GP suspensions deposited on a Si wafer and statistical determination of lateral size.....	68
Figure 30 AFM tapping mode topography of a) single GNP, b) a single GNP covered by B in GB suspension, c) a single GNP covered by P in GP suspension.....	69
Figure 31 FT-IR spectra of neat PAA (P) and BPEI (B) deposited on Si wafer.....	70

Figure 32 a) LbL growth of GB-GP system followed by FT-IR spectroscopy , b)comparison between BP and GBGP LbL regime growth, c) cross-section micrograph of 10BL BP d) and GBGP assembly, e) GNP embedded in GBGP matrix, high magnification FESEM micrograph. ....	72
Figure 33 SPAR (a) of 5 BL BP assembly and (b) 5 BL GBGP assembly....	73
Figure 34 QCM and dissipation of LbL monitored growth of (a, b) 5 BL BP assembly and (c, d) 5 BL GBGP assembly.....	74
Figure 35 SEM micrograph of a PET 10 $\mu\text{m}$ thick coated by 5BL BP (a), 10BL BP (b), 5 BL GBGP (c) and 10 BL GBGP (d) assembly. e) OTR measurements collected on the same samples. ....	75
Figure 36 Chitosan and GO FT-IR spectra. ....	78
Figure 37 a) FT-IR spectra during LbL growth, b) evolution of the signals at 1624 and 1080 $\text{cm}^{-1}$ as function of layer number and c) FE-SEM micrographs of 10 BL assembly on Si wafer. ....	80
Figure 38 SEM micrograph of a) untreated PU foam, b) 3 BL and c) 6 BL foams.....	81
Figure 39 SEM micrograph of untreated PU foam (a, d), 3BL PU foam (b, e), and 6 BL PU foam (c, f). ....	81
Figure 40 Pictures of flammability test in horizontal configuration of untreated PU foam (a-c), 3 BL PU foam (d-f) and 6 BL PU foam (g-i). First column: right after ignition, second column: 15 seconds after ignition and third column: during flame out.....	82
Figure 41 a) HRR and b) TSR curves of untreated and PU foams coated with 3 BL and 6BL. 6BL* indicates non-igniting samples. ....	84
Figure 42 Images of a) untreated PU foam, b) 3 BL and c) 6 BL foams cone calorimeter residue.....	84
Figure 43 FESEM micrograph of 10BL deposited on Si wafer after heat flux exposure (a,b ), FT-IR spectra of 10BL deposited on Si wafer before (c) and after (d) heat flux exposure, Raman spectra of 10BL deposited on Si wafer before (red curve) and after (black curve ) heat flux exposure and SEM micrographs of 3 BL (f, g) and 6 BL (h, i) coated foams residues after forced combustion tests. ....	86
Figure 44 Raman spectra of a) neat GO and b) after exposure to heat flux. Raman spectra of CHIT before (red curve) and after (black curve) exposure to heat flux. ....	87
Figure 45 Tapping mode-AFM characterization of a) GOA, b) GOB and c) GOC .....	88
Figure 46 FE-SEM of 1L of a) GOA, b) GOB d) GOC deposited on Si wafer; c) high magnification FE-SEM micrograph of one GOA nanoplatelets. ....	89

Figure 47 LbL growth of a) GOA-CHIT, b) GOB-CHIT, c) GOC-CHIT assembly followed by FT-IR spectroscopy and conducted on a silicon wafer as substrate.....	91
Figure 48 FE-SEM micrograph of a) 10 BL GOA/CHIT, b) 10 BL GOB/CHIT, c) 10 BL GOC/CHIT assembly.....	92
Figure 49 SEM micrograph of 3BL CHIT a) GOA, b) GBOB, c)GOC. SEM micrograph of 6 BL CHIT d) GOA, e) GOB, f) GOC; high magnification micrograph of 6 BL CHIT g) GOA, h) GOB, i) GOC.....	93
Figure 50 Pictures of flammability test in horizontal configuration of untreated 3 BL GOA-CHIT treat PU foam (a-c), 3 BL GOB-CHIT PU foam (d-f) and 3 BL GOC-CHIT PU foam (g-i). First column: right after ignition, second column: 15 seconds after ignition and third column: during flame out.....	94
Figure 51 Pictures of flammability test in horizontal configuration of untreated 6 BL GOA-CHIT treat PU foam (a-c), 6 BL GOB-CHIT PU foam (d-f) and 6 BL GOC-CHIT PU foam (g-i). First column: right after ignition, second column: 15 seconds after ignition and third column: during flame out.....	94
Figure 52 HRR curves of PU foams coated with a) 3 BL and b) 6BL.....	96
Figure 53 Imagines of 3BL a) GOA-CHIT, b) GOB-CHIT, c) GOC-CHIT coated foams and 6 BL d) GOA-CHIT, e) GOB-CHIT, f) GOC-CHIT coated foams before (left) and after (right) cone calorimeter exposure.....	97
Figure 54 FT-IR spectra of pure PDAC, Graphene Oxyde and APD .....	98
Figure 55 Characterization of the build-up of PDAC/GO at 0 (a, c and e) and 0.5M (b, d and f) APD on model Si substrate: a-b) FT-IR spectra in the 1850-900 cm-1 region during LbL growth; c-d) evolution of the signals ascribed to C=O and COO- as function of bilayer number and e-f) FE-SEM micrographs of 10 BL cross-section on Si wafer.....	100
Figure 56 SEM micrograph of untreated and LbL treated PU foam: a) 3BL, b) 3 BL 0.5 M, c) 6 BL, d) 6 BL 0.5M and e) detail and schematization of coating on the foam edge.....	101
Figure 57 Elemental analysis performed on 3BL 0.5M .....	101
Figure 58 Flame retardant characterization of untreated and LbL treated foams: a) snapshots from flammability test, b) average residues after flammability tests.....	102
Figure 59 Flame retardant characterization of untreated and LbL treated foams: (left) heat release rate vs time plots, (right) average residues.....	104
Figure 60 Digital images of the residues after cone calorimetry tests: a) untreated PU, b) 3 BL, c) 3 BL 0.5M, d) 6 BL, e) 6 BL 0.5M and f) small portion (10x10 mm) of 6 BL 0.5M residue under static compression by a 20g weight...	104

Figure 61 Low magnification SEM micrograph of residues collected after cone calorimetry tests : a) 3 BL, b) 3 BL 0.5M, c) 6 BL, d) 6 BL 0.5M.....	105
Figure 62 Post combustion residue analysis. SEM micrographs of: a) 3 BL, b) 3 BL 0.5M, c) 6 BL and d) 6BL 0.5M). .....	106
Figure 63 Raman spectra of 3BL, 3 BL 0.5M, 6 BL, 6 BL 0.5M cone calorimeter residues. ....	107
Figure 64 ATR-IR spectra of residues collected after cone calorimetry tests. ....	107
Figure 65 Flame penetration tests: a) digital pictures of the uncoated PU and 3 BL 0.5M front surface during the test and b) front and back side temperatures as a function of time for3 BL 0.5M.....	108
Figure 66 Flame penetration tests: a) digital pictures of the 6 BL 0.5M and silica aerogel front surface during the test and b) front and back side temperatures as a function of time for 6 BL 0.5M and silica aerogel front surface during the test.....	109
Figure 67 FE-SEM micrograph of one-pot treated PU foams at low magnification of a) 0 cycles, c) 10 cycles, e) 30 cycles, g) 50 cycles, i) 70 cycles, m) 100 cycles FE-SEM at high magnification of b) 0 cycles, d) 10 cycles, f) 30 cycles, h) 50 cycles, l) 70 cycles, n) 100 cycles. ....	111
Figure 68 FE-SEM micrograph of one-pot treated PU foams at low magnification of a) 0 cycles_P, c) 10 cycles_P, e) 30 cycles_P, g) 50 cycles_P, i) 70 cycles_P, m) 100 cycles_P; FE-SEM at high magnification of b) 0 cycles_P, d) 10 cycles_P, f) 30 cycles_P, h) 50 cycles_P, l) 70 cycles_P, n) 100 cycles_P....	112
Figure 69 Cone calorimeter tests of x_cycles and x_cycles_P PU foams: a) HRR comparison of x cycle foams, b) HRR comparison of x cycles_P foams, c) SPR comparison of x cycles foams, d) SPR comparison of x cycles_P foams..	115
Figure 70 Flame penetration test of a) x cycles treated foam and b)x cycles_P treated foams. c) Temperature interval between the front and the back of x cycles_P PU treated foams, d) picture of 10 cycles_P coated foam residue. ....	117



# List of Acronyms

AFM	Atomic force microscopy
ALG	Alginate
APD	Ammonium phosphate di-basic
APP	Ammonium polyphosphate
avHRR	averaged HRR
B	see BPEI
BL	Bi-layer
Bmim-Tf2N	Bis(trifluoro-methane-sulfonyl)imide
BMT	Bohemite
BPEI	Branched polyethylenimine
CDV	Chemical vapour deposition
CHIT	Chitosan
CNFs	Carbon nano fibres
CNT	Carbon nanotubes
DMF	Dimethylformamide
DMSO	dimethyl sulfoxide
FE-SEM	Field emission SEM
FLG	Few layered graphene
FRs	Flame retardant agents
G	Reduced graphite oxide suspension
GB	Graphite nanoplatelets-BPEI suspension
GICs	Graphite intercalated compounds
GNP	Graphite nanoplatelets
GNR	Graphene nanoribbon
GO	Graphite oxide
GP	Graphite nanoplatelets-PAA suspension
G-PBI	Graphite nanoplatelets-PBI suspension

GRM	Graphene related material
HMIH	1-hexyl-3-methylimidazolium hexafluorophosphate
HRR	Heat release rate
HSM	High shear mixing
LbL	Layer by layer
LDA	Local density approximation
LDHs	Layered double oxides
LPE	Liquid phase exfoliation
MF	Micro fluidization
MLG	Multilayer graphene
MMT	Montmorillonite
N	Number of layers
NMP	n-methyl-2-pyrrolidone
P	see PAA
PAA	Polyacrylic acid
PAH	Polyaromatic hydrocarbons
PBI	Perylene bis-imides
PBS	Phosphate buffered saline solution
PE-CVD	Plasma enhanced chemical vapour deposition
PEI	Polyethylenimine
PEMs	Polyelectrolyte multilayers
PET	Polyethylene terephthalate
pkHRR	Peak heat release rate
PPA	Polyphosphoric acid
PU	Polyurethane
QCM	Quartz crystal microbalance
rGO	Reduced graphite oxide
SEG	Shear exfoliated graphite
SEM	Scanning electron microscopy
SLG	Single layer graphene
SPAR	Stagnation point adsorption reflectometry
SPB	Sodium Polyborates
SW	Stone-Wall
T-CVD	Thermal chemical vapour deposition
THR	Total heat release
TL	Tri-layer
TSR	Total smoke release
TTI	Time to ignition

UV	Ultra-Violet
VMT	Vermiculite
$\gamma$	Interfacial tension



# Chapter 1

## State of the art

Since its isolation from bulk graphite, graphene has attracted the attention of both scientific community and industry as a result of its peculiar properties. Graphene is a single sheet of carbon atoms arranged in a honeycomb structure where all the atoms are hybridized  $sp^2$ . The highly ordered structure, in the absence of defects confers to graphene an extremely high electron mobility of up to 250.000  $cm^2/(Vs)$  at room temperature [1], a huge electrical conductivity of up to 1000S/cm [1] and an exceptional thermal conductivity in the range of 3000 to 5000 W/(Km) [2]. Moreover, graphene is the strongest material ever measured with a Young modulus of 1TPa and an intrinsic breaking strength of 130 GP [3]. Even if the thickness of graphene correspond to the dimension of the carbon atom, the graphene thickness is often assumed as the distance between 002 planes in graphite corresponding to 0.34 nm [4]. The graphene lateral size may be very variable, depending on the preparation conditions, and typically ranges from the nanometers to the microns, affecting mechanical, electrical and thermal properties.

In literature, it is not rare to refer to as graphene for materials which are not purely single layer  $sp^2$  carbon, but rather multilayers of variable thickness and/or oxidized carbons. Consequently, it is necessary to define a nomenclature which can univocally individuate a material owning to the graphene family. One attempt was done by Bianco et al. [5] who classified the graphene based material as a function of the number of stacked layers and defined the term “graphene related materials” (GRMs) as every 2D materials containing the word graphene, but this definitions remained ambiguous because also graphite nanoplatelets and graphite oxide are considered GRMs. Another classification based on the number of stacked layers, the C/O ratio and the average lateral size was proposed by Wick et al. [6]. However, even if graphene and graphene oxide are defined as monolayers, multilayered carbon-based materials can be indicated in more than one way. As an example, in ref [6], *graphene nanosheets* and *ultrafine graphite* are used as synonyms to indicate structure with 100 nm thickness. In this thesis, the term

graphene will be employed only and unequivocally for a single layer of carbon atoms hybridized  $sp^2$  with a thickness equal to the covalent radius of carbon atom. Other layered carbon-based material not fulfilling this specification should not be referred to as graphene and are in fact more properly identified as graphene related materials. In this frame, the term graphene oxide will be adopted to indicate a single layer of carbon atom functionalized with epoxy, hydroxyl and carboxyl groups on the surface and/or on the edge. For multilayer structures, few layered graphene (FLG) is defined as carbonaceous material made of 2 or 3 stacked graphene sheets, as it was proposed by Novoselov and Geim [7]. For further increase in the number of stacked layers, the properties tend to those of graphite, so it seems to be inappropriate to deal with multi-layered graphene. Therefore, it will be much more correct to employ the term graphite nanoplatelets (GNP) for particles with typical thickness in the range of nanometers and variable lateral size. In the literature, there is also some confusion about the acronym GO because it has been adopted for both graphene oxide and graphite oxide i.e a surface oxidized GNP. In this work GO will be used univocally for graphite oxide nanoplatelets.

## 1.1 Production of graphene and related materials

The use of graphene and GRMs in industry requires large-scale production looking to low-cost and easy processing. Moreover, to choose the most suitable production line, it is important to consider the final application. Because GRMs properties are tuned as a function of chemical functionalization and nanoplatelets dimensions, it is possible to prepare graphene-based materials with custom-made properties. As an example, electronic flexible devices can be prepared by inkjet printing of graphite nanoplatelets [8] or sensors can be obtained taking advantage of the interactions between molecules and the GO nanoplatelets, affecting the properties of pristine [9, 10].

GRMs can be made through a wide range of techniques including an atom-by-atom (bottom-up) approach and the exfoliation of bulk graphite and its derivatives (top-down) approach. The range of technique employed to produce graphene in laboratory scale is wide. In the following sections, the most important and useful production techniques will be discussed.

### 1.1.1 Top-down approaches

#### 1.1.1.1 Dry exfoliation

Dry exfoliation consists in the peeling of graphite through the action of a mechanical, electromagnetic or electrostatic force in presence of a liquid solvent, in air or inert atmosphere. Dry exfoliation techniques are:

- Micromechanical cleavage;
- Anodic bonding;
- Photoexfoliation.

Micromechanical cleavage or micromechanical exfoliation consist in the exfoliation of graphite using an adhesive tape. The graphite is peeled off until a layer is collected on the adhesive part of the tape (Figure 1 a). Employing these processes is possible to peel off FLG and graphene, as it was obtained in 1999 by Novoselov at al. [11]. Up to now, the technique is optimized and is easy to obtain high quality FLG with a defined grain size, dependent only on the graphitic source and whose number of layer can be identified by Raman scattering [12, 13]. However, micromechanical cleavage is used only on laboratory scale in order to study fundamental properties of GRMs because of its impracticality to large scale.

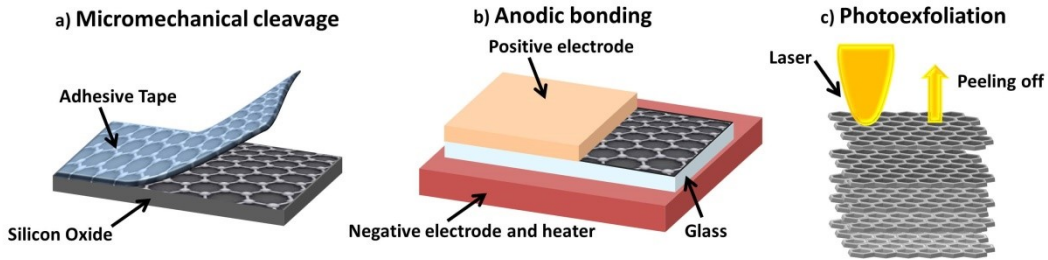


**Figure 1** a) Micromechanical cleavage, b) anodic bonding, c) photoexfoliation of graphite.

Anodic bonding is widely used in microelectronic industry and consist in the electrostatic exfoliation of graphite (Figure 1 b). The pristine graphite is pressed on the surface of a glass and then positioned between two electrodes. The negative one is also connected to a heater. After the application of a certain positive voltage (generally between 0.5 and 2 kV) and temperature (near 200°C) in a determined time range, the sodium cations contained in the glass migrate to the negative electrode while the oxygen anions are restricted to the graphite-glass interface [14, 15]. As a function of the temperature, the time and the applied voltage, the high electric field established on the interface graphite-glass favours the detachment of FLG or graphene. It was demonstrated that it is possible to produce 1 mm x 0.5 mm FLG flakes [15].

In photoexfoliation (Figure 1 c), a pristine graphite substrate is invested by a laser source which allow to detach a part or an entire layer, depending on the laser energy density. In 2011, it was demonstrated that the number of exfoliated layers ( $N$ ) dependence on the energy density is related to the coupling of heat with  $N$ -layered graphene phonons and the specific heat scale as  $1/N$  [16]. The technique can be used in vacuum or inert atmosphere [17, 18]. Moreover, photoexfoliation performed in air is useful for the production of oxidized graphite but newest applications are referred to the laser ablation in liquids [19].

### 1.1.1.2 Liquid phase exfoliation

Liquid phase exfoliation (LPE) is the most versatile technique adopted for the production of GRMs in liquid media. In general this method results in 2D nanosheets with lateral size in the range of 100 nm to 100  $\mu\text{m}$  and thickness ranging between 1 to 10 layers after purification, with a concentration up to 1g/L [20]. The technique involves the production of nanoplatelets by applying ultrasounds [21] or high shear stresses [22]. It is very important to consider that,

for a given approach, some considerations need to be conducted prior to choose the exfoliation methodology. The nanoplatelets source is very important because, as an example, the graphitic grain boundaries limit the lateral size of the exfoliated GRMs. Initially, the pristine graphite needs to be dispersed in a solvent, then the mixture is exfoliated (Figure 2). The suspension is then purified by centrifugation in order to remove the unexfoliated graphite. Centrifugation can be also used to select a range of nanoparticles with defined dimension as it was done by Coleman and co-workers [23].

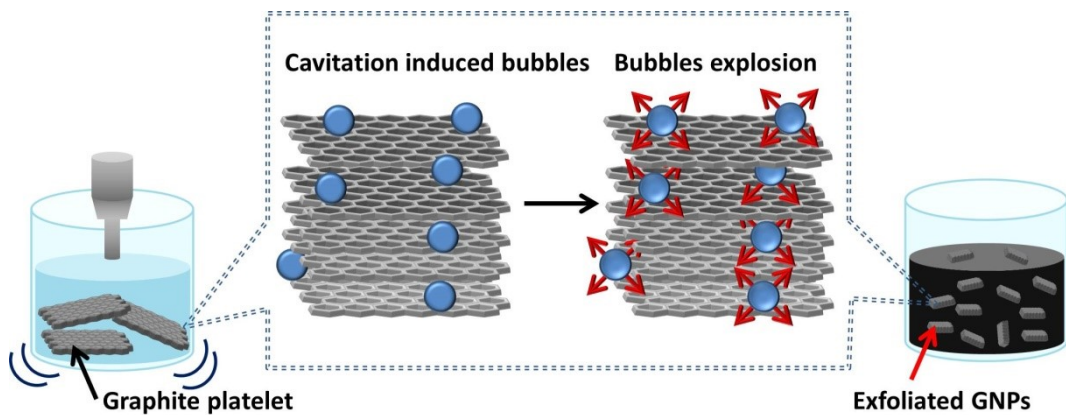


**Figure 2** Tip sonication scheme of graphite platelet in liquid media.

During the sonication process, the formation of cavities and bubbles between graphite layers promotes the swelling of the graphite and, when collapsed for the pressure variation, the exfoliation (Figure 2). The success of LPE depends on the nature of liquid media and the graphene precursor which could be graphite, as well as graphite oxide or intercalated graphite.

Graphite is the reference starting material. It is made of graphene layers held together by Van der Waals forces. Of the two main allotropic forms, the hexagonal graphite is the most stable with layer stacked ABAB [24]. Graphite can be natural or synthetic. Synthetic graphite can be produced by several techniques which lie outside the scope of this section, while extensive literature is available on this subject [25-28]. Graphite derivatives such as expanded graphite, graphite intercalated compounds and graphite oxide can be also employed for the production of GRMs. Expanded graphite is derived by the surface oxidation and the subsequent reduction of graphite, associated with a significant gas release, causing a dramatic volume expansion. The process is used to improve the interlayer space between graphite sheets retaining the long range ordered structure of graphite and expanded graphite can be used as precursor in liquid exfoliation production of GRMs [29]. Graphite can be intercalated with a range of compounds to yield Graphite Intercalated Compounds (GICs). The GICs production is widely reported in literature [30-32]. The result of the intercalation process is the increase of graphite interlayers spacing, making GICs promising to produce GRMs without the employment of high-energy sources. Larger distance means minimizing Van der Waals cohesive forces, which can be translated into easier exfoliation. For presenting some example of most used GICs, K-, Rb-, Cs-

GICs have an interlayers space between 0.53-0.59 nm and DMSO-GICs have interlayer space of 0.9 nm which are 1.5-3 times higher than the graphite interlayer space (0.34 nm). Indeed, GICs can be exfoliated by mechanical stirring but they are air-sensitive and tend to oxidize in ambient atmosphere [33]. As an example, the results of tetrabutylammonium-GICs exfoliation are flakes with a single layer concentration of the 90% and lateral size of 20  $\mu\text{m}$  [34]. However, the air-sensitivity and the necessity to synthesize ad-hoc GICs, make these materials not attractive for the extensive preparation of GRMs via LPE.

Graphite oxide is considered a GRMs but, can be employed as an intermediate in order to obtain other GRMs. GO is produced exposing graphite to a high oxidant mixture of  $\text{KMnO}_4$ ,  $\text{NaNO}_3$  in concentrated  $\text{H}_2\text{SO}_4$  [35]. In these conditions the reaction is safe because the process is not exothermic and no toxic gases are produced. The lateral size and the thickness of the oxidized particles can be tuned by sonicating the starting solution and, in appropriate conditions, is possible to produce graphene oxide. This behaviour is very important because the suspensions of oxidized GRMs depends on the oxidation grade and the thickness: the higher is the concentration of oxygenated groups on the surface, the higher will be the affinity between the GRMs nanoparticles and water due to the hydrogen bonding formation. The most important advantage of the GO synthesis is that it can be suspended in water and can be chemically modified through the typical reaction of carboxylic acid and/or considered as an intermediate for the preparation of GRMs in water. GO-LPE is useful in order to obtain graphene oxide flakes with a lateral size of several microns [36]. The defectiveness of the obtained flakes confers luminescent properties under continuous wave irradiation, making them suitable for lighting application [37] and bio-imaging [38]. GO can also be reduced to reduced graphite oxide (rGO). Hydrazine, sodium borohydride, hydroquinone, have been used for the chemical reduction of GO, as well organic acids [39], alcohols [40], biochemical molecules, amino acids, natural extracts, vitamin C [41] and metals [42] and a few mechanism have been proposed [43]. Based on the reproducibility and the easy scale up, alcohols may be considered the best candidate for rGO preparation [40]. rGO can be also prepared by thermal annealing able to restore the  $\text{sp}^2$  graphene structure by repairing the C-C  $\text{sp}^2$   $\pi$ -bond network at defect regions during the reduction process [44]. Thermal reduction can be conducted in modified atmosphere as it is reported in literature and it is the most cost-efficient technique to obtain highly reduced rGO with an oxygen down to below 1% [45, 46].

The presence of defects influences the properties of final GRMs: defects in layer, such as vacancies, strongly affect properties of GRMs [7]; the grain boundaries influence the final nanoparticles aspect ratio [8-10] and the crystal boundaries have a role in the sonication time [8]. Grain boundaries can also affect oxidation procedure [11], as well as in the chemical structure of reduced graphite oxide obtained after chemical or thermal reduction [12]. Defects and their effect on graphene properties will be discussed in detail in section 1.2.

The stabilization of nanoplatelets in neat solvents depends on the solvent capability to overcome the Van der Waals attraction in the bulk graphite and is

thermodynamically favoured. Because the nanoplatelets are larger and more rigid than molecules, the entropy of solubilisation can be neglected, meaning that the stabilization depends only from the solubility parameters (surface tension is an example [47]). Typical solvents that are known to give stable suspensions are N-methyl-2-pyrrolidone (NMP), N-cyclo-2-pyrrolidone, dimethylformamide (DMF), dimethyl sulfoxide (DMSO) and isopropyl alcohol (IPA) which have surface tension of about 40 N/m. Solvents mixture can improve the exfoliation of GNP when solubility parameter match. Nevertheless, certain solvents like NMP can degrade and polymerize [48, 49] changing the suspension behaviour. Moreover, another important consideration about suitable solvents is that they suffer of a high boiling point limiting the purification of the GNP and are typically toxic [50]. As an alternatives, surfactants can be used for stabilize GNP in water [51-54]. Amphiphilic surfactant can interact with the GNP storing non-covalent interactions by the non-polar region meanwhile the polar head can interact with the solvent preventing the aggregation of the GNP. The exfoliation is also promoted by the steric hindrance of the backbone: the repulsion forces between backbones of surfactants prevent the aggregation of the nanoplatelets. This behaviour is guaranteed until the critical micelle concentration of the surfactants is reached in order to avoid self-nucleation. Popular anionic surfactants are sodium cholate, sodium dodecyl cholate, sodium dodecyl sulphate. Also, cationic and non-ionic surfactant can be used such as cetyltrimethylammonium bromide, and *t*-Octylphenoxy polyethoxyethanol or polyoxyethyleneglycol dodecyl ether respectively. Flakes produced in aqueous surfactant solutions are typically smaller than the ones produced in organic solvents because of the higher viscosity of this solvents respect to the water-based solutions. In organic solvents, the higher viscosity hinders the intercalation of the solvent between the graphite layers. Moreover, viscosity impacts on the size selection in centrifugation by slowing down the sedimentation and a huge population of large and thicker nanoparticles is obtained. It is difficult to completely remove the surfactants from the flake surfaces after processing, as it can be trapped between two platelets, potentially deteriorating the resulting properties. Several studies are reported in literature, focused on the impact of surfactants concentration or chemical structure on the exfoliation degree [51, 55-58]. Studies on the effect on aromatic surfactants such as poly aromatic hydrocarbons (PAH) have been reported correlating the adsorption energy of a single molecule on graphene to the overall exfoliation performance [59, 60]. Thanks to the aromatic core, these molecule act as dispersion stabilizer via non-covalent functionalization. The physisorption of PAH molecules onto GNP surface occurs trough a  $\pi$ - $\pi$  interaction between the planar  $\pi$ -conjugated surfaces. In this configuration both GNP and PAH share the  $\pi$ -orbital electrons resulting in the reduction of the surface free energy of the dispersion [60].

Another approach in liquid exfoliation is the employ of polymers or ionic liquids as coadjuvants to the liquid exfoliation of graphite. 1-hexyl-3-methylimidazolium hexafluorophosphate (HMIH) [61] and 1-butyl-3-methylimidazolium bis(trifluoro-methane-sulfonyl)imide (Bmim-Tf<sub>2</sub>N) [62] are

reported in literature as solvents for the exfoliation of graphite. When graphite is exfoliated in HMIH only flakes with 3-4 microns lateral size were obtained after a long ultrasonication process due to the high viscosity of ionic liquids and no information on graphene concentration are reported [61]. However, more investigations need to be done toward ultrasonication of graphite in ILs. Moreover the resulting exfoliated flakes in Bmim-Tf<sub>2</sub>N were oxidized during the process, due to the interaction with the ILs [62].

At the beginning of this section, it was explained how a precursor can affect the properties of the obtained GRMs but also how it is important the choice of the medium. Looking to the practical aspect, liquid phase exfoliation can be conducted through sonication or applying high shear forces. Sonication can be performed using a tip or bath sonicator. In tip sonication the probe is directly immersed in the mixture whereas in the bath the energy travels through an external medium and the dispersion vial before reaching the flake. Tip sonication is preferred over bath sonication because the higher production rate. It is possible to produce exfoliated solutions in less than 24 hour reaching the concentration of 1 g/L from an initial concentration of 30 g/L [20]. In tip sonication, the type of set up has an impact on the quality of products and to choose the diameter of the tip, it is very important to follow the constructor instructions in order to avoid damaging or contamination by the tip constituents when the sonication is prolonged for more than 5-7 hours. Moreover, the amplitude of sonication is very important. Generally, a 60% of amplitude is enough for obtain good dispersion. Working with lower amplitude than 60% makes poor exfoliation, whereas higher amplitude may overheat the solution or damage the tip. In order to avoid overheating, the tip sonicator can operate in pulse mode. For a given combination of sonicator, tip diameter, operating conditions (sonication time, pulsing, volumes etc.) the tip sonication is reproducible. However, the impact of such parameters is still poorly understood and for this reasons tip sonication cannot be considered scalable, today. Another drawback of tip sonication is its high cost because of instrumentation and its continuous maintenance makes this technique expensive. Unfortunately, tip sonication remains a useful technique only in lab scale because its scalability is not yet demonstrated. A cheaper alternative to tip sonication is the bath sonication. However, longer processing times are needed for achieving the same concentration of tip sonication and the results are less reproducible. In order to maximize the bath sonication efficiency is important to consider the filling level and the positioning of the vial in the bath.

Liquid phase exfoliation can be conducted through the application of high shear forces to a solution. High shear mixing (HSM) is a top down exfoliation process which involves mechanical shear for the exfoliation of graphite in a rotor-stator system. During mixing, the rotor mix graphite and solvents vigorously due to the high speed rotation of rotor blades and the centrifugal forces drive graphite platelets in the periphery of the rotor-stator system (Figure 3) [22]. The exfoliation process occurs primarily because of the shear forces application and secondly, for the collision between graphite platelets and the stator. Micro-jet cavitation also occurs. It has been demonstrated that the most important

parameters of the process are the diameter of the rotor, the mixing time, the initial graphite concentration and the rotor speed.

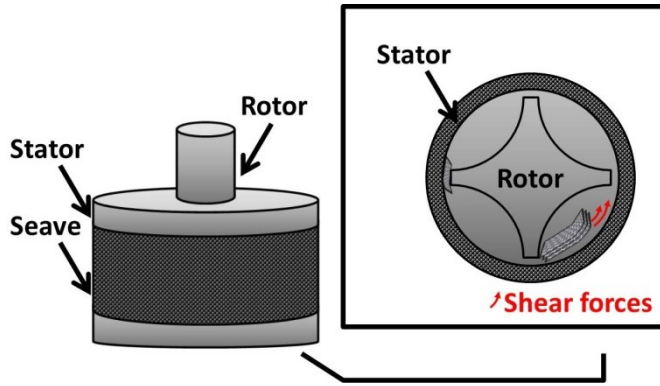


**Figure 3** Scheme of an high shear mixer equipped with a rotor-stator system.

HSM can be performed in organic solvents as well as in water surfactant solutions. The resulting GRMs obtained by the HSM in NMP or in sodium cholate water solution, consist in GRMs with thickness between 4 and 7 graphene layers [22]. Raman spectra performed on these materials also show the absence of basal defects and oxidation of the final material invariantly from the changing the shear conditions. Modelling of the HSM showed that the minimum shear rate able to obtain FLG is proportional to  $10^4 \text{ s}^{-1}$  independently from the diameter and the velocity of the mixer. This result is due to the fact that the parameters which affect significantly the HSM process are the surface energy of GNP and the viscosity of the solvents. Coleman and co-workers also tried to scale up the HSM and, considering that the yield of the process is proportional to the energy dissipated per volume unit, they established that HSM is more efficient than LPE when the considered volumes reach 300 L. However, the yield of shear exfoliated graphene (SEG) is below 0.1% and a lot of cycles (150 min, 1500 rpm) need to be conducted in order to obtain a 3% yield of exfoliated graphite [22]. Notwithstanding this, SEG may be used as additives in melt compounded composites in order to increase mechanical properties [22], or to produce nanopapers able to substitute the Pt/In oxide electrode in dye-sensitized solar cells [22].

The most important drawback of liquid phase exfoliation is the limited control over the exfoliation process, which results in a polydisperse mixture of graphene, GNP and unexfoliated graphite. Hence, a size selection step is required. Liquid cascade centrifugation is a useful technique for separate GRMs with different thickness. The technique consists in the sequential centrifugation of the solution [23]. At the end of each step, the supernatant is collected and used for another centrifugation. As a result, each sediment contains nanosheets with a defined range of thickness. Another type of size selection is the density gradient centrifugation. The size selection can be avoided if the microfluidization technique is adopted for the exfoliation of graphite. Micro-fluidization is often used in food industry [63], cell disintegration [64] but recently it has been employed to produce conductive graphene inks [65]. Microfluidization is a high-

pressure process where the graphite particles pass through channels with a diameter smaller than 100  $\mu\text{m}$  [66] (Figure 4).

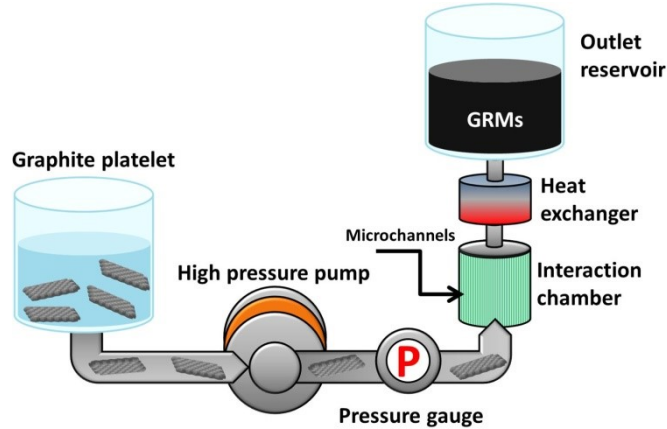


**Figure 4** Scheme of a microfluidization system.

As compared with high shear mixing and LPE, micro-fluidization is more efficient in the production of few layered graphene because exploit a shear rate higher than  $10^6 \text{ s}^{-1}$  which is applied in the whole batch avoiding centrifugation and washing processes. In 2017, Karagiannidis and co-workers demonstrated the exfoliation of graphite in sodium deoxycholate to 10% wt GNP suspension with a concentration of 100 g/L and thickness between 4 and 70 nm. The resulting FLG suspensions were used for the production of conductive inks, as the conductivity of GNP was not compromised by the oxidation, which do not occur during the exfoliation process [65].

## 1.1.2 Bottom-up approaches

### 1.1.2.1 Growth on Silicon carbide

The production of graphene from SiC was reported since 1896 [67] and the growth mechanism was studied since 1960s [68]. It consists in the thermal decomposition of silicon at 1000°C with the consequent migration of C atoms to the surface, making the graphite film (Figure 5) [69, 70]. Modulating the temperature, the time of application and the cooling rate it is possible to predict the thickness of the obtained multi layered graphene (MLG). In this way, it is possible to synthesize high surface MLG with an order on magnitude of  $\text{cm}^2$ . The resulting multilayer is bonded to the silicon surface through a “buffer layer”, that is formed by  $\text{sp}^3$  carbon atom arranged in a honeycomb lattice and it can be remove by hydrogen intercalation [71]. Graphene and few layered graphene sheets can be obtained by confining SiC in a graphitic enclosure that limits Si escape and favours the presence of high Si atmosphere. These conditions are close to the thermodynamic equilibrium for the production of graphene and multilayers in cm scale [72].

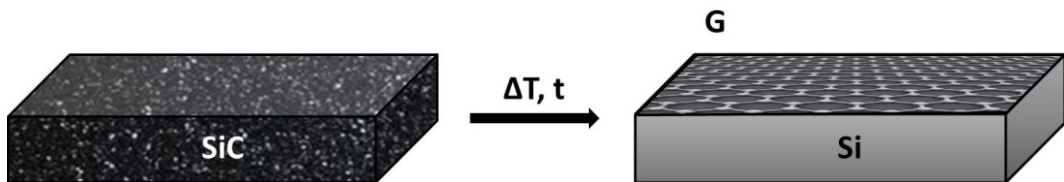


**Figure 5** Graphene growth silicon carbide mechanism.

This procedure is very useful when Si is used for electronic devices because of all the operations are compatible with the environment of semiconductor. Unfortunately, the high cost of SiC and the difficulties in transferring SLG from Si to other substrates affect the industrial scalability of the process.

Even if there is a huge difference in lattice distance between Si-C (3.073 Å) in SiC and C-C in graphene (2.46 Å), the graphene or MLG growth on SiC can be considered as a particular type of epitaxial growth, because in the process the carbon atoms rearrange themselves in an hexagonal lattice as Si evaporates from SiC [73].

### 1.1.2.2 Chemical Vapour Deposition

Chemical Vapour Deposition (CVD) is extensively used to growth or deposit crystalline or amorphous films from liquids, solids or gaseous precursors on a substrate. The deposition conditions depend on the physical state of the precursors that is deposited. For these reasons, a list of CVD procedure was developed looking to the low cost and the quality of the deposited coating. In the case of graphene, the most employed CVD techniques are (Figure 6):

- Thermal CVD (T-CVD)
- Plasma Enhanced CVD (PE-CVD)

The first T-CVD graphene growth was conducted exploiting the thermal catalytic decomposition of methane and the low carbon solubility on a Cu foil [74]. After the decomposition of methane, the carbon atoms have been deposited on the Cu surface as nuclei which grow in large domains up to  $1 \text{ cm}^2$ . It was demonstrated that the nuclei density is a function of the temperature and the pressure. However, when the Cu surface is fully covered, the films become polycrystalline. Moreover, the differences in thermal expansion between the graphene and the substrate affect the topography of the deposited carbon films. As an example, the thermal expansion coefficient of Cu is an order of magnitude higher than the graphene and during cooling a significant wrinkle density can be detected by Raman spectroscopy [75]. Single crystal substrates were considered for graphene growth by CVD but the high cost on this type of substrate make them not suitable for large scale production. Graphene films with size of 50 cm were produced on copper and transferred via roll to roll [76]. The goal is now to grow high quality single crystal sample with a  $1 \text{ mm}^2$  crystal size.

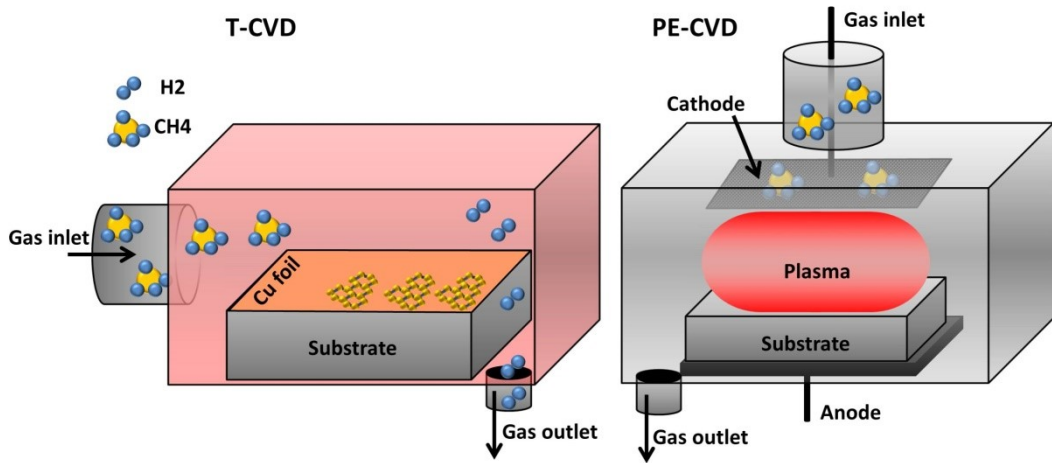


**Figure 6** Thermal-CVD and Plasma Enhanced-CVD scheme.

PE-CVD is one of the most common strategy adopted for graphitic material because the contact between the plasma and the surface favours side reaction which limits the quality of graphene layers [77]. This technique is cheaper than thermal CVD because it avoids the use of a catalyst for the hydrocarbon's decomposition. In this way, the purification step of the coating from the metal catalyst is avoided, but only high defective GRM can be obtained and PE-CVD needs to be more improved. CVD is remarkably a high cost-effective technique if compared to the other reported previously and is not suitable for large-scale production, but developments of new deposition procedure can explain its use in a wide range of application. CVD graphene can be employed for nanotechnology application as well as transparent conductive layers and sensors.

### 1.1.2.3 Chemical synthesis of GRMs

Chemical synthesis of graphene is useful to produce graphene nanoribbon and doped graphene, such as fluorinated-graphene. Depending on the precursor it is possible to scale-up the synthesis towards the formation of micro-sized GRMs, graphene nanoribbons and 3D superstructures. The concept behind the bottom-up synthesis in solution relies on the synthesis of large poly aromatic hydrocarbons, which are often named nanographenes [78, 79]. The reaction is based on the intramolecular oxidative cyclodehydrogenation of polyphenylene polymers. The most critical issue is to achieve a high molecular weight of the precursors because it is directly proportional to the number of repeating units and, as a consequence, to the length of the final graphene nanoribbon. The width of the final nanoribbon is determined by the monomer dimension itself. Polyphenylene polymers can be prepared by Diels-Alder [80], Suzuki or Yamamoto polymerization [81]. Solution synthesis of graphene nanoribbon by Yamamoto reaction enable the synthesis of precursors with 52 kDa higher molecular weight than the one obtained with Suzuki reaction. The cyclodehydrogenation of polyphenylene polymer precursor is carried out by the cyclodehydrogenation mediated by  $\text{FeCl}_3$  named Scholl-reaction [80].

Chemical synthesis of graphene in nanoribbons can be performed on surfaces [82] (Figure 7). The most important parameter is the purity of the precursors in order to avoid undesired coupling with impurities, and the cleanliness of the surface. Generally the most used are Au(111) single crystal or Au on mica (200 nm thick). The reaction is divided in 4 steps conducted in ultra-high vacuum ambient [83-86]: the precursor's deposition (1) is followed by the activation (2), general a halogen cleavage, after that the polymerization starts (3) until the cyclodehydrogenation occurs (4). Steps from 1 to 3 can be combined in a single step by depositing precursor's monomers at the polymerization temperature. In step 4, the control of the temperature is crucial in order to avoid crosslinking between nanoribbon chains (Figure 7). It was demonstrated that at the temperature of 973°C a covalent crosslinking between nanoribbons can occurs on Au(111) substrate [87].

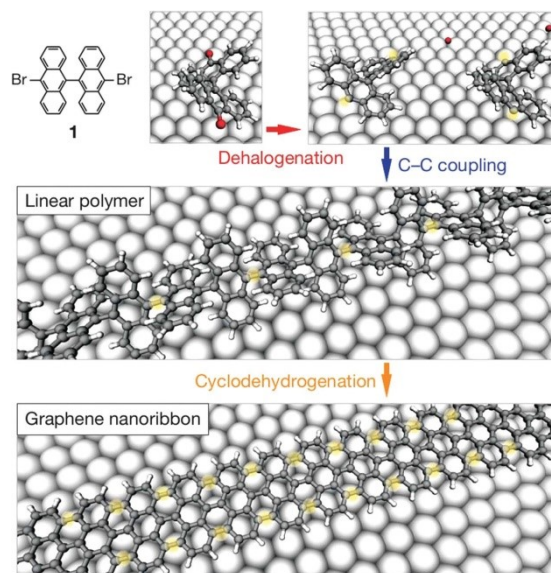


**Figure 7** Bottom-up fabrication of Graphene nanoribbon on surface starting from 10,109-dibromo-9,99-bianthryl monomers (1). Figure reprinted with the permission of Springer Nature from ref.[88].

Another bottom-up synthesis pathway is the conversion of self-assembled monolayer (SAM) in graphene- and carbon nanomembranes. The SAM is formed on a solid substrate [89] and then it is converted to a carbon nano-membrane by electron irradiation (Figure 8). The graphene membrane is obtained after carbon nano-membrane pyrolysis (800°C, in inert atmosphere) [90].

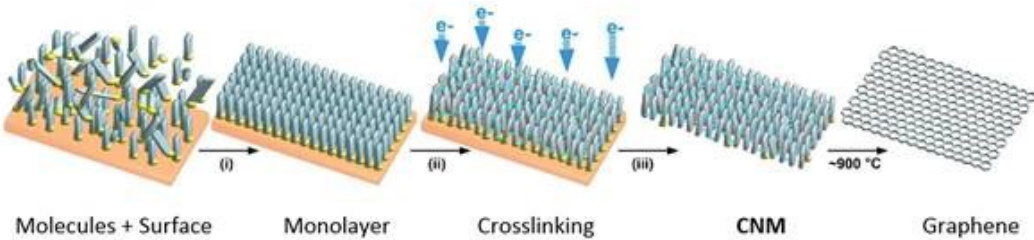


**Figure 8** Fabrication of graphene from SAM deposition on surface. Reprinted with the permission of Wiley and Sons from ref [89].

The self-assembly of aromatic molecules can be performed by vapour phase deposition or from solvents. The process is generally carried out using an

aromatic thiol adsorbed on a metal surface (often Au). Both the methods lead to a good quality SAM formation but, normally, solution deposition achieves a 5% higher packing density for the monolayer. Moreover, the solvents molecule interactions [91] play an important role and the packing density of the SAMs can be adjusted by tuning the solvent polarity and the precursor concentration [92]. The vapour phase deposition is preferred when the adsorption of the aromatic molecules can favour the oxidation of metal substrate, like happens in thiols adsorbed on Cu or Ni. In addition, vapour phase deposition takes only 1h, so it is much more faster than the solvents assisted SAM deposition which takes until 3 days [93]. Electron irradiation of aromatic SAMs results in lateral crosslinking of the constituting molecules and formation of carbon nano-membranes (CNMs) [90, 92, 94]. The mechanisms of the electron irradiation induced crosslinking are in detail discussed in [90] and were reviewed in [95]. CNMs possess an extremely high (up to 800 K), thermal stability [89], which enables their conversion into graphene/GRMs *via* pyrolysis in vacuum or in inert atmosphere [92, 96]. The formation of nano-crystalline GRM sheets by annealing of free-standing CNMs on TEM gold or silicon oxide grids is also described in literature [97, 98]. The thickness of the graphene sheet depends strongly on the structure of the precursors, their ability to form SAMs and to be cross-linked in carbon nanomembranes. Thus, by varying precursors, the thickness of the formed nano-crystalline GRM sheets can be tuned by a factor of ~3 [92]. The resistivity correlates with the thickness of the GRM sheets, with lower resistivity for thicker sheets [92, 97].

Despite the customizable design, graphene obtained by chemical synthesis tends to form insoluble aggregate. This phenomenon can be limited acting on the functionality of the monomer. For example, the use graphene-precursor functionalized with long side chain can favour the solubilisation of the aggregate. However, this expedient works only for small graphene molecules because increasing size the attraction forces between graphene surfaces exceed the interactions, which occur in solubilisation. A valid alternative is the employment of molecules with high aromatic core, which can interact strongly with graphene by  $\pi$ - $\pi$  interaction in many of organic solvents. The most interesting and newest synthetic protocol considers the growth of graphene monolayer on the surface of an insulator for the preparation of graphene origami. Although the chemical synthesis of GRMs is stimulating for chemists, more in depth-analysis is needed in order to study the growth mechanism and stabilize protocols towards industrial production.

### 1.1.3 Final remarks of different synthetic methods for graphene related material

As it was presented in the last sections, graphene and related materials can be prepared using a wide range of techniques as a function of the final application. It has been shown that bottom up approaches can be suitable for the preparation of graphene at laboratory scale. In particular, chemical synthesis can yield graphene

but reaction conditions need to be very carefully controlled in order to avoid side reactions which can contaminate the final products. In addition, the reported procedures are not optimized for the production of graphene in large scale amount.

Growth on metals or SiC are an alternative but the transfer process from the synthesis substrate to the one of application is still difficult and expensive, because requires multistep procedures [99]. Moreover, the use of SiC as substrate is expensive making this procedure less attractive for industrial application. In contrast, CVD is a promising approach to growth 2D crystals and heterostructures as a function of the final application [99]. However, the proposed processes need to be optimized towards the production of large scale single crystal graphene because the CVD chamber dimensions limit the available surface for graphene growth. Notwithstanding this, GRMs synthesized by CVD techniques can be used in microelectronic and for fundamental studies. On the other hand, micromechanical exfoliation of graphite is also limited because it depends on the adhesive tape and graphite precursor dimensions and the obtained graphene is generally used only for fundamental studies.

Among all the considered approaches, liquid phase exfoliation can be adopted as a versatile tool for synthesize large amount of graphene and GRMs with a concentration up to 1g/L and a definite aspect ratio. However, the bath-sonication and tip-sonication scalability is not yet demonstrated. Moreover, the highly time-consuming procedure and the high cost of the systems make these techniques unsuitable for industrial applications. In contrast, microfluidization is currently very attractive because it allows to obtain suspensions where the distribution of lateral size nanoparticles depends on the number of microfluidization cycles. Adopting microfluidization is possible to prepare suspensions with higher concentration of GNP than conventional LPE (compare 1 g/L to 100g/L) which can be used as inks and easily printed, spin coated or deposited by dipping on a substrate like polyethylene terephthalate in order to obtain transparent membranes and flexible electronic devices. However, microfluidization is very expensive because requires a high amount of energy for function. In conclusion, the different techniques proposed for the production of graphene related material needs to be further developed because the exploitation of graphene and GRMs at industrial level requires large-scale production capabilities.

In 2017, the Frost&Sullivan agency published a report focused on the global graphene market, including forecast to 2025 [100]. In that work, they showed that there are two general methods for synthesize GRMs in industry: the oxidation of graphite followed by reduction, and the chemical synthesis. The first is conducted by mechanical or chemical exfoliation to form graphite oxide that could be gradually exfoliated to graphene oxide. The graphene oxide is then reduced to rGO using chemical, electrochemical or thermal processing. However, a 100% exfoliation to graphene oxide or to reduced graphene oxide is never reached, thus the obtained products are employed for the production of nanoplatelets, inks and composites. The chemical synthesis of graphene is conducted by CVD but the process consists of a multistep procedure and requires a transfer process from the

synthesis substrate to the one of the final application. This procedure is also limited to the size of the CVD chamber and it is often used for microelectronics, where generally the transfer process is avoided because the synthesis substrate coincides to the one of final application. From 2017, many industries moved to supplying graphene from mining (i.e. AMG mining and Advanced Northern Graphite Leaders), to synthetic graphene (i.e Cealtech). The most forward-thinking industry have focused their production towards the synthesis low defective graphene (i.e Advanced Graphene Products worked in partnership with the Lodz University of technology for developing high-strength metallurgical graphene, where graphene is crystallised on a liquid metal surface, enabling more freedom of movement for each carbon atom. This leads to very few defects over large areas, being monocrystalline up to 1mm). Notwithstanding this, the high interest towards the graphene industry is growing slowly because:

- the difficulties in producing low-defective graphene in large quantities lead to high cost;
- the main customers are R&D Institutions with a relatively low consumption;
- the lack of focus on final application resulting from the varied possibilities of graphene that limit the growth rate in industry.

In order to overcome this restrictions, Frost&Sullivan also suggested a series of market drivers for the period 2018-2025 like the R&D funding towards scalability studies, the crossing of the processing limitation and production development and the limitation of market fragmentation [100].

## 1.2 Graphene and related materials: properties vs. defects

Depending on the synthetic method, graphene may be affected by various concentration and type of structural defects, which can be divided in 0-dimensional and 1-dimensional defects. 0-dimensional defects are point defects and consist in Stone-Wales defect, vacancies, ad-atoms and substitution. 1-dimensional defects, or line defects, are edge dislocations and grain boundaries. All defects presented in this section were evaluated by transmission electron microscopy.

Stone-Wales defects (SW) are formed by an in-plane 90° rotation of a C-C bond with respect to its midpoint. This rotation results in the transformation of four adjacent hexagon into two separated pentagons and two heptagons which share the rotating bond [101] (Figure 9 a). This defect is indicated like SW(55-77) and density functional theory predict a formation energy of 5 eV [102]. SW defects are stable at room temperature and can be imaged by aberration-corrected transmission electron microscopy (Figure 9 b).

Vacancies can be divided in single, double or multiple and are point defect in which one or more atoms are missing from the lattice.

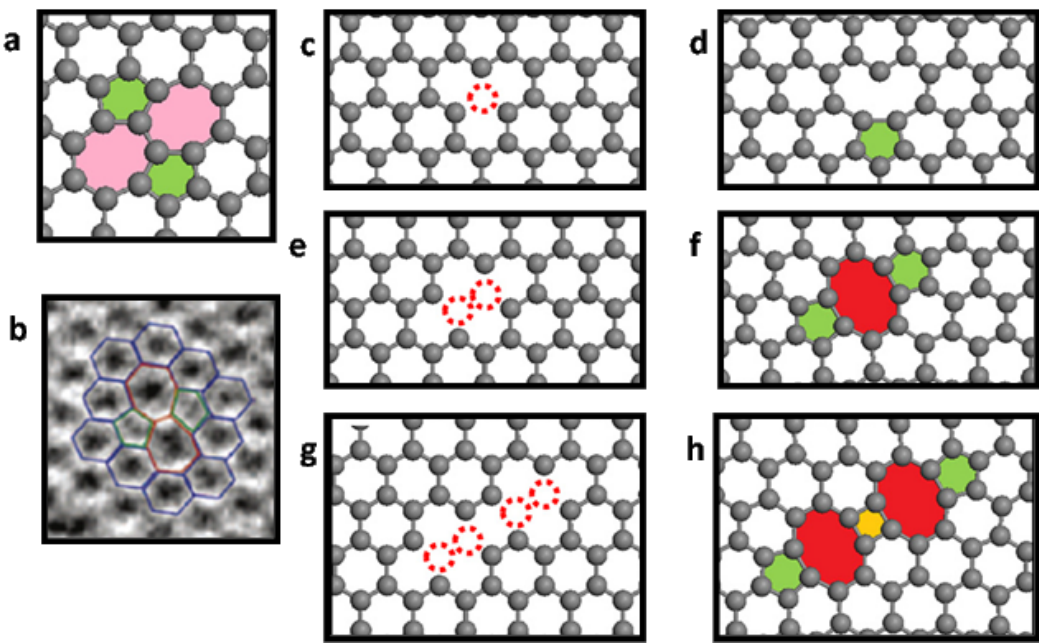


**Figure 9** Atomic model of a) Stone-Wales defect and AC-TEM micrograph; c)-d) single vacancies, e)-f) di-vacancies, g)-h) multi-vacancies before and after reconstruction; Figure is adapted from [103] with permission from Elsevier. b) is adapted from [104] Copyright (2008) American Chemical Society.

A single vacancy leaves three edge atoms with dangling bonds (Figure 9 c). Such a metastable configuration point to Jahn-Teller distortion in order to lower the overall system energy by removing electronic degeneracy [105]. Two of the three dangling bonds are restored by bonding themselves leading to a formation of a pentagon and a nonagon (Figure 9 d), while the third remains dangling. The pentagon formation introduces a contraction which is transmitted to the nonagon that pushes the dangling bond out of plan in order to preserve the bond length. In this way, the energy of the system is minimized and the single vacancy formation energy was calculated to be 7.5 eV [106]. Double vacancies can be obtained by the coalescence of two single vacancy or by the removal of one of the neighbour atoms (Figure 9 e and f). [106]. Generally, multi-vacancies where all bonds are saturated after reconstruction are more stable than the ones with dangling bonds. Besides, multi-vacancies can be considered as a dislocation and zig-zag or armchair orientation can be detected at the edges [107] (Figure 9 g, h). When it happens, hydrogen atoms or chemical groups can react with dangling bonds saturating them and chemically modifying the graphene properties.

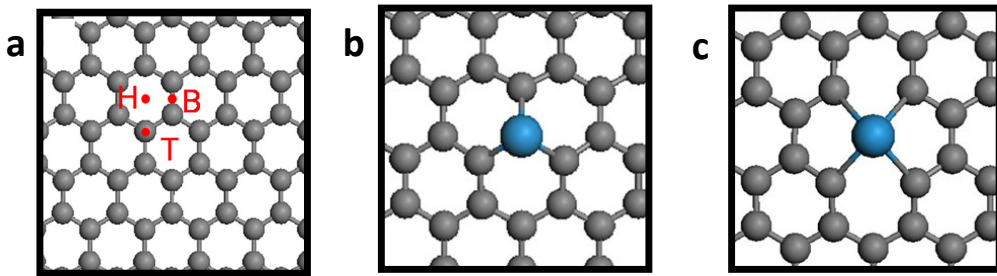


**Figure 10** a) Configuration of a carbon ad-atom in different symmetry. Configuration of ad-atom adsorbed on b) single vacancies and c) double vacancies. Figure is adapted from [103] with permission from Elsevier.

In graphene, additional carbon atoms can find three thermodynamically favoured position over the plane layer. These positions have high symmetry and are: in the middle of the bond between two carbon atoms, named the bridge, directly on top of one carbon atom ,named the T-site and finally in the centre of the hexagon, the H-site (Figure 10 a). When a carbon atom is in proximity of a perfect graphene sheet localized  $sp^3$  hybridization may occurs locally and the ad-atoms can be bond to the sheet. Obviously, the formation energy depends on the number of as-formed bonds. It was calculated that a formation energy of a bridge is lower than 7eV [102]. For a T-site it was calculated to be between 0.5 and 1 eV meanwhile H-site is the most unstable requiring 8eV [102]. Density functional theory calculations have predicted that H-site are favoured position for metals and transition metals with partially filled d shell such as Ti, Fe, Co, Ni, whereas B-site are favoured for non-metallic elements and transition metals with a filled or almost filled d shell. T-site are favoured for hydrogen and haloids [108].

Carbon atoms can also be substituted by other atoms in the lattices on graphene sheet (Figure 10 b, c). Obviously, the substitution depends on the atomic radius of the substituent, so boron and nitrogen are the best candidates in this sense. However, other atoms can be introduced in the lattice, when there are some insaturations caused by vacancies. In this way, sulphur, silicon, transition metals (like vanadium, chromium, manganese, cobalt, gold, and copper), can form covalent bonds with surrounding undercoordinated carbon atoms. The binding energy for this systems was calculated to be in the range between 2-8 eV [109].

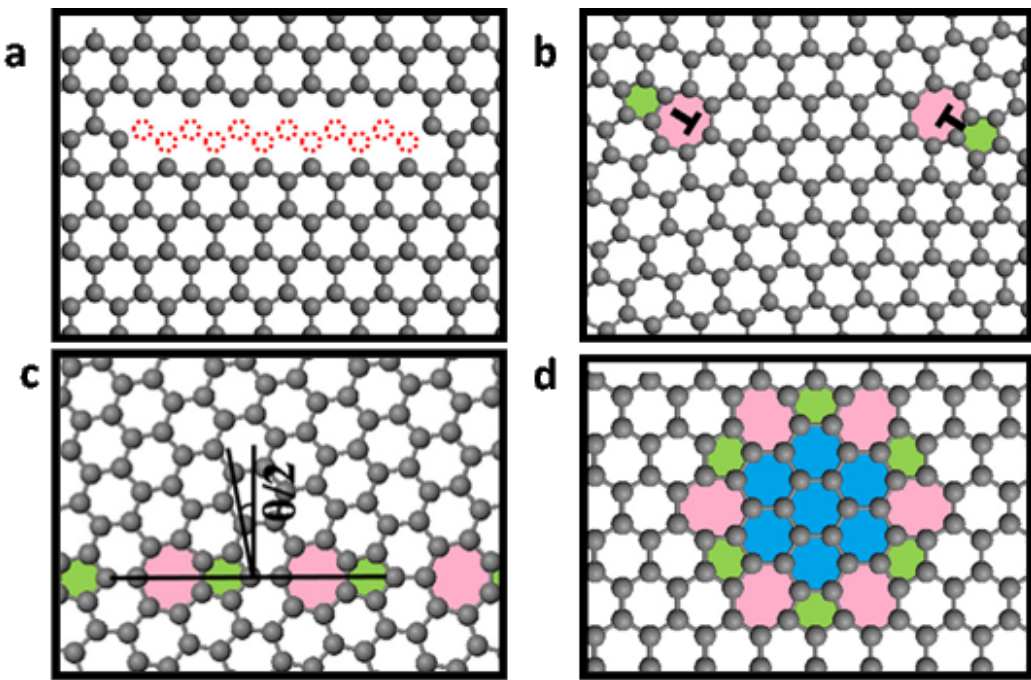


**Figure 11** Modelling of a dislocation a) before and b) after reconstruction along zig-zag direction. Example of a) symmetric grain boundary and b) closed flower-type grain loop defects. Figure adapted from [103] with permission from Elsevier.

Dislocations in graphene can be obtained after the reconstruction of a vacancy chains, which can migrate along their zig-zag or arm chair direction resulting in

edge dislocation (Figure 11 a, b). Even if some computational modelling have been proposed [110], this type of defects need to be more investigated. In contrast, grain boundaries have been well understood and are often observed in CVD growth graphene. Grain boundaries are line defects separating two grains whose lattice are tilted relatively to each other by an angle whose tilt axis is perpendicular to the graphene plane. It is also considered as a line of reconstructed point defects. As an example it was shown that for a CVD growth graphene on nichel grain boundaries are obtained by pairing single vacancies in order 5-8-5 [111] (Figure 11 c). More exotic boundaries, like flower structure, have been detected as a loop of vacancies [112] (Figure 11 d) but this configuration needs to be still investigated.

Despite the most recent experimental and computational researches are focused on graphene defectiveness, graphene related materials are also affected by the same defects of graphene. The presence of defects in graphene related materials depends strongly on the approach selected for their preparation. As an example, top down approaches allow to obtain flakes with an aspect ratio that depends on the grain boundaries of the precursors (graphite or graphite oxide).

The reasons for the interest in graphene are related to the high appreciable amount of properties condensed in the same material; nevertheless, properties are strongly dependent from the nature and the concentration of defects. Several peculiar features of graphene were predicted and, in some cases, measured with high confidential level to the expected values. However, the literature production about fundamentals studies is focused only on graphene or at least on 2 layers graphene, generally indicated as BLG (bi-layer graphene), leaving a gap in knowledge when the number of stacked layers is increased but lower than in graphite. Defects affect significantly graphene properties due to the change in the electronic state of the material. For example, it has been demonstrated that carrier mobility at room temperature is  $2.5 \times 10^5 \text{ cm}^2 \text{V}^{-1} \text{s}^{-1}$  and reached  $6 \times 10^6 \text{ cm}^2 \text{V}^{-1} \text{s}^{-1}$  at 4K due to the fact that the charge carrier in graphene are Dirac-like particles and the high symmetry of the honeycomb structure guarantee the absence of a band gap. However, these amazing properties are valid only for a perfect single sheet. Stone-Wall defects lift the degeneracy of the band at the Fermi level and open up a non-zero band gap suitable for transistors applications [113]. Vacancy acts as scattering centres also for the electron waves resulting in a drop of conductance. Although, the configuration of vacancy affects the electronic transport in different way [114]. Experimentally, it can be measured by local density state by scanning tunnelling microscopy [115]. Grain boundaries may affect the electronic properties of graphene generating scattering with non-linear behaviour. In addition, the resulting broken electron-hole with the inversion of symmetry can promotes thermo power at local rectification affecting the high current performances. Transport measurements on isolated individual grain boundaries confirm that grain boundaries result in higher electrical resistance although the increase of resistance can vary across different grain boundaries [112].

The thermal conductivity of graphene is dominated by phonon transport but depends strongly on the presence of defects, edge scattering and isotropic doping.

In addition, the presence of sample fabrication residues can cause phonon scattering and localization. The intrinsic thermal conductivity of suspended graphene varies in the range between 2000 and 6000  $\text{Wm}^{-1}\text{K}^{-1}$  at room temperature and approximately 600  $\text{Wm}^{-1}\text{K}^{-1}$  for graphene supported on  $\text{SiO}_2$  substrate [116]. In graphene, the thermal conductivity is also affected by the grain size and presence of defects. Stone-Wales defects make the thermal conductivity anisotropic due to the symmetry breaking and quenches the thermal conductivity by reducing the phonon mean free path at low temperature, whereas phonon-phonon scattering over the Brilloin zone becomes predominant at room temperature and above [117]. Only 25% of vacancies can reduce the thermal conductivity by 50% [118]. The thermal properties deterioration is dependent from the defect density. The presence of heteroatoms has been demonstrated to decrease the thermal conductivity of graphene. As an example, in 2016, Mortazavi et al. [119] demonstrated that in N-doped graphene, sharp reduction in graphene thermal conductivity occur up to 0.5% concentration of defects followed by a plateau trend for higher defects concentrations. Increasing the number of stacked layers, the thermal conductivity decrease approaching the value of bulk graphite ( $100\text{-}400 \text{ Wm}^{-1}\text{K}^{-1}$ ). The reduction of thermal conductivity in graphite nanoplatelets is due to the more phase-space states becoming available for phonon scattering and as well to the changes in phonon dispersion. In this context, the newest trend in experimental research is focused on the functionalization of graphite nanoplatelets edges in order to improve the mean free path of phonon [120] or to the thermal annealing of rGO at  $1700^\circ\text{C}$  in vacuum as responsible of a decrease in the nano-flake defectiveness [121].

A perfect graphene is formally a chemically inert material because of the  $\text{sp}^2$  hybridization and the perfect geometrical disposition of atoms in the inner part of the surface favourite the best stable thermodynamic state. In contrast, the edges may be considered always defective. In presence of defects, the graphene electronic state changes becoming reactive to atoms and molecules of different nature. Stone-Wales defects act as adsorption site, DFT calculations predict that their presence has a strong influence on hydrogen chemical reactivity [122, 123], the process is thermodynamically favoured because Stone-Wales defect makes energy neutral the hydrogenation process. Therefore, there is a lot of attention for H-storage of these material. Analogously Li, Na, Ca can be adsorbed on Stone-Wales defects [124, 125] because of the increased charge transfer. This behaviour open the possibility of use Stone-Wales defective graphene as high-capacity anode material for Li-, Ca- Na-batteries [124, 125].

Dangling bonds of vacancies have high reactivity towards hydroxyl and carboxyl functional groups [126] making possible the oxidation of graphene to graphene oxide. This behaviour is due to the fact that, vacancies can coalesce to line defects, that can migrate to the edge leaving dangling bonds able to react with oxygenated functional groups.

Mechanical properties of both graphene and related materials are also affected by the presence of defects. Graphene shows a tensile strength of 130GPa which make it the strongest known material measured by nano-indentation with AFM.

Graphene also takes  $48000 \text{ kNmkg}^{-1}$  specific strength before breaking, comparing to steel it is more or less 200000 times stronger, making graphene desirable for lightweight application. Experimental and computational studies confirm that vacancies decrease the Young modulus and the tensile strength. The Young modulus is decreased with the concentration of single vacancies higher than double vacancies and single vacancies are mode detrimental at low concentration because of the higher number of undercoordinated atoms than in di-vacancies. The distribution of vacancies has also an effect: adjacent vacancies can coalesce to form holes vacancy so there will be predict a drop in stiffness and strength [119].

### 1.3 Graphene and graphene oxide barrier properties towards gasses

It was demonstrated that graphene is impermeable to gas, making it attractive for gas barrier application, typically in combination with flexible materials (e.g. organic polymers) for different types of packaging. In 2008, Bunch and co-workers showed that graphene membranes exhibit no measurable permeability to helium and that graphene can support a pressure difference higher than 1 atmosphere [127]. The high gas barrier properties of graphene are related to the electron density of aromatic rings that is too high for allow the penetration of gas molecules [128]. As an example, when helium is considered, the single crystal graphene monolayer energy barrier was calculated to be 18.8 eV by Local Density Approximation (LDA). The kinetic energy of a helium atom is 18.6 eV, so it is smaller than the energy barrier penetration. In addition, because of obtaining single crystalline perfect graphene is really difficult, LDA was employed for the calculation of defects energy barrier (Table 1).

**Table 1** LDA calculation of Energy barrier in graphene defects.

Defect	Energy barrier [eV]
<b>Stone-Wall</b>	9.21
<b>858- di-vacancies</b>	4.61
<b>Tetravacancies</b>	1.20
<b>Hexavacancies</b>	0.37
<b>Decavacancies</b>	0.05

Even if in defective graphene the energy barrier decreases exponentially, the defects' energy barrier are still too high for allowing to a He atom to pass through a graphene plane [128]. In addition, the geometric pore diameter of carbon rings accessible for gas permeating molecules, corresponding to  $0.64 \text{ \AA}$  [129] in terms of electron density, is smaller than the kinetic diameter of various gases (Table 2) [128].

**Table 2** LDA calculation of gas atoms and molecules kinetic diameter.

Gas	Kinetic Diameter [Å]
He	2.6
H <sub>2</sub>	2.9
CO <sub>2</sub>	3.3
O <sub>2</sub>	3.5
N <sub>2</sub>	3.6
CH <sub>4</sub>	3.8

On the basis of this information, graphene appears to be an ideal candidate for enhancing gas barrier properties when deposited on polymer substrate. Unfortunately, the use of single crystalline perfect graphene is very difficult because, as already discussed, graphene produced by CVD on metals is defective. Moreover, graphene synthesized by this approach needs to be transferred from the substrate to the new one and during transferring the generation of defects is likely to occurs. Notwithstanding this, few layered graphene sheets can be successfully employed as gas barrier membrane because the gas molecules pass through the grain boundaries and the defects but, due to the molecular sieving mechanism occurred between stacked layers, the gas permeability normally decreases with the number of stacked layers [130, 131]. Few layered graphene sheets coating have been employed as metal protecting layer for copper foils in order to protect metals from corrosion [132, 133], oxidation [134-136] and degradation in electrochemical systems [137]. Chemical modification of graphene defects can be performed with the aim of prepare selective membranes. For instance, Jiang et al. [138] have prepared hydrogen functionalized vacancies (2.5 x 3.8 Å) in a graphene layer in order to decrease the electron density in the vacancy and permit to methane to pass through. They obtained a H<sub>2</sub>/CH<sub>4</sub> selectivity of about 10<sup>23</sup> at 300K, but up to now vacancies can be prepared focusing the electron beam of a TEM which is a very expensive process affected by a high grade of error.

Graphene oxide can also be used as well for gas barrier applications. However, some considerations about its chemical structure need to be done. Graphene oxide is a graphene sheet functionalized with hydroxyl and epoxy groups in the basal plane whereas carboxylic and carbonyls groups are generally located on the edge. The presence of this functionalization introduce disorder in the graphene lattice and can be considered as defects. In addition, the presence of oxygen functionalizations makes graphene oxide 1-1.4 nm thick [139, 140], more or less 3-4 times thicker than graphene. Freestanding graphene oxide sheet do not allow to gas molecule to pass thought the plane as it was for graphene, because of the high potential energy barrier. However, the presence of vacancies and other defects in graphene oxide layers induce gas penetration through the film especially for smaller molecules. As a consequence, when graphene oxide sheets are stacked, gas molecules can permeate crossing grain boundaries or along the

interlayer space which is higher than in graphene, because of functionalization on the basal plane [141]. The ability of GO based film to act as a barrier is favoured by the GO aspect ratio: the higher the surface/thickness ratio is, the longer will be the diffusion path for gas molecules. Oxygen-based functionalization in graphene oxide also affect the stacking properties: differently from graphene, graphene oxide stacking is governed by hydrogen bonding which is longer than Van der Waals and the interlayer space is increased. In addition, these functional groups are polar and can trap water in the interlayer spaces. For these reasons graphene oxide barriers suffer in humid conditions [142]. The two main strategies to overcome this problem are the complete elimination of interstitial water or the complete removal of oxygenated functional groups that is explained as a reduction of GO to rGO. Of these two methods, the complete dehydration is only ideal, even if a lot of reduction process have been developed for the removal of oxygenated functionalization. Unfortunately, the resulting rGO nanoparticle are not well aligned and the gas barrier properties are decreased as compared to the same GO film. Moreover, particles tend to wrinkle meaning that the overlap of different nanoparticles is not efficient and voids can be introduced in the film. The presence of these voids increases the gas permeability of the films because it permits to the gas molecules to pass through the films easily.

## **1.4 Gas barrier properties in nanocomposites containing graphene and related materials**

Most of the non-durable consumer goods needs to be packaged both for operational reasons, like transport or handling, and for protection against pollutants. For example, one of the most important functions of food-packaging is the barrier to gases such as oxygen which can modify the taste of food while, accelerating its degradation processes. The most commonly used polymers for food packaging are polyethylene (PE) [143], poly(ethylene terephthalate) (PET) [144], polypropylene (PP) [143] and polystyrene (PS) [145] because of their high mechanical properties and affordable costs. However, despite their high processability, the very low gas barrier properties (from 20 to 200 cc/ m<sup>2</sup>day atm of Oxygen transmission rate in 0% relative humidity conditions and water vapour transmission rate) towards oxygen and water-vapour, limit their use as packaging for innovative technologies. For example, high barrier performances are required for packaging of electronic devices such as OLEDs where the presence of oxygen and moisture can degrade the organic components. For these reasons, new and high performing packaging solutions are required in order to meet the stringent criteria for improved shelf-life of goods and durability of devices. Moreover, in addition to extreme gas barrier, other properties such as optical transparency, flexibility, durability, chemical stability, accessible cost and an easy industrial processing are necessary for ideal packaging material.

Although polymeric films allow satisfying many of the properties mentioned above, multimaterial films needs to be adopted for reaching at high barrier

process. As an example, polymer-laminated aluminium packaging materials are widely used in commerce because of their excellent gas barrier properties and mechanical resistance. In addition, polymer multilayers such as PET/EVOH/PE laminates are commercially available because of their good gas barrier properties (OTR of 1 cc/m<sup>2</sup> day atm, in both dried and humid conditions) [145]. However, regardless of the advantages accomplished by utilizing the multilayer films, the reusing and recycling of such sort of material are extremely troublesome. In order to overcome these limitations, nanotechnology has been proposed as valuable strategy capable of improving the gas barrier properties by means of bulk or surface nanostructuring approaches. In this field, the properties of graphene and its related materials have attracted a lot of interest. Nowadays, the graphene-polymer nanocomposites preparation can be performed by introducing GRMs in bulk or confining them only on the surface. Both strategies will be described separately in the following sub-chapter.

### 1.4.1 Bulk nanocomposites

The employ of GRMs to produce nanocomposites is driven by the necessity of introduce or improve some properties on the neat polymer matrixes and the use of GRMs is preferred instead of graphene because GRMs are cheaper and widely available. The GRM-polymer composites properties depend strongly on the nanoparticles dispersion, the bonding between the matrix and the nanoparticles, the thickness of the nanoparticle, the aspect ratio of the GRMs and the quality of GRMs as a function of the considered application. Similarly to other nanoparticles, like clays, GRMs have the advantage that only few amounts of material is needed to drastically change the properties of the neat polymer matrix.

In these years, three main methods have been developed for the fabrication of graphene-polymer nanocomposites and are commonly used: *in-situ polymerization*, *solution-mixing* and *melt-mixing*. All of these methods have been validated but, in order to select the best processing method, the GRM/polymer interaction, the solvent/GRM interaction as well as the tendency of the nanoparticles to aggregate in the operational conditions should be taken into account. Moreover, the processes scalability and sustainability need to be considered. In the *in-situ polymerization*, the GRM is mixed together with the monomer and the catalyst, if necessary. The polymerization is activated by irradiation or temperature [146, 147]. This technique confers strong interaction between the filler and the polymer thanks to the occurrence of chemical bonding [148]. The most important advantage of this technique is the good dispersion of the filler in the polymer matrix. However, in some cases the use of a solvent is necessary and additional purification steps needs to be performed [149]. In *Melt-mixing technique*, the GRM filler is added to the molten polymer matrix and mixed together at high temperature and in high shear mixing conditions. This method is used for the preparation of polyolefin-GRM nanocomposites, however because of the poor dispersability of the filler in polymer matrix, others methods are normally preferred [150-152]. *Solution mixing* is the most used technique for

polymer-GRM nanocomposite fabrication due to its facile processability in water or organic solvents [146]. It consists in the solubilisation of the filler and the polymer in the same solvent, mixed by sonication or high shear mixing processes. As a preventing measure toward the aggregation of filler particles, it may be useful to functionalize the GRMs to make them more compatible with the selected solvents.

In section 1.3 it was explained that graphene and its related materials can be used as additives in polymer nanocomposites because their excellent barrier properties towards gases even if in presence of defects. When GRMs are incorporated in polymer matrix, the properties of the resulted GRMs-nanocomposite are strongly dependent from the graphene dispersion in the matrix. From a theoretical point of view, the presence of low permeable GRMs nanoparticles leads to an increase in the diffusion path and in a decrease of gas permeability [153]. The same behaviour was also detected for other lamellar additives like inorganic clays. Indeed, GRMs can aggregate in the same way of layered silica nanoparticles because of their face-to-face interaction due to Van der Waals forces, also they tend to have face-to-edge interaction due to the electrostatic forces [154] in mixing solutions [155]. In addition, compared to clays, graphene related material may have larger lateral size thus resulting in higher tortuosity paths in graphene-based nanocomposites with respect to clay-based ones. Moreover, mechanical strength and thermal properties can be improved when the GRMs-based additives are properly dispersed in the matrix. Table 3 reports some examples of Oxygen permeability in graphene-based nanocomposites as a function of concentration and processing.

**Table 3** Oxygen permeability of GRMs bulk nanocomposites as function of process and quantities.

Polymer matrix	GRMs additive	Amount of additive	Processing	O <sub>2</sub> permeability reduction [%]	Ref.
PP	Graphite nanoplatelets	3% vol	Melt-mixing	20	[156]
PET	Graphite nanoplatelets	1.5% wt	Melt-mixing	99	[157]
PVA	Graphite oxide nanoplatelets	0.72% vol	Solution mixing	98.9	[158]
PET	Functionalized graphite oxide nanoplatelet	3% wt	Solution mixing	97.4	[159]
PMMA	Graphite oxide	1%wt	Solution mixing	50	[160]
PMMA	Graphite nanoplatelets	0.5% wt	<i>In-situ</i> polymerization	70	[161]
PVA	Graphite oxide nanoplatelet	0.07%vol	Solution mixing	99	[162]

<b>PLA</b>	Graphite oxide nanoplatelets	1.37% vol	Solution mixing	45	[163]
------------	------------------------------------	-----------	--------------------	----	-------

PP: polypropylene; PET: polyethylenterephthalat; PVA: polyvinyl alcohol; PMMA: polymethyl methacrylate; PLA: polylactic acid.

Looking at Table 3, is apparent that nanocomposites are never loaded with graphene or graphene oxide. This is due to the fact that obtaining this type of material in large scale and purities is quite difficult, so the employment of nanoplatelets is normally preferred. Firstly, graphite or graphite oxide nanoplatelet can be produced by a low energy exfoliation of precursors such as graphite, expanded graphite or graphite oxide and then added to the compounding mixture. This also explain why solution mixing is the most adopted techniques. Secondly, graphite nanoplatelets and graphite oxide nanoplatelets are commercial. Thirdly, mono layered additives are more defective than the multi-layered structure meaning that a high gain in gas barrier properties cannot be reached [74].

It is well known that polymers gas barrier properties depend both on the solubility of the gas in the polymer and from the intrinsic barrier properties of the matrix. However, it was demonstrated that the inclusion of nanoparticles in polymer matrix can affect the gas permeation because it can modify the path of gas molecules crossing the polymer film (Figure 12).

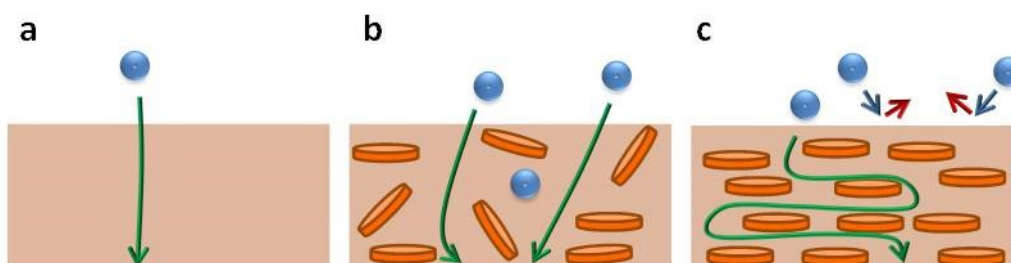


**Figure 12** Schematization of tortuosity model: a) neat polymer is permeable to a gas molecule, b) inclusion of nanoparticles is able to modify the gas molecule path in the polymer matrix; c) effect of highly oriented nanoparticles added to the polymer matrix.

This model is called tortuosity path and its efficiency depends strongly on the nature of the included nanoparticles, their dimensions and their orientation. The mathematical aspects will be described in the next section. In this context graphene and related materials can be used as nanoparticles for improve the gas barrier properties of polymer because of their high aspect ratio and energetic barrier.

#### 1.4.2 Gas barrier properties in polymer nanocomposites

From a mathematical point of view the gas barrier properties of graphene-polymer nanocomposites can be expressed using the same model proposed for the description of lamellar filler-polymer nanocomposites [164]. This can be applied not only for bulk composites but also for surface modified nanocomposites considering the surface modification region as a different section of the material.

In the literature there are some contributions to the explanation of the barrier properties of lamellar filler-polymer nanocomposites. Gas barrier properties can be described by three factors: the solubility of the gas in the matrix, the diffusion path and the permeability of the bulk. It is well known that the gas permeation mechanism is driven by the gradient of gas concentration across the nanocomposites following a diffusion-solubility mechanism. The diffusion coefficient ( $D$ ) describes the kinetic transport of the gas molecule while the thermodynamic aspects (penetrant affinity and transport) are described by the solubility coefficient ( $S$ ). According to the diffusion model the permeability of polymers can be express as:

$$P = DS \quad (1)$$

This equation is valid when  $D$  is independent from the concentration and the value of  $S$  follows the Henry's law. From a general point of view, this equation can be employed to describe the permeability behaviour of nanocomposite with impermeable fillers. In nanocomposites, it is possible to predict the penetrant solubility of gas in a film describing the solubility coefficient as the product of the solubility factor of pristine polymer ( $S_0$ ) and the volume fraction of filler ( $\phi$ )in polymer matrix:

$$S = S_0(1 - \phi) \quad (2)$$

In graphene nanocomposite, the nanoparticles act as impermeable barrier for gas motion so the diffusion coefficient needs to be expressed introducing a tortuosity path factor ( $\tau$ ):

$$D = D_0/\tau \quad (3)$$

where  $D_0$  is the diffusion coefficient of pristine polymer. The tortuosity factor can be expressed as:

$$\tau = t_m/t'_m \quad (4)$$

where the  $t_m$  is the membrane thickness and the  $t'_m$  factor is the shortest pathway for gas molecule.

As exposed earlier, the achieved gas barrier properties depend strongly on the dispersion and the orientation of the filler. If a filler arrangement oriented perpendicularly to the gas flux direction is considered, the tortuosity path can be related to the graphene nanoparticle dimensions. In particular, if graphite nanoplatelets are approximated to a rectangular of  $L$  lengths and  $W$  thickness, the diffusion path  $t'_m$  for the average number of graphene sheets ( $\langle N \rangle$ ) can be expressed as:

$$t'_m = t_m + \langle N \rangle \frac{L}{2} = t_m + \frac{t_m}{D' + W'} \frac{L}{2} \quad (5)$$

where  $D'$  is the distance between graphene nanoparticles. Combining all these equations, the permeability of a graphene-polymer nanocomposite with filler oriented perpendicularly to the gas flux direction, can be expressed as:

$$\frac{P}{P_0} = \frac{1-\phi}{\tau} \quad (6)$$

where  $P_0$  is the permeability of the pure polymer matrix.

The Nielsen model [153] further describes the tortuosity path of gaseous molecule as a function of the aspect ratio of the graphene particles and their volume fraction:

$$\tau = 1 + \alpha\phi \quad (7)$$

It was demonstrated that when  $\phi < 0.01$  permeability can be accurately predicted; however, when  $\phi > 0.01$  graphene layers tend to aggregate and the Nielsen approximation lose its effectiveness. Experimental data are in agreement with predictions made by equation 7. As an example, Kim and co-workers [165] measured the permeability of a PVA-rGO nanocomposites prepared by solution mixing and showed that the diffusivity of the PVA-rGO film follows the Nielsen model. However, this model fails when the volume fraction of the nanofiller is high and the particles tends to aggregate. In this case Cussler and co-worker [166] proposed the following  $\tau$  for a nanocomposites with graphene-based nanofiller oriented perpendicularly to the gas permeation direction as:

$$\tau = 1 + \frac{\alpha^2 \phi^2}{1-\phi} \quad (8)$$

Equation 8 has been demonstrated applicable in real case by Huang and co-workers [158] who prepared a high-barrier GO nanosheet/poly(lactic)acid nanocomposites film and reported that oxygen and water vapour permeability decreased by 98% and 68%, respectively. This result is in good agreement with the Cussler model suggesting that the GO nanosheets are mostly aligned parallel to the film surface.

In the case of multi-layered graphene embedded in polymer matrix, Cui and co-workers [164] proposed the extended form of Aris equation and explored the effects of length, concentration, orientation of nanoplatelets and the degree of delamination on the relative permeability expressing the tortuosity path as:

$$\tau = 1 + \frac{2\alpha\Phi}{3(N)} \left( S + \frac{1}{2} \right) \quad (9)$$

The mathematical modelling of graphene nanocomposites needs more investigation but actually, at this stage, the proposed models can be employed for

the prediction of the barrier properties in graphene-based gas barrier films with a good grade of approximation [164].

### 1.4.3 Surface modification of polymers with graphene and related materials

As an alternative to bulk nanocomposites, surface modification might be exploited to improve the gas barrier properties using graphene-related materials. It is well known that polymer surface is very important for both aesthetic and functional properties. Indeed, surface modifications can be employed to prevent undesired effect, as an example deterioration, or to improve a certain property (e.g. wettability, optical transparency, surface chemistry). The field of surface modification techniques includes a wide range of both chemical and physical modifications, which are well reviewed in literature [167, 168].

Beyond CVD deposition (discussed earlier), the most employed techniques adopted to deposit graphene and graphene related materials nanocoatings on surfaces are drop casting, spin coating, spray coating and Langmuir-Blodgett method. Drop casting method consist of applying a droplet of graphene based dispersion on a substrate, which can be rigid or flexible and then allowing the solvent to evaporate in controlled conditions in order to obtain a thin regular film. It is low waste process but the solvent and the substrate need to be selected very carefully in order to obtain a uniform and controlled morphology of the deposited nanomaterial. As an example, Haar et al. [169] prepared a uniform highly conductive and transparent graphene film developing the spin controlled drop casting method. Spray coating is an evolution of a drop casting process. It consists on the continuous spraying of a suspension towards the substrate by the application of a pressure to a gas used as transporter, such as compressed air. The good result of thin film deposition depends on the nature of the solvents, the particle size, the flux of transporter gas and the nozzle geometry, as well the distance between the nozzle and the substrate surface. In order to avoid speckled and uneven painted surface obtained by drop spattering, the air pressure level must be adjusted. This deposition technique can be applied to most of substrate shape. Recently, Carey et al. [170] demonstrated spray-coating of a graphene ink on the inside of a PMMA sphere, enabling transparent capacitive touch-sensors. Differently from drop casting, spin coating consist in the in the deposition of a droplet of nanosheet suspension onto a flat surface with a subsequent spinning at high speed, generally in the range of 1000-10000 rpm. In particular, a small amount of coating material is added dropwise to the centre of the substrate surface. The substrate is placed into a spin-coater and in this step can spin at low speed or not. The substrate is then rotated at high speed in order to spread the coating material by centrifugal force allowing the evaporation of the solvents. The key parameters governing the deposition process are the concentration, the viscosity of the suspension, the rotation speed and the solvent-substrate wettability [171]. GRMs spin coated surfaces are used for the characterization of the exfoliated nanoparticles by subsequent Raman spectroscopy and/or AFM

microscopy. However, in order to obtain thin homogenous coatings a high concentration of used suspensions and a high rotational speed need to be reached and, even if these prerequisite are satisfied the formation of aggregate during the drying process may occurs [172]. In addition, volatiles solvents are preferred instead of highly boiling points solvents, limiting the exploitation of this technique for water-based suspensions. Langmuir-Blodgett and Langmuir-Schaefer techniques can be employed for the production of high quality thin films with controlled packing density nanoparticle, good reproducibility and little waste of material [173]. The film must be deposited vertically in the case of Langmuir-Blodgett or horizontally if Langmuir-Schaefer procedure is considered. However, these procedures need the organization of the molecules layer on a liquid surface before the deposition which can requires days, resulting in a time consuming procedure. In details, the solution containing the selected molecules has to be added dropwise to a liquid bath where the selected molecules are not soluble, in order to permit the organization of the molecules on the top of the liquid bath. In this condition, the most stable thermodynamic configuration of the molecules implies the assembly as self-assembled monolayer. Then, the substrate is dipped in the liquid bath and during its removal from the bath the monolayer may be deposited on its surface as a consequence of the monolayer-surface interaction. Moreover Langmuir-Blodgett and Langmuir-Schaefer techniques require high pureness of components. Kim et al. [174] reported the Langmuir-Blodgett deposition of a graphene film on a SiO<sub>2</sub> as substrate. In that work, the Langmuir-Blodgett deposition was optimized to obtain deposition thickness ranging from 2 nm to 30 nm, as a function of GNP exfoliation condition and size selection. When the lateral size and the density of the deposited flakes are increased, the electrical conductivity of the obtained coating is increased by an order of magnitude. All the previously presented surface deposition techniques do not take into account the capability of the molecules to be oriented in the most thermodynamically stable configuration in short times. Differently from conventional surface modification techniques, nano-assembly of polyelectrolytes makes it possible for the preparation of layered polymeric multi-composites through self-assembly of macromolecules directly on the substrate surface. The self-assembling process can be defined as “*the autonomous organization of components into patterns or structure without human intervention*” [175] and is considered one strategy for organizing matter from the nano- to the micron-scale.

There are two kinds of self-assembly:

- Statistic self-assembly, which involves systems in thermodynamic equilibrium like folded and globular proteins.
- Dynamic self-assembly, where the formation of patterned structure occurs only when the system is dissipating energy.

In general, self-assembly reflects the inherent properties of an individual component like its magnetic dipole, charge and polarizability. The molecular assembly involves non-covalent and weak interactions such as Van der Waals, electrostatic, hydrophobic and coordination bonding. In addition, self-assembly

requires a medium where molecules have a good mobility. In these cases, the use of a template can avoid defects and control the structures.

In this thesis, Layer-by-Layer (LbL) technique was employed in order to improve the gas barrier properties of PET thin films. LbL assembly was developed in 1966 by Iler [176], but practical applications were reported 30 years later by Decher and his co-workers [177]. The technique is based on the electrostatic interaction occurring during the alternate adsorption of polyanion and polycation on the selected substrate, but many variants based on different interactions (*e.g.* hydrogen bonding) can be considered (Figure 13).

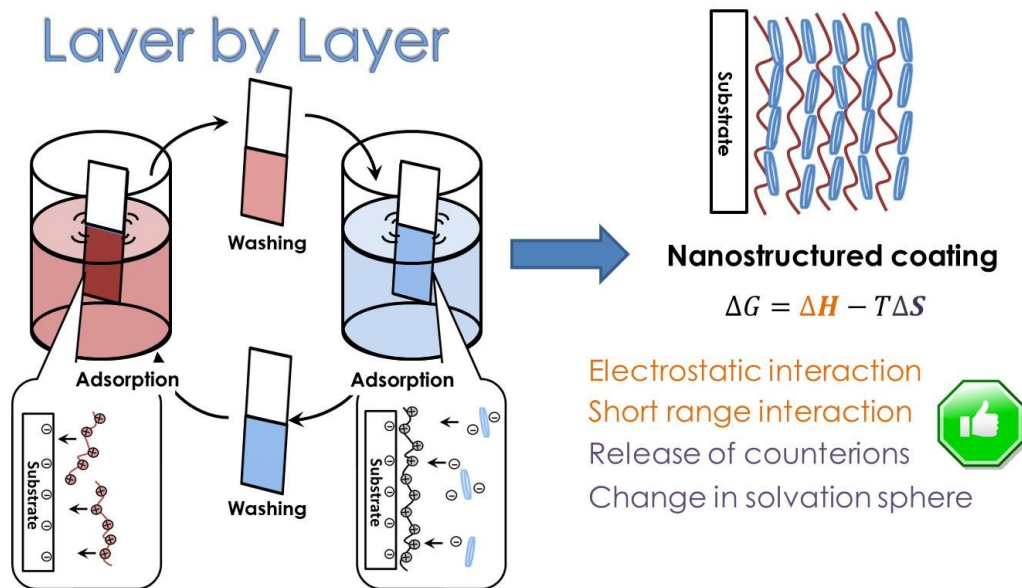


**Figure 13** Scheme of LbL process with details about charge reversal. On the left right, nanostructured coating growth with attention on enthalpy (orange) and entropy (purple) contributions.

The process is quite simple and tunable as it is affected by several parameters like the nature of the employed polyelectrolyte [178], temperature [179], pH [180], the ionic strength [181] and the presence of counterions [182]. By modulating these parameters, it is possible to build coatings with controlled thickness in the 10-1000 nm range. In addition, there are no restriction for what concerns the substrate's shape. LbL assembly is used to build nanoscale multi-material films able to introduce functionalization which can influence the surface chemistry of the substrate and change, for example, its wettability [183-185] or macromolecule anchoring properties.

In principle, the adsorption of macromolecules with more than one equal charge allows for charge reversal on the exposed surface, having two important consequences:

- The repulsion of equally charged molecules is traduced in a self-regulation adsorption restricted to a single layer;
- The possibility of opposed charged macromolecules to be adsorbed in a second step on the top of the first one.

The use of very low concentrations and water as solvents make the technique environmentally friendly and low-cost. Moreover, the possibility to coat every solvent accessible surface make this approach suitable for every kind of substrate (i.e papers, fabrics, open cell foams, films). The most important property of every deposited layer is the thickness, which depends on the nature and the charge density of the deposited component as well the surface roughness of the substrate. The best deposition condition can be reached considering high deposition times, high rinsing volume and using functional groups on the surface:

- the longer is the deposition time, the more controlled and complete is the kinetic adsorption of the components on the considered surface;
- the rinsing volume needs to be higher than the volume of polyelectrolytes suspensions in order to avoid cross-contamination and can help the stabilization of weakly adsorbed polymers;
- the presence of functional groups influences the type of growth.

The use of polyelectrolyte instead of small molecules is preferred because macromolecules have a higher concentration of ionized groups and the adhesion to the substrate is favoured and more efficient. Moreover, the overcompensation of the surface charge by the incoming oppositely charged polyelectrolyte is not affected by the substrate's surface [186]. This is favoured because the polymer has a good mobility and can overcome defects of the surfaces. In addition, the conformation of the adsorbed backbone depends strongly on the environmental conditions. If the substrate surface has a poor charge density, the first layer can bind the substrate with few functional groups exposing the remaining to the solution. This can be correlated to the so defined "island growth" where islands of coating grow after each deposition step eventually coalescing into a continuous assembly leading to a linear deposition regime. On the other hand, when a surface is highly charged an almost homogeneous assembly is reached right after the first deposited layer [187].

Even if the literature is populated of a lot works about polyelectrolyte multilayers (PEMs), the mechanism of coating growth upon deposition steps is not completely understood and normally is strongly dependent on the system studied. In general, two different regimes have been identified:

- the linear regime: is associated to the density of functional groups regardless of the layer number;
- the exponential regime: depends on the diffusion of under layers to the surface and on the diffusion of the polymer substrate inside the coating, increasing the surface coverage of functional groups.

Practically, the LbL build-up can be monitored in several ways. The UV-VIS spectroscopy is the preferred method when the assembly is coloured. X-ray reflectometry and ellipsometry can be employed for the determination of the thickness. Furthermore, quartz crystal microbalance (QCM) [188] and single

stagnation point reflectometry (SPAR) [189] were developed in order to characterize the LbL growth *in-situ*.

Surface modification may be used for the preparation of assembly with more than two components, allowing to tune and introduce more than one functionalization as the final application requires. This advantage is not possible in case of bulk modification. Moreover, surface-confined multilayers can be applied as wavelength-thick transparent coatings. LbL assembly was widely applied to prepare clay-based barrier films reaching good performances when more than 10 BL are deposited on a polymer substrate [190]. Nanoclays typically have 1nm thickness and lateral size of 20-1000 nm, depending on the type and source of the nanoparticles. LbL assembly deposits individual clay platelets from a water based solution in a highly oriented organization parallel to the substrate surface and perpendicular to the diffusion direction of the permeating molecules [166]. The first LbL deposition of polymer and clay was reported by Kleinfeld and Ferguson who layered poly-diallylammoniumchloride (PDAC) with Laponite [191]. Recently several works on clay/polymer LbL assembly have been published. Nevertheless, the presence of layered nanoparticles makes the coating rigid thus promoting the formation of cracks. Moreover, in humid condition, coatings tend to swell increasing the void space between layered structure which became accessible for permeating molecules. LbL coatings were prepared also employing GRMs. However, because LbL is conducted in water-based suspension only graphite oxide nanoplatelets suspensions have been used for preparing LbL coatings for gas barrier application. The first attempt was conducted by Yu [192] who alternatively dipped a PET film (188  $\mu\text{m}$  thick) in BPEI-GO until 5BL were deposited finding that 5 BL deposition was sufficient for detect an oxygen transmission rate (OTR) lower than  $0.005 \text{ cc/m}^2 \text{ day atm}$ . It was also demonstrated that GO suspensions at 3.5 pH exhibited very dense and ordered structure resulting in a OTR lower than  $0.05 \text{ cc/m}^2 \text{ day atm}$  [193]. In another paper, Yang et al. demonstrated that, like silica nanoparticles, the concentration of graphene oxide in the deposited layers affects the permeability behaviour of the coating due to the better overlapping property of the GO nanoplatelets. In addition, they demonstrated the ability of the 20 BL BPEI-GO assembly to act as a selective membrane for hydrogen carbon dioxide separation [194]. However, GO hydrophilic nature promotes the swelling of the coating when in humid atmosphere, thus results in detrimental gas barrier GO-coatings performances at high relative humidity conditions. In order to limit the swelling of the GO-based LbL coatings, Stevens et al. demonstrated that the reduction of GO nanoparticles in mild conditions ( $175^\circ\text{C}$  for 90 min) is sufficient to prepare coatings with exceptional gas barrier properties towards oxygen in 100%RH conditions ( $< 0.005 \text{ cc m}^2 \text{ day atm}$  when 20 BL are deposited)[195]. Furthermore, it has been demonstrated that graphene oxide can be used as molecular sieve for small molecules like helium or hydrogen [196, 197]. Indeed, in a recent paper, graphene oxide (from solutions with 90% concentration of monolayers) was also employed for the preparation of selective gas barrier membranes [198]. It has been demonstrated that graphene oxide can be coupled with PEI in a LbL assembly on

100  $\mu\text{m}$  thick PET film. In selective gas barrier experiments it was found that in a mixture of He/CO<sub>2</sub> or of H<sub>2</sub>/CO<sub>2</sub>, the smallest molecules (H<sub>2</sub> and He) can pass through the space between the polymer backbone of PEI and the high defective graphene oxide. In contrast larger molecules have to pass through larger vacancies, or grain boundaries so their path is longer than for helium or hydrogen. Moreover, the path of permeating molecules is limited by the presence of the PEI backbone which is strictly connected to the graphite oxide nanoparticles. The aforementioned work also proposed that in humid conditions GO assembly have a drop in their gas barrier feature because water has comparable kinetic diameter to helium (265 pm and 260 pm respectively) so water can easily pass through graphene oxide based films when the thickness of this nanoparticles is atomic.

The limitations related to the employment of LbL in gas barrier application are essentially referred to the cyclic nature of the dipping procedure. It is well known that the dipping process proceed from one polyelectrolyte solution to another passing through a rinsing in neat solvents, but this step can lead to carryover from the rinse baths to the proceeding polyelectrolyte solutions, inducing a possible cross-contamination and a change in solution pH, which can affect the charge density of the outer deposited layer. Secondly, the assembly procedure requires time for the efficient assembly of polyelectrolyte on the surface. In order to avoid these problems, automated system or spraying deposition have been proposed [187, 199].

In comparison to bulk modification, LbL assembly allows obtaining coatings where nanoparticles are oriented parallel to the surface of the polymer film thus efficiently limiting the gas permeation. Indeed, the resulting brick and mortar fashion greatly increases the tortuosity path of gas molecules. In contrast, melt-mixing or in-situ polymerization used for the introduction of nanoparticles, like clays or GRMs, in the polymer matrix, suffer from the aggregation of the particles resulting in a non-homogeneous blend. Moreover, bulk dispersion of GRMs and clays often limits the film transparency and results in permeability values higher than what is required for modern packaging application (OLEDs and LCD display) and vacuum-insulating systems. Indeed, the random orientation of nanoparticles and the presence of voids accessible to permeating gas molecules limits the barrier performances.

LbL assembly is not the only technique able to increase the gas barrier properties of polymers by surface modification. Recently, atomic layer deposition (ALD) [200, 201] or molecular layer deposition (MLD) [202, 203] are considered as the most promising techniques for enhancing gas barrier properties of polymers. The two techniques can be distinguished in ALD or MLD as a function of chemical precursors. These techniques are an evolution of CVD where the final coatings consist of alumina, silica or allumino-silica mixed coating deposited in multi-layered structure whose thickness is in the range of tens of nanometers to tens of microns. Such multi-layered inorganic material exhibit extremely low water-vapour transmission rates (WVTR) below 10<sup>-6</sup> g/m<sup>2</sup> day with tens of micron thickness. However, despite the good performances, these coatings are affected by poor mechanical properties and are prone to cracking. Moreover, ALD and MLD

apparatus are expensive and their industrial application is limited due to the deposition conditions that require inert atmosphere and a very high number of deposition cycles [204]. In order to improve the mechanical properties of ALD-coatings, Qin et al. combined the LbL technique with physical vapour deposition of silica preparing a hybrid coating made of 8BL BPEI/PAA-SiO<sub>x</sub> (20 nm thick)-8BL BPEI/PAA showing that it was able to decrease the water vapour transmission rate of a neat PET film by nearly one order of magnitude [205]. It was demonstrated that the presence of the polymer fraction in the coating structure was able to improve the mechanical properties of the coating reducing the residual compressive stresses between the silica and the PET film caused by the high difference in modulus between the substrate and the coating, while the silica thin layer was able to reduce the water vapour permeability.

## 1.5 Fire occurrence and Flame retardancy

Still today, fires can be considered one of the most important causes of loss in terms of things and human lives. The US Fire Administration has recently published the Fire report revised to the 2017 [<https://www.usfa.fema.gov/data/statistics/>]. In that work, it is shown that, in USA, fires are mostly occurring in structures for the 43% of cases (Figure 14). This phenomenon is also reflected in terms of losses of human lives and things. In fact, the 76% of fire injuries and the 78% of fire death occurred in dwelling with a related dollars loss of the 48% of the total fire dollars loss. Particular attention needs to be also directed to the fires occurred in public and private vehicles that have reported a 15% of death, a 7% of injuries and 13% of economic losses in the 2017. The above mentioned data are an example but it is reasonable to think that the same scenario could be valid for Europe, because the most of fires occur accidentally and with high probability in structures and vehicles, where there is a high concentration of igniting materials, like fabrics or polyurethane foams.

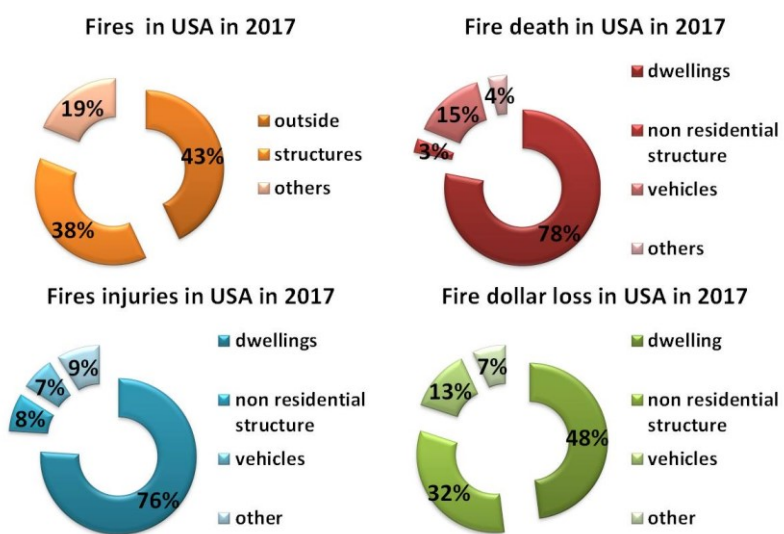


**Figure 14** Fires occurred in USA in 2017

Polyurethane foams are used in a multitude of applications, ranging from soundproofing in public places, such as cinemas and theatres, to thermal insulation of large structures as well as in residential structures. Nonetheless, their use in comfort goods such as seat and mattresses must not be forgotten. Most of the uses of these materials, especially in the public sector, are subjected to the safety evaluation of their use. The most critical point regarding open cell polyurethane foams use is the resistance to heat and the reaction to flames application. It is well known that open cell polyurethane foams have no fire resistance and, when they are put in contact with a small flame, polyurethane foams can ignite immediately, burn very quickly and spread the fire by dripping. The most employed strategy adopted to limit this problem is the use of flame retardant additives. Halogens-base additive, such as chlorinated and brominated compounds have been widely used as flame retardant agents. However, these compounds are generally weakly bound to the polymer matrix so halogen-based flame retardant additives can be released into the environment and absorbed by the ecosystem and humans [206].

The risk assessment of the most widely used flame retardants on the market began in Europe in the 1990s until the transition to the REACH program. In Europe from 2008, REACH regulations (Registration, Evaluation, Authorization and restriction of Chemicals, (REACH, 1907/2006 / EC)) request for all chemicals introduced in the market a toxicological and environmental hazard report, forced by the principle of “no data no market”. In this context, suspicious substances are thoroughly evaluated and their use may be limited or completely prohibited. This practice initially focused on halogenated flame retardants and then extended to non-halogenated compounds such as organo-phosphates. The absorption and bioaccumulation of these materials in human organisms may cause damage of different magnitudes including male infertility and the possibility of interfering with the normal development of foetuses, leading to a premature and underdeveloped birth [207]. Therefore, Governments promulgated stringent regulations regarding the use of halogens-based flame retardants additives aimed to the protection of mankind and ecosystems [208]. The enter in force of REACH program affected the market of halogenated flame retardant additives reducing their consumption. At the same time, the Halogen-Free brand was promoted in order to easily recognize flame retarded materials with low toxicological and environmental risk. For the mentioned reasons, researchers have been working on the development of novel foams characterized by improved flame retardant properties exploiting sustainable solutions.

At the state of the art, flame retarded PU foams are made by the addition of flame retardant agents in bulk. Generally, the additives used for the preparation of bulk flame retarded PU foams are phosphorus-, nitrogen- and silicon-containing compounds. In addition, nanoparticles with sheet-like or tubular morphology, such as polyhedral oligomeric silsesquioxane [209-211], carbon nanotubes (CNTs) [212-214], montmorillonite (MMT) [215, 216] and graphite nanoplatelets [217] have been used to impart superior fire retardancy to PU foams. Due to their morphology, nanoparticles act as robust barriers for heat and mass transfer, can

slow down the heat release rate and may reduce rate of the smoke evolution during the combustion of polymers. However, nanoparticle-based flame retardant additives are incompatible with the PU foaming process, because the nanoparticle addition change the viscosity of the PU mixture and the standard foaming procedure do not work. As an alternative, surface modification may preserve the standard foaming process and, if the coating is thin, the changes of mechanical properties are negligible. Adopting the surface modification, the flame retardant agent are confined only on the surface, which is the main region interested by heat and mass transfer phenomena controlling the combustion process [218]. The state of the art of surface coating deposition comprise *in situ* deposition process [219], layer-by-layer (LBL) assembly [215, 216, 220, 221], dip coating and sol-gel treatments [222]. The sol-gel process involves a two-step hydrolysis/condensation reactions of (semi) metal alkoxides, such as tetramethoxysilane and aluminium isopropoxide, forming fully inorganic or organic-inorganic hybrid coatings [222]. Firstly, Bellayer et al.[222, 223] used a sol-gel process to reduce the flammability of PU foam by preparing a tetraethoxysilane, methyl triethoxysilane with (3-amino propyl triethoxysilane) and diethyl phosphite mixed solution. During combustion an insulating char layer can be formed comprising silica and orthophosphate species protecting the PU during burning and reducing the rate of volatiles feed to the flame. Ellison et al. [219] prepared flame retarded PU foams by immersing the substrate in an aqueous solution of dopamine at different times, resulting in the formation of uniform polydopamine nano-layer on the surface of PU foam. The polydopamine deposition enables PU foams to self-extinguish and the char formation effects of polydopamine is responsible for the 67% reduction of pkHRR relative to control foams, with a 300 nm thick coating and an add-on of about 15%. Although the *in situ* deposition approach allows for a tailored coating thickness, this process is usually time-consuming (in terms of days) and strongly dependent on the reaction time, limiting its industrial application. Compared with *in situ* deposition, Wu et al. [224] have developed a facile strategy to prepare silicone resin coatings for flame retarded PU foams by a dip-coating process. This process is based on the condensation polymerization where the silicone polymer coating is produced on the surface of PU foam. Following this work, the same group further developed hierarchical coatings composed of silicone resin and graphene oxide onto different combustible substrates as smart sensors for rapid flame detection [225]. The resulting coatings reached a self-extinguishment time less than 20 s without melt dripping in flammability tests and a decrease in the peak of heat released up to ~78% due to the char forming properties of the coating (600-800 nm thickness).

In this thesis work, LbL has been chosen as the main technique in order to deposit coatings able to reduce flammability and fire reaction of polyurethane foams. Differently from the other coating procedure presented before, LbL consists in a simple to handle, cost-effective and environmental friendly approach to fabricate flame retardant nano-coatings with a typical thickness less than 1  $\mu\text{m}$  [226, 227]. In this procedure, the PU foam is alternately dipped into two oppositely charged polyelectrolyte solutions or suspensions [228]. The wide range

of operational procedure spaces from the nature of the polyelectrolytes to their charge density and make this procedure scalable and widely applied in industrial application. It will be showed that the presented coatings grow up by electrostatic interaction and the thickness will be modulated by ionic strength. There will be presented coatings able to suppress melt dripping and flame spread in flammability test and effective heat shielded samples due to the incorporation of graphite oxide nanoplatelets through organic-inorganic or inorganic-inorganic coatings with a number of deposited bi-layers less than 10.

## 1.6 Flame retardancy in polymer nanocomposites

It is well known that fires in residential environment are one of the most important causes of losses in terms of properties and human lives. This problem led local administrations and safety commissions to focus on fire prevention and fire retardancy.

Polymers are the most diffused materials employed to produce a large number of items found in buildings, including appliances, furnishings and various objects of common use. Unfortunately, polymers are typically flammable, and the exposure to a small flame can easily produce their ignition and rapid combustion. This behaviour strongly limits their use in a wide range of applications and, as countermeasure, the inclusion of flame retardant additives has been exploited in order to limit the probability of fire occurrence and propagation.

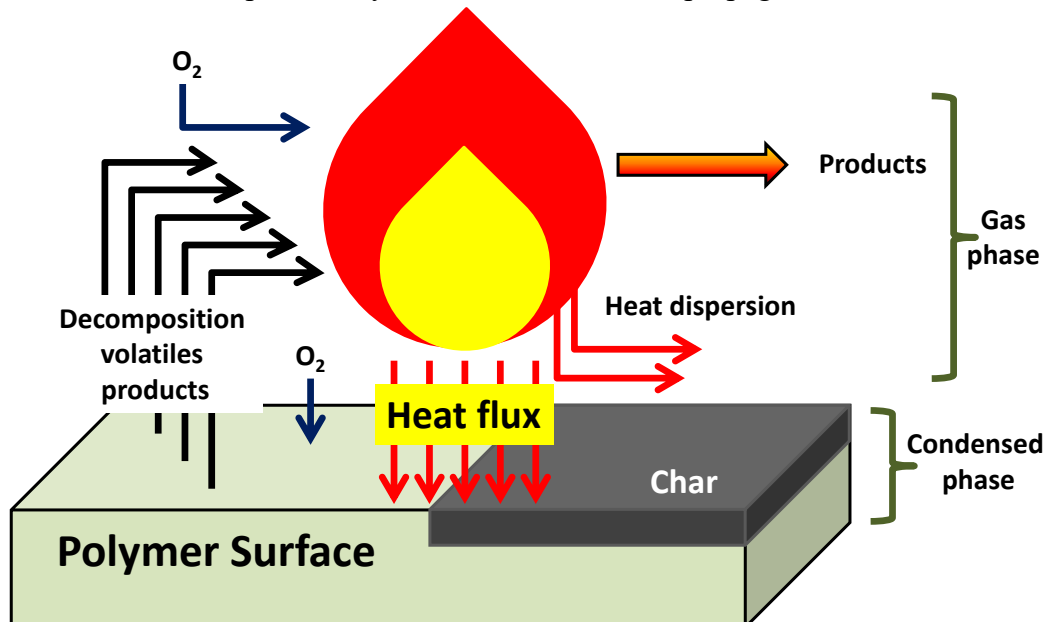


Figure 15 Polymer surface combustion cycle.

In general, when a polymer is exposed to a heat flux, the first process that takes place is the thermal decomposition of the surface layer followed by the ignition of the polymer at the polymer-fire-air interface. The thermal decomposition produces volatiles that enter in the vapour phase and react with oxygen as long as the temperature is above the ignition temperature or a suitable ignition source is present (Figure 15). Combustion is an exothermic process where

complex reactions and highly reactive chemical species, such as radicals, can be produced and part of the developed thermal energy sustains the degradation processes that occur in the condensed phase of the polymer. During combustion, depending on the material structure and the degradation processes involved, a charred residue may be produced.

Fire retardant additives can be added to the polymers in order to improve their flame retardant properties. These additives were developed aiming at different flame retardant effects: i) increase the ignition temperature of the material, ii) reduce the flame spreading rate, iii) reduce the amount and the opacity of volatiles species evolved during the combustion process and iv) reduce the rate of combustion. In the past, halogen-based additives, such as brominated and chlorinated chemicals, were employed in order to interfere in the radical processes occurring in the gas phase. These additives prevent or delay the ignition and slow down the rate of burning in early flaming. However, their employment is responsible for an increase in smoke and toxic product yields because, during burning, the relative haloid acid is produced. Nowadays, their use is strongly limited because of strict laws related to both their toxicity to human and environmental concerns. As an alternative, inorganic compounds such as aluminium hydroxide and magnesium hydroxide, can be used. These compounds work releasing water vapour that dilutes gas volatiles mixtures, which feed the combustion process, while cooling the substrate. This mechanism is known as gas phase effect. In addition, the decomposition of inorganic hydroxides leaves a metal oxide layer on the surface of the burning polymer that is further protected from heat and oxygen. Inorganic compounds are cheap and environmental friendly but in order to affect the flammability behaviour of polymers a minimum loading amount of 40% in weight is required. In addition, nitrogen based flame retardants (i.e melamine) and phosphorous flame retardants (including organophosphate, organophosphonates, halophosphonates, phosphine oxides and red phosphorous), can act in both gas phase and condensed phase yielding a flame retardant mechanism depending on the used compound and the polymer.

In the past, the preferred strategy to flame retard polymers was the bulk inclusion but, in some cases, a 60% loading was required with subsequent detrimental effects on polymer properties while also giving rise to processing difficulties [229]. Another approach considered in order to improve the flame retardant properties of polymers is the employment of intumescent systems [230]. These additives act in the condensed phase and, when an intumescent system is exposed to a heat flow, it develops an expanded carbonaceous shield on the surface of the polymer. This structure can act as a barrier limiting heat transfer between the flame and the polymer, and in the same time also limits the oxygen diffusion toward polymer and volatiles from polymer to the flame. This type of system needs the simultaneous presence of the three components: an acidic source, a carbon source and a blowing agent. As an example, ammonium phosphate and ammonium polyphosphate can act as both acidic source and blowing agent because they can release ammonia during combustion. The carbon source is a compound capable of yielding a carbonaceous structure.

The possibility to modify the polymer surface with flame retardants based coatings was proposed as an alternative to the bulk inclusion because the surface controls the heat and mass transfer, that are the responsible processes of flame feeding. Indeed, ignition occurs when the volatiles, the oxygen concentrations and the heat flux reach a definite value. Probably, volatiles come from the most exposed surface region of polymer surface meaning that the pyrolysis reaction is confined in a thin layer near the surface. This layer must be raised to a higher temperature to achieve the critical mass flux for ignition than at lower radiant flux, when the thermal wave penetrate deeper into the solid and involve a larger volume in the pyrolysis process [231]. When subjected to a known radiant flux, the polymer's time to ignition and mass loss rate are mainly controlled by the material's thermodynamics and chemical kinetic properties related to the transfer of heat into the material such as density, thermal conductivity and specific heat. Linteris et al., showed that when a polymer is invested by a constant heat flux, the flux increases with the time because, after the adsorption of the radiation, the polymer heats up meaning that re-irradiation occurs by the polymer surface. They also determined that the transmittance is a function of sample thickness [232] opening to the possibility of use coatings able to protect the bulk of the polymer by re-irradiation. One of the most investigated and valuable option able to act as a barrier to mass and heat exchange is the production of a thermally stable barrier surface layer. This layer needs to be produced during the early stage of combustion as a consequence of polymer decomposition promoted by heat in the presence of fire retardant additives. Nanoparticles have been widely employed for this purpose. Indeed, it is well known that layered silicate or silicate-carbon polymer nanocomposites achieve flame retardancy through a shielding effect against heat flux. The reduction of heat used in pyrolysis, through conductivity into the specimen, vanishes when the thermal diffusion layer becomes larger than the thickness of the remaining specimen. The re-radiation of hot surface is approximated to scale with the factor  $T^4$  [233]. In details, the re-radiation from the considerably hotter surface is responsible for a reduction of the heat flux in the pyrolysis zone. The main effect of this process is the HRR reduction and the prolonged time of burning. Thus, meaning that the shielding effect is the main fire retardant mechanism in fire retardancy silica-based nanocomposites.

Graphene and related materials can be used as flame retardant additives because of their high thermal stability and high aspect ratio, which added to the probability of nanoparticles overlapping during burning process can results in the formation of a compact, thermally stable and dense char layer, that may reach temperatures significantly higher than for a decomposing pristine polymer, thus increasing the surface temperature, with a consequent enhancement of heat re-radiation. In the next section, the impact of graphene related material on the flammability and combustion of polymers will be presented and discussed. In a first section, GRMs-bulk nanocomposites are briefly presented. In the second, the use of LbL technique to improve the polymer flame retardancy is discussed.

### **1.6.1 Graphene related material bulk nanocomposites for flame retardancy**

Graphene related materials are considered additives capable of enhancing the flame retardant properties in polymers with the synergy of three main effects [234]:

- The carbonaceous structure of GRMs is stable at high temperature in inert atmosphere and is slowly oxidized in air at temperatures below 600°C. Furthermore, the presence of percolating networks of carbonaceous structures may act as a template for the further carbonaceous char formation from the polymer decomposition, promoting the production of a layered structure that can improve the tortuosity path of the gases feeding the flame;
- the re-radiation of the carbonaceous structure from the surface can considerably improve the heat barrier effect toward heat flux penetration in the polymer matrix;
- GRMs may adsorb the organic volatile species developed by the polymer pyrolysis due to their high specific surface area (SSA).

GRMs are considered good flame retardant candidates; however, their successful exploitation still faces significant challenges. Indeed, pristine graphene possesses poor dispersability in polymer matrices due to the high  $\pi$ - $\pi$  interaction between layers. From another point of view, at temperature higher than 400°C GO may undergo reduction processes normally associated with exothermic reactions. Moreover, if GO and rGO are in presence of KOH (from the synthesis), they can undergo self-propagating thermal deoxygenating reaction with the production of CO and CO<sub>2</sub> [235] with detrimental effects on the polymer flame retardant.

The pioneering work on the employment of carbon based additives for improving the flame retardancy in polymers was reported by Dittrich et al.[236] and Hoffman et al. [237]. In their works, they incorporated rGO, expanded graphite, spherical carbon black and multi-walled carbon nanotubes into polypropylene (PP) in a range concentration between 0.5% wt and 5% wt. The works demonstrated that a high rGO concentration favours the formation of dense carbonaceous protection structures that reduce the peak of heat release (pkHRR). Consideration on the effects of the morphology of the employed carbon-based additives can provide an insight on the achieved FR properties. Indeed, in previous sections (1.4.1 and 1.4.2) it was explained that particles with high aspect ratio can improve the tortuosity path of permeating gases. The spherical carbon black particles and nanotubes packing is not sufficient for enhancing the tortuosity path of developed gases leaving many accessible voids. The pkHRR reduction at 5% wt loading follows the order : rGO > carbon black > expanded graphite > multi-walled carbon nanotubes, probably because of the best lamellar packing and the high number of interfaces of rGO nanoparticles with respect to the other carbon-based additives.

The flame retardancy properties of bulk nanocomposites are also affected by the GRMs-additive loading. To this aim, Bao et al, [238] focused their attention

on the effects of the rGO additive loading towards flame retardancy of rGO-PLA. By cone calorimetry, they found that when the rGO loading was less than 0.5% wt, the time to ignition was decreased but, when the rGO loading was higher than 0.5%wt the pkHRR values decreases of about 40% respect to the neat PLA, and the sample burned slowly. From this evidence, they concluded that when the rGO content is smaller than the 0.5% the nanocomposites are degraded and burn faster than the neat polymer because the mass barrier effect of rGO is inefficient and the rGO heat conductivity accelerate the degradation of PLA matrix. When the rGO loading is higher than 0.5% the barrier effect is more pronounced and the higher concentration of rGO nanoplatelets allows to re-radiate the heat and the flame retardant properties of rGO-PLA are improved.

In order to investigate the effect of the graphene oxidation on flame retardant properties of GO loaded nanocomposites, Han and collaborators [239] reported the melt-mixing preparation of graphite nanoplatelets/polystyrene (GNP-PS) and graphite oxide/polystyrene (GO-PS) nanocomposites with different grade of oxidation. By thermogravimetric analysis they found that the higher thermal resistance was in GNP-PS nanocomposites with 5% wt GNP loading meanwhile a high oxidation degree of GO is harmful to the thermal stability of the GO-PS nanocomposites. However, by cone calorimetry measurements, the GNP or GO loading to the PS matrix tends to cause a decrease in the time to ignition and a reduction of HRR-values. They concluded that, initially, GO or GNP absorbs and re-radiates the heat to cause a rapid charring of the polymer surface, followed by the thermal degradation of the polymer, which is slower than that of the neat polymer, because the GO or GNP act as a barrier to mass transport and insulates the underlying polymer from the heat source by the char layer.

In order to improve the flame retardancy of GRM-loaded nanocomposites, scientists combined associated graphene-based fillers with conventional flame retardants such as inorganic hydroxides as well as polyphosphates. As an example, Huang et al. [240] reported the preparation of poly(methyl methacrylate) nanocomposites by incorporating microencapsulated ammonium polyphosphate and melamine in ratio 2:1 as intumescence flame retardant agents coupled with graphene and layered double hydroxides (LDHs) via *in-situ* polymerization. They found that the nanocomposite exhibits good dispersion and very little deterioration of mechanical properties if compared to the neat polymer. Moreover, the presence of GNPs and LDHs improved flame retardancy properties of the employed intumescence system due to the formation of a more compact char.

While the above mentioned studies suggested the suitability of graphene related materials for flame retardant application in polymer nanocomposites, there are still many challenges that need to be addressed for the effective exploitation of these materials, including the use of solvents that are difficult to remove/dispose as well as the aggregation phenomena occurred when GRMs are not compatible with the polymer matrix. For these reasons, bulk processing currently remains challenging. On the other hand, the improvement of flame retardancy in polymer by the surface deposition of GRMs appears to be promising, as discussed in the next section.

## 1.6.2 Layer by Layer coatings for flame retardancy

Because heat and mass exchanges during combustion depend on the surface properties, modification of the polymer surface with thermally stable coatings may directly affect the flame reaction of the material. In this context, the LbL approach to surface modification may be considered a good option for the preparation of flame retarded polymers without modifying the bulk composition, due the possibility to deposit coatings with different thickness as a function of the process parameters and polyelectrolytes nature. Moreover, it can be adopted for a variety of substrates ranging from fabrics, foams and bulk polymers. In this thesis work, polyurethane foams (PU) were chosen. The choice of this substrate was related to the fact that PU are widely used in upholstered furniture as well as in seats for public transport, automotive vehicles, in theatres even as phono-absorbent panel, all of these applications being associated to the risk of initiating or propagating fire. Indeed, it is well known that PU are highly flammable, exhibit high burning rate and contribute to the fire spread because of the melt dripping phenomena [241]. In addition, the released combustion gases are a mixture including hydrocyanic acid, carbon monoxide, diols and isocyanides precursors that, if inhaled, can potentially cause asphyxiation or long term lung damage [242]. Due to the high surface vs volume ratio of open cell PU foams, the use of a surface approach could be particularly convenient to confer flame retardancy to this type of materials.

The first attempt to LbL coat PU with a fire protective coating was reported by Kim et al employing bi-layers of carbon nanofibers (CNFs) stabilized in poly(acrylic acid) and polyethylenimine (PEI). The LbL assembly was capable to coat the internal structure of the PU and resulted in 40% reduction in pkHRR with only 4BL of CNF-PAA/CNF-PEI. This result is comparable to the same performances reached when 20% wt amount of halogen flame retardant agents is added in PU foam bulk [243]. However, these results are not sufficient for make safe the employment of PU in some application like public transport because combustion occurs.

Subsequently, nanoclays have been widely employed in LbL-flame retardant coatings because of their high aspect-ratios, the ability to form stable water suspensions and their char forming nucleating action during combustion. Laufer et al. [216] reported the first attempt to clay-based multilayer flame-retardant coating using chitosan (CHIT) and montmorillonite (MMT). They demonstrated that 10 BL are enough for reducing the pkHRR by 52% during cone calorimetry and confine combustion on the upper surface of the specimen after exposure to a flame source. From this work, MMT based coatings were widely used for the preparation of LbL flame retarded coatings on PU foams. For example, Cain et al. [215] reported a MMT/sodium hexametaphosphate (NaPn)/ poly(allylamine hydrochloride) coating able to suppress melt-dripping and while reducing the pkHRR by 55% with the deposition of only 4 tri-layers (TL). The overall weight-gain of the foam is less than the CH/MMT system, meaning that the presence of phosphate makes the coatings more efficient. The flame retardant properties of

clay-based LbL coatings are also affected by the clay concentration. Li and collaborators [244] studied the influence of the deposition solution concentration highlighting that high clay contents results in better flame retardancy of the LbL coated PU foams. In their study the deposition of PAA/PEI/MMT TL at the concentration of 0.5:0.5:1% wt respectively. Notwithstanding the low concentration of the solution, the coating was able to decrease the pkHRR and the average HRR by the 33% and the 80% respectively. Moreover, they verified the mechanical resiliency of these coatings after compression testing and proved that flame retardant behaviours are retained. Clays can be also used in presence of other nanoparticles such as carbon nanotubes (CNT). Pan et al. [245] reported the preparation of a CNT-CHIT/MMT/Alginate (ALG) LbL coating. The deposition of 8 TL was responsible for a 65% reduction in pkHRR as well as a substantial reduction of the CO and CO<sub>2</sub> emissions due to the formation of a percolated network made by CNT-MMT particles. The study of the pyrolysis gases by thermogravimetric/FT-IR analysis revealed that the degradation stages of PU foams are unchanged thus suggesting that the MMT-CNT barrier limits the heat transfer between the surfaces and the bulk of the material.

With the aim of the formation of an efficient heat barrier, Holder et al [246] prepared a double LbL system composed by 4 BL CHIT-Vermiculite (VMT) followed by 20 BL CHIT/ammonium polyphosphate (APP) which completely self-extinguished the flame during flammability and reduced the pkHRR by 65% compared to the untreated PUF when samples are exposed to a heat flux of 35 kW/m<sup>2</sup>. The two LbL systems were studied separately underlining that the CHIT/VMT assembly alone significantly reduces the total smoke release (TSR) while the CHIT/APP assembly slightly increases it. Flammability tests combined with cone calorimetry measurements suggest that CHIT-VMT assembly creates a thermal barrier while CHIT/APP coating create a physical barrier towards volatiles able to prevent flame spreading for the surface of the specimen, due to its intumescent characteristics. Comparing the above-mentioned results and considering the coating composition, it is possible to conclude that the flame-retardant characteristics imparted by the deposition of clay-based LbL coating can be greatly affected by the aspect ratio of the employed nanoparticles (VMT aspect ratio is higher than MMT). Starting from this consideration, Patra et al. [247] built a coating made of 1 BL of bohemite (BMT) and VMT. The melt dripping was suppressed and the pkHRR was decreased by 50%. These results were achieved thank to the formation of a nanobrick wall composed by BMT and VMT nanoparticles which act as a heat shield during combustion. In addition, BMT is an alumina hydrate able to undergo endothermic dehydration during combustion. The so released water can contribute to the dilution of gases feeding the flame and thus to the overall FR effect.

From the comparison of all the presented studies, it is suggested that the flame retardancy action of nanoparticle-based coatings is strongly dependent on the nanoparticles ability to overlap and act as a barrier to volatiles diffusion from the bulk to the flaming zone and is thus strictly dependent on the nanoparticles lateral size. Looking to this prerequisite, graphene related material can be considered the

ideal candidate for flame retardant LbL-coatings, as GRMs lateral size can vary from hundreds of nanometers to tens of microns as a function of synthetic procedure and graphitic precursors. This means that the overlapping between nanoparticles can be very efficient during a LbL assembly. Moreover, the carbonaceous structure of GRMs is potentially stable at high temperature and is slowly oxidized at temperatures above 600°C. Furthermore the presence of percolating networks of carbonaceous structures may act as a template for further carbonaceous char formation from the polymer decomposition products, promoting the constitution of a layered structure that can improve the tortuosity path of the gases feeding the flame [234]. Notwithstanding this, in order to perform a LbL deposition, GRMs need to be suspended in liquid phase. As it was mentioned in sub-chapter 1.1.1.2, liquid phase exfoliation is a versatile tool to stabilize GRMs in different solvents. However, organic solvents can exhibit marked toxicity and high boiling point which means that they are very difficult to remove. In contrast, water is the perfect solvent because it is safe and eco-friendly, but it is not suitable as such for GRMs stabilization. There is still a great challenge in the water stabilization of GRMs, but it is possible to exploit the oxidation of graphite to graphite oxide which is the water suspendable form of graphite. In graphite oxide, the oxygenated functionalization makes the stabilization of graphite through hydrogen bonding stored between the oxygen based functional groups present on the surface, on the edges of the graphite platelet and the water molecules. As an alternative, graphite could be suspended in water with the aim of polyaromatic ionic surfactants or polyelectrolytes which can complex graphite nanoplatelets with the non-polar backbone and coordinate water with the polar part [51]. A preliminary study employed low concentration GO suspensions for the production of FR LbL coatings where the main constituents were chitosan and alginate; this study demonstrated the potential of GO in conferring FR characteristics to PU foams.

## Scope of the thesis

In the state of the art description, it was showed that graphene related material can be used for a wide range of applications, among which gas barrier and flame retardancy appears to be of particular scientific and practical interest.

In this thesis, different approaches employing GRMs for the enhancement of gas barrier properties and flame retardant properties of different polymer substrate were developed and validated. The LbL method was used as assembly technique for the deposition of graphene related materials coupled with natural or synthetic polymers assembled on polymer substrates, namely a dense PET film and a foamed PU.

In **Chapter 2**, all experimental details including materials used, adopted procedures and characterizations methods are described.

In **Chapter 3**, graphite nanoplatelets (GNP) were exploited for the deposition of LbL coatings on PET to improve their gas barrier properties. The choice of GNP was performed based on the consideration that GO is high defective and

humidity sensible and previous literature suggested this to cause poor gas barrier properties in moist environments. Because of LbL needs deposition from liquid phase, LPE of graphite was chosen for the preparation of GNP suspensions. In a first attempt graphite was tip-sonicated in presence of a perylene-based ionic surfactant exploiting the stabilization effect promoted by the  $\pi$ - $\pi$  interaction shared between the perylene and graphene sheets. Alternatively, the stabilization mechanism of GNP by different polyelectrolytes was investigated. The obtained suspensions were studied to investigate the mechanism behind the stabilization effect and then, polyelectrolyte-stabilized GNP were coupled in a LbL assembly on PET film. The obtained suspensions were characterized by atomic force microscopy, Field Emission electron microscopy and Raman spectroscopy. Moreover, the LbL mechanism assembly was studied *in-situ* combining QCM and SPAR techniques. Coated PET films were tested to assess the gas barrier effect gained by the deposited LbL coatings, showing dramatically enhanced gas barrier in both dried and humid conditions.

In **Chapter 4**, GRM were employed to improve the flame retardant properties of open cell flexible PU foam. In this part of the work, GO suspensions were combined with both natural and synthetic polymers. In a first attempt, GO and chitosan were coupled in order to prepare a coating with char-forming properties due to the presence of chitosan. In addition, the effect of the GO-nanoparticles aspect ratio on flame retardancy was studied. Afterwards, the effect of ionic strength on the thickness of the deposited coatings was investigated employing a phosphate salts in the GO suspensions and depositing 3BL and 6 BL either modified or unmodified ionic strength. The best performing samples were also tested by flame penetration tests (i.e a fire resistance test). Moreover, the evolution of GO/CHIT, GO/PDAC GO/PDAC/phosphate coatings during force combustion tests was evaluated employing vibrational spectroscopies. Furthermore, in order to improve the efficiency of the deposition, a new one-pot method for the deposition of flame retardant coatings on PU foam was developed. In order to make surface deposition more eco-friendly and less time consuming, a new one-pot method was applied for the deposition of flame retardant coatings on PU foam.

Finally, **Conclusions** chapter recaps final considerations.

# **Chapter 2**

## **Materials and methods**

### **2.1 Materials**

#### **2.1.1 Materials adopted for sample preparation**

Perylene bisimides derivative (PBI) was provided by the Università di Bologna and was synthetized by the Prof. Montalti research group following the procedure explained in literature [248]. Reduced graphite oxide platelets and Graphite Oxide as 1 wt% suspension were supplied by AVANZARE Innovacion Tecnologica (Navarrete-La Rioja, Spain). High shear mixed graphite suspensions were provided by Prof. Ferrari research group from the University of Cambridge and prepared following the procedure described in [65]. Six suspensions at the 100g/L (or 10% wt) concentration were supplied with different grade of exfoliation/dimensions and, on the basis of the number of cycles in the high shear mixer, 0 cycles, 10 cycles, 30 cycles, 50 cycles, 70 cycles and 100 cycles were named. The materials listed above were provided by the producers as collaboration inside the Graphene Flagship Core 1.

Polyacrylic acid (PAA, solution average Mw ~100,000, 35 wt.-% in H<sub>2</sub>O), branched poly(ethylene imine) (BPEI, Mw ~25,000 by Laser Scattering, Mn ~10,000 by Gel Permeation Chromatography, as reported in the material datasheet), Chitosan (CHIT, 75-85% deacetylated), acetic acid (glacial, Reagent plus®, ≥ 99%), poly(diallyldimethylammonium chloride) (PDAC, average Mw 400000-500000, 20 wt.-% in H<sub>2</sub>O, sodium examethaphosphate [(NaPO<sub>3</sub>)<sub>n</sub>] and ammonium phosphate dibasic (APD) were purchased from Sigma-Aldrich (Milano, Italy). Poly(ethylene terephthalate) (PET) with a thickness of 10 µm, amorphous and not surface activated was purchased from the local warehouse. PET films were washed with ethanol and deionized water. Then they were dried in oven at the temperature of 70°C. Polyurethane foams (PU) with a density of 24-20 g/dm<sup>3</sup> and thickness of 15-20 mm were purchased from the local warehouse. PU foams were washed with deionized water and dried in oven at the temperature

of 80°C prior to the LbL deposition. Solutions and suspensions employed in this section were prepared using ultrapure water having a resistance of 18.2 MΩ, supplied by a Q20 Millipore system (Milano, Italy). Single side polished (100) silicon wafers were used for monitoring LbL growth.

### 2.1.2 Reduced graphite oxide synthesis

The following procedure was supplied by the producer AVANZARE Innovacion Tecnologica (Navarrete -La Rioja, Spain) and is reported for completeness. Water dispersion of graphite oxide was prepared using a modified Hummers' method in H<sub>2</sub>SO<sub>4</sub>. Starting from large flakes of natural graphite and using a proportion of graphite/KMnO<sub>4</sub>/NaNO<sub>3</sub> 1:4:0.25. The reaction temperature inside the reactor was kept between 0 and 6 °C during the oxidant's addition (24 h). After that time, resulting solution was slowly warmed up to 20°C and maintained for 72 hours of reaction. To remove the excess of MnO<sub>4</sub><sup>-</sup>, H<sub>2</sub>O<sub>2</sub> solution was added to the reaction mixture and stirred overnight. After sedimentation, the solution was washed with a mechanical stirred HCl 4 wt.% solution by 2h. The solid was filtered off obtaining wet graphite oxide. Wet Graphite oxide was dispersed in water and stirred using a mixer helix at 1000 rpm for 30 minutes. This dispersion was ultrasonicated with a UP400S HIELCHER for 60 min using a H22 sonotrode with 100% of amplitude and full cycle condition to exfoliate the graphite oxide. Graphite oxide was obtained by centrifugation at 4000 rpm. The so obtained GO, was thermally reduced in an oven in argon atmosphere at 1060°C obtaining the reduced graphene oxide. The reduced graphite oxide was characterized by Field Emission Scanning Electron Microscopy (FESEM, Zeiss Merlin 4248, beam voltage: 5kV ) and Raman spectroscopy (InVia Raman Microscope, Renishaw, argon laser source 514 nm/50mW, 10 scansions) coupled with a Leica DM 2500 optical microscope ( I<sub>d</sub>/I<sub>g</sub>= 1.25). Figure 16 shows FE-SEM micrographs of the final reduced graphite oxide. Low magnification micrograph underlines that the ordered layered structure of graphite is retained. The detail of single sheet surface at high magnification demonstrate the wrinkle nature of sheet due to the reduction process.

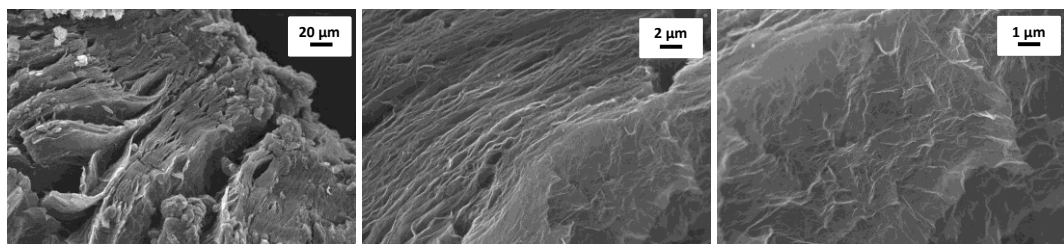


Figure 16 FE-SEM micrograph of reduced graphite oxide.

### 2.1.3 Graphite oxide synthesis

The following procedure was supplied by the producer AVANZARE Innovacion Tecnologica (Navarrete -La Rioja, Spain) and is reported for completeness. Water

dispersion of GO was prepared using a modified Hummers' method in H<sub>2</sub>SO<sub>4</sub>. Starting from large flakes of natural graphite (supplied by NGS-Naturgraphit) and using a proportion of graphite/KMnO<sub>4</sub>/NaNO<sub>3</sub> 1:3.75:0.25. The reaction temperature inside the reactor was kept between 0 and 4 °C during the oxidants addition (reaction time 72 h). The resulting solution was slowly warmed up to 20°C and maintained for 72 hours of reaction. To remove the excess of MnO<sub>4</sub><sup>-</sup>, H<sub>2</sub>O<sub>2</sub> solution was added to the reaction mixture and stirred overnight. After sedimentation, the solution was washed with HCl 4 wt% solution by 2 h under mechanical stirring. The solid was filtered obtaining wet graphite oxide. Wet graphite oxide was dispersed in osmotic water (1 wt% based on dry graphene oxide) and stirred in a Dispermat LC75 using a mixer helix at 1000 rpm for 10 minutes and then at 20.000 rpm for 60 seconds. This dispersion was ultrasonicated with a UP400S HIELCHER for 1 hour using a H40 sonotrode with 90% of amplitude and full cycle condition to exfoliate the graphite oxide and obtain the graphite oxide water dispersion. The pH of the solution was measured during the first 24h after its preparation with a calibrated pH meter obtaining a value of 1.89±0.06. The viscosity of 1 wt% GO water suspension has been determined using a rotational viscosimeter Brookfield EVO Expert R. The measurement was done employing a low-viscosity-adapter tool, due to the low viscosity of the suspension. The container with sample was submerged in a thermostatic bath to ensure constant temperature during the measurement (25°C). The viscosity was found to be 9.7±0.6 cP. For Transmission Electron Microscopy (TEM) characterization, GO water suspensions were dispersed in isopropyl alcohol and sonicated with in a COBOS bath sonicator for 15 minutes. Transmission electron microscopy (TEM) experiments were performed on a JEOL model JEM-2010 electron microscope. The resulting micrographs are reported in Figure 17. The average lateral size has been evaluated as 50 microns.

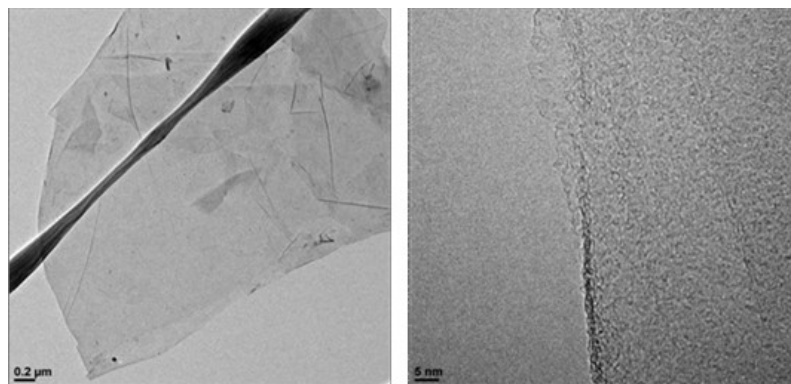
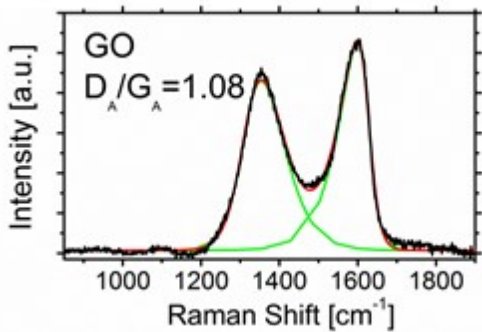


Figure 17 TEM micrographs of graphene oxide (GO) at different magnification.

Figure 18 reports Raman spectrum of prepared GO. Raman spectra were performed on an InVia Raman Microscope (Renishaw, argon laser source 514 nm/50mW, 10 scans) coupled with a Leica DM 2500 optical microscope. D and G bands were fitted with Lorentzian functions in order to determine their ratio. The D/G area ratio indicate the presence of defects, in part attributed to the oxygen functional groups.



**Figure 18** Raman Spectrum of prepared GO.

The obtained dispersion was ultrasonicated with a UP400S HIELCHER using a H22 sonotrode with 90% of amplitude and full cycle condition to exfoliate the graphite oxide for different times in order to obtain GO with different average lateral size: 30 min for GOA, 60 min for GOB and 120 min for GOC. Table 4 reports pH, viscosity and average lateral sizes for the obtained GO suspensions.

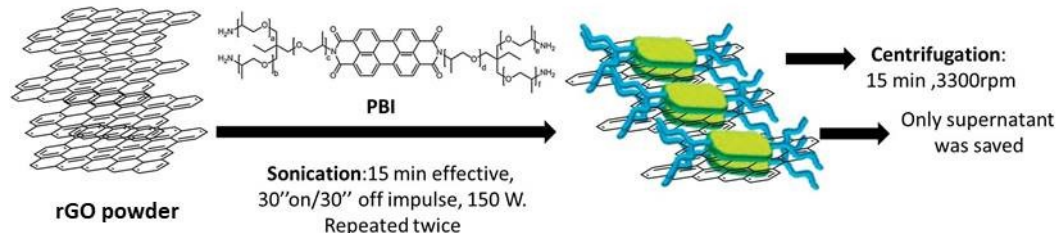
**Table 4** GOA, GOB, GOC, characterization furnished by the producer.

Sample	pH ± σ	Viscosity ± σ [cP]	D50 ± σ [μm]
<b>GOA</b>	1.58 ± 0.078	10.8 ± 0.4	61 ± 2
<b>GOB</b>	1.51 ± 0.028	30.5 ± 0.7	39 ± 2
<b>GOC</b>	1.39 ± 0.057	77.5 ± 3.5	34 ± 3

## 2.2 Procedure

### 2.2.1 Suspension preparation

The PBI used in this work was supplied by the research group of professor Montalti, from the Università di Bologna as partner in the Flagship Core1 project. The suspensions were prepared following the procedure described in Scheme 1:



**Scheme 1** Procedure followed for the preparation of a suspension containing 0.25% p/v of GNP in a  $1 \times 10^{-5}$  M PBI solution.

In detail, 25 mg of reduced graphite oxide powder were added to 100 ml of a  $1 \times 10^{-4}$  M PBI solution and the mixture was sonicated by a tip sonicator (Sonics, Vibra-Cell VCX-505, 20 mm tip) at 150W applying an impulse of 30 seconds on/30 seconds off for 15 min. The sonication procedure was repeated twice. The

suspension was then centrifuged (Eppendorf Centrifuge 5702) for 15 min at 3300 rpm and only the supernatant was collected (G-PBI suspension). The same procedure was followed for the preparation of reduced graphite oxide-BPEI colloidal suspension (GB, 0.1wt% of BPEI) and reduced graphite oxide-PAA colloidal suspension (GP, 0.1wt% of PAA). GNP concentration in GB and GP was determined by thermogravimetric analysis of  $\pm$  10 mg dried suspension (TGA Q-500 TA instruments, 100-800°C, 10°C/min, N<sub>2</sub>).

### **2.2.2 Layer by layer deposition of PAA/GNP-PBI assembly**

The prepared G-PBI suspensions were employed in a LbL assembly coupled with PAA 0.2 wt % solution obtained by diluting the original PAA solution with ultrapure water. A glass wafer was employed as model substrate in order to monitor the LbL growth by UV-VIS spectroscopy. The glass surface was activated by 5 min dipping in a BPEI 0.2 wt% solution followed by 1 minute rinsing in ultrapure water by static dipping. The glass was dried by dust- and oil-filtered compressed air. The first deposited layer was PAA, obtained by dipping the glass in PAA 0.2% wt for 5 minutes, rinsing it for 1 minute in MilliQ water and drying with compressed air. The glass was then immersed in the reduced graphite oxide-PBI suspension (G-PBI) for the same time and rinsed in MilliQ water for 1 minute. After this deposition step, the glass was dried prior UV-VIS analysis. The same procedure was repeated until 10 BL were deposited, the dipping time was decreased from 5 to 1 minute for subsequent layers. The LbL growth was also investigated by FT-IR spectroscopy, using a Si wafer as substrate and the same procedure adopted for to VIS experiments. The same procedure was repeated in order to deposit 10BL PAA/GNP-PBI on a PET 10  $\mu$ m thick film.

### **2.2.3 Layer by layer deposition of GBGP assembly**

Single side polished (100) silicon wafer was used as a model substrate for monitoring LbL growth by FT-IR spectroscopy. The silicon wafer was dipped in the BPEI 0.1 wt% solution for 10 minutes and after a water-jet washing was dried by dust- and oil-filtered compressed air. After this step, the model surface was dipped in the PAA 0.1 wt% solution for the same time, washed and dried with compressed air. After the first bi-layer, the silicon wafer was alternatively dipped in the positive and negative solution until a 10 BL BP coating was obtained. The dipping time was set to 1 minute, the washing and drying steps kept constant through the duration of the deposition. IR spectra were collected after each deposited layer for the first 5 BL and after each BL from the 6<sup>th</sup> to 10<sup>th</sup> deposited BL. The same procedure was followed for the deposition of the GBGP assembly. PET films were alternatively immersed in the positively and negatively charged solutions, washed by water jet with ultrapure water and dried in oven at the temperature of 70°C. This procedure was followed after each deposition step. The dipping time was set to 10 min for the first BL deposition and decreased to 1 min for the subsequent BLs. The process was performed until 10 BL were deposited.

## 2.2.4 Layer by layer deposition of CHIT-GO assembly

CHIT solution (0.25 wt%) was prepared by adding ultrapure water to the chitosan powder and adjusting pH to 4 with acetic acid. The resulting light-yellow solution was kept under magnetic stirring for one night. The GO suspension (1 wt%) was diluted with ultrapure water to 0.5 wt% and kept under magnetic stirring for 4 hours. PAA 1% wt. solution was obtained by diluting the original PAA solution with ultrapure water. BPEI was employed at 0.1% wt solution.

Si wafer was employed as model substrate in order to monitor the LbL growth by FT-IR spectroscopy. The surface of Si wafers was activated by 10 min dipping in the BPEI followed by 10 minutes in the PAA solution. After these two steps the Si wafer was alternately dipped in the CHIT and GO solution/suspension. The dipping time was set to 10 minutes for the first bi-layer (BL, *i.e.* one CHIT/GO pair) and then reduced to 1 min for subsequent layers. After each deposition step, the Si wafer was washed by static dipping in ultrapure water for 1 min and subsequently dried using dust- and oil-filtered compressed air prior to FTIR analysis. IR spectra were collected after each deposition step, up to 10 BL.

PU foams were first immersed in the PAA solution for 10 minutes in order to activate the surface and create a negatively charged surface. After this activation step, PU foams were alternatively immersed into the positively (CHIT) and negatively (GO) charged baths and washed with ultrapure water after each deposition. During the deposition and washing steps the PU foams were squeezed several times in order to let the solution/suspension or washing water penetrate inside the foam structure. The dipping times were maintained the same as for Si wafer. The process was repeated until 3 and 6 BL were built on PU foam. At the end of the process, LbL-treated foams were dried to constant weight in a ventilated oven at 80°C. The mass gain, evaluated by weighting the samples before and after the LbL deposition, was found to be 10% and 13% for 3 and 6 BL, respectively.

The mass gain, evaluated by weighting the samples before and after the LbL deposition for all of so obtained samples is reported in Table 5.

**Table 5** PU fomas weight gain after LbL GOX-CHIT deposition.

Sample	Add-on $\pm \sigma$ [%]
<b>3 BL GOA-CHIT</b>	11 $\pm$ 2
<b>6 BL GOA-CHIT</b>	27 $\pm$ 2
<b>3 BL GOB-CHIT</b>	8. $\pm$ 1
<b>6 BL GOB-CHIT</b>	24 $\pm$ 2
<b>3 BL GOC-CHIT</b>	6 $\pm$ 1
<b>6 BL GOC-CHIT</b>	12 $\pm$ 1

## 2.2.5 Layer by layer deposition of PDAC-GO assembly

BPEI and PDAC solutions were employed at 0.1wt%, while PAA was diluted to 1 wt%. GO suspension was diluted to 0.5 wt%; APD 0.5 M was added to the

GO suspension in order to modify ionic strength. All solutions and suspensions were kept under magnetic stirring for at least 12 hours. Si wafer was employed as model substrate in order to monitor the LbL growth by FT-IR spectroscopy. In order to prime the surface and prepare it for the LbL deposition, Si wafers were dipped for 10 min in the BPEI solution followed by 10 minutes in the PAA solution. This pre-treatment activates the substrate with a negative charge and mimic the procedure employed on PU foams. After this surface activation, the Si wafers were alternately dipped in the PDAC solution and GO suspension. The dipping time for the first bi-layer (i.e. one PDAC/GO pair) was set to 5 minutes; subsequent layers were obtained after 1 minute. After each deposition step (including the first BPEI and PAA deposition), the Si wafer was washed by static dipping in ultrapure water for 1 min and then dried using dust- and oil-filtered compressed air. IR spectra were collected on dried samples after each deposition step, up to 10 BL. This procedure was employed to monitor the assembly of the PDAC/GO and PDAC/GO\_0.5M\_APD systems.

Pre-washed PU foams were firstly exposed to the PAA solution in order to activate the surface due to hydrogen bonding between the urethane groups and the undissociated carboxylic groups (the degree of dissociation of PAA in 1wt% is averagely below 5%). Then, PU foams were alternatively dipped into the positively (PDAC) and negatively (GO or GO\_0.5M\_APD) charged baths and washed with ultrapure water after each deposition. During each deposition and washing step the foams were vigorously squeezed several times. Dipping times were kept consistent with the ones employed for Si wafers. The process was repeated in order to deposit 3 or 6 BL. At the end of the LbL deposition, the so treated foams were dried to constant weight in a ventilated oven at 80°C. In the followings 3BL denotes a sample coated with 3BL of the PDAC/GO assembly while 3BL 0.5M denotes a sample coated with the PDAC/GO 0.5M APD assembly (Table 6).

**Table 6** Mass add-on of LbL treated foams.

Sample	Coating composition	Mass add-on [%]
3BL	PDAC/GO	10 ± 2
6BL		31 ± 3
3BL_0.5M	PDAC/GO_0.5M	22 ± 4
6BL_0.5M		56 ± 5

## 2.2.6 One-pot deposition on PU foams

High shear mixed graphite suspensions were provided by Prof. Ferrari research group from the University of Cambridge as collaboration inside the Graphene Flagship Core 1. Suspension reparation is described in [65].

Two different type of suspensions were considered: one with only GNP nanoparticles and a second one adding a sodium phosphate as flame retardant

agent in addition to GNP. The former type of suspension was prepared from the 1:5 dilution of native ink in order to achieve a 2 wt% GNP concentration. The latter suspensions, were prepared adding phosphate salt to the native suspensions setting a weight ratio of ink and  $[(\text{NaPO}_3)_n]$  to 1:1. The final GNP concentration was 1 wt%. Figure 19 reports a schematization of the adopted procedure reported in [249].

**Activation step: Layer by Layer procedure (one Bi layer deposition)**

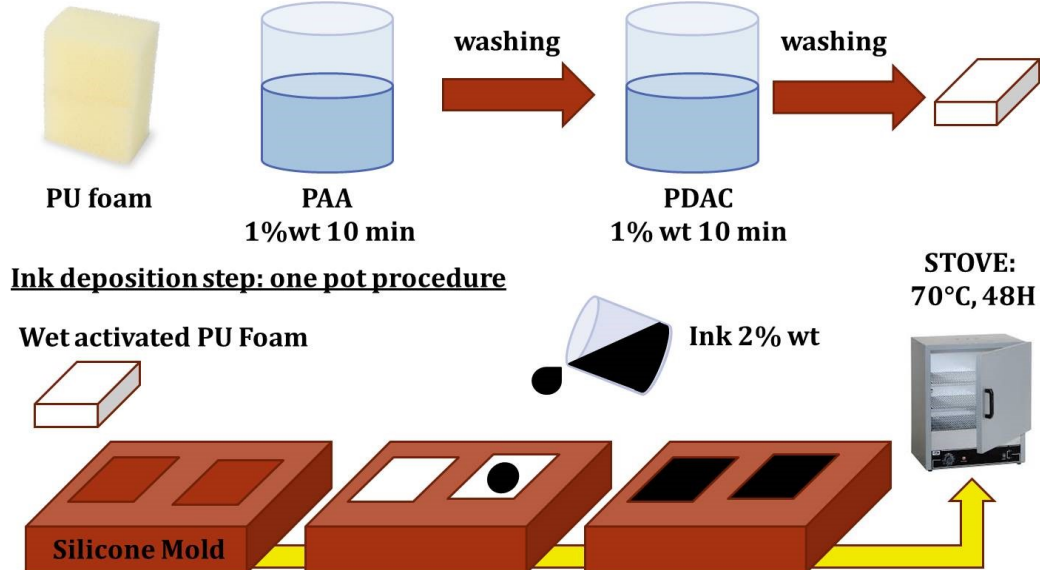


Figure 19 One pot deposition operative scheme.

Pre-washed PU foams were firstly exposed to the PAA. After washing in MilliQ water, the PU foams were exposed to PDAC solution as reported in the upper part of Figure 19. After the activation step, the foams were transferred into a silicone mold and the prepared suspension was subsequently poured on the foam using 1ml per  $\text{cm}^3$  of foam. The mold was placed in the stove for 48 hours until completely dry at the temperature of 70°C (see downer part of Figure 19). The amount of deposited suspension was chosen in order to achieve a 100% of add-on at the end of the sample preparation. After drying, the foams were weighed and the weight gain for every deposited suspension is reported in Table 7.

Table 7 Mass gain of one-pot coated PU foams.

Sample	Add-on [%]	Sample	Add-on [%]
0 cycles	87 ± 4	0 cycle + P	127 ± 6
10 cycles	128 ± 5	10 cycles + P	118 ± 10
30 cycles	110 ± 6	30 cycles + P	111 ± 6
50 cycles	115 ± 5	50 cycles + P	114 ± 9

70 cycles	$108 \pm 3$	70 cycles + P	$110 \pm 5$
100cycles	$106 \pm 3$	100cycles + P	$113 \pm 4$

As reference for flame retardancy characterization a 2 wt% mixture of  $[(\text{NaPO}_3)_n]:\text{CarboxyMethylCellulose:sodiumColate}$  in 85:10:5 ratio respectively was prepared and deposited in the same way schematized in Figure 19.

## 2.3 Characterization

### 2.3.1 Nanoplatelets characterization

The nanoplatelets aspect ratio of graphite oxide suspensions was studied combining SEM micrographs and AFM. SEM imaging was performed by high resolution Field Emission Scanning Electron Microscopy (FESEM, Zeiss Merlin 4248, beam voltage: 5kV). Samples were prepared dipping the Si wafer substrate in a 0.1% wt BPEI solution and, after washing, in the 1% wt GO suspension. The silicon was dried in air. Before FE-SEM imaging, the sample was chromium coated. The same procedure was adopted for all GO suspensions. AFM measurements were carried out in tapping mode using a Innova AFM from Bruker Corporation equipped with the RTESPA-300 probe which feature a resonant frequency of about 200-400 kHz and spring constant of 20-80 N/m. GO suspensions were deposited by drop casting on a silicon substrate after a dilution in 1:1000 v/v. The same procedure was adopted for all of the samples.

For all the experiments silicon double side 285 nm  $\text{SiO}_2$  wafers for optical application were used as substrate for the deposition of G, GB and GP. Advanced microscopy techniques such as scanning electron microscopy (SEM) and atomic force microscopy (AFM) were applied to measure size and thickness of the graphite sheets. SEM experiment were carried out on a LEO-1450VP Scanning Electron Microscope (SEM, imaging beam voltage: 5kV). The colloidal suspensions GB and GP were diluted ten times and 10  $\mu\text{L}$  were deposited dropwise on a  $\text{SiO}_2$  wafer. A reduced graphite oxide suspension (G) was prepared in order to obtain a reference sample for the AFM characterization. In details, 25 mg of reduced graphite oxide were dispersed in ultrapure water following the same procedure adopted for GB and GP suspensions (without employing polyelectrolyte). G topography maps were obtained by depositing 1 layer of graphite by dipping the substrate in a suspension of G in water. Raman spectra were performed on an InVia Raman Microscope (Renishaw, argon laser source 514 nm/50mW, 10 scansions) coupled with a Leica DM 2500 optical microscope. D and G bands were fitted with Lorentzian functions in order to determine the band area. Samples were prepared by depositing and drying the suspension on a glass for microscopy uses. Samples were deposited by drop-casting using a microscope glass as substrate. Graphite nanoplatelets concentration in GB and GP suspension was determined by TGA (TGA TAQ500 weight sensitivity of  $\pm 0.1 \mu\text{g}$ ,

a dynamic baseline drift of  $\pm 50 \mu\text{g}$  (calculated by the producer using empty platinum pans in the range of temperature 50-1000°C with 20°C/min, no baseline correction) and a temperature sensitivity of  $\pm 0.01^\circ\text{C}$ ). An aliquot of both suspensions was dried in oven and then  $\sim 8\text{mg}$  were employed to perform the measurements and analysed in the range 100-800°C, 10°C/min.

### 2.3.2 Layer by layer growth characterization

The growth of the LbL assembly was monitored by FT-IR spectroscopy (Perkin-Elmer Frontier, 32 scans, 4 cm<sup>-1</sup> resolution) using single side polished (100) Si wafer as substrate and by UV-VIS spectroscopy (Shimadzu, UV-21d PC spectrometer) using a glass (VWR microscope glass). Cross section of LbL treated Si wafer was imaged by high resolution Field Emission Scanning Electron Microscopy (FESEM, Zeiss Merlin 4248, beam voltage: 5kV). Samples were chromium coated prior to FESEM observations.

Quartz crystal microbalance with dissipation (QCM-D, E4 model, Q-Sense Ab, Gothenburg, Sweden) was employed for study the B-P and GB-GP LbL growth. All the crystals used in all the experiments were cleaned with ultrapure water and EtOH and after, activated in oxygen plasma. All the QCM experiments were carried out at the constant temperature of 24°C with a flow rate of 0.15 ml/min and with a concentration of 0.025 g/L of B, P, GB and GP. The 5<sup>th</sup> harmonics have been reported for both frequency variations ( $\Delta f/v$ ) and dissipation ( $\Delta D$ ). The LbL assembly was also studied by Stagnation point adsorption reflectometry (SPAR, Laboratory of Physical Chemistry and Colloidal Science, Wageningen University, the Netherlands). A complete description of the method can be found in the original publication by Dijt et al. [189]. In all the SPAR experiments silicon wafers activated in oxygen plasma were employed as model surfaces. The cross-section of LbL-treated PET-thin films was studied using a LEO-1450VP Scanning Electron Microscope (SEM, imaging beam voltage: 5kV). LbL-PET thin films were immersed in liquid nitrogen, cracked in two pieces and pinned up on conductive adhesive tapes and gold-metallized prior to SEM imaging.

### 2.3.3 Fluorescence characterization of perylene bisimides based suspensions

Emission properties of PBI solutions were investigated by using a Horiba Scientific Fluorolog spectrofluorimeter equipped with a 450 W Xenon lamp and a Hamamatsu R928 photomultiplier. The spectral response was corrected for the spectral sensitivity of the photomultiplier.

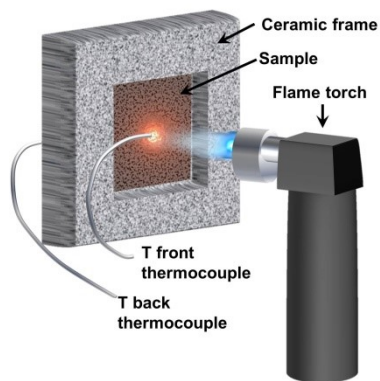
### 2.3.4 Gas barrier properties characterization

Gas barrier properties of untreated and LbL-treated thin film were evaluated by permeability test on 100 cm<sup>2</sup> film surface and were measured using a MOCON

OX-TRAN 2/21 module SH. Oxygen Transmission rate (OTR) were evaluated (single test) in 0% and 50% of relative humidity conditions (RH) at 23°C.

### 2.3.5 Flame retardant characterization

Flammability tests were performed in horizontal configuration by applying a 20mm methane flame for 3 seconds on the short side of samples (50x150x15 mm<sup>3</sup>). The test was repeated 3 times for each formulation. During the test, parameters such as final residue and formation of incandescent droplets of molten polymer were evaluated. Prior to flammability tests, all specimens were conditioned at 23±1°C for 48h at 50% R.H. in a climatic chamber. To investigate the combustion behaviours cone calorimetry (Fire Testing Technology, FTT) was employed. 50x50x15-20 mm<sup>3</sup> specimens were analysed under 35kW/m<sup>2</sup> radiative heat flux. Measurements were performed four times for each formulation evaluating Time to Ignition (TTI), average and peak of Heat Release Rate (avHRR and pkHRR), Total Heat Release (THR), Total smoke release (TSR) and final residue. Average values and plots are presented. Prior to cone calorimetry tests, all specimens were conditioned at 23±1°C for 48h at 50% R.H. in a climatic chamber. Flame penetration test (Scheme 2) were performed in order to assess the resistance of coated samples to penetration of a small flame (150W) generated from a butane flame torch. The test is carried out by placing square specimens (50x50x15 mm<sup>3</sup>) in a ceramic frame, held in vertical configuration, and applying the flame toward the specimen centre. The torch, positioned at 50 mm distance from the surface of the specimen, was applied continuously for 5 minutes. The temperature profiles on the front side surface (exposed to the flame) and on the back side of the specimen were measured by two thermocouples (stainless steel sheathed K-type; 1 mm diameter). The thermocouples were placed into contact with the sample and fixed ensuring that no change in positioning occurs during the test. The test was duplicated for each different formulation.



Scheme 2 Flame penetration test equipment.

### 2.3.6 Flame retardant residue characterization

Cone calorimetry residues of CHIT/GO and PDAC/GO treated PU foams were characterized by SEM and Raman. Raman spectra were performed on an InVia Raman Microscope (Renishaw, argon laser source 514 nm/50mW, 10 scansions)

coupled with a Leica DM 2500 optical microscope. D and G bands were fitted with Lorentzian functions in order to determine the band area. Samples were prepared placing a fraction of cone calorimetry residue between two glasses for microscopy uses. Reference material were prepared exposing neat polyelectrolyte to the cone calorimetry heat flux for 60 seconds. SEM experiments were carried out on a LEO-1450VP Scanning Electron Microscope (SEM, imaging beam voltage: 5kV).

# Chapter 3

## GRMs for enhanced gas barrier

Graphene and graphene related materials have high aspect ratio and, in the case of graphene oxide and graphite oxide, localised charge, so they have attracted a lot of attention for the development of LbL assembly. Moreover, a graphene foil would exhibit remarkable barrier properties to any gases because of the highly ordered honeycomb structure and the huge kinetic energy barrier as it was demonstrated by computational modelling [128, 250] and experiments [127]. Only GO have been used as polyelectrolyte in LbL assembly with good results owing to difficulties in suspension of non-oxidized GRM. Differently from graphene, GO is stable in water because part of the edges have carboxylic acid groups that impart negative charges when exfoliated in water [251]. The high aspect ratio and the localised negative charge makes GO suitable for LbL assembly. GO-PEI LbL assembly have shown a reduction in OTR of 92% in PET 179 µm thick in dried conditions for 10 BL deposition. It was demonstrated that increasing the number of deposited layer and the concentration of GO suspension the gas barrier properties can be improved but the transparency of the film is loosed. Moreover, when the relative humidity is set to 100% the gas barrier properties are decreased and only a 80% of OTR reduction is registered [194]. This behaviour is due to the fact that GO has an amphiphilic nature so tend to hold water swelling the film introducing voids which are accessible to gas molecules. In order to avoid this problem GO nanoplatelets can be reduced in mild condition after the deposition [195]. Another option is the use of graphene and graphite nanoplatelets or replacing GO in the assembly process. To this aim, it has been demonstrated that is possible prepare single layer graphene and isolate graphite nanoplatelets with a defined lateral size and thickness by several techniques like liquid phase exfoliation (LPE) [20]. The situation is different when the considered solvent is water, because the high difference in surface tension, water cannot stabilize graphene and graphite nanoplatelets as such but the introduction of additives of stabilizers is needed. The surfactant assisted LPE in water is well documented [252] but the same is not true for polyelectrolyte assisted LPE.

In this chapter, the exploitation of graphite nanoplatelets (GNP) for the preparation of nano-coatings capable to improve gas barrier properties of PET film is presented based on the consideration that GO is humidity sensible and previous literature suggested this to cause poor gas barrier properties in moist environments. In order to obtain graphite nanoplatelets water-based suspensions, as required for the LbL deposition, LPE of graphite was performed either in presence of a perylene-based ionic surfactant or in presence of polyelectrolytes for the preparation of GNP suspensions. In this thesis, a perylene bisimides derivative, labelled PBI, provided by the group of Prof. Montalti from the Università di Bologna as partner in Flagship Project Core1, was employed for the preparation of GNP-PBI suspension. PBI was selected due to the aromatic core that may act as dispersion stabilizer via non-covalent functionalization. Indeed, the physisorption of PBI onto GNP surface can occur through a  $\pi$ - $\pi$  interaction between the planar  $\pi$ -conjugated surfaces. In this configuration, both GNP and PBI share the  $\pi$ -orbital electrons resulting in the reduction of the surface free energy of the dispersion [60, 253]. Moreover, the perylene bis-imides derivative used in this work was synthesized with a long polar chain in order to make it more hydrophilic and reduce PBI aggregation in water as a consequence of the increased steric hindrance as reported in literature [253]. In addition, from a LbL point of view, the polar functionality may interact with negative polyelectrolytes, such as PAA, allowing for a proper LbL assembly through electrostatic interactions. In the other section, GNP were ultrasonicated in PAA and BPEI solutions, in order to introduce graphite nanoplatelets in a BPEI-PAA LbL assembly which is a well-known system able to enhance gas barrier properties of polymer substrates such as PET in dry conditions [220]. Lu et al.[254] investigated whether graphite nanoplatelets could be stabilized in either 0.1wt% PAA or 0.1wt% BPEI based solutions by sonication in mild condition (23 W for 30 min) obtaining low stable GNP-PAA suspension, and stable GNP-BPEI suspension after 24 hours decanting. They further demonstrated that graphite/BPEI suspension coupled with poly(styrene)sulfonate can be LbL assembled by monitoring the transmittance variation of LBL treated glass. On the other hand, PAA is a water soluble polymer negatively charged in water due to the partial dissociation of the carboxylic functionalizations. Therefore, in absence of pH modifier, PAA solutions present a pH ~5 so it can be considered a weak acid where only a part of the functional groups are deprotonated. From this consideration, PAA can be considered as an amphiphilic macromolecule where the deprotonated functionalizations act as polar functionalization with high affinity for water promoting solubilisation, while the backbone with the non-dissociated carboxylic functionalization can be considered as the hydrophobic part that can interact with graphite nanoplatelets by Van der Waals interactions stabilizing the GNP in water. The same considerations are valid for BPEI. BPEI is a polymer that contains primary, secondary and tertiary amine as functional groups. Of these three classes of amine, the primary are the most favourable to the protonation in

water so they can act as hydrophilic part of the macromolecule while secondary and tertiary can promote the GNP stabilization through Van der Waals interactions with the amine. The obtained GNP suspensions were employed in a LbL assembly and gas barrier properties were evaluated.

### 3.1 Water based suspension of graphite nanoplatelets stabilized in perylene bisimides solution for gas barrier application

Perylene bisimides are molecules derived by the chemical functionalization of perylene and are well-known as stabilizing agent for graphite nanoplatelets in water [255]. Synthesis of perylene bisimides typically starts from perylene-3,4,9,10-tetracarboxylic bi-anhydride (PBA) and in some cases requires quite high temperatures (from room temperature to 200°C), long production times (multi step synthesis) and the use of specific solvents (i.e dichloromethane or molten imidazole) [256]. Perylene bisimides seem to be suitable for many applications in aqueous media because the carbonyl acceptors of the imide groups can promote water solubility through hydrogen bonding. This can come into play also in  $\pi-\pi$  aggregates of the perylene because of the peripheral position of the carbonyl groups and its ability of being in contact with the aqueous medium (see Figure 20).

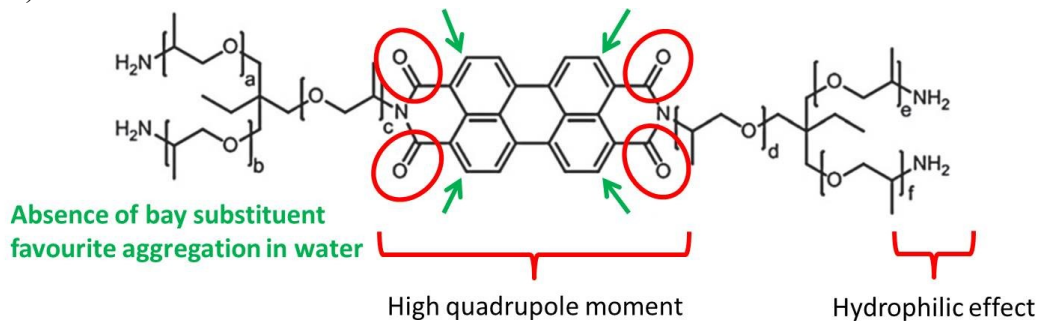


**Figure 20** Perylene bisimides derivative used in this work (named PBI) as an example of all perylene bisimides derivative solubilisation in water and stabilization effect.

Moreover, the high quadrupole moment of the perylene scaffold should have a positive influence on the water solubility. Indeed, it was demonstrated that perylene bisimides derivatives are able to stabilize single wall carbon nanotube (SWCNTs) in water [257, 258]. This is linked to a strong  $\pi-\pi$  interaction between the electron poor perylene bis-imide derivative and the  $\pi$  surface of the carbon materials. The interaction of SWCNTs with the water-soluble perylene bisimides led to the dispersion of carbon nanotubes, and isolated individual nanotubes were also produced. In the next section, a perylene bisimides derivative (PBI) will be employed as additive to stabilize GNP in water.

#### 3.1.1 Characterization of suspensions and Layer by layer growth

Absorption spectra of neat PBI ( $1 \times 10^{-4}$  M) and GNP-PBI ( $1 \times 10^{-4}$  M concentration of PBI) solutions in ultrapure water were collected and reported in

Figure 21. PBI visible absorption spectrum (Figure 21) displays the typical structure band of perylene, exhibiting a vibronic progression with main bands located at 465 (named c), 500 (named b) and 532 nm (named a). As already reported by Montalti et al.[248], absorption bands in aqueous solvents are broader and the vibrational structure is less defined with respect to the spectrum obtained in organic solvents, such as chloroform. This behaviour has been reported for other PBI derivatives and has been ascribed to aggregation phenomena, due to the  $\pi-\pi$  stacking interactions which are particularly favoured in aqueous environment and at high concentration [259]. As it is possible to see in Figure 21, PBI VIS spectrum in water present the same transitions that can be observed in  $\text{CHCl}_3$  shifted of some nm due to a solvent effect [248]. In contrast, when graphite nanoplatelets are added to the solution, the VIS spectra of the PBI changes drastically (Figure 21 b). In particular, there is an evident change in the relative intensities of the three main components, with the signals at 465 and 500 nm becoming broader and less resolved. Furthermore, an overall red shift of the spectrum is observed. All these spectral modifications are compatible either with the increase in aggregates formation and with the effects of the interaction of PBI with GNP [260].

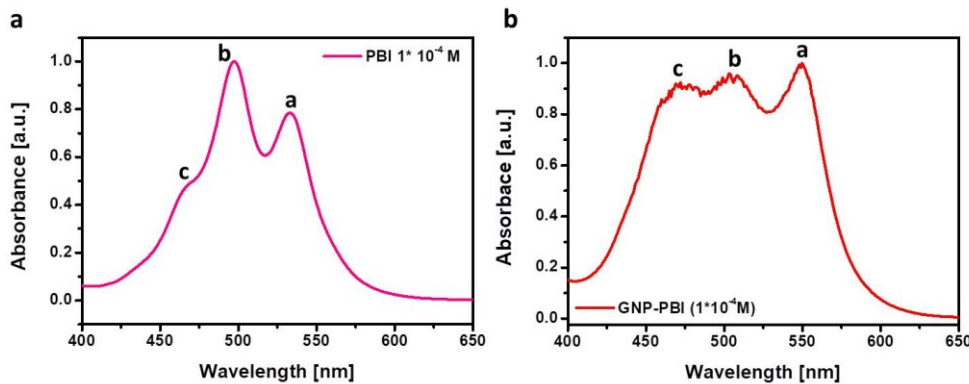


**Figure 21** a) VIS spectra of PBI  $1 \times 10^{-4}$  M solution and b) VIS spectra of GNP-PBI ( $1 \times 10^{-4}$  M) suspension.

In details, the bands at 465 nm and 500 nm become broader, due to presence of GNP which tends to push up the baseline because of the scattering of the particles [261]. The PAA spectrum present only one absorption band at 264 nm attributed to the  $n \rightarrow \Pi^*$  [253] and was not reported.

In order to better investigate the aggregation behaviour of PBI in aqueous solution, a VIS absorption and fluorescence spectroscopies study was performed on PBI aqueous solutions at different pH. Solutions of PBI ( $1 \times 10^{-5}$  M) in ultrapure water at unmodified pH, ultrapure water acidified at pH 2 through the addition of HCl (1M), ultrapure water basified at pH 8 through the addition of NaOH (1M) and PBS buffer at pH 7.4 were prepared and absorption, excitation and emission spectra were measured. The obtained spectra are reported in Figure 22.

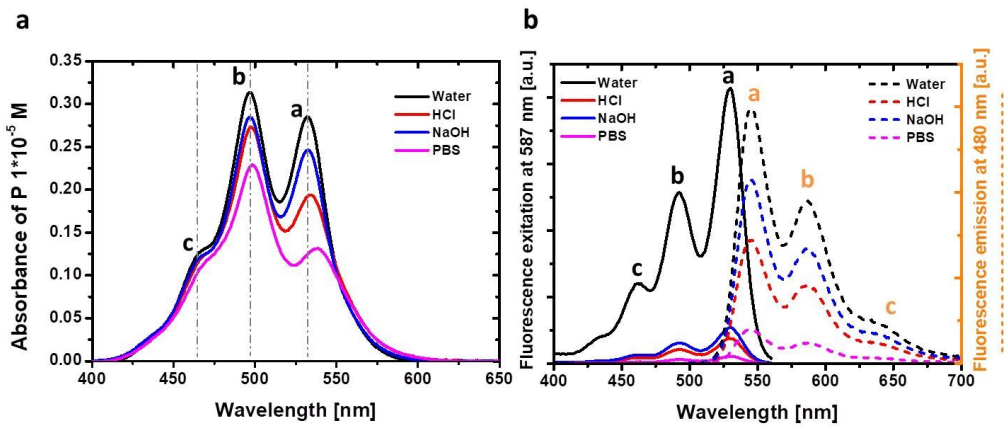


**Figure 22** UV-VIS spectra of  $10^{-5}$ M PBI solution in ultrapure water, ultrapure water at pH 2, ultrapure water at pH 8, PBS buffer pH 7.4 (a). Fluorescence spectra of  $10^{-5}$ M PBI solution in ultrapure water, ultrapure water at pH 2, ultrapure water at pH 8, PBS buffer pH 7.4 (b).

The extent of aggregation of PBI in solution can be correlated to the ratio between the higher wavelength peak and the intermediate-wavelength peak (labelled as a and b, respectively, in Figure 22 a). In fact, when PBI molecules are in monomer form [253], their absorption spectra are characterized by a vibronic progression where the intensity of the three main band is as follows a > b > c. According to this, it is possible to conclude that PBI molecules undergo less aggregation in ultrapure water (black line) than in the other aqueous media; in particular the heaviest aggregation is observed in PBS, as it is further underlined by a more evident red shift of 6 nm (from 532 to 538 nm).

Excitation (solid lines) and emission (dashed lines) spectra are reported in Figure 22 b. The spectral profile of PBI emission in all the aqueous media presents the typical vibrational structure of non-aggregated PBI, with three partially resolved components where the intensity trend is as follows: I<sub>a</sub>>I<sub>b</sub>>I<sub>c</sub>. Interestingly, excitation profiles are significantly different from absorption profiles and present the same vibrational structure of non-aggregated PBI as well. It can be then concluded that, beside severe aggregation occurs in all PBI aqueous solutions, a fraction of non-aggregated fluorescent PBI molecules is still present, which are responsible of the residual fluorescence of the solutions. As expected, fluorescence intensity is directly correlated to the aggregation behaviour, the less the aggregation, the more intense the fluorescence. Fluorescence measurements confirm what observed in visible spectroscopy, concluding that ultrapure water is the best solvents for this PBI derivative in the considered conditions.

In order to investigate the interaction between PBI and GNP, the fluorescence spectra of neat GNP-PBI (named A) and filtered GNP-PBI (named Af) suspension were collected (Figure 23).

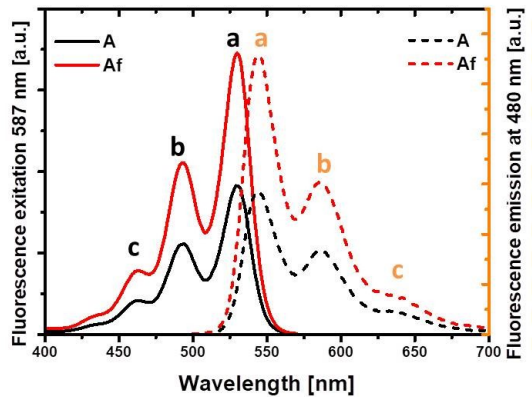


**Figure 23** Fluorescence spectrum of GNP-PBI suspension A, and fluorescence spectrum of filtered GNP-PBI suspension named Af.

Both filtered and unfiltered suspensions have the same profile of neat PBI solution, and the filtered solution displays higher fluorescence intensity with respect to the unfiltered suspension. This suggests that only a small fraction of PBI is strongly interacting with graphene and most of the molecules remains in solution after filtration. Nevertheless, the correlation between fluorescence intensity and PBI concentration is not so straightforward when comparing a solution to a suspension. The presence of graphene nanoplatelets, in fact, can affect the fluorescence of PBI molecules by absorbing part of the emitted fluorescence through the well-known inner-filter effect [262].

In conclusion, the characterization of PBI solutions and PBI-GNP suspension by means of electronic spectroscopies revealed that PBI molecules are mostly present in aggregated form in aqueous solution. At this stage it is not possible to further investigate the role of molecular aggregates vs non-aggregated molecules in the interaction with GNP; nevertheless, because GNP-PBI suspensions present a stability of some days in terms of time, the opportunity of using these systems in a LbL approach was investigated.

The possibility to obtain an LBL assembly with PAA and PBI, was investigated using VIS absorbance spectroscopy and the results are reported in Figure 24. When PBI is assembled with PAA its absorption spectra (Figure 24) considerably changes. The shape of the signal, originally made of 3 well defined bands, became broader and the signal at 465 nm appears as a shoulder. Increasing the number of deposited layers, the signal at 532 nm shifts to 543 nm (peak a in Figure 24) suggesting that there is a change in the polarity environment of the molecule, due to the electrostatic interaction established with PAA. During the LbL deposition the signals grow meaning that the macromolecules interact with each other presumably with electrostatic interactions, driving the growth of the assembly.

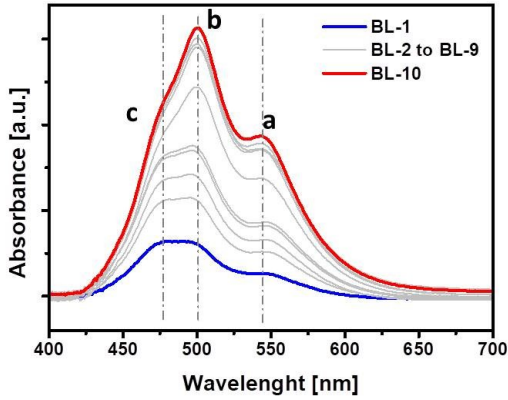


**Figure 24** VIS LbL growth of PBI-PAA system.

On the basis of these results, which demonstrate the possibility for the PAA-PBI LbL, the PAA/G-PBI assembly was studied in order to exploit the GNP effect on the gas barrier properties of the assembly. The VIS LbL growth of PAA/G-PBI assembly is reported in Figure 25 a. The presence of GNP in the assembly is apparent since the first BL deposition as GNP tends to shift the baseline to higher values because of the scattering of the particles. By increasing the number of deposited layers, the signal at 546 nm (labelled a in Figure 25 a) grows in intensity until 10 BL are deposited and the adsorption at 475 nm (labelled c in Figure 25 a) became broader than in the first deposited BL. In contrast, the signal at 497 nm (labelled b in Figure 25 a) remains almost unchanged. Evaluating the trend of the adsorption signals, it is clear that the presence of an increasing GNP concentration within the assembly, as the layers add up, is responsible for a general broadening of the signals. To further investigate the coating growth, FT-IR spectrometry was adopted (reported in Figure 25 b). in the reported spectra it is possible to distinguish the signals related to functional groups of both PBI and PAA, that grow in intensity by increasing the number of BL. The  $3700\text{-}2000\text{ cm}^{-1}$  region is dominated by the stretching of N-H and O-H groups owing to PBI and PAA, respectively and by the presence of water as an intense broad band from  $3700$  to  $2750\text{ cm}^{-1}$ . The sharp signal centred at  $2900\text{ cm}^{-1}$  is attributed to the NH asymmetric stretching of  $\text{NH}_2$  functionalization of lateral pendant in PBI and to the CH asymmetric stretching vibration mode of the same pendant (signal a' in Figure 25 b). In the  $2000\text{-}800$  region, the signal at  $1706\text{ cm}^{-1}$  can be attributed the C=O stretching vibration mode of PAA combined with the C=O stretching vibration mode of imide carbonyl group in PBI that appears as a shoulder at  $1740\text{ cm}^{-1}$  (signal b' in Figure 25 b). Signals at  $1260\text{ cm}^{-1}$  and  $1018\text{ cm}^{-1}$  correspond to the C-O-C  $\nu_{\text{asym}}$  and to the C-O-C  $\nu_{\text{sym}}$  mode of PBI (signal c' and d' in Figure 25 b respectively). Finally the signal at  $800\text{ cm}^{-1}$  is attributed to the  $\text{NH}_2$  wagging of amine pendant in PBI (signal e' in Figure 25 b) [261]. Although the characteristic peaks of each component are clearly distinguishable in the spectra, it was not possible to establish the growth regime of the assembly because the aforementioned signals do not growth in intensity with the number of deposited layers. As an example, 10 BL spectrum shows signals less intense than the 6 BL.

This behaviour may be related to the PBI which is not strongly bound to the GNP due to the stacking phenomena of the molecules as observed by UV and fluorescence investigations. During the assembly, the PBI is thus solubilized when exposed to the PAA solution. This is also suggested by the fact that during the deposition procedure, the PAA solution change from uncoloured to pink, which is the colour of a neat PBI solution.

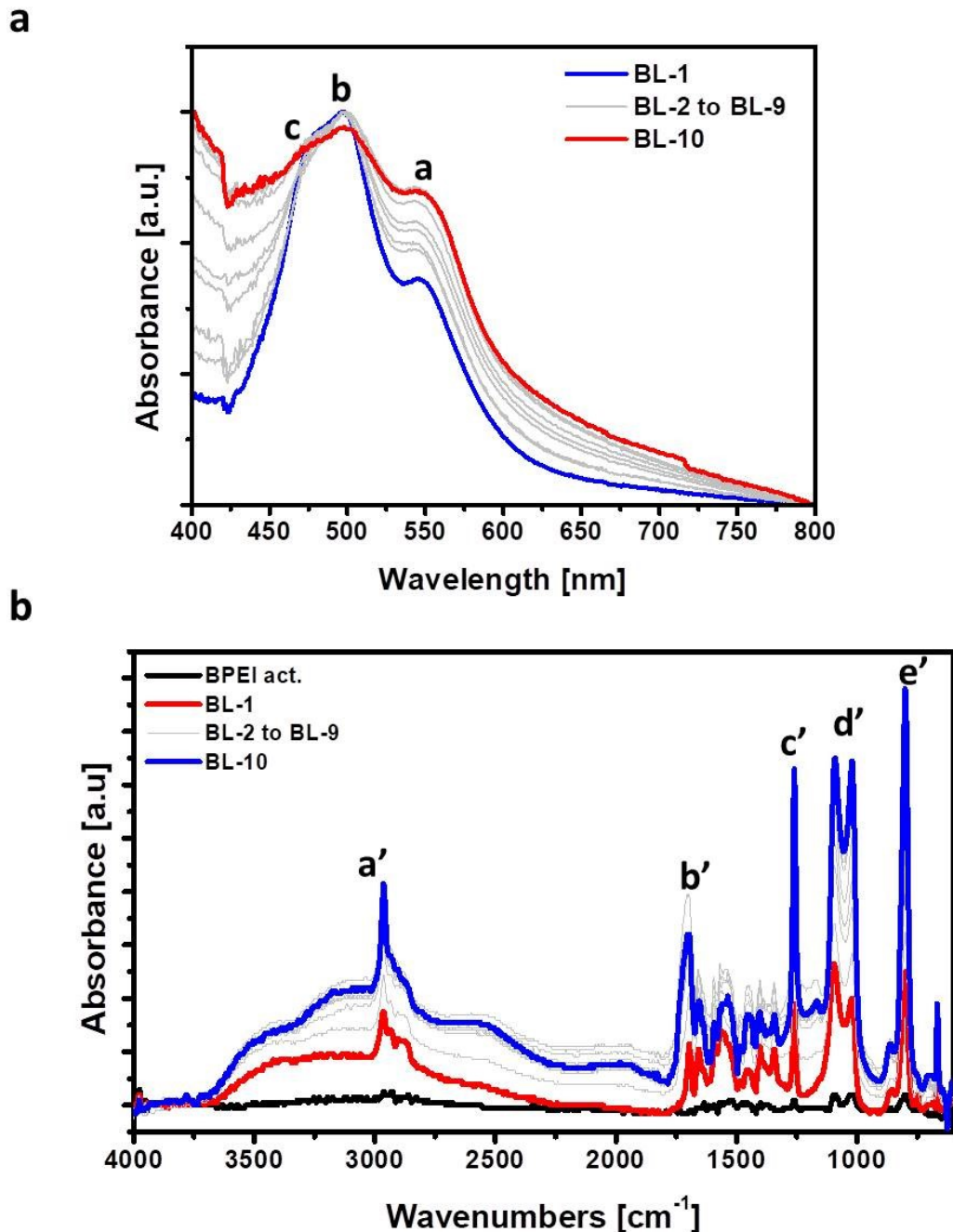


**Figure 25** LBL growth of PAA/GNP-BPI followed by a) VIS spectroscopy and b) FT-IR spectrometry.

A 10 BL PAA/GNP-PBI coating was assembled on a polyethylene terephthalate film following the procedure adopted for the LbL assembly in Vis and FT-IR study. Neat PET film (10  $\mu\text{m}$  thickness) exhibits an oxygen transmission rate of 140 [ $\text{cm}^3/\text{m}^2 \text{ atm day}$ ] and 120 [ $\text{cm}^3/\text{m}^2 \text{ atm day}$ ] values at

0% and 50% RH conditions, respectively. 10 BL of PAA/GNP-BPI assembly impart a rose colour to the film (Figure 26 b); the transparency of the PET is retained and the OTR is reduced by 30% in both dry and humid conditions. This improvement in gas barrier properties of PET thin film is ascribed GNP embedded within the coating matrix between the PAA and the PBI (Figure 26 c). These results well below those achieved for other LbL treated PET film reported in the section 1.4.3. this can be linked to two main reasons: i) the PBI is not able to efficiently stabilize GNP in water because the high tendency to aggregate with itself, as it was demonstrated by fluorescence experiments; ii) the low concentration of dispersed GNP is deposited in aggregate resulting in a not-efficient barrier. From these considerations, it is apparent that a better stabilization is required. In the following section, polyelectrolytes are then employed as stabilizing agents replacing PBI.

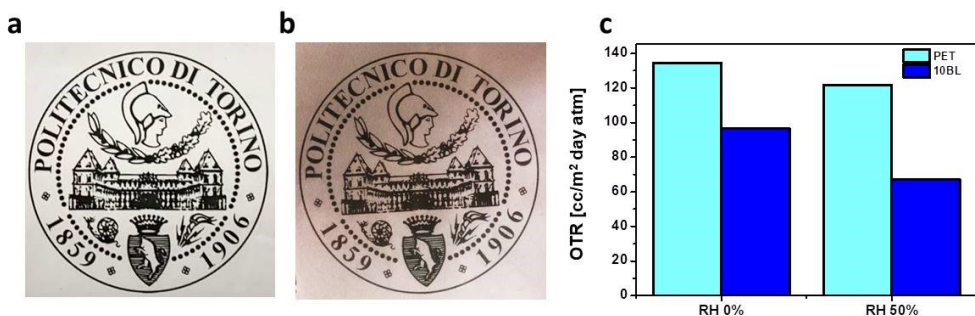


**Figure 26** Digital image of a) neat PET 10 um thick and of b) the 10 BL PAA/GNP-PBI treated PET 10 um thick. c) Oxygen Transmission rate of LBL coated and untreated PET thin film.

### 3.2 Multilayers of GNP-polymer based suspensions for the preparation of gas barrier membrane

As described in the previous section, the stabilization of graphene in water is still a great challenge and although this topic has attracted the interest of the scientific community as demonstrated by preliminary publications, the mechanism behind the stabilization effects is not completely understood [254]. In this section, water solutions of PolyAcrylicAcid (PAA) or BranchedPolyEthylenImine (BPEI) were used for dispersing graphite in water by ultrasonication. The obtained suspensions were examined by advanced scanning probes microscopy, SEM and Raman spectroscopy in order to characterize the quality of the suspensions. In conclusion, the suspensions were employed for the preparation of a LbL assembly able to improve the gas barrier properties of PET 10  $\mu$ m thick films.

#### 3.2.1 Characterization of GNP-polymer suspensions

The colloidal suspensions of GB and GP were fully characterized in order to determine the dimensions and the interaction of the platelet with the polyelectrolyte in water. The concentration of GNP was evaluated by

thermogravimetric analysis of dried suspensions between 100°C and 800°C in nitrogen atmosphere (Figure 27) [99]. Considering that GNP are practically stable in the considered conditions (Figure 27 a), it is possible to evaluate the amount of GNP in the colloidal suspension by the sum of the percentage of GNP and polymer (B in one case and P in the other) as solid in the final residues. For the calculation of GNP concentration in GB and GP it was assumed that there are no effects of the GNP on the degradation process of the neat polymers. Table 8 reports the percentage of mass residue from thermogravimetric analysis for neat polymers and suspensions. Considering data reported in Table 8, it was possible to estimate a concentration of 0.019% wt of G in GP and 0.006% wt in GB (concentration referred to the colloidal suspension).

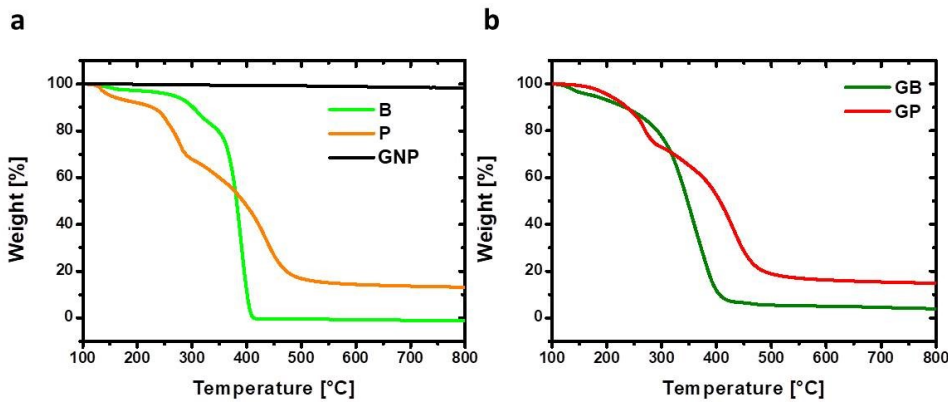


**Figure 27** a) TGA in  $N_2$  atmosphere of neat B, P, and GNP. b) TGA measurements of GB and GP in  $N_2$  atmosphere.

**Table 8** TGA residues of neat polymer and suspensions.

Sample	Residue [%]	Sample	Residue [%]
G	98.4		
B	0	GB	3.9
P	13.1	GP	14.8

GB and GP dried suspensions were characterized by Raman spectroscopy (Figure 28). The Raman spectrum of neat graphite present two sets of signals: the first includes the D, G and  $D^I$  set while the second is composed by the 2D,  $2D^I$  signals. In the first set, the D band correspond to the breathing mode of six-atoms rings and requires defects for its activation, while G band correspond to the  $E_{2g}$  phonon mode and  $D^I$  is generated from the phonon double resonance around the Brillouin zone. In the second set, 2D and  $2D^I$  are the overtone signals of D and  $D^I$  bands, respectively. These signals are originated from a process were the momentum conservation is satisfied by two phonons with opposite wave vector, and no defects are required for their activation thus are always present. Moreover the shape of 2D band is typical of multi-layered graphene-based structures [12]. In GP, as suggested by the comparison of the obtained Raman spectra with the one of the neat GNP, the presence of the D signal proves the formation of defected nano-crystalline graphite and the shape of 2D signal is typical of GNP structures. Moreover, the presence of  $2D^I$  and 2D confirms the retention of a general

honeycomb arrangements for nano-crystalline platelets of graphite after the exfoliation process [12]. The situation is different in the case of GB: indeed, the shift of the G band at lower wavenumbers, the shape of the 2D band and the low intensity of the  $2D'$  signal compared to the 2D intensity suggest that B might stabilize thicker graphite nanoplatelets with respect to P [12].

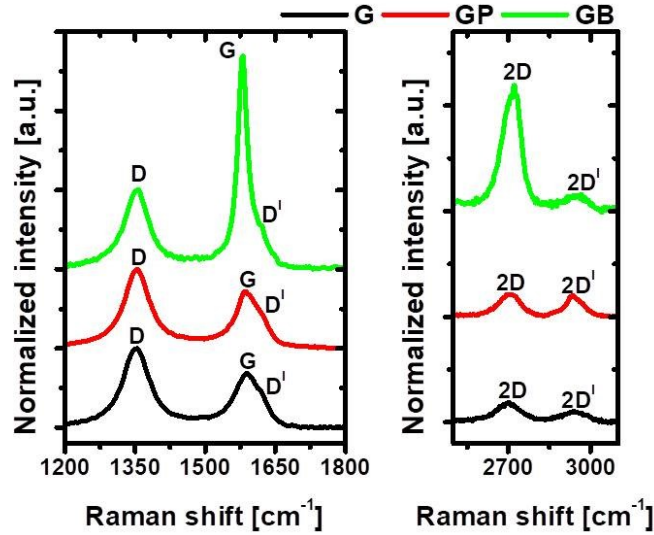


**Figure 28** Raman spectra of GB, GP, and GNP.

SEM microscopy and AFM measurements were then employed for the determination of the GNP aspect ratio. SEM measurements performed on GB and GP show big wrinkle GNP with a medium length of approx. 3 micron, as calculated by statistical method (Figure 29).

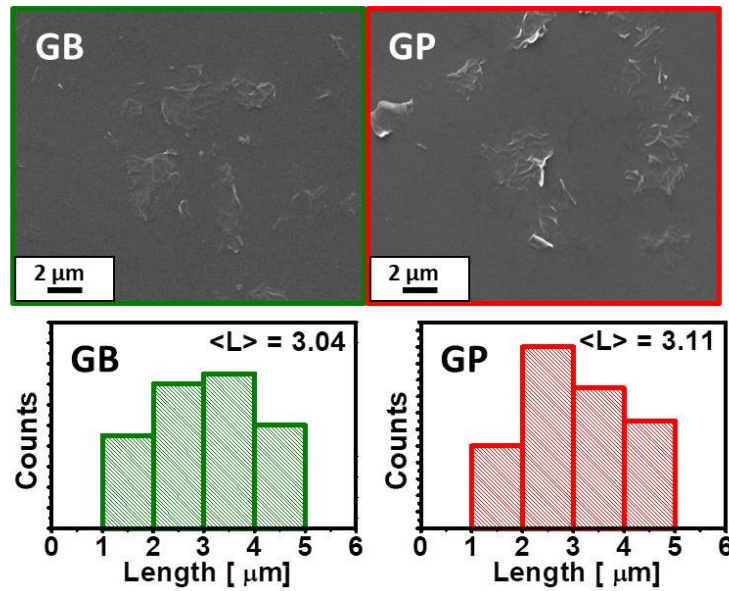


**Figure 29** SEM micrographs of GB and GP suspensions deposited on a Si wafer and statistical determination of lateral size.

The evaluation of the thickness of neat and polyelectrolyte coated GNP was conducted by tapping mode-AFM (Figure 30). The neat GNP simply tip-sonicated in water is characterized by flakes of close packed sheets with a medium thickness

of 20 nm (Figure 30 a). Differently from the neat GNP suspension, in GB the surface of the silicon wafer is well covered by a thick layer of polymer embedding the GNP and resulting in an adduct of graphite-BPEI with a wrinkle surface and 130 nm thick (Figure 30 b). The same morphology is observed for the graphite-PAA sample. P shows a good affinity with the graphite platelet yielding 110 nm thick nanoparticles are present (Figure 30 c).

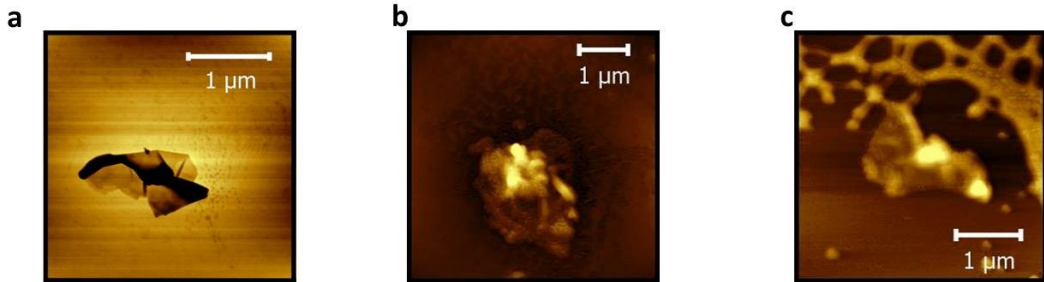


**Figure 30** AFM tapping mode topography of a) single GNP, b) a single GNP covered by B in GB suspension, c) a single GNP covered by P in GP suspension.

### 3.2.2 Coating growth by FT-IR, QCM-D and SPAR.

The prepared GNP suspensions have been employed in a LbL assembly. The coating growths of neat BP and GB-GP assemblies were monitored by FT-IR spectroscopy, QCM-D and SPAR. In FT-IR spectroscopy, the spectra of neat B and P were evaluated as reference (Figure 31 and Table 9). The main bands appearing in the spectrum of B are related to the asymmetric and symmetric stretching vibration mode of -NH groups at 3368 and 3299 cm<sup>-1</sup> respectively; these signals are overlapped to the stretching vibration mode of hydroxyl group of the adsorbed water [263]. Alkyl stretching vibrations attributed to the C-H asymmetric and symmetric stretching vibration modes are visible at 2959 and is at 2849 cm<sup>-1</sup>, respectively. However, the most important signals are related to the bending of N-H group of primary and secondary amine at 1570 and 1477 cm<sup>-1</sup> respectively. Furthermore, it is possible to distinguish C-N stretching mode of secondary amine at 1154 cm<sup>-1</sup> from the primary at 1049 cm<sup>-1</sup>. Wagging vibration mode of NH<sub>2</sub> groups are also visible at 817 cm<sup>-1</sup>. The spectrum of neat P is affected by the presence of water in the region between 3500-2500 so the O-H stretching vibration modes of the polymer are mostly broad. However, the most intense band is located at 1714 cm<sup>-1</sup> and it is related to the C=O symmetric stretching vibration mode of the carboxylic functional groups. A shoulder is attributed to the presence of carboxylate as a consequence of the interaction of the -COOH functional groups with atmospheric water. In the fingerprint region is possible to identify a broad band composed by C-O symmetric stretching vibration mode coupled with the O-H in plane bending.

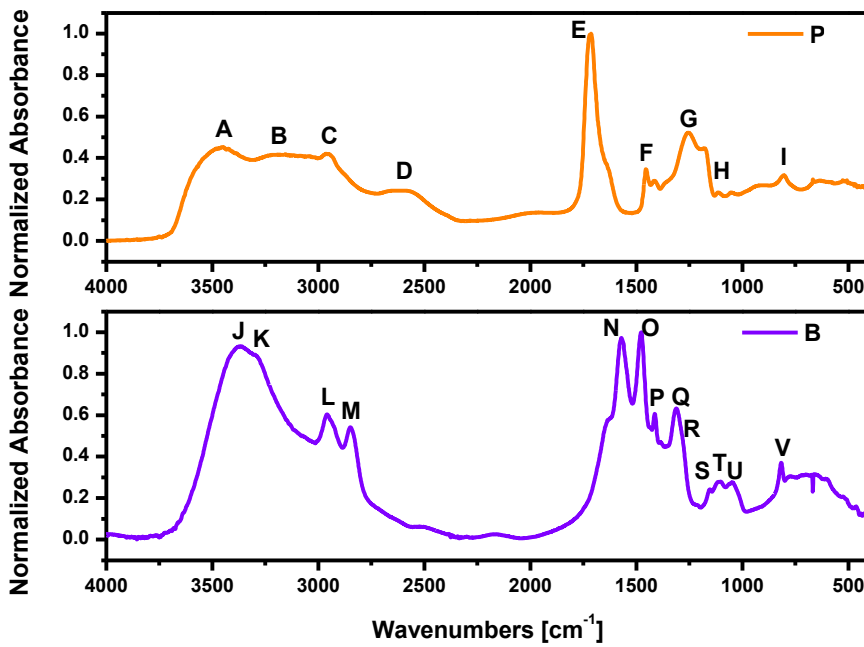


**Figure 31** FT-IR spectra of neat PAA (P) and BPEI (B) deposited on Si wafer.

**Table 9** Signal attribution of P and B.

PAA			BPEI		
Absorbance [cm <sup>-1</sup> ]	Signal	Attribution	Absorbance [cm <sup>-1</sup> ]	Signal	Attribution
3455	A	OH <sub>as</sub> of water	3368	J	NH $\nu_{as}$
3180	B	OH <sub>as</sub> of PAA	3299	K	NH $\nu_s$
2954	C	CH <sub>2</sub> $\nu_{as}$ and CH $\nu_{as}$	2959	L	CH <sub>2</sub> $\nu_{as}$ and CH $\nu_{as}$
2880 and 2591	D	Overtones and combination of bands H and I enhanced by Fermi resonance with the broad OH $\nu_{as}$ band	2849	M	CH <sub>2</sub> $\nu_s$ and CH $\nu_s$
1714	E	C=O $\nu_s$	1570	N	NH $\delta_I$
1453	F	CH <sub>2</sub> deformation	1477	O	NH $\delta_{II}$
1415, 1255 and 1180	G	C-O $\nu_s$ coupled O-H $\delta_{in\ plane}$	1413	P	CH <sub>3</sub> $\nu_s$ of secondary and tertiary amines
1111	H	C-CH <sub>2</sub> $\nu$	1312	Q	CH <sub>2</sub> $\delta_{wagging}$
804	I	C-CH <sub>2</sub> $\delta_{twist}$ and C-COOH $\nu$	1281	R	CH <sub>2</sub> $\delta_{twist-rocking}$
			1154	S	CN $\nu_{II}$
			1108 and 1011	T	CH <sub>3</sub> $\delta_{rocking}$
			1049	U	CN $\nu_I$
			817	V	NH <sub>2</sub> $\delta_{wagging}$

Figure 32 reports the IR signals as function of deposited BL on model Si wafer, the intensity of the peaks ascribed to COOH and  $\text{COO}^-$  plotted as a function of BL number and the cross-section images of the 10BL coating imaged by FESEM. The interaction between GB and GP significantly changes the infrared spectra of neat polymers. The characteristic peaks associated to functional groups of both components are shifted and new signals attributed to protonated amines of B ( $1555 \text{ cm}^{-1}$ ) and carboxylate groups of P ( $1706$  and  $1666 \text{ cm}^{-1}$ ) grow up proportionally to the deposition BL number, indicating the occurrence of LbL self-assembly (Figure 32 a). The strongest peak at  $1555 \text{ cm}^{-1}$  is ascribed to the asymmetric stretching vibration mode of  $\text{NH}_3^+$  in B combined with the symmetric stretching vibration mode of  $\text{COO}^-$  in P. Moreover, two shoulders at  $1706 \text{ cm}^{-1}$  and  $1666 \text{ cm}^{-1}$  are related to characteristic signals of P relative to C=O and  $\text{COO}^-$  asymmetric stretching respectively [264]. The final resulting convolution of this signal is also affected by the presence of water molecules, which yield a signal at  $1640 \text{ cm}^{-1}$ . By plotting the absorbance of the signal at  $1555 \text{ cm}^{-1}$  as a function of bi-layer number it is apparent that this GB-GP system follows a superlinear growth regime. This is in agreement with previously reported literature studies dealing with B-P self-assembled coatings (Figure 32 b) [220, 265]. The exponential growth of the BPEI-PAA system can be ascribed to the density of carboxylate groups owing to the PAA which is pH dependent. Indeed, during the PAA deposition the pH of the acidic solution is  $\sim 4$  and the ionization degree of the PAA is lower than the 5%, thus most of carboxyl groups of the adsorbed PAA exist in the -COOH form. Conversely, when the substrate is immersed in the BPEI suspension, the PAA adsorbed layer is exposed to a pH 9 solution, which promotes the dissociation of -COOH groups to  $\text{COO}^-$ , with a subsequent increase of the related contribution to the  $1555 \text{ cm}^{-1}$  band [220, 266, 267]. This is also corroborated by previous literature reports. In 2011, Yang et al. [265] studied the BPEI-PAA assembly with different pH combinations, such as  $10/4$ ,  $8/6$ ,  $7/7$  and  $4/4$  for BPEI-PAA combination showing thickness order of  $10/4$  ( $1\mu\text{m}$ )  $> 8/6$  ( $890 \text{ nm}$ )  $> 4/4$  ( $349 \text{ nm}$ )  $> 7/7$  ( $90 \text{ nm}$ ). This behaviour was attributed to the pH sensitivity of functional groups of both weak polyelectrolytes and to the interactive charge overcompensation from the BPEI (basic) and the PAA (acid). When PAA is low charged, the pKa of PAA is very sensitive to local pH [268, 269] and the basic BPEI solution improves the charge of PAA promoting the -COOH dissociation. Similarly BPEI exhibits an increased charge density when exposed to the acidic PAA solution. Once the charge density is increased, more charged groups are needed for overcompensation. As this process continues, with each deposition step, more BPEI and PAA are adsorbed, resulting in the dramatic increase in film thickness as a function of deposited layers. When both PAA and BPEI are at pH7 they are in their highly charged state and during the assembly they undergo intrasegmental repulsion and deposit thinner layers.

Interestingly, GNP nanoparticles block the polymers diffusion through the assembly as it is common in LbL with exponential growth [270]. This behaviour explain the decreased absorbance values of  $1555 \text{ cm}^{-1}$  signal plotted as a function of the number of deposited layers in GBGP assembly with respect to the BP.

Moreover, the limited diffusion of the polymers inside the coating is reflected in the final coating thickness. The 10 BL cross section of both B-P and GB-GP coatings on Si wafer has been imaged by FE-SEM (Figure 32 c and d). Both coatings appear continuous, the two polyelectrolytes alone yield a wrinkled coating likely due to the complete water removal from the structure. The BP coating at 10BL have a thickness of  $1.23 \pm 0.3$   $\mu\text{m}$  and is thicker than GB-GP which is  $985 \pm 13$  nm thick. Moreover, GBGP cross-section shows some irregularities due to the presence of G nanoparticles. High magnification micrographs reveal a continuous structure where G sheets are embedded within the B-P matrix (Figure 32 e).

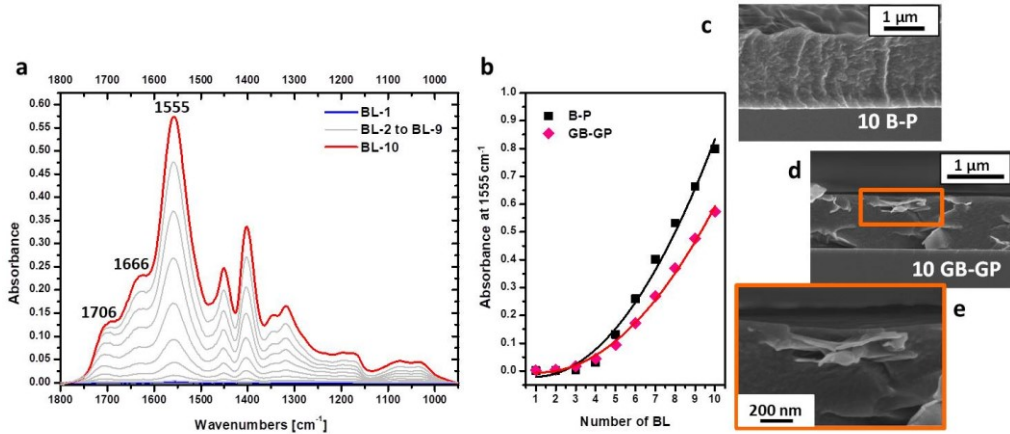


**Figure 32** a) LbL growth of GB-GP system followed by FT-IR spectroscopy , b)comparison between BP and GBGP LbL regime growth, c) cross-section micrograph of 10BL BP d) and GBGP assembly, e) GNP embedded in GBGP matrix, high magnification FESEM micrograph.

SPAR and QCM-D were employed for further study qualitatively the LbL growth of GB-GP in comparison with the B-P assembly. SPAR was employed to study the LbL growth of 5 BL BP and 5 BL GBGP assemblies. This technique allows to continuously and quantitatively measure the adsorbed amount of polymer per unit area on a macroscopic flat surface in real time using a linear polarized light beam which is reflected by the surface. The reflected beam is split into its perpendicular and parallel components using a polarized beam splitter. The intensity of the normal and the parallel polarization directions (respect to the incidence plane) are measured continuously and is indicated as S value. Upon adsorption the S value changes and this change can be correlated to the adsorbed amount of polyelectrolytes after proper calibration. The technique is very sensitive because the variation in intensity of S signal depends also from the refractive index of the adsorbed layer. In order to measure the S value during assembly formation, the substrate is immersed in a chamber were polyelectrolytes are flushed and the measurements is collected to the stagnation point [189]. When BP system is assembled (Figure 33 a), the S value increases with the number of the deposited layers meaning that the thickness of the assembly is increased at every deposition step. The steep increase of S in between two deposited layers underline that the assembly grows exponentially, in agreement with FT-IR experiments [271]. A superlinear growth is also evidenced for the 5 BL GBGP system (Figure 33 b).

Unfortunately, GNPs absorb part of the incident light as a function of the thickness of the deposited amount. This behaviour impedes the quantification of the adsorbed amount of polymer-graphite nanoplatelets. This consideration also explains why the S value of 5 BL GBGP assembly is considerably reduced with respect of 5 BL BP.

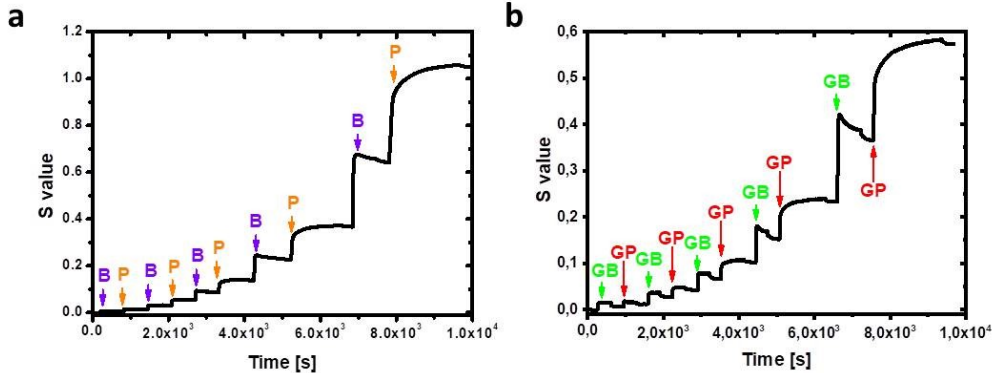


**Figure 33** SPAR (a) of 5 BL BP assembly and (b) 5 BL GBGP assembly.

Because the amount of deposited mass at each deposition step and the thickness of these layers was not able with SPAR, QCM-D (Figure 34) was selected to study the LbL built-up in real time of both 5BL BP and 5BL GBGP coatings in order to calculate the amount of deposited mass from the frequency oscillation variation and valuating the rigidity of the assembled coatings with dissipation measurements, as complement to SPAR. In both systems, the LbL assembly was detected by the decrement of the oscillation frequency of the sensor and by considering that this decrement is usually more and more pronounced when the multilayer grows in a superlinear regime [272]. Interestingly, the dissipation graph is very different from one system to the other. In BP system it is evident that the assembly is viscoelastic since the first BL deposition. Considering the frequency variation, in these conditions the prerequisite to adopt the Sauerbrey relation are not satisfied and the calculation of the amount of deposited mass for each layer is not possible [273] (Figure 34 a). Indeed, Sauerbrey equation is limited to the scenario where a thin, rigid and firmly attached layer of material is deposited to the surface of the sensor so the thin added layer can be approximated to be a part of the oscillating sensor. In the under study systems the frequency curves suggest that the amount of deposited mass is very high, so the Sauerbrey model is not valid. The situation is further complicated by the presence of water, which is weakly bound to the last exposed layer. In fact, every time a new layer is deposited on the most external surfaces the release of water leads the assembly to collapse. This collapse is evidenced by the partial decrement of dissipation in between layer adsorptions. In addition, as shown in dissipation curve, the amount of released water is not constant (Figure 34 b).

When GNP are embedded in the LbL assembly, the situation is quite different. The  $\Delta f/v$  signal is less decreased compared to the BP assembly and the dissipation signals are more resolved than in the BP assembly (Figure 34 c). The combination of these observations suggests that 5BL GBGP assembly is more rigid than the reference. However, considering the dissipation (Figure 34 d), this

is true only for the first and the second BLs because, starting from the fifth deposition step, the content of adsorbed water is considerable and the assembly becomes soft affecting the possibility to quantify the adsorbed mass.

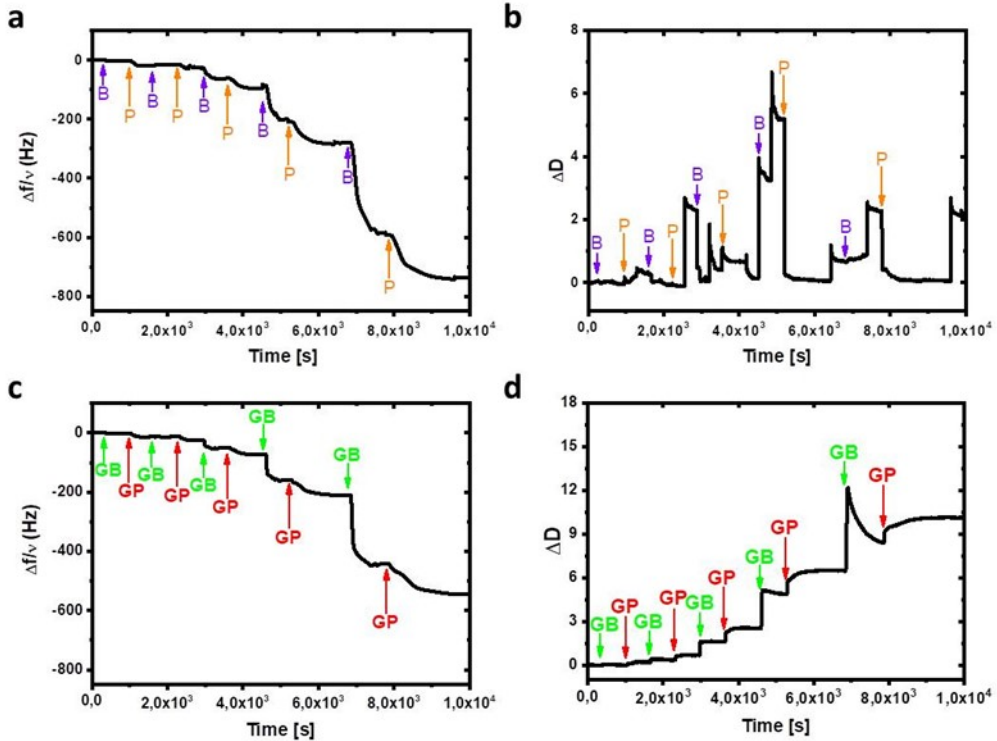


**Figure 34** QCM and dissipation of LbL monitored growth of (a, b) 5 BL BP assembly and (c, d) 5 BL GBGP assembly.

### 3.2.3 Morphology on PET thin film and Gas Barrier properties

Both systems have been deposited on 10  $\mu\text{m}$  thick PET in order to improve its gas barrier properties. The morphology of the deposited film in cross section and the resulting gas barrier properties in both dry and humid conditions are reported in Figure 35. As observed for the deposition on silicon wafer, 10 BL BP is thicker than the 10 BL GBGP assembly due to the presence of GNP embedded in the matrix. The presence of cracks in SEM micrograph is due to the fracture of the sample conducted in liquid nitrogen. Neat PET 10  $\mu\text{m}$  film exhibit 120 [ $\text{cm}^3/\text{m}^2 \text{ atm day}$ ] and 140 [ $\text{cm}^3/\text{m}^2 \text{ atm day}$ ] values of OTR at 0% and 50% RH conditions but after the deposition of the coatings the gas barrier properties towards oxygen improve drastically. In general, as it is possible to see from the bar chart in Figure 35, GBGP coated PET film exhibit better performances than those of BP in dry conditions. Indeed, when 5 BL are deposited for both of the systems a 50% reduction in OTR for 5BL GBGP with respect to 5BL BP, is measured. Increasing the number of deposited layers, this trend is further improved an OTR under 0.005  $\text{cm}^3 / \text{m}^2 \text{ day atm}$  is obtained when 10 BL of GBGP assembly are deposited on the PET film. In humid condition the situation is quite different: even if 5 BL of GBGP are able to decrease the OTR with respect to 5BL BP PET films, increasing the number of deposited layers is not

sufficient to reach the exceptional gas barrier properties showed in dry conditions. Notwithstanding this, 10 BL GBGP OTR is 24% lower than 10 BP.

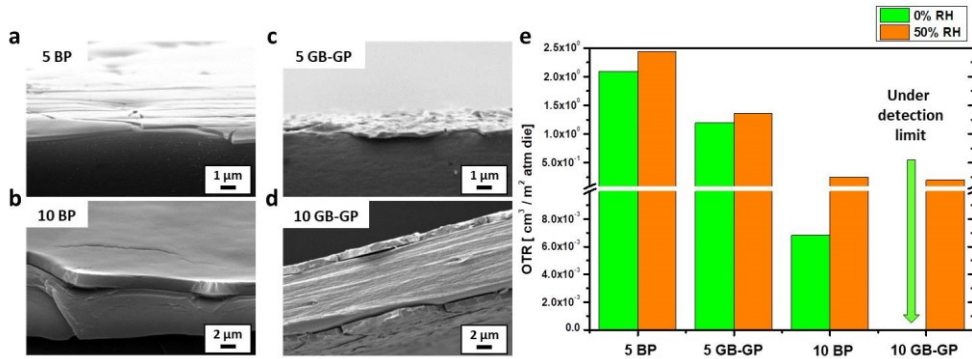


**Figure 35** SEM micrograph of a PET 10 µm thick coated by 5BL BP (a), 10BL BP (b), 5 BL GBGP (c) and 10 BL GBGP (d) assembly. e) OTR measurements collected on the same samples.

The performances of obtained samples were compared to others in literature and the permeability of examined samples have been calculated (Table 10). Samples containing the same polymer (P) and different nanoparticles like GO, MMT and silica have been considered for the comparison. 10 BL coatings of P/MMT are enough to drastically improve the gas barrier properties of PET films in dried conditions [274]. However, due to the high aspect ratio of graphene related material, the use of GO more significantly increases the tortuosity path of gas molecules permeating the film resulting in better performances. GBGP coating shows better performances than P/GO assembly, probably due to the fact that in GBGP assembly the presence of preferentially oriented GNPs acts as an additional barrier in a LBL assembly that contains polyelectrolytes capable of showing very good barrier properties. Even if the 50% of relative humidity condition is detrimental for GBGP gas barrier properties, the performance of the considered assembly is comparable to what observed for SiO<sub>x</sub> coatings obtained by ALD deposition.

**Table 10** Comparison between BP and GBGP system permeability with literature.

Sample	Oxygen Permeability [cc mm/m <sup>2</sup> day atm]	Oxygen Permeability [cc mm/m <sup>2</sup> day atm]	Ref.
	RH 0%	RH 50%	
PET 10 µm	1.34	1.21	This thesis
10 BL BP	$8.68 \times 10^{-5}$	0.003	This thesis
10 BL GB-GP	OTR < detection limits	0.0023	This thesis
<b>10 BL P/GO<sub>0.1%</sub><sup>a</sup></b>	0.28	na <sup>c</sup>	[194]
<b>10 BL P/MMT<sub>0.2%</sub><sup>a</sup></b>	1.15	na <sup>c</sup>	[274]
<b>10 BL P/MMT<sub>0.5%</sub><sup>a</sup></b>	1.41	na <sup>c</sup>	[274]
<b>SiO<sub>x</sub><sup>b</sup></b>	na <sup>c</sup>	0.06-0.006	[145]

<sup>a</sup> performed on PET 179 µm; <sup>b</sup> performed on PET 12 µm. <sup>c</sup> not reported; 0.1%, 0.2% and 0.5% indicate the% wt concentration on lamellar filler used for LbL assembly.

# **Chapter 4**

## **GRMs for flame retardancy application**

The use of surface modification techniques to impart flame retardancy properties to foams has been established as one of the best solution to address the needs for sustainable, non-toxic and high-performing materials [208]. The majority of the published papers on PU foam protection deals with the use of inorganic nanoparticles like sodium montmorillonite [216], while limited attention has been directed towards the use of GRM. This class of materials showed promising FR results when employed in bulk thermoplastic or thermoset polymer nanocomposites [275, 276]. GRM may be successfully exploited in water based LbL assemblies by employing partially oxidised graphene sheets normally referred as graphene oxide [194]. From a chemical point of view, graphene oxide is negatively charged in water due to the presence of oxygenated functionalization obtained by exposing graphene to strong oxidizers, typically sulphuric acid and potassium permanganate [35]. In this manner, it is possible to prepare stable graphene oxide suspensions in water or polar organic solvents. A first study employed low concentration graphene oxide suspensions for the production of FR LbL coatings where the main constituents were chitosan and alginate; this study demonstrated the potential of graphene oxide in conferring FR characteristics to PU foams [277]. In this chapter, graphite oxide (GO) was coupled with synthetic and natural polymers in order prepare LbL coatings capable to confer flame retardant properties of PU foams. The effect of ionic strength on the LbL deposition and the resulting properties were evaluated as well. LbL assembly of CHIT/GO and PDAC/GO coatings was studied until 10BL were deposited in order to determine the regime growth by FT-IR spectroscopy. It is not rare that a LbL assembly can change the regime growth increasing the number of deposited layer. When weakly charged polyelectrolytes are adsorbed on a surface they tend to form islands that growth until they coalesce in a dense layer increasing the number of deposited layers. The islands coalescence changes the growth regime

and in some cases a double linear trend can be observed [186]. This behaviour is common when weakly charged polyelectrolytes are considered in a LbL assembly and the change in regime growth can normally be detected before 10BL deposition. For example, adopting the free energy model approximation, Park et al. [278] calculated that the amount of deposited polyelectrolytes in the PAA/Poly(allylamine hydrochloride) assembly at pH5 became constant after 4BL deposition while before 4BL the amount of deposited polymers was lower, demonstrating that the complex regime growth was made of two linear regime. In another work, Negrell-Guirao et al. [279] observed that within 5 BL deposition the phosphonated poly(allylamine)/chlorate poly(allylamine) assembly grows linearly adsorbing small amounts of polymers in islands configuration. From 5 BL deposition, the amount of adsorbed polymers becomes constant and the assembly grows up showing a linear trend. This fact evidences the coalescence of the islands to a dense layer. In the studied systems, both PDAC/GO and CHIT/GO assemblies present a single linear regime growth, so the number of BL deposited on PU foams was set to 3 and 6 in order to limit the time spent during the deposition procedure and the volume of used solvents for rinsing bath. In addition, since the most performing flame retardant PU foams reported in literature showed marked reduction of peak of heat released and the ability to self-extinguishing the flame during flammability tests only when more than 5-6 BL are deposited 3 and 6 BL would allow for further improvement in the coating FR efficiency [280]. This chapter ends with a sub-section dedicated to a new deposition procedure developed in the last three year in the Politecnico di Torino [249] where the assembly of GRMs on the surface of PU foams is forced by the solvent removal. In this process, graphite nanoplatelets suspensions were employed instead of graphite oxide. GNP water-based suspension were employed for coat PU foams considering different grade of exfoliation.

## 4.1 Multilayer of Chitosan and GO to reduce flame retardancy of PU-Foam

The first system under study evaluates the LbL assembly of a FR coating comprising chitosan (CHIT) and Graphite Oxide (GO) for the protection of open cell PU foams. High aspect ratio GO nanoplatelets are the main constituents of the assembly. This assembly aims to deliver strong FR performances with a reduced number of deposition cycles and to obtain a deeper insight on the thermal degradation and structural evolution of this GO-based coating during combustion.

Chitosan is a biopolymer and is found in nature only in some fungi but it is easily synthesized by the thermochemical deacetylation of chitin [281, 282], which is largely available in nature. The reduction of acetylated units in chitosan ensure the presence of free amino groups that, in acidic conditions, allow its employment as a cationic polyelectrolyte [283]. Within the coating compositions CHIT represents the continuous matrix that holds together GO platelets in a so-defined “brick and mortar” structure. Upon the application of a flame or radiative

heat flux, CHIT may evolve towards the formation of thermally stable aromatic structures that, along with the presence of high aspect ratio GO, will produce a protective coating capable of protecting the PU foam [284]. The LbL growth of this CHIT/GO assembly was monitored with FT-IR spectroscopy and the morphology of the deposited coatings on PU foams was characterized by scanning electron microscopy (SEM). Flammability and forced combustion behaviour of untreated and LbL-treated foams have been investigated by horizontal flammability testing and cone calorimetry, respectively. The evolution of the coating during combustion was investigated by infrared and Raman spectroscopies as well as by electron microscopy.

#### 4.1.1 Layer by layer growth and characterization

The LbL growth was monitored by FT-IR spectroscopy. Initially, the IR spectra of neat CHIT and GO were evaluated (Figure 36). Table 11 reports FT-IR signal attribution for both CHIT and GO. The stretching vibration mode of –OH groups signals of CHIT are visible in a range between 3800 and 3000 cm<sup>-1</sup>; these signals are overlapped to the stretching vibration mode of amine groups. Alkyl stretching vibrations are found at 2900 and 2880 cm<sup>-1</sup> for C-H bond in CH<sub>2</sub> and CH<sub>3</sub> groups, respectively [285]. The bending vibration mode is also visible for the same groups at 1411 cm<sup>-1</sup>. However, the most important signals are related to the 2000-1000 cm<sup>-1</sup> region of the spectrum where is possible to identify the asymmetric and symmetric stretching vibration mode of the protonated amine NH<sub>3</sub><sup>+</sup> at 1640 and 1556 cm<sup>-1</sup>, respectively [263]. The latter signal appears broad due to the presence of the bending vibration mode of water. The peak at 1156 cm<sup>-1</sup> is attributed to the NH<sub>3</sub><sup>+</sup> rocking vibration mode. The most intense band of CHIT is located at 1080 cm<sup>-1</sup> and it is related to the stretching vibrations of the C-O-C group in the glycosidic linkage [263] (Table 11). The spectrum of neat GO shows the presence of oxygenated species on the surface of graphitic planes with the bands at 1725, 1627 and 1054 cm<sup>-1</sup> assigned to the stretching vibrations mode of C=O, COO<sup>-</sup>, and C-O, respectively [286]. Hydroxyl group stretching vibration modes are also visible in the range between 3800-3000 cm<sup>-1</sup>. The two components have been LbL assembled on Si surfaces following the procedure described in chapter 2.

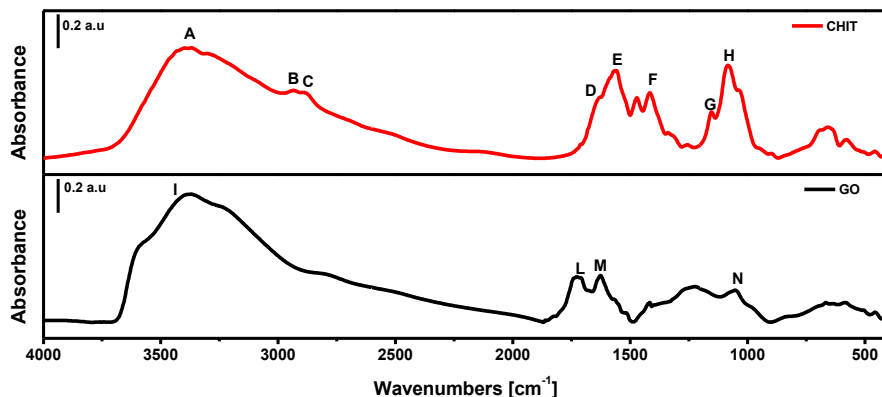
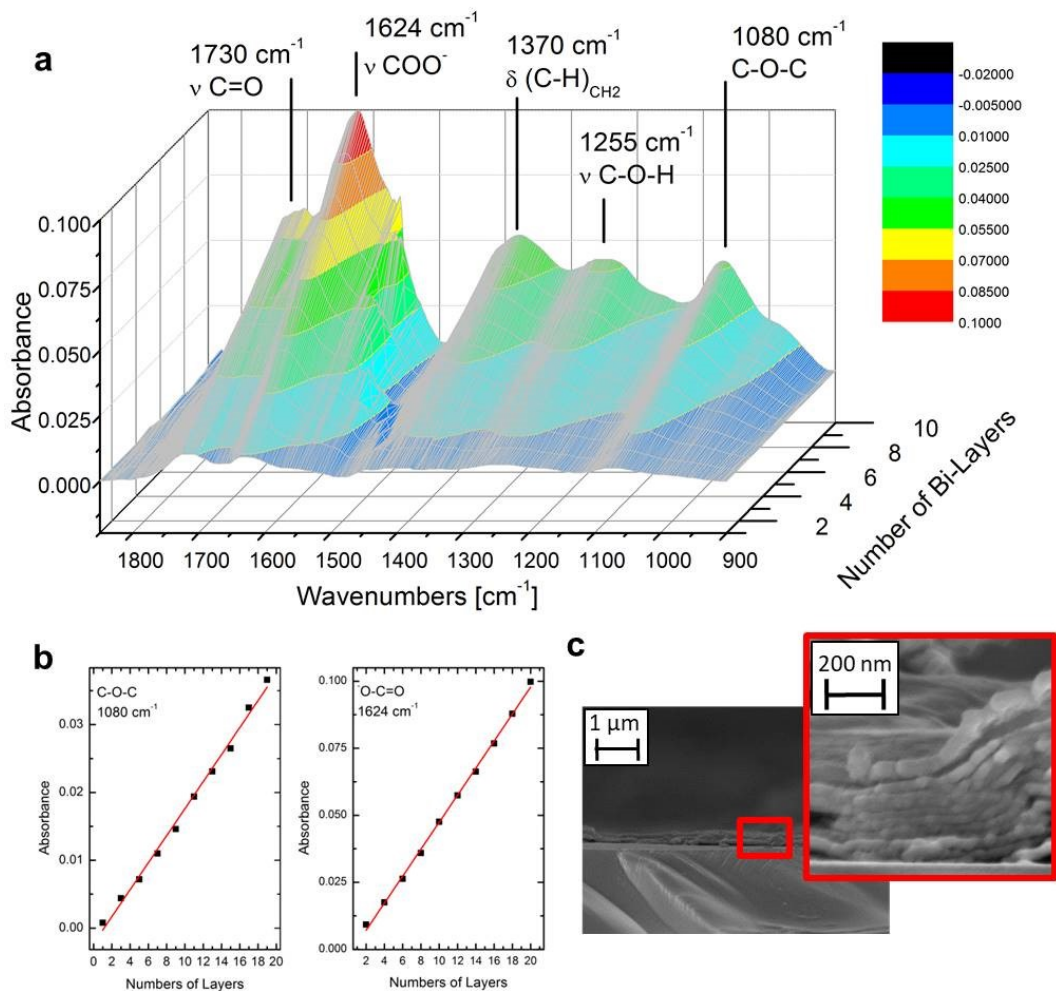


Figure 36 Chitosan and GO FT-IR spectra.

**Table 11** Attribution of CHIT and GO FT-IR signals.

	<b>Signal</b>	<b>Wavenumbers (cm<sup>-1</sup>)</b>	<b>Attribution</b>
<b>Chitosan</b>	A	3800 - 3000	v (O-H) and v (N-H)
	B	2900	v (C-H) of CH <sub>2</sub>
	C	2880	v (C-H) of CH <sub>3</sub>
	D	1640	v <sub>as</sub> (NH <sub>3</sub> <sup>+</sup> ), v (O-H)H <sub>2</sub> O
	E	1556	v <sub>s</sub> (NH <sub>3</sub> <sup>+</sup> )
	F	1156	NH <sub>3</sub> <sup>+</sup> rocking
	G	1411	δ(C-H) of CH <sub>2</sub>
	H	1070	v(C-O-C) of glycosidic units
<b>Graphene Oxide</b>	I	3800 - 3000	v (O-H)
	L	1725	v (C=O)
	M	1627	v (O-C=O)
	N	1054	v (C-O)

Figure 37 reports 3D projection of restricted IR region, the intensity of the peaks at 1080 and 1624 cm<sup>-1</sup> plotted as a function of BL number and the FESEM cross section images of the 10BL coating on Si wafer. In the assembled coating, the characteristic peaks of both CHIT and GO can be easily distinguished, the signals grow proportionally to the deposited BL number thus indicating the occurrence of a LbL assembly (Figure 37 a). The strongest peak at 1624 cm<sup>-1</sup> is ascribed to the stretching vibration mode of COO<sup>-</sup> in GO and it overlaps with the two CHIT NH<sub>3</sub><sup>+</sup> stretching vibrations in the same region (compare Figure 36). Of these two latter, only the symmetric stretching is observable as a shoulder at 1580 cm<sup>-1</sup>. Additional signals, characteristic of both GO and CHIT, can be found at 1730 and 1080 cm<sup>-1</sup> ascribed to C=O in GO and glycosidic C-O-C in CHIT, respectively. By plotting the absorbance of the signals at 1624 cm<sup>-1</sup> and at 1080 cm<sup>-1</sup> as a function of layer number it is apparent that this CHIT/GO system follows a linear growth regime (Figure 37 b). This is in accordance with previously reported literature studies dealing with LbL coatings containing CHIT and lamellar shape nanoparticles (i.e. sodium montmorillonite) [216]. The 10 BL cross section on Si wafer was imaged by FESEM (Figure 37 c). The coating appears continuous with some irregularities in thickness due to the wrinkled nature and high aspect ratio of the GO. High magnification micrographs reveal a layered structure where GO sheets are embedded within a CHIT continuous matrix thus confirming the assembly of a brick and mortar-like structure.



**Figure 37** a) FT-IR spectra during LbL growth, b) evolution of the signals at  $1624$  and  $1080 \text{ cm}^{-1}$  as function of layer number and c) FE-SEM micrographs of  $10$  BL assembly on Si wafer.

#### 4.1.2 Morphology of the coating on PU foams

Scanning Electron microscopy was employed in order to characterize the surface of PU foams after the LbL deposition. Low magnification micrographs are reported in Figure 38 while zoomed in details of the coatings are collected in Figure 39. Untreated PU foams shows a typical structure made of open cells connected to each other (Figure 38); when imaged at high magnifications, the cell surface appears smooth and homogeneous (Figure 39 a and d). From low magnification micrographs it is apparent that the LbL deposition completely changes this surface morphology without altering the macroscopic structure of the PU foam that maintains its open cell nature (compare Figure 38 a, b and c).

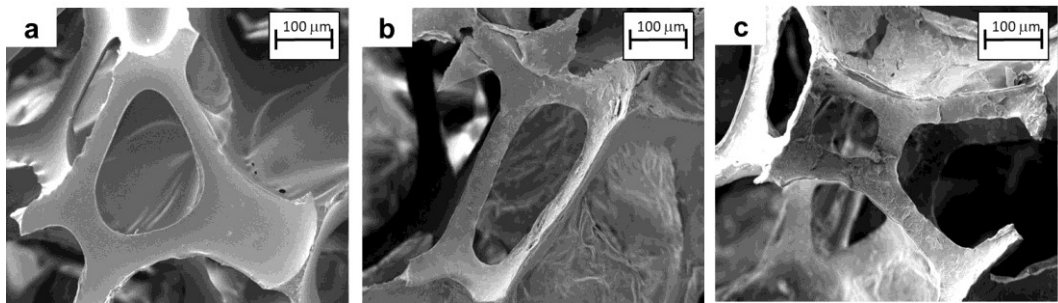


**Figure 38** SEM micrograph of a) untreated PU foam, b) 3 BL and c) 6 BL foams.

After the deposition of 3 BL every surface is covered with a continuous nanostructured coating that imparts apparent changes in roughness (Figure 39b and e). This is similar to what already observed on model Si wafer as reported in Figure 37c. By increasing the number of deposited layers the coating increases in thickness and tends to be more rigid leading to the formation of small cracks upon sample cutting prior to SEM imaging (Figure 39c and f).

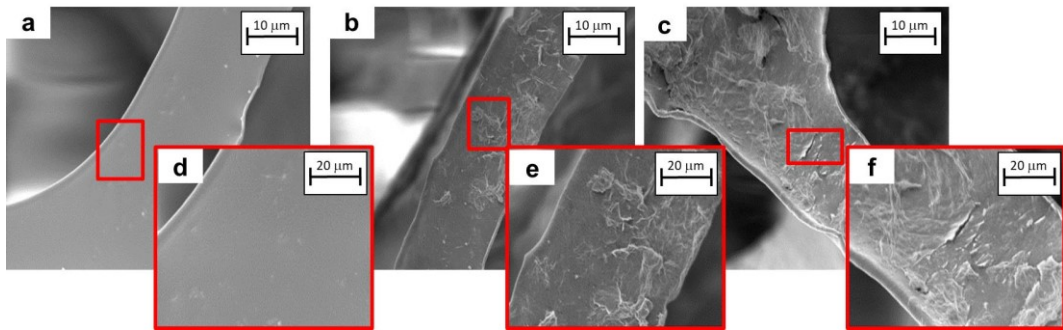


**Figure 39** SEM micrograph of untreated PU foam (a, d), 3BL PU foam (b, e), and 6 BL PU foam (c, f).

#### 4.1.3 Flammability tests

Because of the large exposed surface and high oxygen permeability, open cell PU are highly flammable. Thus, in order to evaluate the foam propensity to start a fire, it is important to test the reaction of untreated and LbL-treated foams to a small flame exposure. For this purpose, flammability tests in horizontal configuration were performed; the collected results are summarized in Table 12 while Figure 40 reports digital pictures of the foam during the test. Upon application of the methane flame the untreated PU ignites instantaneously and completely burns in averagely 63 seconds (see Figure 40 a-c) leaving no residue at the end of the test. During combustion, the melt dripping phenomenon occurs and flaming droplets of molten PU fall from the sample and ignite the dry cotton placed underneath. This behaviour is well known for PU foams and represents an extremely dangerous fire threat as it can easily spread the fire to other ignitable materials.

The deposition of 3 BL of CHIT/GO assembly significantly changes the burning behaviour of PU foams. Indeed, no melt dripping phenomena occur and, even if the flame still entirely propagates along the sample by mainly moving on the edges as reported in Figure 40, at the end on the test is possible to collect a

self-standing residue that averages 61% of the initial weight (Figure 40 f). The deposition of 6BL yields similar results with an increase in after flame time. By evaluating the calculated parameters in Table 12 it is worth pointing out that LbL treated PU foams show an increased flame spread rate. This is due to the flame preferentially moving on the edges of the foam and eventually converging towards the centre of the specimen. In addition, the flames are apparently less intense with respect to the untreated PU foam (Figure 40 e). Moreover, the 6BL after flame time is much higher than the 3BL sample probably due to the presence of the cracks within the coating (compare Figure 39 f) that allows more degradation products from the PU foam to escape and feed the flame. For this reason, the final residue of the 6BL is lower than the 3BL. Notwithstanding this, the high residues obtained by both samples point out that the flame self-extinguishes before being able to completely consume the PU. From an overall point of view, LbL treated PU foams show an improved behaviour due to the formation of a protective coating that prevents foam collapsing and limits the release of combustible volatiles. This completely suppresses melt dripping but does not allow for the self-extinguishing of the flame before it spreads to the whole specimen.

**Table 12** Horizontal flammability test data of untreated and LbL treated foams.

Sample	Dripping and cotton ignition	Burning rate $\pm \sigma$ [mm/s]	After flame time $\pm \sigma$ [s]	Residue $\pm \sigma$ [%]
PU	Yes	$2.8 \pm 0.6$	$63 \pm 1$	$\approx 0$
3 BL	No	$6.9 \pm 0.5$	$66 \pm 1$	$61 \pm 4$
6 BL	No	$6.1 \pm 0.9$	$104 \pm 2$	$46 \pm 3$

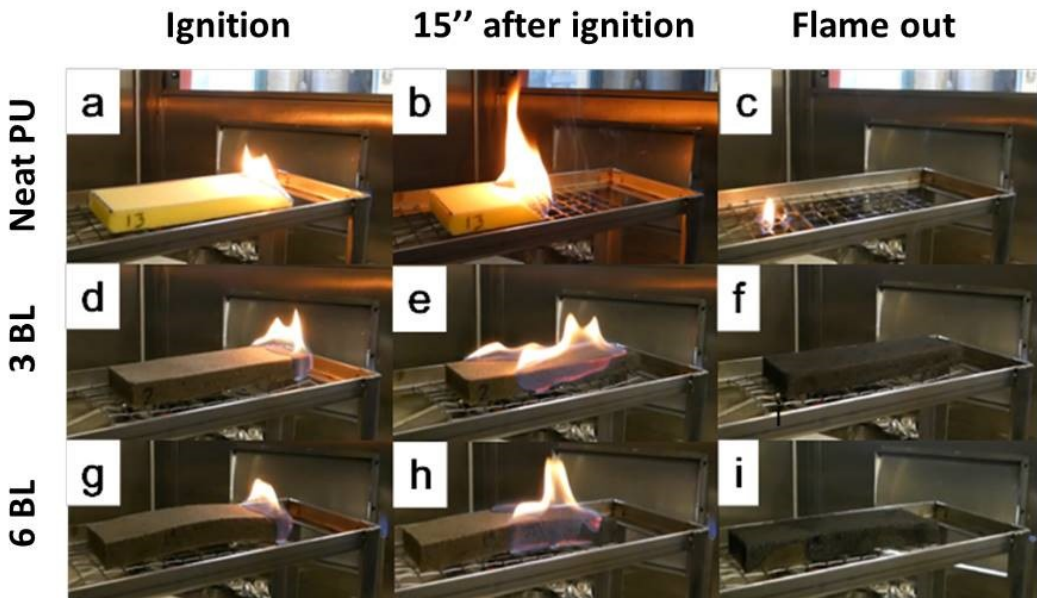


**Figure 40** Pictures of flammability test in horizontal configuration of untreated PU foam (a-c), 3 BL PU foam (d-f) and 6 BL PU foam (g-i). First column: right after ignition, second column: 15 seconds after ignition and third column: during flame out.

#### 4.1.4 Forced combustion tests

To better understand combustion behaviour of treated and untreated PU foams, the prepared samples have been subjected to forced combustion tests performed by cone calorimetry at  $35\text{ kW/m}^2$  that correspond to the early stages of a developing fire [287]. This test can be considered as complementary to flammability and provides a general overview of the burning behaviour of a material for most applications. Table 13 reports cone calorimetry data of untreated and LbL-treated PU foams, Figure 41 reports HRR and TSR plots as function of time and Figure 42 collects snapshots of the residues at the end of the test. As a consequence of the exposure to the cone heat flux, unmodified PU foams quickly melt and partially collapse while releasing volatiles gases that lead to the ignition of the sample. After ignition the foam completely collapses forming a vigorously burning pool of a low viscosity liquid and reaching the maximum in heat release rate ( $312\text{ kW/m}^2$ ) [288]. 3BL samples show an anticipation in TTI and a strong reduction in the pkHRR and average HRR (namely 54 and 15%, respectively). As observed during flammability test the presence of the LbL coating can prevent the structural collapse of the foam and the high aspect ratio of the employed GO can produce a barrier that slows down volatile release (see digital pictures of the residues in Figure 42). This results in hindered combustion kinetics as demonstrated by the reduction in HRR values. As far as 6BL samples are concerned, two different behaviours have been observed. Indeed, 50% of the tested samples showed no ignition during test; for this reason, the data and plots of igniting and non-igniting samples have been reported in Table 13 and Figure 41. This behaviour can be ascribed to the barrier effect of the coating that reduces volatile release to the limits of non-ignitability concentration [289]. When ignition occurs the performances of 6BL foams are similar to the 3BL ones. On the other hand, for non-igniting samples extremely low heat related parameters have been registered and a broad band with values below  $40\text{ kW/m}^2$  can still be observed. This is explained considering that, although there is no flame, the sample is subjected to high temperatures and, while the majority of the PU foam undergoes pyrolysis a small portion of volatiles released undergoes thermal-oxidation. This process consumes oxygen and is registered by the cone as very low HRR. As far as smoke parameters are concerned, the presence of the CHIT/GO coating can substantially reduce the TSR value as reported in Table 13 and Figure 41 b. The highest reduction is achieved for 3BL samples (-59%). On the other hand, due to the substantial release of degradation products from non-igniting 6BL samples, TSR values are considerably higher than untreated foams [290]. The final residues are not affected by the presence of the coating as they remain within the 6% of the original mass similarly to unmodified PU. This suggests that all the PU, is consumed during the test as also confirmed by the increase of THR values reported in Table 13. The coating evolution during forced combustion tests was studied and is reported in the next section. From cone calorimetry analysis it is apparent that the deposited CHIT/GO multilayers can strongly affect the performance of PU foams in forced combustion tests. Since this test has been

widely employed in order to assess the FR properties of LbL coated PU foams it would be of interest to make a comparison with previously published papers.

**Table 13** Cone calorimetry data of untreated and LbL-treated PU foams.

Sample	TTI $\pm \sigma$ [kW/m <sup>2</sup> ]	Av.HRR $\pm \sigma$ [kW/m <sup>2</sup> ]	pkHRR $\pm \sigma$ [kW/m <sup>2</sup> ]	THR $\pm \sigma$ [MJ/m <sup>2</sup> ]	EHC $\pm \sigma$ [MJ/kg]	TSR $\pm \sigma$ [m <sup>2</sup> /m <sup>2</sup> ]	Residue $\pm \sigma$ [%]
PU	12 $\pm$ 4	60 $\pm$ 3	312 $\pm$ 24	7.9 $\pm$ 0.1	24.3 $\pm$ 3.5	78 $\pm$ 8	6 $\pm$ 1
3 BL	4 $\pm$ 1	51 $\pm$ 1	145 $\pm$ 8	8.8 $\pm$ 0.4	19.3 $\pm$ 3.5	32 $\pm$ 6	7 $\pm$ 2
6 BL	7 $\pm$ 1	55 $\pm$ 5	170 $\pm$ 19	8.7 $\pm$ 0.1	20.5 $\pm$ 2.5	58 $\pm$ 8	6 $\pm$ 1
6 BL*	—	20 $\pm$ 2	42 $\pm$ 2	3.1 $\pm$ 0.5	6.5 $\pm$ 1.5	300 $\pm$ 14	10 $\pm$ 1

\* Denotes non-igniting samples. During the test only 50% of the samples showed ignition.

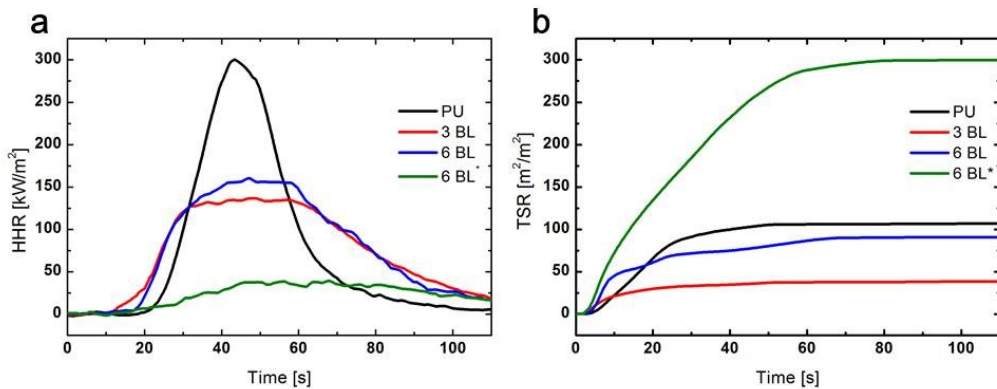


**Figure 41** a) HRR and b) TSR curves of untreated and PU foams coated with 3 BL and 6BL. 6BL\* indicates non-igniting samples.



**Figure 42** Images of a) untreated PU foam, b) 3 BL and c) 6 BL foams cone calorimeter residue.

Table 14 summarizes the results in terms of number of layers, mass gain and pkHRR reduction for some most efficient and innovative LbL coatings on PU foams. All of the reported coatings were prepared using LbL techniques comprising chitosan and 2D nanoparticles. The LbL coatings range from 8 to 48 deposited monolayers, mass add-ons from 1 to 48% and pkHRR reductions in between 37-70%. From results in Table 14 it is quite apparent that the CHIT/GO coatings developed within this section are capable to deliver comparable FR performance in terms of pkHRR reduction. Indeed, as demonstrated earlier, 6 BL can result in non-igniting behaviour with a theoretical 100% reduction in pkHRR. Furthermore, this result is achieved with only 13.4% of added weight. Similarly to what reported in literature, for inorganic clay containing LbL coatings, these impressive results can be ascribed to the high aspect ratio of the employed GO

that allow for improve surface coverage with few deposited BL and provide better protection [291].

**Table 14** Comparison of pkHRR reduction between the CHIT/GO coatings reported in this paper and previously published Chitosan based LbL coatings on PU foams.

Composition	N. of monolayers	Coating mass [%]	pkHRR reduction [%]	Ref.
<b>3 BL CHIT-GO</b>	<b>6</b>	<b>10</b>	<b>54</b>	This work
<b>6 BL CHIT-GO</b>	<b>12</b>	<b>13</b>	<b>46</b>	
<b>6 BL CHIT-GO non igniting</b>			<b>100</b>	
CHIT-GO-Alginate	30	8	60	[277]
CHIT-MMT pH 3	20	1	37	[216]
CHIT-MMT pH 6	20	4	52	[216]
PAA-CHIT-PPA-CHIT	20	48	55	[221]
CHIT-VMT	8	3	55	[246]
(CHIT-PPA) <sub>20BL</sub> -(CHIT-VMT) <sub>8BL</sub>	48	20	66	[246]
CHIT-MoS	16	8.5	70	[292]
CHIT/CNT-MMT-Alginate	24	4	70	[245]

In the table, PPA: polyphosphoric acid and MoS: molybdenum sulfide.

#### 4.1.5 Coating evolution during combustion and residue analysis

In order to better understand the evolution of the deposited LbL-coating during combustion, Si wafers treated with 10 BL of the CHIT/GO assembly have been exposed to the cone heat flux ( $35 \text{ kW/m}^2$ , 30 sec) and the changes in coating morphology and chemical composition have been investigated by means of FESEM, IR and Raman spectroscopy. Figure 43 reports collected data and SEM micrographs of the 3 and 6 BL PU foam residues collected at the end of the cone test. The cross-section morphology of the coating after exposure to the cone heat flux (Figure 43 a) reveals a compaction of the structure that becomes more irregular with aggregate of GO platelets more clearly visible with respect to the original assembly (compare Figure 43 a with Figure 37 c). This behaviour can be ascribed to the thermal degradation of CHIT that, as a consequence of the temperature increase, evolves towards the formation of a carbonaceous char that joins together the GO. On the contrary from how it is expected for brick and mortar assembly which tends to expand during combustion, the evolution of the CHIT-GO assembly provokes a contraction of the coating itself. This counterintuitive contraction is peculiar of CHIT as it was already observed in CHIT/phosphorylated cellulose LbL assembly [293].

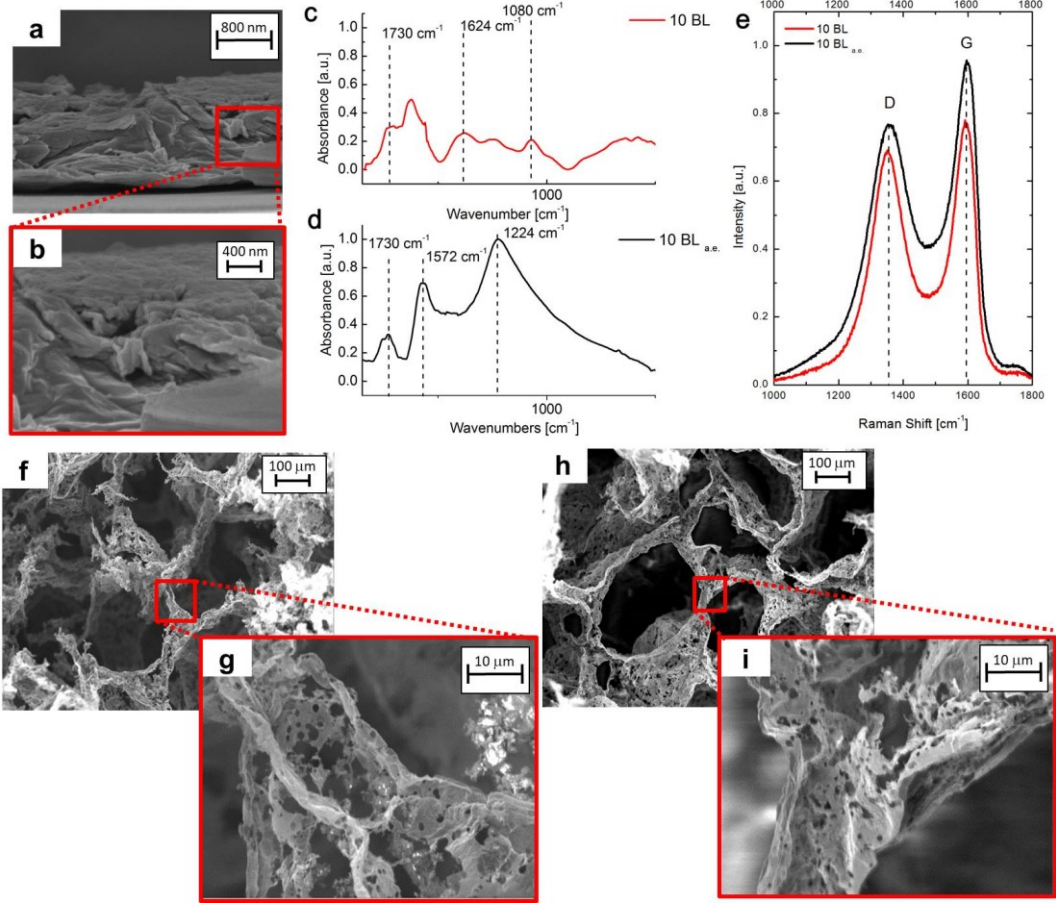


**Figure 43** FESEM micrograph of 10BL deposited on Si wafer after heat flux exposure (a,b ), FT-IR spectra of 10BL deposited on Si wafer before (c) and after (d) heat flux exposure, Raman spectra of 10BL deposited on Si wafer before (red curve) and after (black curve ) heat flux exposure and SEM micrographs of 3 BL (f, g) and 6 BL (h, i) coated foams residues after forced combustion tests.

The char formation from chitosan was also confirmed by IR and Raman spectroscopy. Indeed, by IR it is possible to observe a strong change in the signal associated to the LbL coating with the formation of a band at  $1572\text{ cm}^{-1}$  characteristic of aromatic carbonaceous structures [285]. This is corroborated by Raman spectroscopy performed on neat CHIT powder before and after cone exposure (Figure 44 a) that reveals the formation of two characteristic signals, known as G and D bands, associated to aromatic carbons clearly visible at  $1590$  and  $1350\text{ cm}^{-1}$ . Similar bands are present for GO (Figure 44 b), in this case the bands are already visible before cone exposure due to the graphitic-like structure of GO. Moreover, by a simple evaluation of the ratio between the area underneath the G and D bands it is possible to obtain information about the quality of the aromatic carbon structure. Indeed, as reported in the literature [12], the D band is usually associated to defects and is employed to evaluate the quality of graphene-based material; as an example, a perfect graphene structure would result in a strong and sharp G peak. Neat GO shows a D/G ratio of 1.35 due to the presence of defects; this ratio further increases after the exposure to the cone heat flux indicating an increased number of defects( D/G of 1.66). When the two components are LbL assembled the evolution of the Raman spectra show an increase of the D/G ratio (from 1.57 to 1.99, Figure 43e) ratio that can be mainly

ascribed to the CHIT contribution. From the collected characterization, it seems that upon heat flux exposure the coating undergoes structural rearrangements, due to the thermal degradation of CHIT that produces an aromatic char that glue together the GO in a compacted and thermally stable structure. Being deposited on all available surfaces of the PU foam, this structure can mechanically sustain the foam and prevent its collapse while acting as barrier to volatiles. SEM observations performed on the 3 and 6BL residues collected after cone tests confirm this hypothesis (Figure 43 f, g, h, i). For both samples, the original 3D structure is still visible and high magnification micrographs reveal the presence of a hollow structure mainly made by the charred coating which structure is not continuous and characterized by defects. This confirms the results obtained by flammability and cone calorimetry where it was apparent that although the coating controlled and slowed down volatile release this effect was not enough to allow for early self-extinguishing behavior during flammability or prevent the complete combustion/pyrolysis of the PU during cone calorimetry.

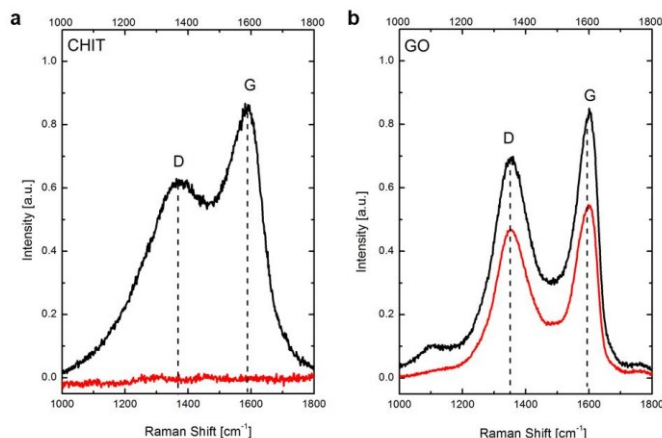


**Figure 44** Raman spectra of a) neat GO and b) after exposure to heat flux. Raman spectra of CHIT before (red curve) and after (black curve) exposure to heat flux.

## 4.2 Effect of nanoparticles aspect ratio on flame retardant properties of GO-CHIT layer by layer treated PU foams

As it was reported in the state of the art, the employment of nanoplatelets in LbL assembly can significantly increase the flame retardancy of PU foams due to the brick and mortar structure, which improve considerably the tortuosity path of volatiles produced by the thermal decomposition of the substrate. With this aim, the flame retardant properties of GO nanoparticles with different aspect ratio were evaluated focusing the attention on the effects of the coatings in flame retardancy. In this sub-chapter, three GO suspensions with different aspect ratio were coupled with CHIT. In a first attempt, the GO nanoparticles dimensions were determined combining advanced microscopies (AFM and FE-SEM) with viscosity measurements and dynamic light scattering, meanwhile LbL growth was monitored by FT-IR spectroscopy. As for the previous sub-chapter, flame retardancy was evaluated by flammability test and cone calorimetry measurements.

#### 4.2.1 Nanoparticles characterization

Three suspensions of GO named GOA, GOB and GOC, were characterized combining AFM and FE-SEM microscopies in order to determine the aspect ratio of nanoplatelets. Figure 45 and Figure 46 report the tapping mode-AFM characterization and the FE-SEM imaging of GOA, GOB and GOC suspensions respectively. The comparison of tapping mode-AFM images collected for all the suspensions shows that the three type of nanoparticles have the same thickness in the range of 2-4 nm. However, this result is not representative for all of the dispersed nanoparticles, because the dilution of the sample was responsible for the precipitation of bigger nanoparticles. In addition, when particles with a high thickness values are in a mixture with thin nanoparticles, the AFM shows big loss in sensitivity because of the lateral sharpness of the tip. In order to bypass this problem, the GO suspensions were characterized combining SEM microscopy, dynamic light scattering and viscosity measurements.

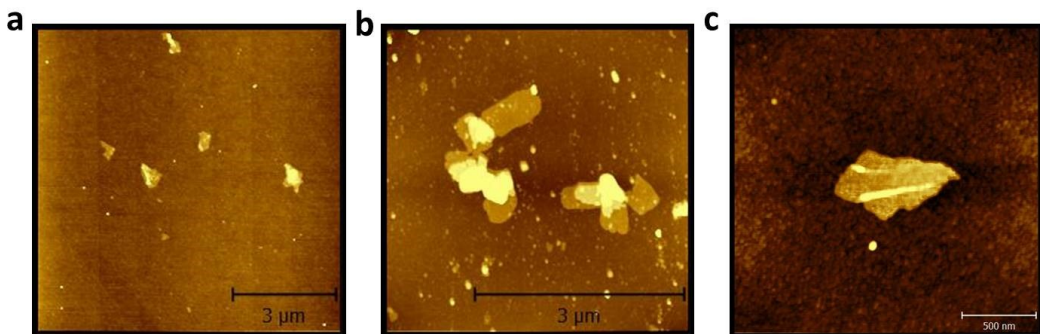


**Figure 45** Tapping mode-AFM characterization of a) GOA, b) GOB and c) GOC.

FE-SEM micrographs were collected on samples prepared by dipping the silicon wafer in the native GO suspensions after an activation step in BPEI. As it is possible to see in Figure 46 the number of nanoparticles included in all of the micrographs is higher than in AFM and the dispersity of the later size is very large. However, the thinnest nanoparticles cannot be detected because of the low contrast between the GO nanoplatelets and the substrate. In contrast with what observed in AFM experiment, only bigger nanoparticles have been detected in SEM imaging so the lateral size measured with this technique is representative of the bigger nanoparticles suspended in water. Notwithstanding this, comparing images, is possible to state that GOA nanoparticles are on coverage larger than GOB which have bigger lateral size than GOC.

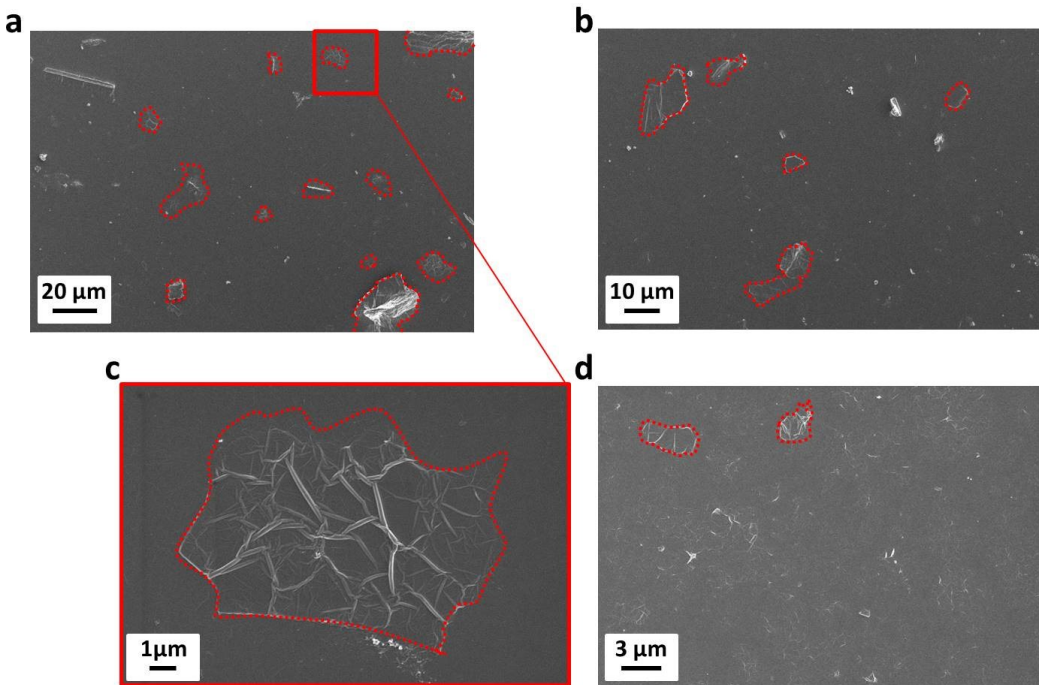


**Figure 46** FE-SEM of 1L of a) GOA, b) GOB d) GOC deposited on Si wafer; c) high magnification FE-SEM micrograph of one GOA nanoplatelets.

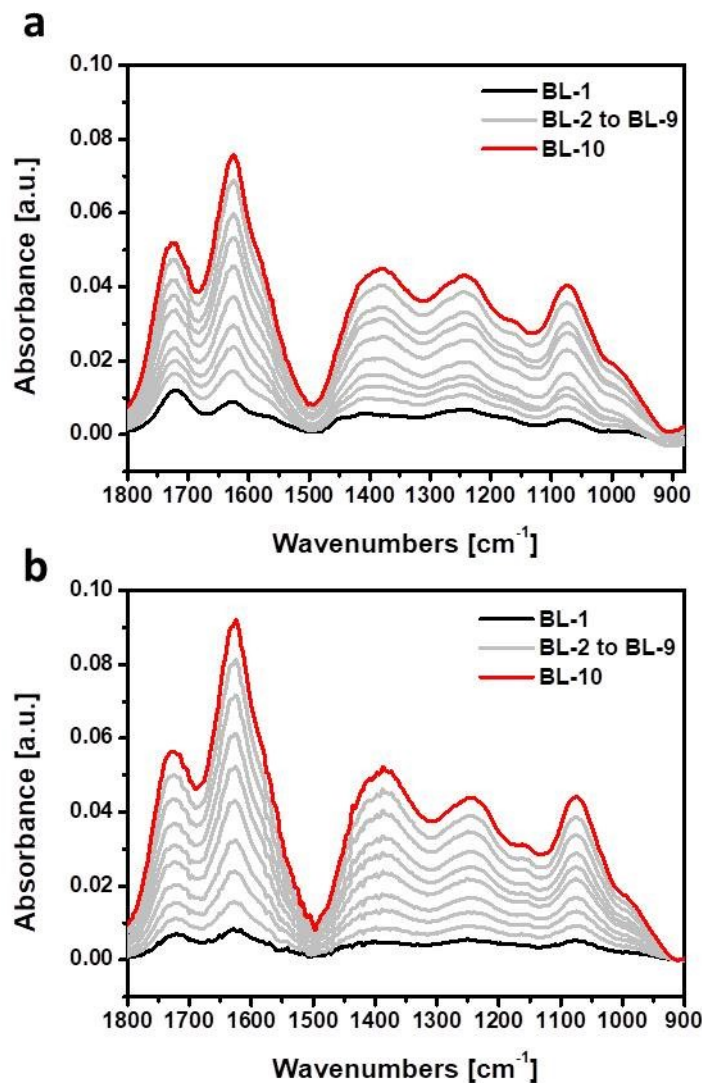
These results are in agreement with the data supplied by the producer (see in Table 4, Chapter 2). It is well known that the viscosity of a suspension is dependent from the nanoparticle dimensions when the considered concentration is the same. In this work GOA, GOB and GOC have the same concentration. From a general point of view, the smallest are the nanoparticles higher is the viscosity because the net of Van der Waals and adhesion forces stored between nanoparticles [294]. The GOA suspension viscosity is 10.8 cP, the GOB suspension viscosity is 30.5 cP and the GOC suspensions viscosity 77.5 cP. This result is in accord with the dimension ranking GOA > GOB > GOC.

DLS measurements are widely used for the characterization of spherical nanoparticles, however this technique has been adopted for the characterization of 2D nanoplatelets suspensions in order to determine the average lateral dimensions of suspended nanoparticles in liquids because it is easy to perform and time saving, if compared to AFM [295]. DLS measurements confirm the trend GOA > GOB > GOC and assess 61 μm, 39 μm and 34 μm respectively (refer to Table 4 in chapter 2). However, as mentioned above, DLS is generally applied to the characterization of spherical nanoparticles, so the measurements conducted on platelets can be considered over-estimated because the provided data are related to the medium lateral size and not to the lateral size distribution.

#### 4.2.2 Layer by layer growth and characterization

The LbL growth of the three systems under study was investigated by FT-IR spectroscopy using a silicon wafer as model substrate. The spectra of neat CHIT and GO are reported in Figure 36 and signal attributions are summarized in Table 11. Figure 47 reports LbL assembly growth of GOA-CHIT, GOB-CHIT, GOC-

CHIT 10 BL assembly followed by FT-IR spectroscopy. As it was reported in 4.1.1 Layer by layer growth and characterization, the assembly grows up and, increasing the number of deposited layers, the absorbance related to the signals associated to both CHIT and GO increase in intensity (Figure 47). The signals intensities of the assemblies under study are comparable, even if the dimensions of nanoparticles are different. This behaviour can be ascribed to the fact that the density of functional groups (that are detected by FT-IR spectroscopy) depends mainly on the oxidation process which is carried out in the same way for all suspensions and before the sonication step.



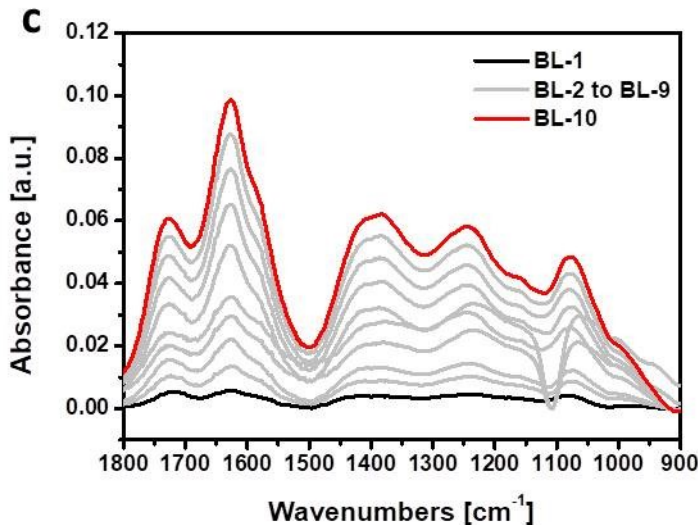


**Figure 47** LbL growth of a) GOA-CHIT, b) GOB-CHIT, c) GOC-CHIT assembly followed by FT-IR spectroscopy and conducted on a silicon wafer as substrate.

The cross-section of silicon wafer coated with 10 BL was imaged by FE-SEM, collected micrographs are reported in Figure 48 and measured thicknesses are reported in Table 15. The deposited assemblies consist in a dense, continuous and layered structure where the GO nanoplatelets are embedded within a CHIT matrix. Wrinkles can be attributed to the presence of high aspect ratio GO nanoparticles. The three coatings were assembled in the same conditions and it seems that their thicknesses are dependent from nanoparticle dimensions. In fact, 10 BL GOA-CHIT assembly is thicker than 10 BL GOB-CHIT, that is thicker than 10 BL GOC-CHIT. The detection of a dense structured coatings for all the under study assemblies confirm that the LbL growth based on the electrostatic interaction established between two polyelectrolytes depends strongly on the number of interacting functional groups.

Depending on the synthetic procedure, the density of functional groups per unit of nanoparticle is similar in the three analysed assemblies. Thus, the same number of deposited layers correspond to a similar number of interacting functional groups and the IR signals intensity is similar in the GOA-, GOB- and GOC-CHIT coatings. However, GOC nanoparticles are thinner than GOB, that are thinner than GOA thus the GOC-CHIT coating is thinner than GOB-CHIT, which is thinner than GOA-CHIT, as it was confirmed by high magnification micrographs.

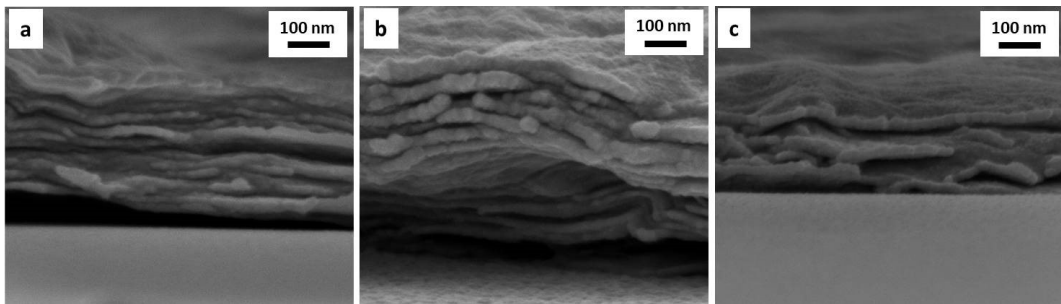


**Figure 48** FE-SEM micrograph of a) 10 BL GOA/CHIT, b) 10 BL GOB/CHIT, c) 10 BL GOC/CHIT assembly.

**Table 15** Thickness of 10 BL GOx/CHIT assemblies.

Assembly	GOA/CHIT	GOB/CHIT	GOC/CHIT
Thickness $\pm \sigma$ [nm]	286 $\pm$ 35	224 $\pm$ 13	185 $\pm$ 10

#### 4.2.3 Morphology on PU foams

Subsequently the LbL deposition, the weight gain after 3 and 6 BL was evaluated (Table 5 in chapter 2). Interestingly, the weight gain follows the same trends of GO nanoparticles dimensions. Indeed, when 3BL are deposited the weight gain ranges from 6% to 11% for the 3 BL assembly increasing the dimensions of GO nanoparticles following the trend GOA>GOB>GOC. The same tendency is also present for the 6 BL treated samples. For all the assemblies, 6 BL coating is responsible for a weight-gain roughly two times higher than 3BL (see Table 5 in chapter 2). This trend is in agreement with the linear growth regime explained in the previous section for GO-CHIT assembly.

Figure 49 collects micrographs of PU foam coated by 3 and 6 BL of each GO/CHIT assembly. As observed before, the LbL deposition can alter the cell wall morphology of the PU foams, while retaining its open cell structure. By increasing the number of deposited layers, the coating generally became more wrinkled and irregular while still showing GO nanoparticles well embedded in the assembly (see Figure 49 g-i).

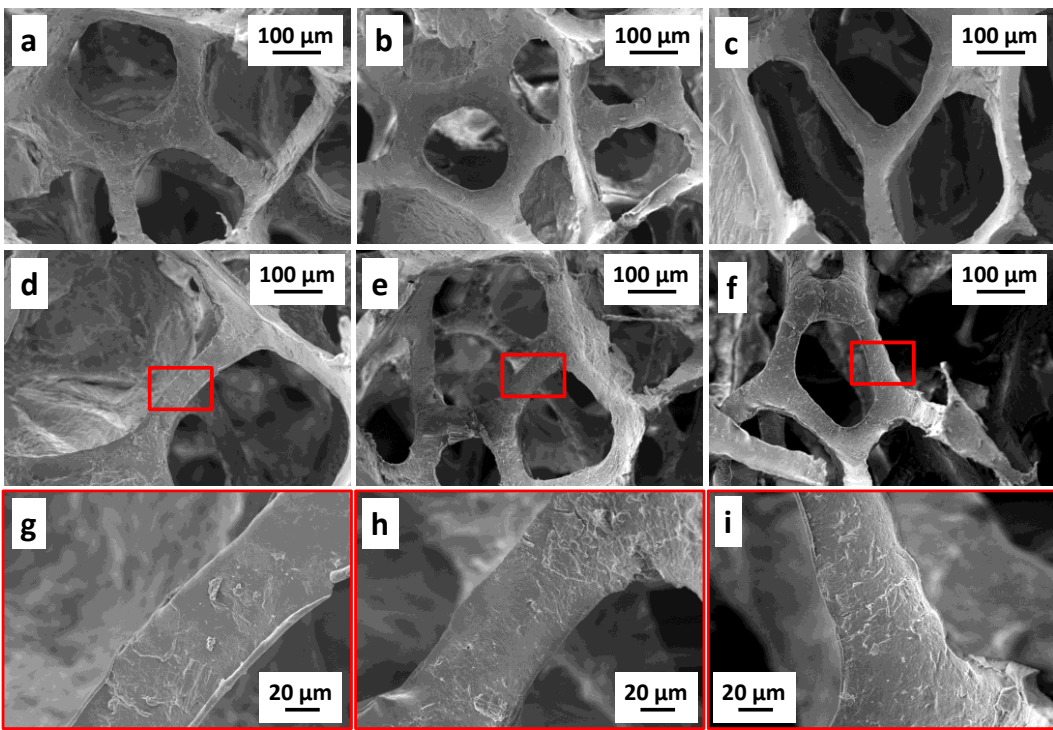


**Figure 49** SEM micrograph of 3BL CHIT a) GOA, b) GBOB, c)GOC. SEM micrograph of 6 BL CHIT d) GOA, e) GOB, f) GOC; high magnification micrograph of 6 BL CHIT g) GOA, h) GOB, i) GOC.

#### 4.2.4 Flammability tests

The reaction to flame of coated foams was evaluated by flammability tests. The aim is to establish whether the GO nanoparticles dimensions can affect the performance of the treated foam. Figure 50 and Figure 51 report snapshots of the foams during the test while calculated parameters such as burning rate and residues are collected in Table 16. As shown before, all GO-CHIT based assembly are able to suppress the melt-dripping phenomenon occurred when a direct flame is applied on PU foam. In Figure 50, the flammability test of 3BL treated foams are summarized for all of the GO samples. As it is possible to see by comparing the figures, the 3BL treated foams display similar performances: when the flame is applied the sample ignite immediately and the flame is propagated along the edges and the upper surface of the LbL treated foams. The flame is then extinguished, leaving a coherent residue that maintains the original shape of the starting foam. Moreover, the final residues and the flame spreading rates are quite similar for all of the examined samples (see Table 16). When 6BL are deposited on PU foams the flame is propagated similarly to the 3BL treated foams (Figure 51). The flame propagation has similar rates for all of the 6 BL analysed assembly and the self-standing residue collected at the end of the test have similar weight for GOA-CHIT and GOB-CHIT deposition, meanwhile GOC-CHIT residue is lighter than the other two (Table 16). At the end of these tests, the 6BL GOC-CHIT residue is 12% lighter than the other 6 BL foams. Interestingly, the 6BL residues are nearly double mass compared to 6BL examined in the previous section (4.1.3 Flammability tests) probably due to the fact that the latter samples presented cracks in the coatings which favour thermal decomposition of PU foam

(compare Figure 39 f with Figure 49 g, h, i) while the examined specimens showed no cracks during morphology evaluation.

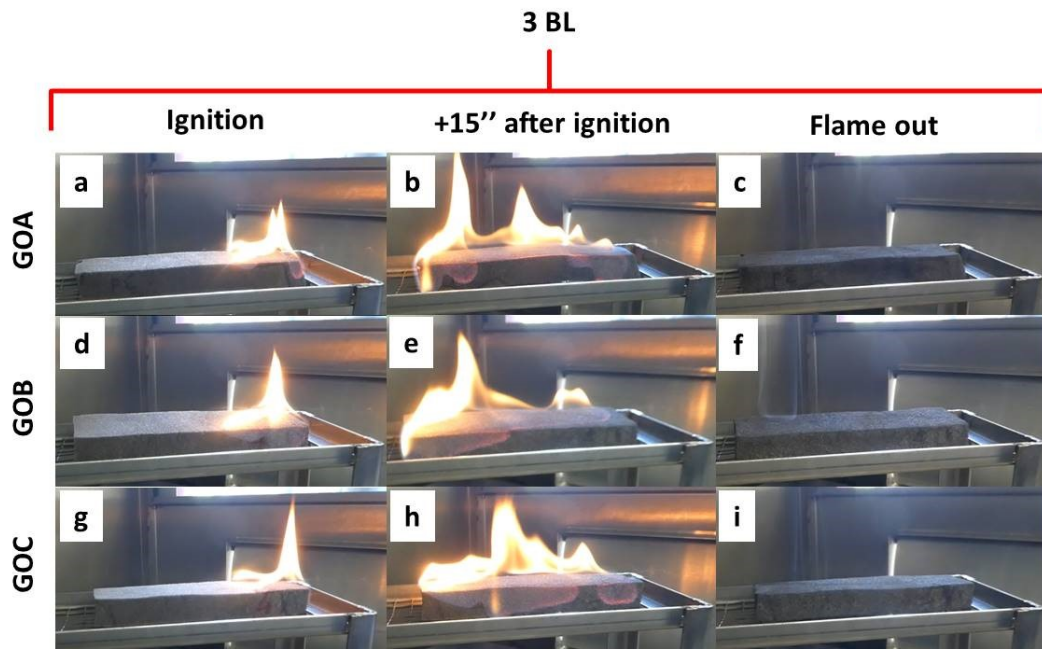


**Figure 50** Pictures of flammability test in horizontal configuration of untreated 3 BL GOA-CHIT treat PU foam (a-c), 3 BL GOB-CHIT PU foam (d-f) and 3 BL GOC-CHIT PU foam (g-i). First column: right after ignition, second column: 15 seconds after ignition and third column: during flame out.

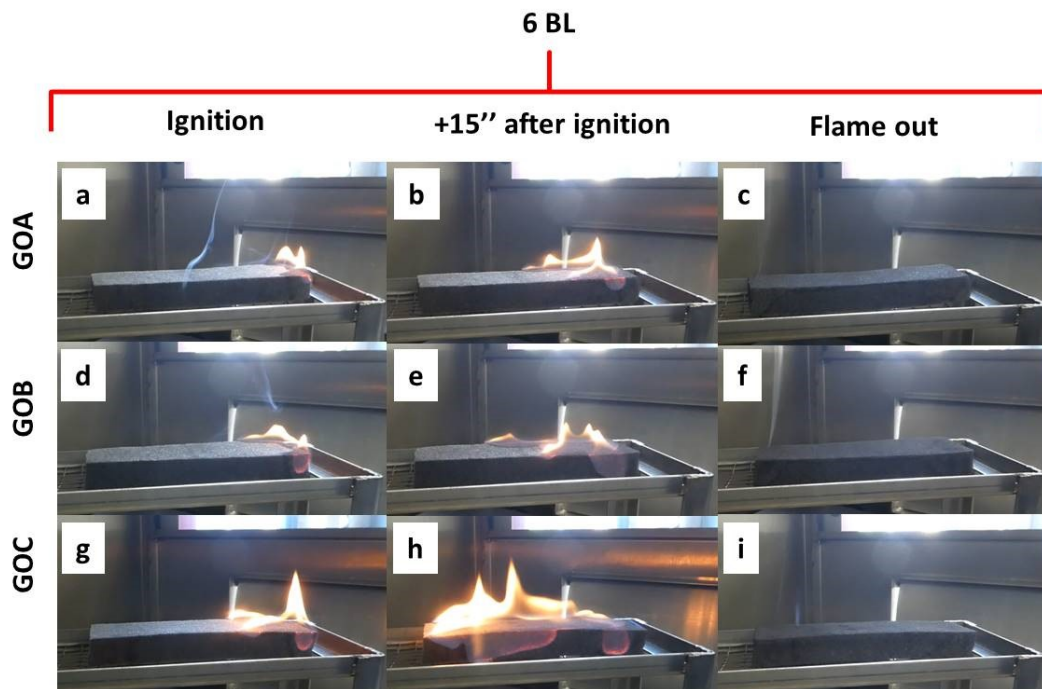


**Figure 51** Pictures of flammability test in horizontal configuration of untreated 6 BL GOA-CHIT treat PU foam (a-c), 6 BL GOB-CHIT PU foam (d-f) and 6 BL GOC-CHIT PU foam (g-i). First column: right after ignition, second column: 15 seconds after ignition and third column: during flame out.

**Table 16** Horizontal flammability test data of untreated and LbL treated foams.

Sample	Melt dripping	Burning rate $\pm \sigma$ [mm/s]	Residue $\pm \sigma$ [%]
PUF	Yes	4.9 $\pm$ 0.4	-
3 BL GOA-CHIT	No	6.4 $\pm$ 1.6	67 $\pm$ 1
3 BL GOB-CHIT	No	6.5 $\pm$ 0.4	67 $\pm$ 1
3 BL GOC-CHIT	No	5.9 $\pm$ 0.7	63 $\pm$ 1
6 BL GOA-CHIT	No	4.9 $\pm$ 1.2	79 $\pm$ 1
6 BL GOB-CHIT	No	4.3 $\pm$ 0.1	80 $\pm$ 1
6 BL GOC-CHIT	No	5.5 $\pm$ 0.6	70 $\pm$ 1

#### 4.2.5 Forced combustion test

Forced combustion tests were conducted in order to study the performance of treated PU foams in early stages of developing fires situation. Figure 52 and Table 17 report HRR curves and cone calorimetry parameters collected for untreated and LbL treated foams. After ignition the pristine PU foam collapse and is degraded in a low viscous liquid, burn vigorously and is quickly consumed. During combustion a  $308 \pm 25$  kW/m<sup>2</sup> HRR peak value is reached.

When 3 BL are deposited, the burning behaviour changes. The structural collapse is prevented and the peak of heat release is decreased by the 52% for 3 BL GOA-CHIT sample and by the 48% in the case of 3 BL GOB- and 3 BL GOC-CHIT assembly (Table 17). These values have to be considered similar because of the errors associated to the measurements. Even if all samples have comparable HRR and pkHRR values, it is important to notice that the same results obtained for bigger GO nanoparticles and 11.2% as add-on can be reached employing the smallest GOC suspension with only 6% of add-on. This suggests a possible effect of the GO aspect ratio in forced combustion tests (Figure 52 a). At the end of the test, a self-standing residue was collected. The mass of the residue follows the same order of GO nanoparticles dimensions, also reflected by the weight gain of PU foam after deposition: GOA-CHIT residue is heavier than GOB-CHIT which is heavier than GOC-CHIT (Table 17 and Figure 53 a, b and c). Increasing the number of deposited layers does not lead to a substantial increase in performances. It therefore seems that 3 BL is sufficient to obtain the optimal performances to deposited BL ratio. At the end of the test, the collected self-standing residue (Figure 53 d, e, f) are heavier than the corresponding 3BL assembly following the trend observed for the initial add-on after deposition. As far as the smoke parameter is concerned, the presence of both 3BL and 6 BL GOx-CHIT coatings can significantly affect the TSR value as reported in Table 17. GOA-CHIT assembly exhibit the best performances in terms of TSR resulting in 69% and 77% reduction for 3 and 6 BL respectively (Table 17). This behaviour may be explained by the higher surface of GOA nanoparticles that can overlap more efficiently than the other GOs. In this way, the tortuosity path is modified more efficiently than in the other 3BL assemblies and the decomposed gases need more time for reach the surface and feed the flame. In addition, the decomposition gases can be physisorbed to the high exposed GOA surface.

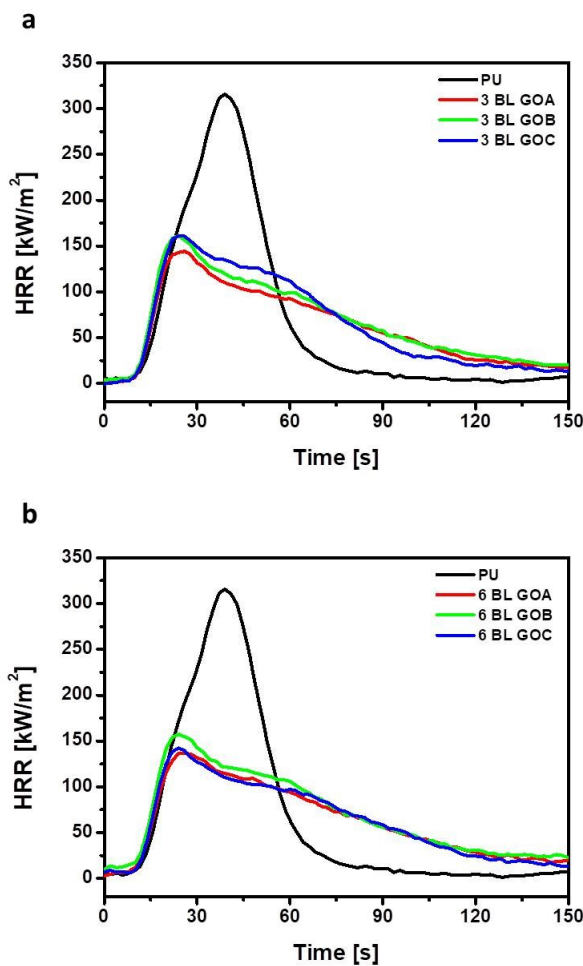


**Figure 52** HRR curves of PU foams coated with a) 3 BL and b) 6BL.

**Table 17** Cone calorimetry data of LbL-treated PU foams.

Sample	TTI $\pm \sigma$ [s]	Av.HRR $\pm \sigma$ [kW/m <sup>2</sup> ]	pkHRR $\pm \sigma$ [kW/m <sup>2</sup> ]	THR $\pm \sigma$ [MJ/m <sup>2</sup> ]	TSR $\pm \sigma$ [m <sup>2</sup> /m <sup>2</sup> ]	Residue $\pm \sigma$ [%]
<b>PU</b>	3 $\pm$ 1	75 $\pm$ 3	308 $\pm$ 25	10 $\pm$ 2	170 $\pm$ 11	7 $\pm$ 1
<b>3 BL GOA-CHIT</b>	2 $\pm$ 1	74 $\pm$ 12	149 $\pm$ 3	9 $\pm$ 1	54 $\pm$ 1	11 $\pm$ 1
<b>3 BL GOB-CHIT</b>	2 $\pm$ 1	67 $\pm$ 3	162 $\pm$ 19	10 $\pm$ 2	56 $\pm$ 12	10 $\pm$ 1
<b>3 BL GOC-CHIT</b>	2 $\pm$ 1	51 $\pm$ 3	162 $\pm$ 10	9 $\pm$ 1	81 $\pm$ 10	8 $\pm$ 1
<b>6 BL GOA-CHIT</b>	2 $\pm$ 1	61 $\pm$ 15	143 $\pm$ 4	9 $\pm$ 1	40 $\pm$ 3	12 $\pm$ 1
<b>6 BL GOB-CHI</b>	2 $\pm$ 1	57 $\pm$ 15	154 $\pm$ 9	11 $\pm$ 5	74 $\pm$ 27	12 $\pm$ 1
<b>6 BL GOC-CHIT</b>	2 $\pm$ 1	51 $\pm$ 5	143 $\pm$ 7	10 $\pm$ 11	64 $\pm$ 8	11 $\pm$ 1

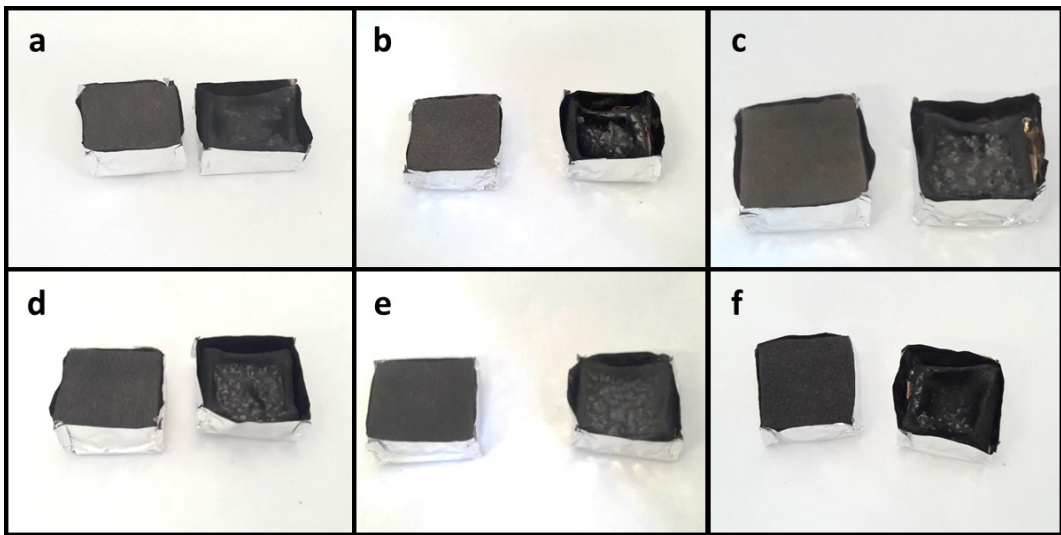


**Figure 53** Imagines of 3BL a) GOA-CHIT, b) GOB-CHIT, c) GOC-CHIT coated foams and 6 BL d) GOA-CHIT, e) GOB-CHIT, f) GOC-CHIT coated foams before (left) and after (right) cone calorimeter exposure.

#### 4.3 Polydiallylammonium-chloride and graphite oxide layer by layer treated PU foams: effect of ionic strength on the assembly and flame retardancy.

In the previous sections, it was shown that CHIT/GO LbL assembly is able to improve the flame retardant properties of PU foam due to the brick and mortar structure of the coating. However, increasing the number of deposited layers, the coatings became rigid and prone to cracking as detected by SEM imaging. The presence of these cracks favours the path of volatiles towards the gas phase thus limiting the efficiency of the coating. More flexible coatings may overcome this problem because they can better adapt to the PU foam complex geometry. To this aim, GO was coupled with Polydiallylammonium chloride (PDAC). PDAC has been reported as capable to deliver flexible coatings due to its high charge density [296]. In the reference paper, Rubner et al. developed an antireflection coating able to be adapted to flexible substrate such as PDMS. After the activation of the PDMS substrate with oxygen plasma in order to make the substrate more hydrophilic, they assembled 14BL of PDAC/poly(styrene)sulfonate-1BL PDAC/SiO<sub>2</sub> (100 nm lateral size) demonstrating by AFM measurements the absence of cracks on the PDMS lenses after a deformation of 2.6%. The adhesion of the coating to the substrate was promoted by the high charge density of the PDAC that in the operational conditions is fully charged and able to strongly adhere to the highly charged oxygenated substrate surface [264]. Differently from CHIT, PDAC has a high charge density that can promote the adhesion to the substrate and can be more adapted to the complex geometry of the foam. In addition, the same assembly was studied in presence of a phosphate salt which has two important effects. Firstly, the addition of a phosphate salt to the GO suspension can change the ionic strength of the solution thus leading to the deposition of thicker coatings. Secondly, phosphorous containing compounds can

be embedded in the coating during LbL assembly and improve the FR properties of the coating. Indeed, phosphates like di-ammonium phosphate (APD) are a well-known char forming agent [297, 298], and can promote the formation of a fire-proofing exoskeleton. The best performing samples were also subjected to flame penetration tests. This test evaluates the resistance of the foam to the penetration of a flame focused on one side of the sample and simulates a larger scale test normally employed to evaluate the fire resistance of composites containing a relatively high fraction of inorganic filler.

#### 4.3.1 Layer by layer growth and characterization

The LbL growth was followed by FT-IR spectroscopy. The spectra of neat components were evaluated. Figure 54 reports the acquired spectra while Table 18 collects the detailed list of signals. PDAC shows main and characteristic bands associated to C-H bonds in  $\text{CH}_2$  (3020 and  $1472\text{ cm}^{-1}$ ) and  $\text{CH}_3$  (2944 and  $2871\text{ cm}^{-1}$ ) and N-C bonds ( $1145\text{ cm}^{-1}$ ) [299]. Signals ascribed to adsorbed water are recognizable as well in the 3600-3200 region and from the peak at  $1640\text{ cm}^{-1}$ . Neat GO spectrum evidences the presence of oxygen containing functionalities with bands at 1725, 1627 and  $1054\text{ cm}^{-1}$  that can be related to  $\text{C=O}$ ,  $\text{COO}^-$ , and  $\text{C-O}$ , respectively [286]. Hydroxyl groups are also visible in the range between 3800-3000  $\text{cm}^{-1}$ . As far as the employed salt is concerned, neat APD yields signals ascribed to N-H<sup>+</sup> and N-H vibrations in  $\text{NH}_4^+$  at 3300-3030 and  $1410\text{ cm}^{-1}$ , respectively. Phosphate groups  $\text{P=O}$ ,  $\text{PO}_3^{2-}$  and P-O are visible at 1260, 1080 and  $900\text{ cm}^{-1}$ , respectively [300].

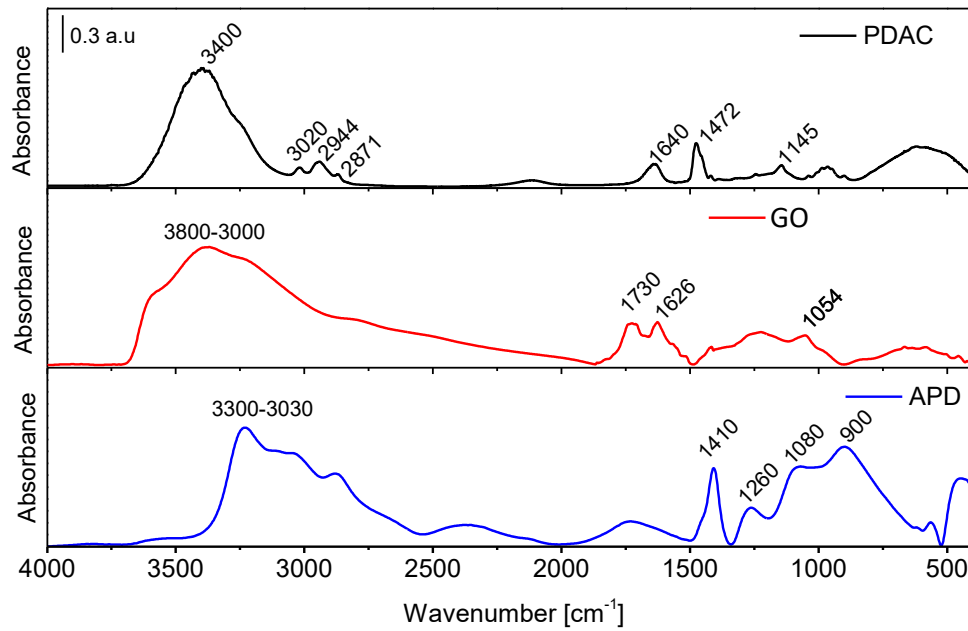


**Figure 54** FT-IR spectra of pure PDAC, Graphene Oxyde and APD

**Table 18** Signals and attribution of PDAC, Graphene Oxyde and APD

	Wavenumbers (cm <sup>-1</sup> )	Attribution
<b>PDAC</b>	3400	v (O-H)
	3020	v (C-H) of CH <sub>2</sub> of CH <sub>2</sub> -N <sup>+</sup> (CH <sub>3</sub> ) <sub>2</sub>
	2944, 2871	v (C-H) of CH <sub>3</sub>
	1640	v (O-H)H <sub>2</sub> O
	1472	def (C-H) of CH <sub>2</sub> , v (O-H)H <sub>2</sub> O
	1145	v (N-C)
	3800 - 3000	v (O-H)
<b>Graphene Oxide</b>	1725	v (C=O)
	1627	v (O-C=O)
<b>Ammonium phosphate dibasic</b>	1054	v (C-O)
	3300-3030	N-H+ str vib, v (O-H)
<b>phosphate</b>	1410	N-H def vib
	1260	P=O
<b>dibasic</b>	1080	PO <sub>3</sub> <sup>2-</sup> str
	900	P-O

The LbL assembly growth of PDAC/GO system under 0 and 0.5M ionic strength conditions was monitored by FT-IR spectroscopy. Figure 55 reports the resulting 3D projection of restricted IR region, the intensity of the peaks ascribed to C=O and COO<sup>-</sup> plotted as a function of BL number and the cross-section images of the 10BL coating imaged by FESEM. When PDAC and GO are LbL assembled together, their characteristic IR peaks add up in a single spectrum that grows in intensity as the number of deposited bi-layers is increased (Figure 55 a). The most intense peaks are ascribed to GO indicating this latter as the main component of the assembly. The evaluation of the intensity of C=O and COO<sup>-</sup> signals as a function of the deposited BL number clearly depicts a linear growth regime for the assembly. The incorporation of APD in the GO suspension changes the coating growth and the relative intensity of the IR signals associated to GO. Indeed, as reported in Figure 55 b, GO signals ascribed to COO<sup>-</sup> groups strongly increase in intensity while the C=O absorption of the undissociated COOH group is considerably reduced to a shoulder of the main peak centred at 1624 cm<sup>-1</sup>. The dissolution of APD in GO suspension results in an increase of pH which promotes the dissociation of GO carboxyl groups with a subsequent increase of COO<sup>-</sup> related signals and a decrease of C=O. [266, 267] In addition, the presence of N-H and P=O signals (1434 and 1260 cm<sup>-1</sup>, respectively) suggests that the employed APD remains deposited within the coating structure and its amount increases by increasing BL number. This is in accordance with previously reported literature for LbL system assembled at modified ionic strength [301]. The growth regime of the coating remains linear as confirmed by intensity vs BL number plots in Figure 55 d. Nevertheless, the presence of APD in the GO suspension allows for the deposition of a thicker ( $\pm$  70%) coating as pointed out by cross-section FESEM

images of Si wafers coated by 10 BL assembled with and without APD (Figure 55e, f).

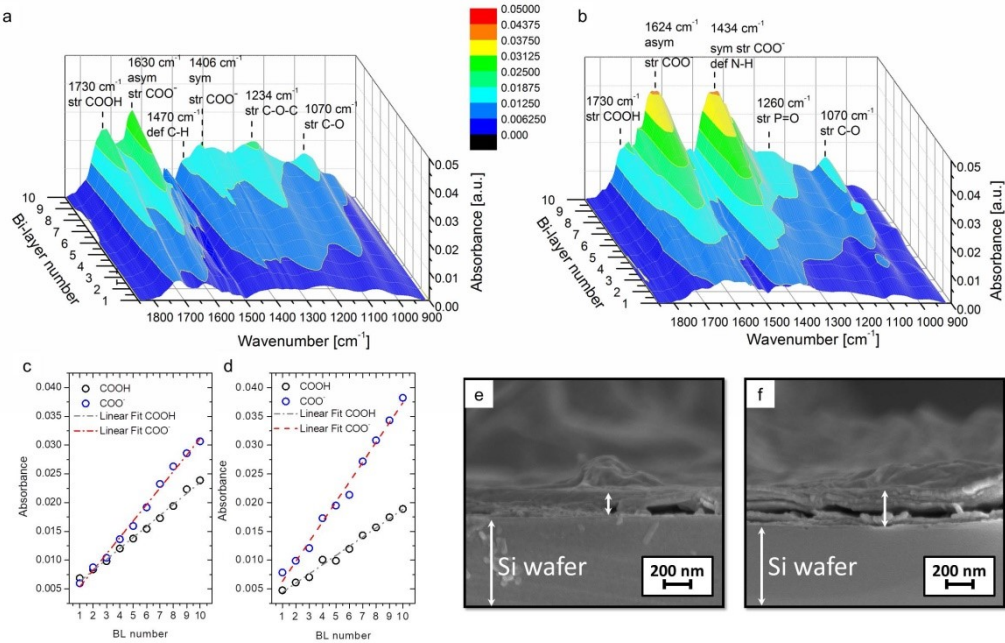


**Figure 55** Characterization of the build-up of PDAC/GO at 0 (a, c and e) and 0.5M (b, d and f) APD on model Si substrate: a-b) FT-IR spectra in the 1850-900 cm<sup>-1</sup> region during LbL growth; c-d) evolution of the signals ascribed to C=O and COO<sup>-</sup> as function of bilayer number and e-f) FE-SEM micrographs of 10 BL cross-section on Si wafer.

The layered structure of the coating comprising GO nanoplatelets held together by PDAC is apparent for both assemblies. From the above-mentioned observations, it seems that the presence of APD allows for the deposition of thicker coatings that embed the salt within their structure. Comparing 10 BL PDAC/GO assembly cross-section with the 10 BL CHIT/GO system, it is evident the latter is thicker due to the lower CHIT charge density compared to the PDAC. This behaviour is also evident in 10 BL PDAC/GO 0.5M assembly, meaning that the charge density of the adopted polyelectrolyte is one of the most important parameter for the coating growth.

#### 4.3.2 Morphology of the coating on PU foams

The LbL assembly of PDAC and GO has been performed on PU foams in both unmodified and modified ionic strength conditions aiming to a total of 3 and 6 BL. The resulting changes in surface morphology were imaged by FESEM. Figure 56 reports micrographs of modified foams in comparison with the unmodified one. The LbL assembled PDAC/GO homogenously coat every surface available resulting in a conformal coating that extends through the entire thickness of the foam regardless of the BL numbers (Figure 56 a-d). The thickness of the deposited coating increases by increasing the number of deposited BL and its maximized by the presence of APD in the GO suspension. This is in agreement with what previously observed on model Si surfaces (compare Figure 56a with 55e and Figure 56c with 55f). Similarly, APD crystals are found on the surface of

GO nanoplatelets as clearly observable from Figure 56c and Figure 56d. In addition, the flexibility of employed GO nanoplatelets allow the nanoplatelets to bend by more than 90° in order to follow the PU complex geometry as imaged and schematized in Figure 56 e. The high flexibility favours the deposition of conformal coatings on all the exposed surfaces of PU foams and avoids the formation of cracks, as it was shown for the CHIT/GO system (Figure 39 c).

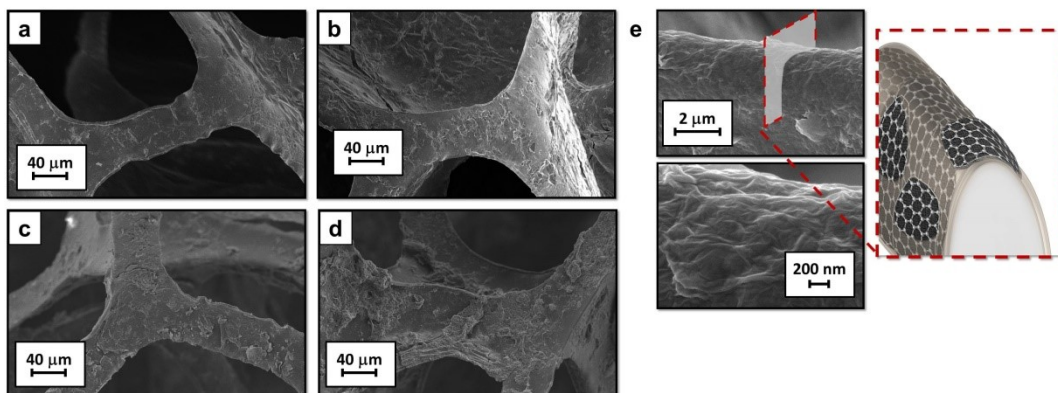


**Figure 56** SEM micrograph of untreated and LbL treated PU foam: a) 3BL, b) 3 BL 0.5 M, c) 6 BL, d) 6 BL 0.5M and e) detail and schematization of coating on the foam edge.

To further investigate the presence of phosphate salts EDS analyses have been performed (Figure 57). Collected spectra pointed out the presence of phosphate which crystals can be found on the top and within the coating structure (Figure 57).

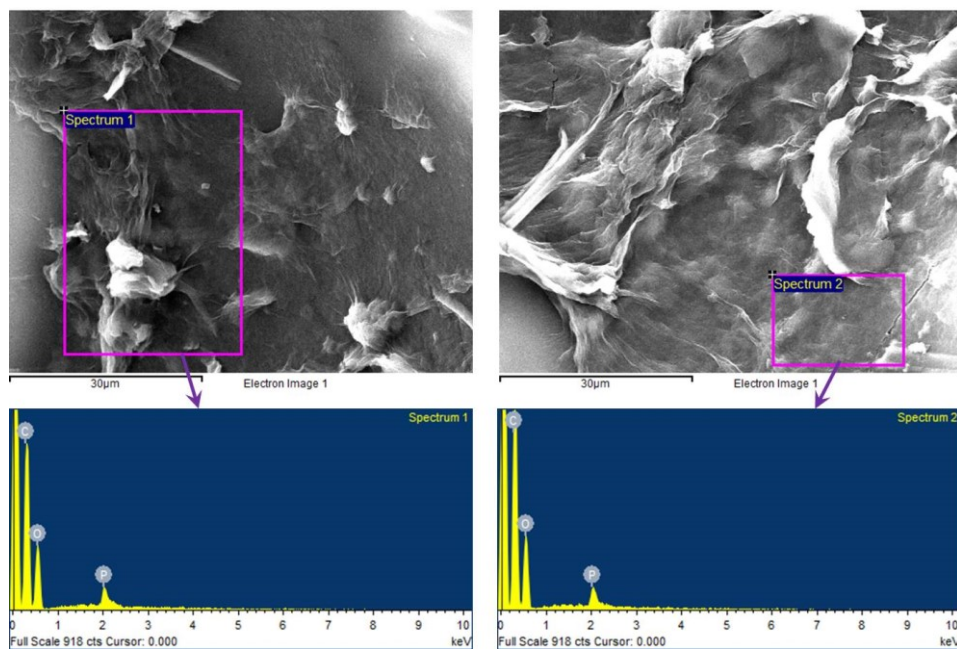


**Figure 57** Elemental analysis performed on 3BL 0.5M

#### 4.3.3 Flammability tests

As described in the previous sections, PU foams are normally considered a highly flammable material. The application of a small flame can indeed set them on fire

while also causing the formation of incandescent/flaming droplets (melt-dripping). The modified foams were evaluated from the flammability point of view as reported in Figure 58 and Table 19. As already observed for CHIT/GO coatings, coated foams show modified burning behaviour with respect to the unmodified ones. Indeed, 3 and 6 BL coatings assembled at unmodified ionic strength are capable of suppressing the melt dripping behaviour and completely maintain the original shape of the foam. The flames spread to the entire length of the sample but are confined only on the surface of the sample. This is also confirmed by the high residues obtained (60 and 78% for 3 and 6 BL, respectively) indicating that the flame self-extinguishes before being able to completely volatilize the PU (Table 19).

On the other hand, coatings assembled at modified ionic strength are capable of not only suppressing the melt dripping but also completely preventing flame spreading by self-extinguishing the flame within 5-10 seconds after flame application. Subsequent flame applications cannot ignite the sample again. For this reason, the final residues are as high as 98-99% (Table 19). The enhancement of flame spreading resistance of this sample can be attributed to the presence of phosphate salt which increase the propensity of the coating to form a char layer which efficiently limits the release of volatiles feeding the flame. Samples coated with 3BL PDAC/GO assembly cannot stop flame spreading because of the absence of phosphorous and a reduced char formation for PDAC.

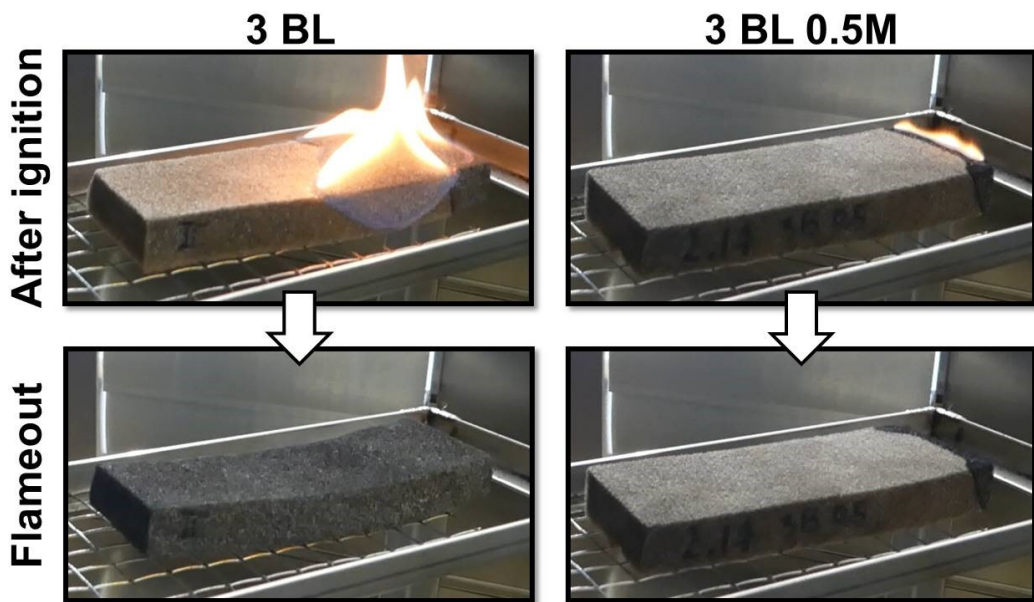


**Figure 58** Flame retardant characterization of untreated and LbL treated foams: a) snapshots from flammability test, b) average residues after flammability tests.

**Table 19** Horizontal flame test data related to untreated, 3 BL , 3BL and 6 BL treated PU Foam with unmodified and modified ionic strength.

Sample	Melt-dripping	Self-extinguishments	Residue $\pm \sigma$ [%]
<b>PU</b>	Yes	No	-
<b>3 BL</b>	No	No	60 $\pm$ 2
<b>3 BL 0.5M</b>	No	Yes	98 $\pm$ 1
<b>6 BL</b>	No	No	78 $\pm$ 3
<b>6 BL 0.5M</b>	No	Yes	99 $\pm$ 1

#### 4.3.4 Forced combustion tests

In order to better understand the heat resistance of LbL treated PU foams, cone calorimetry tests have been performed in the same conditions adopted for the CHIT/GO assembly. Collected data are reported in Figure 59 a and Table 20. The unmodified PU foam show a well-known behaviour with quick ignition followed by melting and structural collapse eventually creating a pool of low viscosity liquid with a steeply increase in the heat release rate ( $\text{pkHRR}=322 \text{ kW/m}^2$ ). The foam is completely consumed by combustion leaving a residue accounting for 1-2% of the original mass (Figure 59 b). The deposition of 3 BL at unmodified ionic strength can prevent the foam structural collapse after ignition and considerably reduce the pkHRR values by 60%. Unexpectedly, all the other samples showed no ignition at all during the test. The exposure to  $35 \text{ kW/m}^2$  can still trigger the release of flammable volatiles; however, the concentration of such volatiles remains below flammability limits, so that ignition does not occur. It is worth mentioning that such impressive behaviour is highly uncommon and rarely reported among polymeric foams; yet it enormously increases the fire safety of prepared foams. All non-igniting foams yielded a coherent residue that maintained the original dimensions of the starting sample also displaying a certain degree of mechanical resistance (Figure 60 a-f). The TSR of non-igniting samples is higher than the sample in which combustion occurs. This behaviour is typical of non-igniting samples, due to the fact that, when ignition occurs, smokes are reduced because volatiles take part in the combustion.

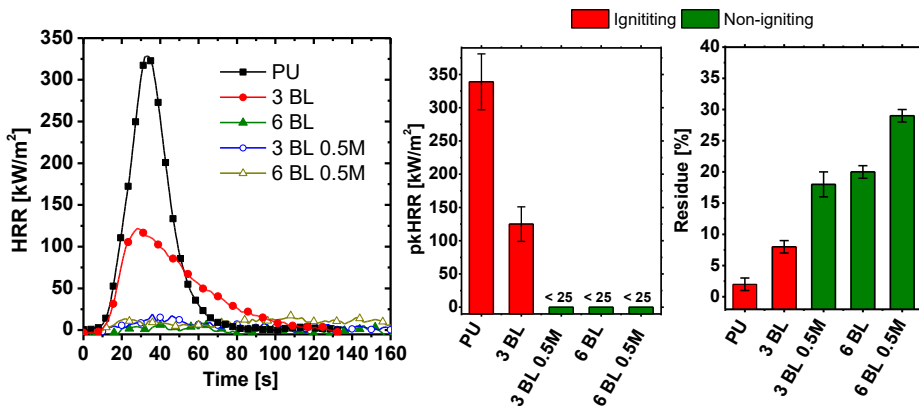


**Figure 59** Flame retardant characterization of untreated and LbL treated foams: (left) heat release rate vs time plots, (right) average residues.

**Table 20** Cone calorimetry data of untreated and LbL-treated foams.

Sample	TTI $\pm \sigma$ [s]	pkHRR $\pm \sigma$ [ $\text{MW/m}^2$ ]	THR $\pm \sigma$ [ $\text{MJ/m}^2$ ]	TSR $\pm \sigma$ [ $\text{m}^2/\text{m}^2$ ]	Residue $\pm \sigma$ [%]
PU	$3 \pm 1$	$339 \pm 42$	$8.4 \pm 1.3$	$171 \pm 20$	$2 \pm 1$
3 BL	$5 \pm 1$	$125 \pm 26$	$5.4 \pm 0.8$	$79 \pm 10$	$8 \pm 1$
6 BL	*	*	*	$234 \pm 11$	$18 \pm 2$
3 BL 0.5M	*	*	*	$276 \pm 19$	$20 \pm 1$
6 BL 0.5M	*	*	*	$225 \pm 13$	$29 \pm 1$

\* denotes non-igniting samples. For non-igniting samples the behaviour is dominated by thermo-oxidation processes thus parameter associated to combustion such as TTI, pkHRR and THR cannot be reported.

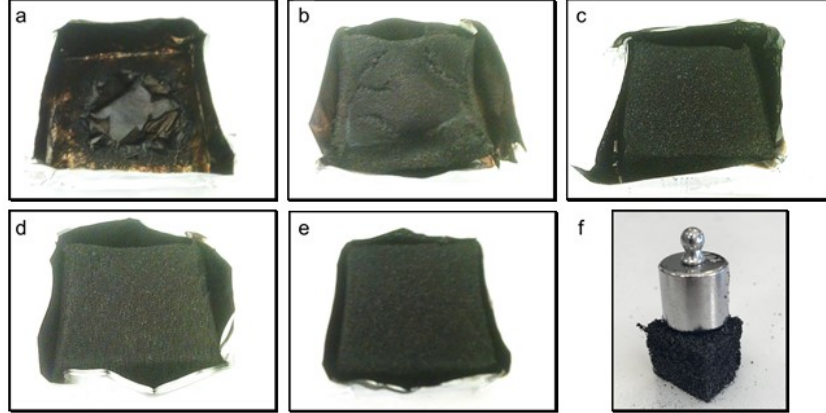


**Figure 60** Digital images of the residues after cone calorimetry tests: a) untreated PU, b) 3 BL, c) 3 BL 0.5M, d) 6 BL, e) 6 BL 0.5M and f) small portion ( $10 \times 10$  mm) of 6 BL 0.5M residue under static compression by a 20g weight.

#### 4.3.5 Coating evolution during combustion and residues analysis

The microstructure and chemical composition of the residues collected at the end of forced combustion test were analysed by means of SEM, Raman and ATR-IR spectroscopy in order to investigate the evolution of the PDAC/GO assembly during combustion. SEM images of residues are reported in Figure 61 and in Figure 62 that collect low magnification and high magnification SEM micrographs, respectively. From Figure 61, the morphology of the residue closely

resembles the one of the un-combusted samples (also compare Figure 62 with Figure 56). The presence of a hollow structure comprising GO nanoplatelets is apparent as reported in high magnification micrographs. This exoskeleton, similarly to the original LbL coating, wraps the entire 3D structure of the original PU foam that was volatilized during the testing. Its thickness and structural integrity increase by increasing the number of deposited BL and by moving from unmodified to modified ionic strength. The 3 BL samples that displayed ignition during the test shows the formation of small cracks in the above-mentioned structure. Such cracks might have compromised the integrity of the coating and thus reduced its flame retardant efficiency. On the other hand, the remaining residues appear undamaged, indicating that an increase in coating thickness is beneficial in terms of flame retardant performances.

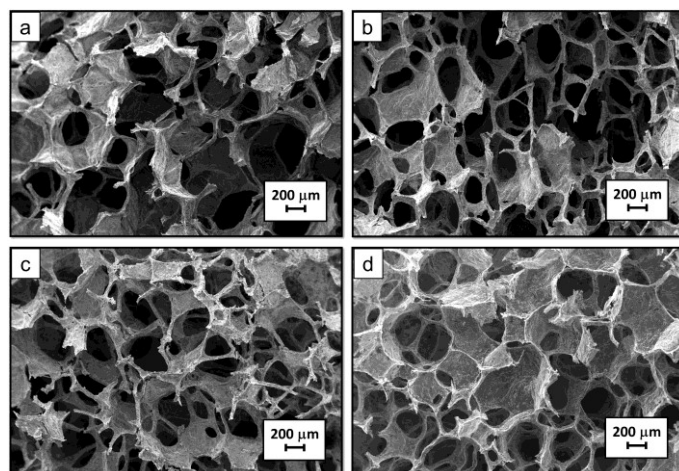


**Figure 61** Low magnification SEM micrograph of residues collected after cone calorimetry tests : a) 3 BL, b) 3 BL 0.5M, c) 6 BL, d) 6 BL 0.5M.

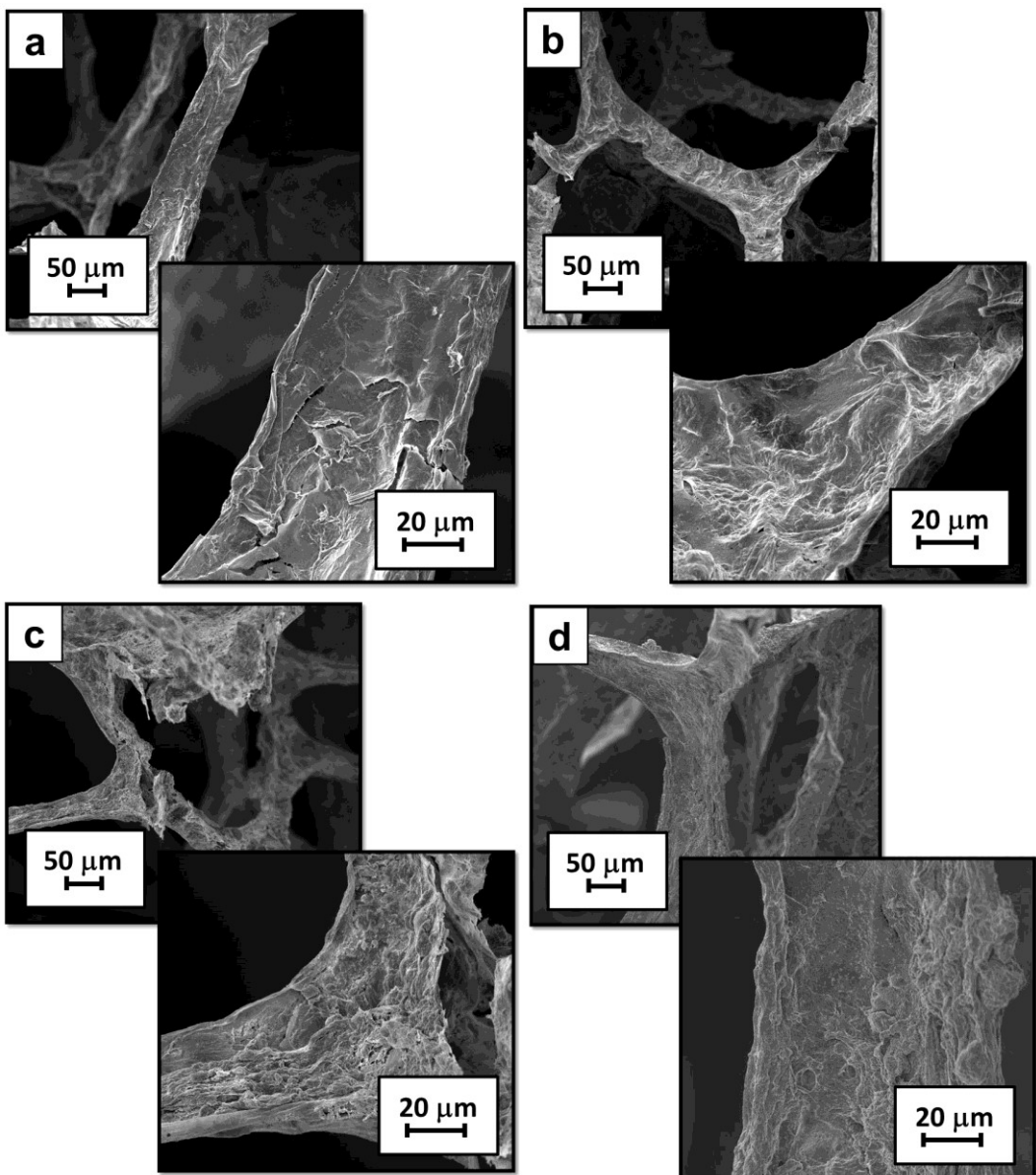


**Figure 62** Post combustion residue analysis. SEM micrographs of: a) 3 BL, b) 3 BL 0.5M, c) 6 BL and d) 6BL 0.5M).

Raman and ATR spectroscopies were employed to further investigate the composition of the residues (Figure 63 and Figure 64 respectively). Raman spectroscopy performed on the residues reveal the presence of two characteristic signals, known as G and D bands naturally present in the original GO (Figure 18) and associated to polyaromatic structure clearly visible at  $1590$  and  $1350\text{ cm}^{-1}$  [302]. The starting GO had a D/G ratio of 1.08 that is increased for all the samples after combustion tests due to char formation reactions of both PU and PDAC (see values in Figure 63), as it was just commented for the CHIT/GO assembly. 3 BL and 6 BL at unmodified ionic strength achieve the highest and lowest ratios, respectively whereas samples at modified ionic strength fall within these values.

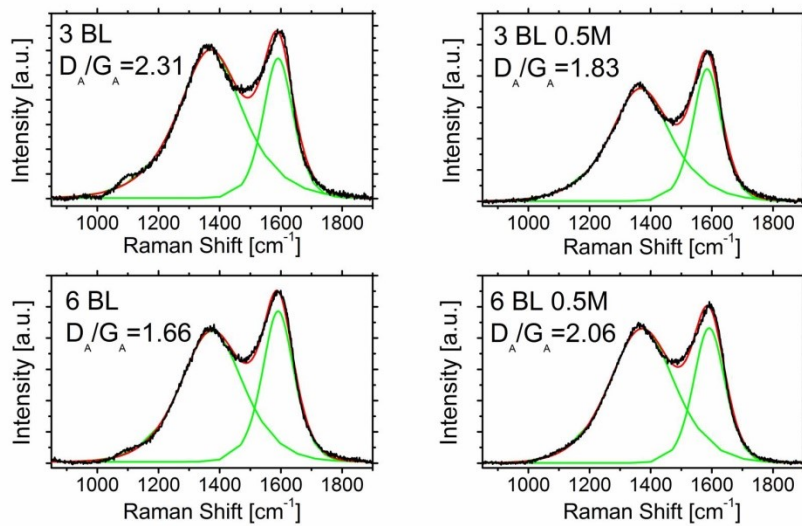


**Figure 63** Raman spectra of 3BL, 3 BL 0.5M, 6 BL, 6 BL 0.5M cone calorimeter residues.

ATR spectroscopy confirms the presence of conjugated C=C bonds ( $1570\text{ cm}^{-1}$ ) as well as C=O ( $1730\text{ cm}^{-1}$ ) and P-O-C ( $1085\text{ cm}^{-1}$ ) functional groups, these latter only visible for samples prepared at modified ionic strength (Figure 64) [300]. From reported data, it seems that the occurrence of ignition is responsible for an increased number of defects; in addition, the presence of APD can also increase the defectiveness of the structure as pointed out by P-O-C bonds. The above-mentioned results suggest a possible interpretation of the LbL coating flame retardant action. The highly oriented and stratified GO nanoplatelets that cover every surface of the foam can mechanically sustain the foam structure while limiting volatile release, while the presence of APD further improves this reduction. Indeed, the presence of phosphates can promote char formation in the condensed phase while the release of ammonia can acts as diluent of produced volatile in the gas phase [303]. The combination of the described contributions can thus limit the release of volatiles so that flame propagation cannot be sustained in flammability tests and ignition does not occur during cone calorimetry.

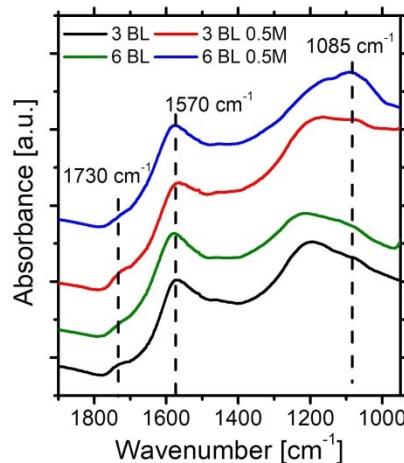


**Figure 64** ATR-IR spectra of residues collected after cone calorimetry tests.

#### 4.3.6 Flame penetration tests

Self-extinguishing and non-igniting samples have been selected for flame penetration tests. Figure 65 collects snapshots of untreated PU and 3 BL 0.5M as well as the temperature profiles for this latter. As reported in Figure 65, the unmodified PU foam is immediately destroyed by the flame torch and the tests only last for few seconds. Conversely, the 3 BL 0.5M samples can withstand the penetration of the flame effectively shielding the unexposed side of the foam. During the test, the sample is gradually consumed by the impinging flame that eventually manages to pierce through after an average 90 s.

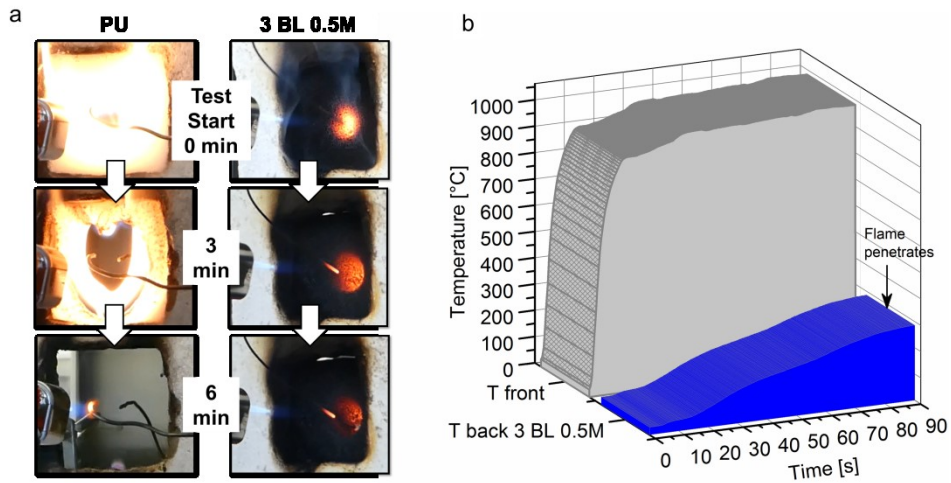


**Figure 65** Flame penetration tests: a) digital pictures of the uncoated PU and 3 BL 0.5M front surface during the test and b) front and back side temperatures as a function of time for 3 BL 0.5M.

Figure 66 reports flame penetration test performed on 6 BL 0.5M sample in comparison with silica aerogel. The 6BL 0.5M foam tremendously improves this behaviour by completely shielding the flame for more than 6 minutes (Figure 66 b). During this time the foam maintains its structure and integrity and successfully insulates the unexposed side achieving a temperature plateau of 104°C on the unexposed side of the foam (Figure 66 c). This indicates a temperature drop from the exposed side of 850°C with a temperature gradient of about 570°C/cm. These performances are compared with those of a silica aerogel, that is well-known as the state of the art thermal insulating material. During the tests, the aerogel shows the formation of small cracks on the surface directly exposed to the flame. A plateau of 102°C on the unexposed side points out a temperature drop similar to the 6 BL 0.5M samples although this is achieved with thinner samples (1 Vs 1.5 cm for aerogel and treated PU foams, respectively). This comparison further highlights the impressive results achieved by an organic foam that make it comparable with a completely inorganic silica aerogel or recently developed freeze-casted foams whose production is much more expensive and complicated [289, 304]. In addition, it is well-known that silica aerogel is unable to withstand mechanical deformation because of its very high brittleness, while the PU foams retain their high flexibility even after LbL deposition.

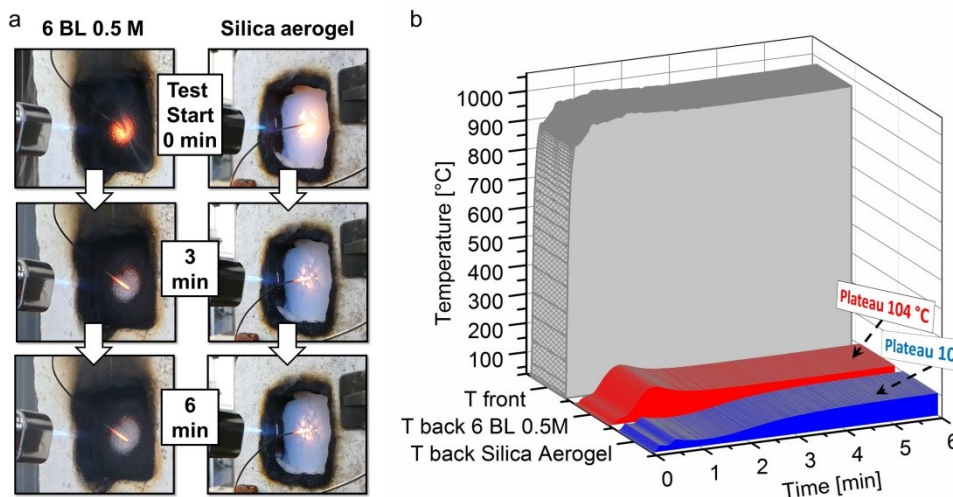


**Figure 66** Flame penetration tests: a) digital pictures of the 6 BL 0.5M and silica aerogel front surface during the test and b) front and back side temperatures as a function of time for 6 BL 0.5M and silica aerogel front surface during the test.

#### 4.4 Heat shielded PU foam obtained by one-pot deposition of high shear mixed graphite

In the previous sections, it has been demonstrated that the LbL of GRMs is a versatile tool able to drastically modify the FR properties of PU foams. Unfortunately, the LbL has some drawbacks: the high volume of solution/suspensions requested for the deposition, the multistep nature of the process and the need for rinsing baths linked to the specimen dimensions. In order to avoid these problems and to further improve the amount of deposited nanoparticles, a new one step approach, where the assembly of GRMs on the surface of PU foams is forced by the solvent removal, was developed. In this process, graphite nanoplatelets suspensions were employed instead of graphite oxide. GNP water-based suspension were employed for coat PU foams considering different grade of exfoliation. Several samples were prepared following the same procedure schematized in materials and method section and using different GNP suspension obtained after different amount of high shear mixing cycles (namely 0, 10, 30, 50, 70, 100). In the following section, samples named “x cycles” refer to one pot treated PU foams coated with a suspension obtained after x cycles in high shear mixers. As an example, a 100 cycle named sample refers to a PU foam coated by a one pot deposition of a suspension subjected to 100 shear mixing cycles. Moreover, in the last previous section, it was demonstrated that the presence of a phosphate salt can drastically increase the FR properties of treated PU foams. In this section, a sodium examethaphosphate salt  $[(NaPO_3)_n]$  was added to the GNP suspensions in a ratio mass of 1:1 in order to retain a 100% of final add-on. Sodium hexametaphosphate has been already employed as flame retardant additives in other LbL assembly highlighting its intumescent and char forming behaviour [215]. Indeed, in section 4.3, it was demonstrated that phosphate additives may improve the flame retardant properties of 0.5 M PDAC/GO treated foams, with just 3 BL deposition. SEM, Raman and

ATR spectroscopy conducted on the cone calorimetry residue confirm that the presence of phosphate salt promote the formation of a compact char layer that limit the volatiles to reach the polymer surface so the flame propagation cannot be sustained in flammability tests and ignition does not occur during cone calorimetry. In fact, SEM micrographs evidence the presence of a continuous exoskeleton formed after heat flux exposure, the presence of the P-O-C vibration mode at  $1085\text{ cm}^{-1}$  in ATR measurements testify the presence of phosphorous based species bonded to the structure, that also increase the disorder of the final char structure, as showed by Raman spectroscopy. Samples prepared with the addition of  $(\text{NaPO}_3)_n$  in the GNP suspensions are named “x cycles\_P”.

#### 4.4.1 Morphology of the coating

The morphology of prepared samples was evaluated by FE-SEM, collected micrographs are reported in Figure 67 and Figure 68. After the GNP deposition the surface morphology of PU foams is remarkably changed as a function of the homogenization cycles employed in the suspension preparation. When the 0 cycles suspension is deposited on the substrate (Figure 67 a and b), the graphite platelets tend to agglomerate in large clusters as shown in Figure 67 b. From 10 cycles to 100 cycles, the morphology of the samples changes drastically compared to the 0 cycles deposition. At low magnification, all surfaces appear to be covered by a homogenous GNPs coating. Higher magnification micrographs (Figure 67 b, d, f, h, l, n) allow for the evaluation of defects in the coatings as well the degree of aggregation phenomena. Indeed, GNP aggregation is restricted to the inhomogeneity of the PU surface topography like edges and corners. As it is possible to see from Figure 67 d and f, for 10 and 30 cycles samples, GNP platelets tend to aggregate and result in a non-uniform coating. When 50 cycles (Figure 67 h), 70 cycles (Figure 67 l) and 100 cycles (Figure 67 n) suspensions are deposited, the coatings become more homogeneous and the coverage of edges is more effective. This behaviour is attributed to the GNP dimensions: upon solvent removal the bigger nanoparticles may be conveyed mainly by the attraction forces between each other and aggregation occurs. For smaller nanoparticles, the contribution of solvation forces overcome the attraction between nanoparticles and aggregation is mostly avoided [305]. Moreover, by increasing the number of exfoliation cycles the GNP nanoparticles become thinner so they can be bended more easily thus more efficiently following the foam morphology.

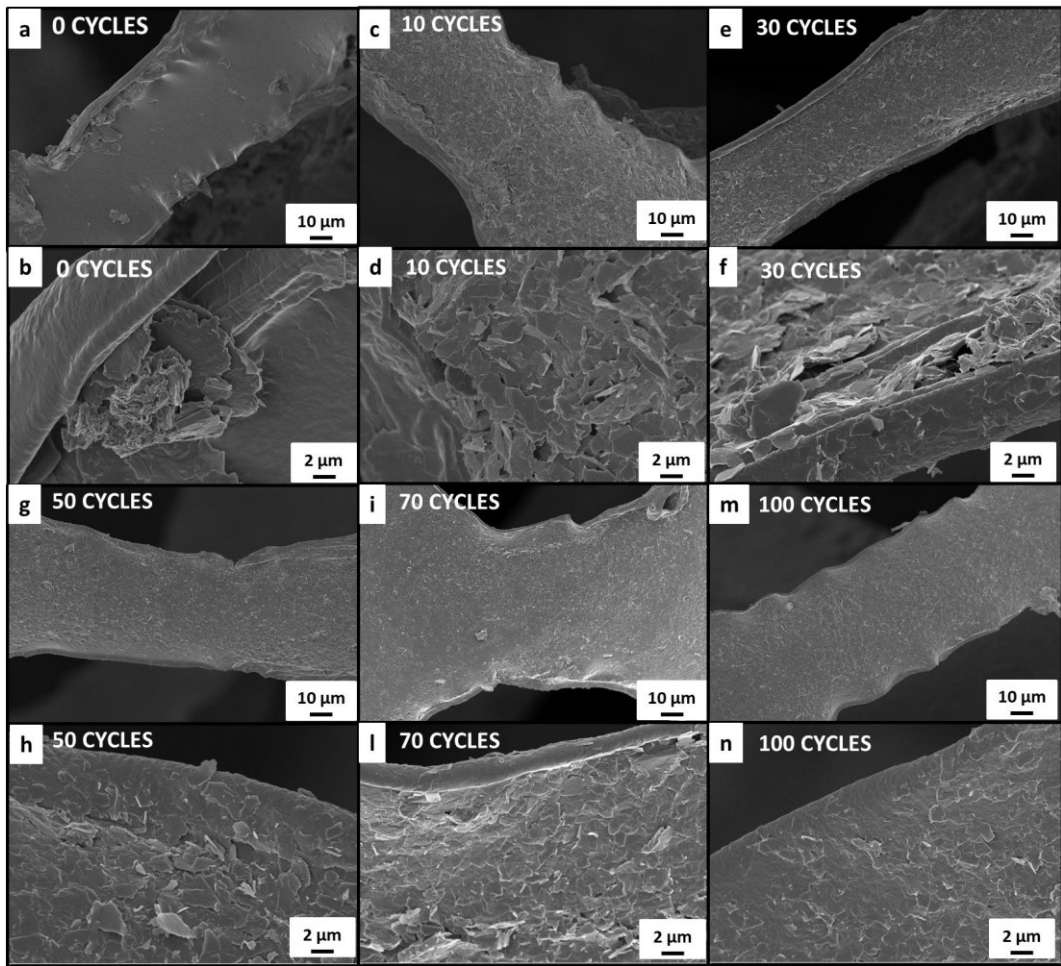


**Figure 67** FE-SEM micrograph of one-pot treated PU foams at low magnification of a) 0 cycles, c) 10 cycles, e) 30 cycles, g) 50 cycles, i) 70 cycles, m) 100 cycles FE-SEM at high magnification of b) 0 cycles, d) 10 cycles, f) 30 cycles, h) 50 cycles, l) 70 cycles, n) 100 cycles.

The effect of  $(\text{NaPO}_3)_n$  addition on the morphology of the resulting coatings was evaluated as well, collected micrographs are reported in Figure 68. By analysing the FESEM micrograph of samples obtained from the deposition of GNP/ $(\text{NaPO}_3)_n$  suspensions no significant differences can be evidenced compared to GNP suspension deposition. However, it is interesting to note that even if  $x$  cycles\_P samples are 50% less concentrated in GNP than the relative  $x$  cycles samples, all the surface are still covered. This suggest that the required amount of GNP able to completely cover the PU foam surfaces has a threshold below 1 wt% GNP concentration. In addition to this, it is possible to notice that the 0 cycles\_P foam (Figure 68 a and b) appears to be more covered than the 0 cycles samples, suggesting that also the concentration of the employed suspension has a role in aggregation phenomena. As it was observed for the other samples, by increasing the number of exfoliation cycles the homogeneity of the treatments increases (Figure 68). In addition, the absence of  $(\text{NaPO}_3)_n$  crystals in SEM morphology suggest that the salt is well solubilized in the suspension and after deposition it may be well distributed within the coating.

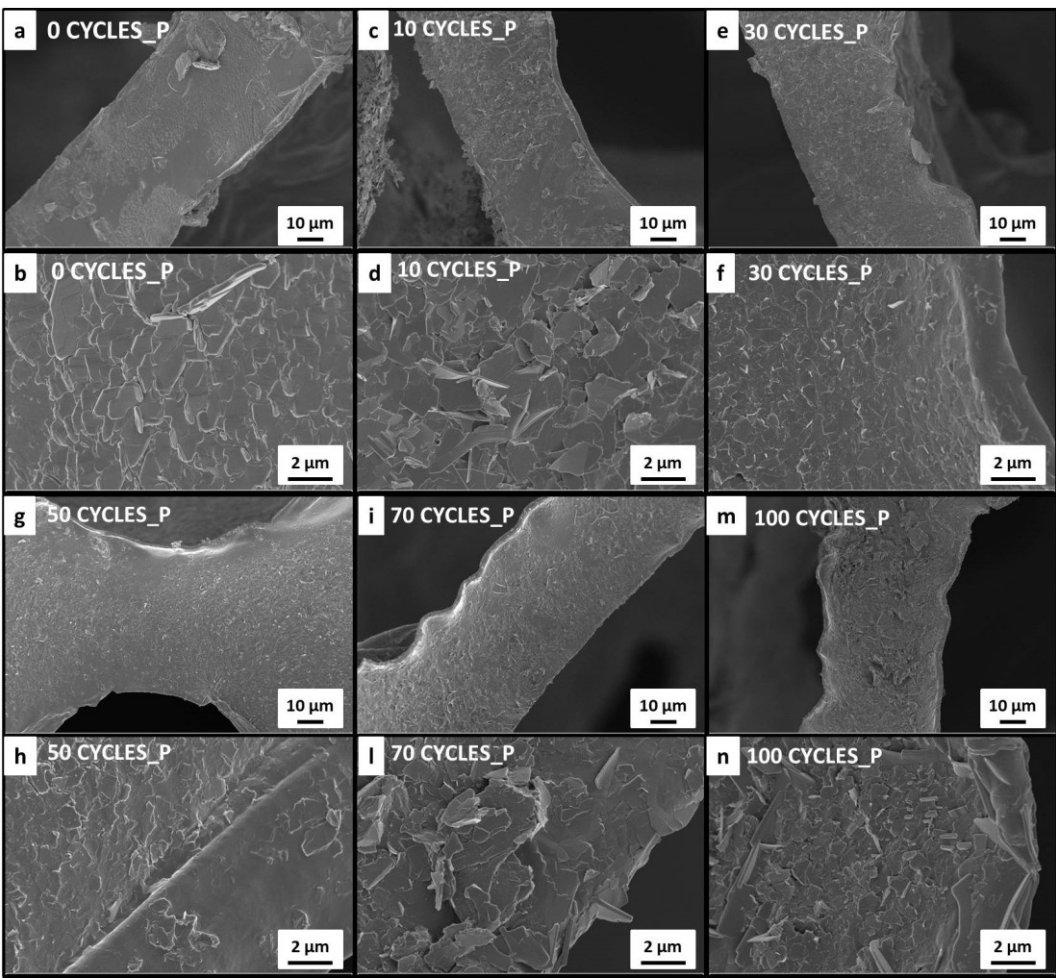


**Figure 68** FE-SEM micrograph of one-pot treated PU foams at low magnification of a) 0 cycles\_P, c) 10 cycles\_P, e) 30 cycles\_P, g) 50 cycles\_P, i) 70 cycles\_P, m) 100 cycles\_P; FE-SEM at high magnification of b) 0 cycles\_P, d) 10 cycles\_P, f) 30 cycles\_P, h) 50 cycles\_P, l) 70 cycles\_P, n) 100 cycles\_P.

#### 4.4.2 Flammability tests

Flame reaction of the GNP-coated PU foams was tested by flammability tests in horizontal configuration. A neat PU foam was tested as reference for samples treated by only GNP suspensions x cycles samples. Table 21 reports flammability results for these samples, and Table 22 reports flammability results for x cycles\_P samples. When the flame is applied to the 0 cycles treated PU foam, the sample is ignited as for the reference foam, but no melt dripping occurs. The flame spreads to all the sample and after its extinguishment the specimen keep releasing smoke, suggesting the occurrence of smouldering, i.e combustion in absence of a flame [306-308]. For all the tested 0 cycles specimens the combustion is arrested after an average 3 minutes burning and a self-standing residue is collected (Table 21). By increasing the number of cycles, a self-extinguishment behaviour occurs after few seconds of flame application. However, after the flame extinguishes, combustion is continued by smouldering. Surprisingly, 30 cycles samples show the best performances in flame spreading because 30 cycles coated foams do not ignite after the flame application and do not show smouldering leaving nearly 100% residue ate the end of the test. On the other hand, samples coated by 50, 70

and 100 cycles undergo flaming ignition, show self-extinguishment behaviour and smouldering combustion leaving a final residues of 95, 59 and 77% for 50, 70, 100 cycles, respectively (Table 21).

**Table 21** Flammability test of x cycles treated PU foams.

Sample	Melt-dripping	Observation	Residue $\pm \sigma$ [%]
		Self-extinguishment	Smouldering
<b>PU ref</b>	Yes	No	No -
<b>0 cycles</b>	No	No	Yes $35 \pm 2$
<b>10 cycles</b>	No	Yes	Yes $52 \pm 3$
<b>30 cycles</b>	No	*	*
<b>50 cycles</b>	No	Yes	Yes $95 \pm 8$
<b>70 cycles</b>	No	Yes	Yes $59 \pm 36$
<b>100 cycles</b>	No	Yes	Yes $77 \pm 22$

\*no ignition after flame application.

The flammability properties change significantly when the phosphate salt is added to the suspensions. The PU\_P reference was prepared employing the same suspension composition except for the GNPs. In this way it is possible to evaluate the effects of the GNP. When the flame is applied to the reference samples, ignition occurs almost immediately and the flame is spread along the edges of the samples; self-extinguishment then occurs within the first 5 cm of the sample. The presence of GNP and  $(NaPO_3)_n$  substantially changes the flammability properties of 0 cycles treated foam. Indeed, after the flame application, the sample is ignited but, in this case, the flame is immediately extinguished with no smouldering. The same behaviour is observed for samples coated by suspensions at higher mixing cycles.

**Table 22** Flammability test of x cycles\_P treated PU foams.

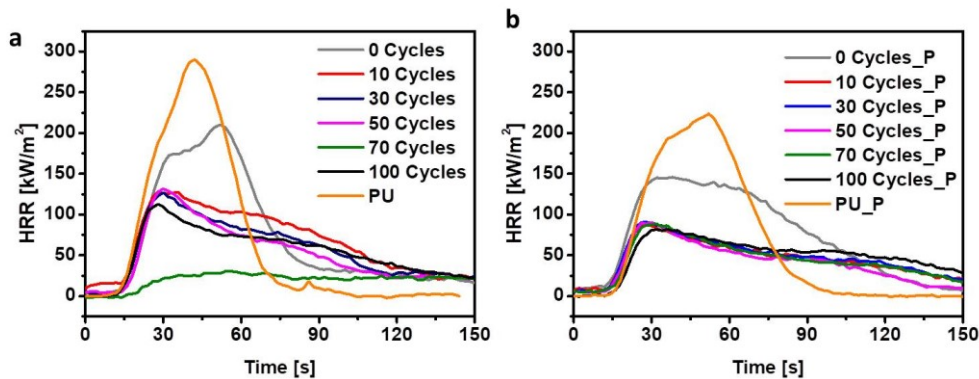
Sample	Melt-dripping	Observations	Residue $\pm \sigma$ [%]
		Self-extinguishment	Smouldering
<b>PU-P ref</b>	No	Yes	No $88 \pm 2$
<b>0 cycles P</b>	No	Yes	No $98 \pm 1$
<b>10 cycles P</b>	No	*	** 100
<b>30 cycles P</b>	No	*	** 100
<b>50 cycles P</b>	No	*	** 100
<b>70 cycles P</b>	No	*	** 100
<b>100 cycles P</b>	No	*	** 100

\*No ignition after flame application; \*\*No smouldering phenomenon after flame application.

#### 4.4.3 Forced combustion tests

Figure 69 reports plots concerning HRR vs Time and SPR vs Time for untreated and treated PU foams. Table 23 resume cone calorimetry data of all samples.

When exposed to a  $35 \text{ kW/m}^2$  heat flux, the untreated PU foams ignite immediately and burn quickly reaching a pkHRR at  $310 \text{ kW/m}^2$ . The deposition of 0 cycles suspension on PU foam allows to decrease the peak of heat release by 30% (Figure 69 a and Table 23). During the test the foam structure collapsed but the geometry of the specimen was partially retained allowing for the recovery of a self-standing residue at the end of the test. Samples made by 10 to 50 cycles suspensions and 100 cycles suspension, exhibit better performances than the 0 cycles samples. The average HRR and the HRR peak are reduced by the 30% and by the 60%, respectively, if compared to the neat PU foam performances. The presence of the coating also affects the smoke production rate (Figure 69 c). In 0 cycles treated samples, immediately after the ignition a maximum of smoke production rate is reached and after another peak of SPR occurs around 60s of combustion because of the scarce coating quality (see Figure 67 a and b). The two peaks may be reasonably attributed to two processes that are responsible for the production of aerosols that are optically opaque and are overlapped in time. The SPR of 10 to 50 and 100 cycles treated PU foams is reached immediately after the ignition and the smoke is consumed within 15 sec. Surprisingly, 70 cycles coated foams exhibit no ignition and therefore a very low HRR. As observed before, non-igniting samples, are consumed by pyrolysis and oxidation phenomena occurring in the condensed phase still consume the sample. For this reason, at the end of the test, a self-standing residue averaging 50% is collected. For this reason, 70 cycles foams reveal a huge SPR (Figure 69 c). Interestingly, TSR value of 70 cycles treated sample is very low, near one third, compared to the TSR of 6BL CHIT/GO and PDAC/GO non-igniting samples (6 BL, 3 BL 0.5M and 6 BL 0.5 M). This behaviour may be attributed to the 70 cycles coating capability to physisorb pyrolysis volatiles more efficiently than the other considered coatings due to the higher number of deposited nanoparticles.



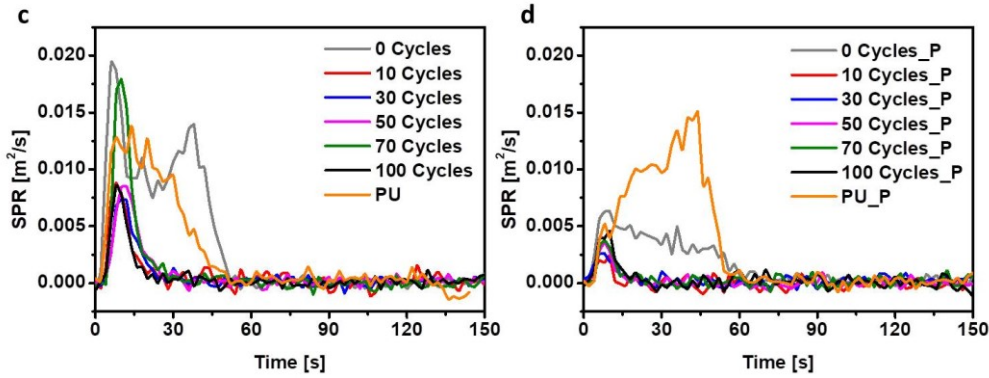


**Figure 69** Cone calorimeter tests of x\_cycles and x\_cycles\_P PU foams: a) HRR comparison of x cycle foams, b) HRR comparison of x cycles\_P foams, c) SPR comparison of x cycles foams, d) SPR comparison of x cycles\_P foams.

**Table 23** Cone calorimetry data of untreated and one pot treated PU foams.

Sample	TTI $\pm \sigma$ [s]	Av.HRR $\pm \sigma$ [ $\text{kW}/\text{m}^2$ ]	pk HRR $\pm \sigma$ [ $\text{kW}/\text{m}^2$ ]	THR $\pm \sigma$ [ $\text{MJ}/\text{m}^2$ ]	TSR $\pm \sigma$ [ $\text{m}^2/\text{m}^2$ ]	Residue $\pm \sigma$ [%]
PU ref	3 $\pm$ 1	69 $\pm$ 10	310 $\pm$ 46	9.2 $\pm$ 0.8	161 $\pm$ 20	7 $\pm$ 1
0 cycles	6 $\pm$ 2	78 $\pm$ 5	219 $\pm$ 7	10.8 $\pm$ 0.7	208 $\pm$ 15	34 $\pm$ 1
10 cycles	4 $\pm$ 1	54 $\pm$ 5	130 $\pm$ 6	9.9 $\pm$ 1.5	89 $\pm$ 14	50 $\pm$ 2
30 cycles	3 $\pm$ 1	52 $\pm$ 6	127 $\pm$ 8	9.3 $\pm$ 1.0	55 $\pm$ 12	50 $\pm$ 3
50 cycles	5 $\pm$ 2	48 $\pm$ 5	126 $\pm$ 2	8.3 $\pm$ 0.9	62 $\pm$ 10	50 $\pm$ 3
70 cycles	-	20 $\pm$ 7	33 $\pm$ 9	3.2 $\pm$ 1.0	79 $\pm$ 14	50 $\pm$ 4
100 cycles	4 $\pm$ 1	46 $\pm$ 5	115 $\pm$ 2	9.3 $\pm$ 1.0	51 $\pm$ 12	45 $\pm$ 2

As far as  $(\text{NaPO}_3)_n$  containing suspensions are concerned (Figure 69 b and Table 24), the reference sample prepared without the presence of GNP show a 27% reduction of the pkHRR compared to the untreated PU sample and higher TSR due to the presence of phosphate salt that, as it is well-known, induce less efficient combustion thus enhancing the smoke productions. The deposition of 0 cycles\_P suspension is sufficient for a 53% reduction of the heat release peak compared to the PU\_P reference. All the tested samples did ignite during the test but the pkHRR values are considerably reduced yielding a value below  $100 \text{ kW}/\text{m}^2$ . The smoke production rate is minimized and confined in the first 15 seconds even if x\_cycles\_P samples have a lower concentration of graphite nanoparticles with respect to the relative x cycle treated foams (Figure 69 d). This behaviour may be attributed to the more efficient capability of the coating, where nanoparticles are held together in a stable char, to act as gas barrier towards volatiles promoted by presence of the phosphate. Differently from the analogue 70 cycles sample, the 70 cycles P suspension treated foams ignite. This behaviour could be ascribed to the lower concentration of GNP in 70 cycles P sample, resulting in a less efficient barrier toward volatiles that reach the surface and reach the critical ignition concentration.

**Table 24** Cone calorimetry data of untreated and one pot treated PU foams with phosphate salt.

Sample	TTI $\pm \sigma$ [s]	Av.HRR $\pm \sigma$ [kW/m <sup>2</sup> ]	pk HRR $\pm \sigma$ [kW/m <sup>2</sup> ]	THR $\pm \sigma$ [MJ/m <sup>2</sup> ]	TSR $\pm \sigma$ [m <sup>2</sup> /m <sup>2</sup> ]	Residue $\pm \sigma$ [%]
<b>PU ref P</b>	6 $\pm$ 1	69 $\pm$ 2	227 $\pm$ 15	10.3 $\pm$ 0.3	200 $\pm$ 17	42.2 $\pm$ 1
<b>0 cycles +P</b>	4 $\pm$ 1	58 $\pm$ 6	148 $\pm$ 8	10.7 $\pm$ 1.2	112 $\pm$ 17	50.7 $\pm$ 1
<b>10 cycles +P</b>	4 $\pm$ 1	35 $\pm$ 3	88 $\pm$ 5	7.43 $\pm$ 0.3	33 $\pm$ 8	53.7 $\pm$ 2
<b>30 cycles +P</b>	3 $\pm$ 1	36 $\pm$ 6	91 $\pm$ 12	7.85 $\pm$ 1.5	44 $\pm$ 15	55.2 $\pm$ 1
<b>50 cycles +P</b>	4 $\pm$ 1	33 $\pm$ 4	91 $\pm$ 4	6.45 $\pm$ 1.2	31 $\pm$ 10	58.5 $\pm$ 2
<b>70 cycles +P</b>	5 $\pm$ 1	38 $\pm$ 4	89 $\pm$ 8	8.7 $\pm$ 1.4	24 $\pm$ 4	52.0 $\pm$ 4
<b>100 cycles +P</b>	7 $\pm$ 2	38 $\pm$ 5	83 $\pm$ 8	8.6 $\pm$ 1.8	54 $\pm$ 23	50.5 $\pm$ 2

#### 4.4.4 Flame penetration test

Flame penetration tests were performed on all treated samples and results are shown in Figure 70, which reports the temperature profile collected during flame penetration tests for all the tested samples. The application of a focused flame impinging directly on the surface of the sample was sufficient to penetrate all the x cycles treated PU foams thus failing in maintaining structural integrity during the test (Figure 70 a). However, differently from the neat PU foam, the treated samples are only partially consumed by the flame and at the end of the test a self-standing residue can be collected for all of the treated samples. As far as phosphate containing samples are concerned, PU\_P reference sample is consumed after 60 seconds of flame application. Conversely, GNP/phosphate based suspensions treated samples can resist to the penetration of the flame shielding the unexposed side of the foam. During the test, the exposed sample surface change considerably its morphology. From a general point of view, the surface layer of the foam is partially consumed by the impinging flame producing a char layer on the exposed surface shielding the flame for more than 6 minutes (Figure 70 b). During this time the foams keep their structure and integrity and successfully insulates the unexposed side achieving a temperature plateau below 90°C (Figure 70 c). This results is a temperature drop with respect to the exposed side of 600°C with a temperature gradient of ~500°C/cm. By evaluating the temperature plateau reached during the test (Figure 70 c), it seems that 50 cycles\_P treated foam exhibit higher heat shielding properties. However, taking into account the experimental deviations, the performances can be considered in the same range of 10, 30 and 70 cycles P treated samples.

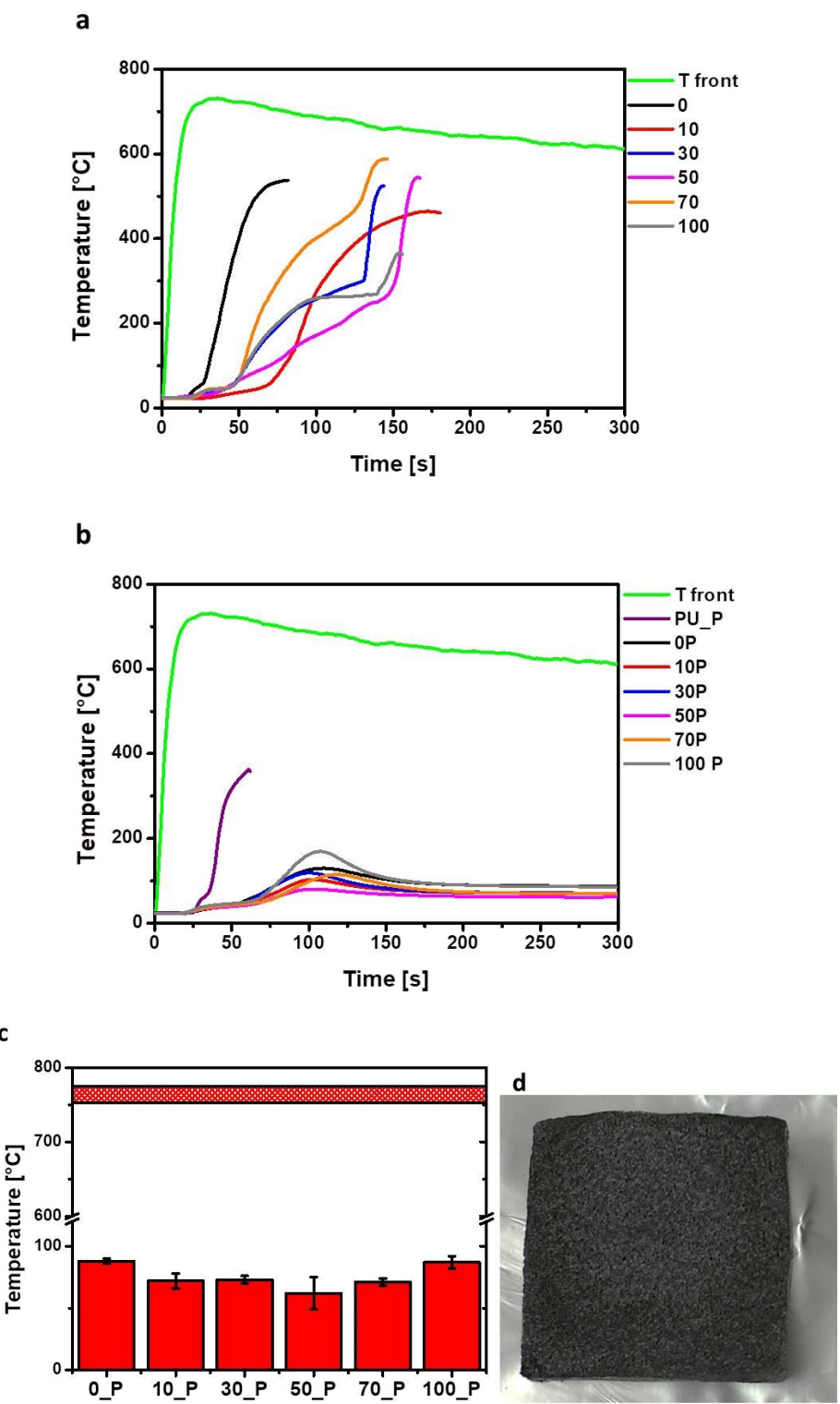


**Figure 70** Flame penetration test of a) x cycles treated foam and b)x cycles\_P treated foams. c) Temperature interval between the front and the back of x cycles\_P PU treated foams, d) picture of 10 cycles\_P coated foam residue.

# Conclusions

This PhD thesis was focused on the exploitation of graphene related material for the preparation of coatings able to act as a barrier towards gases permeability and heat transfer exploited in gas barrier and flame retardancy applications. GRMs were selected as coating components after several considerations regarding their morphological and thermal properties. Indeed, it has been demonstrated that nanoparticles with high aspect ratio can be exploited in order to change the surface properties of polymers and modify the tortuosity path of permeating molecules making them attractive for gas barrier application. Similarly, the high heat resistance and radiative properties of graphene related materials makes them attractive for heat shielding. A surface approach was applied in recent literature, clearly demonstrated that the barrier and heat shielding properties in bulk GNP nanocomposites are greatly affected by un-optimized dispersion and orientation of the nanoparticles. To this aim, Layer by Layer technique has been adopted as main approach to coat the surface of polymers like polyethylene terephthalate and polyurethane foams yielding GRM assemblies with optimal nanoparticle orientations. However, the need for stable and diluted GRMs suspensions, pointed out the attention on the stabilization of graphene related materials in water. The main graphene related materials used in this work are graphite oxide and graphite nanoplatelets. Graphite oxide is the water-soluble form of graphite and can be used as negative component in LbL assemblies. However, the presence of oxygen-based functionalizations results in defects and makes graphite oxide water sensible and thus not suitable for gas barrier applications where oxygen transmission rate under the value of  $10^{-5}$  cc/m<sup>2</sup> day atm are required. In contrast, graphite nanoplatelets are normally associated to a reduced number of defects. Unfortunately, their dispersion in water is difficult due to the high interfacial tension between water molecules and graphitic planes at the particle/liquid interface. For this reason, the first part of this thesis was focused on the stabilization of graphite nanoplatelets in water considering two different strategies: i) the tip-sonication in perylene bis-imides derivative solution and ii) the tip-sonication in polyelectrolyte solutions. In the first case study, a perylene bis-imides derivative was used as surfactant aiming at possibility to exploit the  $\pi$ - $\pi$  interaction between the aromatic part of perylene and the honeycomb structure of graphitic planes. The presence of polar functionalizations in the perylene bis-imides derivative side chains is able to interact with water promoting the stabilization of complexed graphite nanoplatelets. Unfortunately, the obtained suspensions were not sufficiently stable, as graphite nanoplatelets precipitated after 1-2 days from the sonication. Fluorescence spectroscopy was employed in order to study the solubility of this molecules in water as it is well known that only the monomer form of the perylene bis-imides derivative is fluorescent meanwhile the self-aggregation of the molecules quenches the light emission.

Results revealed that the perylene bisimides derivative adopted in this work tends to stack with itself instead of graphite nanoplatelets. The fluorescence measurements were also conducted on perylene bisimides solutions at pH 2, 8, and buffer 7 but this strategy was not sufficient to prevent the molecules self-stacking in water. As an alternative to perylene bis-imides based dye, graphite nanoplatelets were stabilized in water-based solutions of positively and negatively charged polyelectrolytes such as branched polyethylene imine and polyacrylic acid, respectively. The so obtained suspensions showed good in time stability in the order of 4-5 months, and the dispersed nanoparticles had lateral size in the range of 3-5  $\mu\text{m}$  in both suspensions. The final concentration of suspended graphite nanoplatelets was determined by thermogravimetric analysis and was found to be 0.006 wt% and 0.019 wt% in branched polyethylene imine and polyacrylic acid, respectively. The produced suspensions were employed in a LbL assembly yielding thin coatings where GNPs are preferentially oriented parallel to the substrate surface and embedded within the two polyelectrolytes assembly. The resulting “brick and mortar” morphology is able to increase the tortuosity path of permeating molecules, to the point that a 10 BL deposited assembly on a polyethylene terephthalate film was sufficient to obtain an oxygen transmission rate below  $5 \times 10^{-3}$  [cc mm/m<sup>2</sup> day atm], in 0% of relative humidity condition. Comparing permeability results obtained in this work and the reported literature, this result outperforms 10 BL assemblies comprising layered silicate or graphite oxide obtained employing ten times more concentrated solutions than in this work and resulted in more than one order of magnitude higher permeability values.

GRM-based coatings with similar structures were employed for fire retardant purposes exploiting high aspect ratio nanoparticles in order to prepare coatings able to act as a barrier to the release of volatiles during combustion. To this aim, GO nanoplatelets were used in LbL assemblies for improving the flame retardancy of open cell Polyurethane foams (PU). GO was coupled with either Chitosan (CHIT) or polydiallylammoniumchloride (PDAC). Flammability tests showed that 3BL of GO/polycations assembly can completely suppress the melt-dripping phenomenon and the flame spreading before the complete consumption of the PU yielding final residues as high as 61%. The effect of nanoparticles aspect ratio was also investigated in CHIT/GO assemblies showing that similar flame retardant performances can be obtained by employing thinner nanoparticles with the advantage of reduced coating add-ons at the same number of deposited BLs. However, the best flame retardant properties were achieved by PDAC/GO coatings assembled modifying the ionic strength of the GO suspensions by the addition of a phosphate salt. This has been proven to increase the thickness of the deposited coatings and confer additional flame retardant features to the coated foams. The deposition of only 3BL at modified ionic strength granted self-extinguishment behavior during flammability tests and no ignition occurred when exposed to heat flux typical of developing fires (35 kW/m<sup>2</sup>). In addition, foams coated by 6 BL have been found capable of withstanding the penetration of an impinging flame torch (T surface 950°C), successfully insulating the unexposed side of the sample which temperature remained below 100°C until the end of the

test (5 minutes of flame application). This result was never reported in literature regarding PU foams and is similar to those achieved by silica aerogel which is considered the state of the art in heat shielding. In addition, while silica aerogels are brittle and prone to cracking, the PDAC/GO coated foams retained the mechanical flexibility of substrate. Comparing the results obtained from this thesis and what reported in literature for LbL treated PU foam encompassing nanoparticles and polymers it is apparent that, although substantial reductions of pkHRR (in the range of 60-70%) were previously reported in literature, a minimum number of 10 deposited layers are needed to achieve self-extinguishing behaviour during flammability tests. Conversely, in the present thesis it was shown that 7 deposited layers are enough to self-extinguish the flame in flammability tests and prevent ignition during cone calorimetry tests, which is a unique set of properties never reported before. Furthermore, heat shielded samples can be prepared only depositing a less than 300 nm thick coating at modified ionic strength. The effect of the nanoparticle aspect ratio was also evaluated concluding that the LbL growth depends strongly on the density of functional groups that electrostatically interact with a positive polyelectrolyte and allow to deposit coatings with thicknesses that depends on the nanoparticle dimensions. Moreover, it was demonstrated that the barrier effect towards developed gases depends on the lateral size of nanoparticles; the larger the nanoparticles the higher the nanoparticles overlapping. This feature results in a more efficiently modified tortuosity path that volatiles from the pyrolysis of the polymer substrate have to traverse for reach the surface. Moreover, the decomposition gases can be physisorbed to the high exposed nanoparticle surface. However, the best results were reached by after the addition of a phosphate salt to the graphite oxide suspensions meaning that the presence of just the nanoparticles is not enough to decrease the flammability of polyurethane foams. Obviously, further work could be performed in order to shed light on the fundamental aspects related to the observed properties. Possible strategies involve: i) study the effective thermal shielding effect of graphite oxide nanoparticles, ii) evaluate the decomposition mechanism of neat and treated-PU during combustion.

In order to improve the number of deposited nanoparticles while reducing the number of deposition steps, a new one-step approach where the self-assembly of GRMs on the surface of PU foams is forced by the solvent removal was developed. The proposed deposition technique requires only 3 steps: the activation of the substrate, the deposition of the suspension by wet impregnation and the evaporation of the solvents. Although the obtained results are comparable to LbL, the presented first study about one-pot deposition shows some potentialities under different point of view. Indeed, some advantages with respect to LbL can be potentially achieved from the processing point of view:

- 1- The LbL is a cyclic deposition that needs washing and deposition baths that have to be changed after a certain number of deposition in order to avoid cross-contaminations. In contrast, one-pot deposition limit the amount of waste water solutions and deposition baths. In this configuration, the one-pot procedure appears easier to automatize and

more environmental friendly. Indeed, the solvent employed in the one pot deposition procedure can be simply re-condensed after the evaporation without the need for further purification processes. On the other hand, solvent recovery (from deposition and washing baths) could also be performed for LbL but in this case purification steps are mandatory.

- 2- In the one pot deposition the amount of deposited coatings can be set prior to the deposition. In this manner, it is possible to reach high weight gain (like 100% add-on, as presented in this thesis work) or lower add-on as function of the final application. This would still require only one deposition step. In contrast, the LbL can reach high weight gain only by increasing the number of deposition cycles and limiting practicability of the process.

Graphite nanoplatelets suspensions were employed instead of graphite oxide because of their better film forming ability upon solvent removal. This is related to the surface charge density of graphite nanoplatelets which favors the packing of graphite sheets through a  $\pi$ - $\pi$  stacking. GNP water-based suspensions were employed to coat PU foams considering different grade of exfoliation and yielding morphologies similar to previously developed LbL assemblies. FE-SEM micrographs showed that it is possible to deposit homogenous coating on every exposed surfaces of PU foam using high concentration of GNP (2%wt and 1wt% in phosphate added samples). Treated samples showed melt-dripping suppression, as it was observed for each LbL treated PU foam, and a 50% decrease of the pkHRR. However, only the addition of a phosphate allows for the best performances such as self-extinguishments during flammability tests and thermal shielding properties comparable to state of the art inorganic insulation materials (i.e. silica aerogels). As already observed for LbL systems, the introduction of phosphate salts was required in order to achieve best heat shielding and flame retardant behaviour. Moreover, it seems that there is no correlation between the exfoliation grade and flame retardant performances even when the phosphate salt is added. However, the presence of the phosphate alone does not guarantee sufficient flame retardant properties. The same consideration is valid for just GNP suggesting that the simultaneous presence of the two components is needed for the best results. Looking to the future, could be very interesting study the mechanism behind this synergic effect. Since the presented one pot procedure is a preliminary study, it is reasonable to think of reducing the concentration of used suspensions and evaluating the various effects on weight gain, fire retardancy and mechanical properties.

# References

- [1] A.S. Mayorov, R.V. Gorbachev, S.V. Morozov, L. Britnell, R. Jalil, L.A. Ponomarenko, P. Blake, K.S. Novoselov, K. Watanabe, T. Taniguchi, A.K. Geim, Micrometer-Scale Ballistic Transport in Encapsulated Graphene at Room Temperature, *Nano Letters* 11(6) (2011) 2396-2399.
- [2] A.A. Balandin, Thermal properties of graphene and nanostructured carbon materials, *Nature Materials* 10(8) (2011) 569-581.
- [3] C. Lee, X. Wei, J.W. Kysar, J. Hone, Measurement of the Elastic Properties and Intrinsic Strength of Monolayer Graphene, *Science* 321(5887) (2008) 385.
- [4] J.B. Aladekomo, R.H. Bragg, Structural transformations induced in graphite by grinding: Analysis of 002 X-ray diffraction line profiles, *Carbon* 28(6) (1990) 897-906.
- [5] A. Bianco, H.-M. Cheng, T. Enoki, Y. Gogotsi, R.H. Hurt, N. Koratkar, T. Kyotani, M. Monthioux, C.R. Park, J.M.D. Tascon, J. Zhang, All in the graphene family – A recommended nomenclature for two-dimensional carbon materials, *Carbon* 65 (2013) 1-6.
- [6] P. Wick, A.E. Louw-Gaume, M. Kucki, H.F. Krug, K. Kostarelos, B. Fadeel, K.A. Dawson, A. Salvati, E. Vázquez, L. Ballerini, M. Tretiach, F. Benfenati, E. Flahaut, L. Gauthier, M. Prato, A. Bianco, Classification Framework for Graphene-Based Materials, *Angewandte Chemie International Edition* 53(30) (2014) 7714-7718.
- [7] K.S. Novoselov, A.K. Geim, S.V. Morozov, D. Jiang, Y. Zhang, S.V. Dubonos, I.V. Grigorieva, A.A. Firsov, Electric Field Effect in Atomically Thin Carbon Films, *Science* 306(5696) (2004) 666-669.
- [8] F. Torrisi, T. Hasan, W. Wu, Z. Sun, A. Lombardo, T.S. Kulmala, G.-W. Hsieh, S. Jung, F. Bonaccorso, P.J. Paul, D. Chu, A.C. Ferrari, Inkjet-Printed Graphene Electronics, *ACS Nano* 6(4) (2012) 2992-3006.
- [9] S. Borini, R. White, D. Wei, M. Astley, S. Haque, E. Spigone, N. Harris, J. Kivioja, T. Ryhänen, Ultrafast Graphene Oxide Humidity Sensors, *ACS Nano* 7(12) (2013) 11166-11173.
- [10] S. Basu, P. Bhattacharyya, Recent developments on graphene and graphene oxide based solid state gas sensors, *Sensors and Actuators B: Chemical* 173 (2012) 1-21.
- [11] K.S. Novoselov, D. Jiang, F. Schedin, T.J. Booth, V.V. Khotkevich, S.V. Morozov, A.K. Geim, Two-dimensional atomic crystals, *Proceedings of the National Academy of Sciences of the United States of America* 102(30) (2005) 10451-10453.
- [12] A.C. Ferrari, D.M. Basko, Raman spectroscopy as a versatile tool for studying the properties of graphene, *Nature Nanotechnology* 8 (2013) 235.
- [13] C. Casiraghi, A. Hartschuh, E. Lidorikis, H. Qian, H. Harutyunyan, T. Gokus, K.S. Novoselov, A.C. Ferrari, Rayleigh Imaging of Graphene and Graphene Layers, *Nano Letters* 7(9) (2007) 2711-2717.
- [14] T. Moldt, A. Eckmann, P. Klar, S.V. Morozov, A.A. Zhukov, K.S. Novoselov, C. Casiraghi, High-Yield Production and Transfer of Graphene Flakes Obtained by Anodic Bonding, *ACS Nano* 5(10) (2011) 7700-7706.
- [15] A. Shukla, R. Kumar, J. Mazher, A. Balan, Graphene made easy: High quality, large-area samples, *Solid State Communications* 149(17) (2009) 718-721.

- [16] S. Dhar, A.R. Barman, G.X. Ni, X. Wang, X.F. Xu, Y. Zheng, S. Tripathy, Ariando, A. Rusydi, K.P. Loh, M. Rubhausen, A.H.C. Neto, B. Özyilmaz, T. Venkatesan, A new route to graphene layers by selective laser ablation, *AIP Advances* 1(2) (2011) 022109.
- [17] S. Lee, M.F. Toney, W. Ko, J.C. Randel, H.J. Jung, K. Munakata, J. Lu, T.H. Geballe, M.R. Beasley, R. Sinclair, H.C. Manoharan, A. Salleo, Laser-Synthesized Epitaxial Graphene, *ACS Nano* 4(12) (2010) 7524-7530.
- [18] M. Qian, Y.S. Zhou, Y. Gao, J.B. Park, T. Feng, S.M. Huang, Z. Sun, L. Jiang, Y.F. Lu, Formation of graphene sheets through laser exfoliation of highly ordered pyrolytic graphite, *Applied Physics Letters* 98(17) (2011) 173108.
- [19] A. De Giacomo, A. De Bonis, M. Dell'Aglio, O. De Pascale, R. Gaudiuso, S. Orlando, A. Santagata, G.S. Senesi, F. Taccogna, R. Teghil, Laser Ablation of Graphite in Water in a Range of Pressure from 1 to 146 atm Using Single and Double Pulse Techniques for the Production of Carbon Nanostructures, *The Journal of Physical Chemistry C* 115(12) (2011) 5123-5130.
- [20] C. Backes, T.M. Higgins, A. Kelly, C. Boland, A. Harvey, D. Hanlon, J.N. Coleman, Guidelines for Exfoliation, Characterization and Processing of Layered Materials Produced by Liquid Exfoliation, *Chemistry of Materials* 29(1) (2017) 243-255.
- [21] J.N. Coleman, M. Lotya, A. O'Neill, S.D. Bergin, P.J. King, U. Khan, K. Young, A. Gaucher, S. De, R.J. Smith, I.V. Shvets, S.K. Arora, G. Stanton, H.-Y. Kim, K. Lee, G.T. Kim, G.S. Duesberg, T. Hallam, J.J. Boland, J.J. Wang, J.F. Donegan, J.C. Grunlan, G. Moriarty, A. Shmeliov, R.J. Nicholls, J.M. Perkins, E.M. Grieveson, K. Theuwissen, D.W. McComb, P.D. Nellist, V. Nicolosi, Two-Dimensional Nanosheets Produced by Liquid Exfoliation of Layered Materials, *Science* 331(6017) (2011) 568-571.
- [22] K.R. Paton, E. Varrla, C. Backes, R.J. Smith, U. Khan, A. O'Neill, C. Boland, M. Lotya, O.M. Istrate, P. King, T. Higgins, S. Barwick, P. May, P. Puczkarski, I. Ahmed, M. Moebius, H. Pettersson, E. Long, J. Coelho, S.E. O'Brien, E.K. McGuire, B.M. Sanchez, G.S. Duesberg, N. McEvoy, T.J. Pennycook, C. Downing, A. Crossley, V. Nicolosi, J.N. Coleman, Scalable production of large quantities of defect-free few-layer graphene by shear exfoliation in liquids, *Nature Materials* 13 (2014) 624.
- [23] C. Backes, B.M. Szydłowska, A. Harvey, S. Yuan, V. Vega-Mayoral, B.R. Davies, P.-l. Zhao, D. Hanlon, E.J.G. Santos, M.I. Katsnelson, W.J. Blau, C. Gadermaier, J.N. Coleman, Production of Highly Monolayer Enriched Dispersions of Liquid-Exfoliated Nanosheets by Liquid Cascade Centrifugation, *ACS Nano* 10(1) (2016) 1589-1601.
- [24] J.D. Bernal, W.L. Bragg, The structure of graphite, *Proceedings of the Royal Society of London. Series A, Containing Papers of a Mathematical and Physical Character* 106(740) (1924) 749-773.
- [25] R.E. Franklin, J.T. Randall, Crystallite growth in graphitizing and non-graphitizing carbons, *Proceedings of the Royal Society of London. Series A. Mathematical and Physical Sciences* 209(1097) (1951) 196-218.
- [26] G.C. Loh, D. Baillargeat, Graphitization of amorphous carbon and its transformation pathways, *Journal of Applied Physics* 114(3) (2013) 033534.
- [27] X. Li, C.W. Magnuson, A. Venugopal, R.M. Tromp, J.B. Hannon, E.M. Vogel, L. Colombo, R.S. Ruoff, Large-Area Graphene Single Crystals Grown by Low-Pressure Chemical Vapor Deposition of Methane on Copper, *Journal of the American Chemical Society* 133(9) (2011) 2816-2819.

- [28] J.K. Wassei, M. Mecklenburg, J.A. Torres, J.D. Fowler, B.C. Regan, R.B. Kaner, B.H. Weiller, Chemical Vapor Deposition of Graphene on Copper from Methane, Ethane and Propane: Evidence for Bilayer Selectivity, *Small* 8(9) (2012) 1415-1422.
- [29] L. Sun, B. Fugetsu, Mass production of graphene oxide from expanded graphite, *Materials Letters* 109 (2013) 207-210.
- [30] M.S. Dresselhaus, G. Dresselhaus, Intercalation compounds of graphite, *Advances in Physics* 30(2) (1981) 139-326.
- [31] M. Inagaki, Applications of graphite intercalation compounds, *Journal of Materials Research* 4(6) (2011) 1560-1568.
- [32] W. Zhao, P.H. Tan, J. Liu, A.C. Ferrari, Intercalation of Few-Layer Graphite Flakes with FeCl<sub>3</sub>: Raman Determination of Fermi Level, Layer by Layer Decoupling, and Stability, *Journal of the American Chemical Society* 133(15) (2011) 5941-5946.
- [33] M.S. Dresselhaus, G. Dresselhaus, Intercalation compounds of graphite, *Advances in Physics* 51(1) (2002) 1-186.
- [34] P.K. Ang, S. Wang, Q. Bao, J.T.L. Thong, K.P. Loh, High-Throughput Synthesis of Graphene by Intercalation-Exfoliation of Graphite Oxide and Study of Ionic Screening in Graphene Transistor, *ACS Nano* 3(11) (2009) 3587-3594.
- [35] W.S. Hummers, R.E. Offeman, Preparation of Graphitic Oxide, *Journal of the American Chemical Society* 80(6) (1958) 1339-1339.
- [36] C.-Y. Su, Y. Xu, W. Zhang, J. Zhao, X. Tang, C.-H. Tsai, L.-J. Li, Electrical and Spectroscopic Characterizations of Ultra-Large Reduced Graphene Oxide Monolayers, *Chemistry of Materials* 21(23) (2009) 5674-5680.
- [37] P. Matyba, H. Yamaguchi, G. Eda, M. Chhowalla, L. Edman, N.D. Robinson, Graphene and Mobile Ions: The Key to All-Plastic, Solution-Processed Light-Emitting Devices, *ACS Nano* 4(2) (2010) 637-642.
- [38] X. Sun, Z. Liu, K. Welsher, J.T. Robinson, A. Goodwin, S. Zaric, H. Dai, Nano-graphene oxide for cellular imaging and drug delivery, *Nano Research* 1(3) (2008) 203-212.
- [39] Z. Bo, X. Shuai, S. Mao, H. Yang, J. Qian, J. Chen, J. Yan, K. Cen, Green preparation of reduced graphene oxide for sensing and energy storage applications, *Scientific Reports* 4 (2014) 4684.
- [40] D.R. Dreyer, S. Murali, Y. Zhu, R.S. Ruoff, C.W. Bielawski, Reduction of graphite oxide using alcohols, *Journal of Materials Chemistry* 21(10) (2011) 3443-3447.
- [41] S. Eigler, S. Grimm, M. Enzelberger-Heim, P. Müller, A. Hirsch, Graphene oxide: efficiency of reducing agents, *Chemical Communications* 49(67) (2013) 7391-7393.
- [42] M. Agharkar, S. Kochrekar, S. Hidouri, M. Azeez, Trends in green reduction of graphene oxides, issues and challenges: A review, *Materials Research Bulletin* 59 (2014) 323-328.
- [43] C.K. Chua, M. Pumera, Chemical reduction of graphene oxide: a synthetic chemistry viewpoint, *Chemical Society Reviews* 43(1) (2014) 291-312.
- [44] J. Gómez, E. Villaro, A. Navas, I. Recio, Testing the influence of the temperature, RH and filler type and content on the universal power law for new reduced graphene oxide TPU composites, *Materials Research Express* 4(10) (2017) 105020.
- [45] M. Acik, G. Lee, C. Mattevi, A. Pirkle, R.M. Wallace, M. Chhowalla, K. Cho, Y. Chabal, The Role of Oxygen during Thermal Reduction of Graphene

- Oxide Studied by Infrared Absorption Spectroscopy, *The Journal of Physical Chemistry C* 115(40) (2011) 19761-19781.
- [46] C.-Y. Su, Y. Xu, W. Zhang, J. Zhao, A. Liu, X. Tang, C.-H. Tsai, Y. Huang, L.-J. Li, Highly Efficient Restoration of Graphitic Structure in Graphene Oxide Using Alcohol Vapors, *ACS Nano* 4(9) (2010) 5285-5292.
- [47] J.N. Coleman, Liquid Exfoliation of Defect-Free Graphene, *Accounts of Chemical Research* 46(1) (2013) 14-22.
- [48] S. Niyogi, M.A. Hamon, D.E. Perea, C.B. Kang, B. Zhao, S.K. Pal, A.E. Wyant, M.E. Itkis, R.C. Haddon, Ultrasonic Dispersions of Single-Walled Carbon Nanotubes, *The Journal of Physical Chemistry B* 107(34) (2003) 8799-8804.
- [49] H.C. Yau, M.K. Bayazit, J.H.G. Steinke, M.S.P. Shaffer, Sonochemical degradation of N-methylpyrrolidone and its influence on single walled carbon nanotube dispersion, *Chemical Communications* 51(93) (2015) 16621-16624.
- [50] H.M. Solomon, B.A. Burgess, G.L. Kennedy, R.E. Staples, 1-methyl-2-pyrrolidone (nmp): reproductive and developmental toxicity study by inhalation in the rat, *Drug and Chemical Toxicology* 18(4) (1995) 271-293.
- [51] A. Ciesielski, P. Samori, Graphene via sonication assisted liquid-phase exfoliation, *Chemical Society Reviews* 43(1) (2014) 381-398.
- [52] L. Guardia, M.J. Fernández-Merino, J.I. Paredes, P. Solís-Fernández, S. Villar-Rodil, A. Martínez-Alonso, J.M.D. Tascon, High-throughput production of pristine graphene in an aqueous dispersion assisted by non-ionic surfactants, *Carbon* 49(5) (2011) 1653-1662.
- [53] A.A. Green, M.C. Hersam, Solution Phase Production of Graphene with Controlled Thickness via Density Differentiation, *Nano Letters* 9(12) (2009) 4031-4036.
- [54] M. Lotya, Y. Hernandez, P.J. King, R.J. Smith, V. Nicolosi, L.S. Karlsson, F.M. Blighe, S. De, Z. Wang, I.T. McGovern, G.S. Duesberg, J.N. Coleman, Liquid Phase Production of Graphene by Exfoliation of Graphite in Surfactant/Water Solutions, *Journal of the American Chemical Society* 131(10) (2009) 3611-3620.
- [55] M. Yi, Z. Shen, A review on mechanical exfoliation for the scalable production of graphene, *Journal of Materials Chemistry A* 3(22) (2015) 11700-11715.
- [56] H. Tao, Y. Zhang, Y. Gao, Z. Sun, C. Yan, J. Texter, Scalable exfoliation and dispersion of two-dimensional materials – an update, *Physical Chemistry Chemical Physics* 19(2) (2017) 921-960.
- [57] F. Bonaccorso, A. Bartolotta, J.N. Coleman, C. Backes, 2D-Crystal-Based Functional Inks, *Advanced Materials* 28(29) (2016) 6136-6166.
- [58] K. Parvez, S. Yang, X. Feng, K. Müllen, Exfoliation of graphene via wet chemical routes, *Synthetic Metals* 210 (2015) 123-132.
- [59] A. Liscio, K. Kouroupis-Agalou, A. Kovtun, E. Gebremedhn, M. El Garah, W. Rekab, E. Orgiu, L. Giorgini, P. Samori, D. Beljonne, V. Palermo, Exfoliation of Few-Layer Graphene in Volatile Solvents Using Aromatic Perylene Diimide Derivatives as Surfactants, *ChemPlusChem* 82(3) (2017) 358-367.
- [60] A. Schlierf, H. Yang, E. Gebremedhn, E. Treossi, L. Ortolani, L. Chen, A. Minoia, V. Morandi, P. Samori, C. Casiraghi, D. Beljonne, V. Palermo, Nanoscale insight into the exfoliation mechanism of graphene with organic dyes: effect of charge, dipole and molecular structure, *Nanoscale* 5(10) (2013) 4205-4216.
- [61] D. Nuvoli, L. Valentini, V. Alzari, S. Scognamillo, S.B. Bon, M. Piccinini, J. Illescas, A. Mariani, High concentration few-layer graphene sheets obtained by

- liquid phase exfoliation of graphite in ionic liquid, *Journal of Materials Chemistry* 21(10) (2011) 3428-3431.
- [62] X. Wang, P.F. Fulvio, G.A. Baker, G.M. Veith, R.R. Unocic, S.M. Mahurin, M. Chi, S. Dai, Direct exfoliation of natural graphite into micrometre size few layers graphene sheets using ionic liquids, *Chemical Communications* 46(25) (2010) 4487-4489.
- [63] M. Jafari, Y. He, B. Bhandari, Production of sub-micron emulsions by ultrasound and microfluidization techniques, *Journal of Food Engineering* 82 (2007) 478-488.
- [64] I. Agerkvist, S.-O. Enfors, Characterization of *E. coli* cell disintegrates from a bead mill and high pressure homogenizers, *Biotechnology and Bioengineering* 36(11) (1990) 1083-1089.
- [65] P.G. Karagiannidis, S.A. Hodge, L. Lombardi, F. Tomarchio, N. Decorde, S. Milana, I. Goykhman, Y. Su, S.V. Mesite, D.N. Johnstone, R.K. Leary, P.A. Midgley, N.M. Pugno, F. Torrisi, A.C. Ferrari, Microfluidization of Graphite and Formulation of Graphene-Based Conductive Inks, *ACS Nano* 11(3) (2017) 2742-2755.
- [66] K.R. Paton, J. Anderson, A.J. Pollard, T. Sainsbury, Production of few-layer graphene by microfluidization, *Materials Research Express* 4(2) (2017) 025604.
- [67] E.G. Acheson, manufacture of graphite, USA, 1865.
- [68] A.J. Van Bommel, J.E. Crombeen, A. Van Tooren, LEED and Auger electron observations of the SiC(0001) surface, *Surface Science* 48(2) (1975) 463-472.
- [69] C. Berger, Z. Song, T. Li, X. Li, A.Y. Ogbazghi, R. Feng, Z. Dai, A.N. Marchenkov, E.H. Conrad, P.N. First, W.A. de Heer, Ultrathin Epitaxial Graphite: 2D Electron Gas Properties and a Route toward Graphene-based Nanoelectronics, *The Journal of Physical Chemistry B* 108(52) (2004) 19912-19916.
- [70] K.V. Emtsev, A. Bostwick, K. Horn, J. Jobst, G.L. Kellogg, L. Ley, J.L. McChesney, T. Ohta, S.A. Reshanov, J. Röhrl, E. Rotenberg, A.K. Schmid, D. Waldmann, H.B. Weber, T. Seyller, Towards wafer-size graphene layers by atmospheric pressure graphitization of silicon carbide, *Nature Materials* 8(3) (2009) 203-207.
- [71] C. Riedl, C. Coletti, T. Iwasaki, A.A. Zakharov, U. Starke, Quasi-Free-Standing Epitaxial Graphene on SiC Obtained by Hydrogen Intercalation, *Physical Review Letters* 103(24) (2009) 246804.
- [72] W.A. de Heer, C. Berger, M. Ruan, M. Sprinkle, X. Li, Y. Hu, B. Zhang, J. Hankinson, E. Conrad, Large area and structured epitaxial graphene produced by confinement controlled sublimation of silicon carbide, *Proceedings of the National Academy of Sciences* 108(41) (2011) 16900-16905.
- [73] K.V. Emtsev, F. Speck, T. Seyller, L. Ley, J.D. Riley, Interaction, growth, and ordering of epitaxial graphene on SiC{0001} surfaces: A comparative photoelectron spectroscopy study, *Physical Review B* 77(15) (2008) 155303.
- [74] X. Li, W. Cai, J. An, S. Kim, J. Nah, D. Yang, R. Piner, A. Velamakanni, I. Jung, E. Tutuc, S.K. Banerjee, L. Colombo, R.S. Ruoff, Large-Area Synthesis of High-Quality and Uniform Graphene Films on Copper Foils, *Science* 324(5932) (2009) 1312-1314.
- [75] D. Yoon, Y.-W. Son, H. Cheong, Negative Thermal Expansion Coefficient of Graphene Measured by Raman Spectroscopy, *Nano Letters* 11(8) (2011) 3227-3231.
- [76] T. Kobayashi, M. Bando, N. Kimura, K. Shimizu, K. Kadono, N. Umezu, K. Miyahara, S. Hayazaki, S. Nagai, Y. Mizuguchi, Y. Murakami, D. Hobara,

Production of a 100-m-long high-quality graphene transparent conductive film by roll-to-roll chemical vapor deposition and transfer process, *Applied Physics Letters* 102 (2013).

- [77] A.T.H. Chuang, J. Robertson, B.O. Boskovic, K.K.K. Koziol, Three-dimensional carbon nanowall structures, *Applied Physics Letters* 90(12) (2007) 123107.
- [78] A. Narita, X.-Y. Wang, X. Feng, K. Müllen, New advances in nanographene chemistry, *Chemical Society Reviews* 44(18) (2015) 6616-6643.
- [79] X.-Y. Wang, A. Narita, K. Müllen, Precision synthesis versus bulk-scale fabrication of graphenes, *Nature Reviews Chemistry* 2 (2017) 0100.
- [80] L. Dössel, L. Gherghel, X. Feng, K. Müllen, Graphene Nanoribbons by Chemists: Nanometer-Sized, Soluble, and Defect-Free, *Angewandte Chemie International Edition* 50(11) (2011) 2540-2543.
- [81] M.G. Schwab, A. Narita, Y. Hernandez, T. Balandina, K.S. Mali, S. De Feyter, X. Feng, K. Müllen, Structurally Defined Graphene Nanoribbons with High Lateral Extension, *Journal of the American Chemical Society* 134(44) (2012) 18169-18172.
- [82] L. Talirz, P. Ruffieux, R. Fasel, On-Surface Synthesis of Atomically Precise Graphene Nanoribbons, *Advanced Materials* 28(29) (2016) 6222-6231.
- [83] L. Talirz, H. Söde, T. Dumslaff, S. Wang, J.R. Sanchez-Valencia, J. Liu, P. Shinde, C.A. Pignedoli, L. Liang, V. Meunier, N.C. Plumb, M. Shi, X. Feng, A. Narita, K. Müllen, R. Fasel, P. Ruffieux, On-Surface Synthesis and Characterization of 9-Atom Wide Armchair Graphene Nanoribbons, *ACS Nano* 11(2) (2017) 1380-1388.
- [84] J. Cai, C.A. Pignedoli, L. Talirz, P. Ruffieux, H. Söde, L. Liang, V. Meunier, R. Berger, R. Li, X. Feng, K. Müllen, R. Fasel, Graphene nanoribbon heterojunctions, *Nature Nanotechnology* 9 (2014) 896.
- [85] P. Ruffieux, S. Wang, B. Yang, C. Sánchez-Sánchez, J. Liu, T. Dienel, L. Talirz, P. Shinde, C.A. Pignedoli, D. Passerone, T. Dumslaff, X. Feng, K. Müllen, R. Fasel, On-surface synthesis of graphene nanoribbons with zigzag edge topology, *Nature* 531 (2016) 489.
- [86] D.G. de Oteyza, A. García-Lekue, M. Vilas-Varela, N. Merino-Díez, E. Carbonell-Sanromà, M. Corso, G. Vasseur, C. Rogero, E. Gutián, J.I. Pascual, J.E. Ortega, Y. Wakayama, D. Peña, Substrate-Independent Growth of Atomically Precise Chiral Graphene Nanoribbons, *ACS Nano* 10(9) (2016) 9000-9008.
- [87] H. Huang, D. Wei, J. Sun, S.L. Wong, Y.P. Feng, A.H.C. Neto, A.T.S. Wee, Spatially Resolved Electronic Structures of Atomically Precise Armchair Graphene Nanoribbons, *Scientific Reports* 2 (2012) 983.
- [88] J. Cai, P. Ruffieux, R. Jaafar, M. Bieri, T. Braun, S. Blankenburg, M. Muoth, A.P. Seitsonen, M. Saleh, X. Feng, K. Müllen, R. Fasel, Atomically precise bottom-up fabrication of graphene nanoribbons, *Nature* 466(7305) (2010) 470-473.
- [89] A. Turchanin, A. Gölzhäuser, Carbon Nanomembranes, *Advanced Materials* 28(29) (2016) 6075-6103.
- [90] A. Turchanin, D. Käfer, M. El-Desawy, C. Wöll, G. Witte, A. Gölzhäuser, Molecular Mechanisms of Electron-Induced Cross-Linking in Aromatic SAMs, *Langmuir* 25(13) (2009) 7342-7352.
- [91] J.C. Love, L.A. Estroff, J.K. Kriebel, R.G. Nuzzo, G.M. Whitesides, Self-Assembled Monolayers of Thiolates on Metals as a Form of Nanotechnology, *Chemical Reviews* 105(4) (2005) 1103-1170.

- [92] P. Angelova, H. Vieker, N.-E. Weber, D. Matei, O. Reimer, I. Meier, S. Kurasch, J. Biskupek, D. Lorbach, K. Wunderlich, L. Chen, A. Terfort, M. Klapper, K. Müllen, U. Kaiser, A. Gölzhäuser, A. Turchanin, A Universal Scheme to Convert Aromatic Molecular Monolayers into Functional Carbon Nanomembranes, *ACS Nano* 7(8) (2013) 6489-6497.
- [93] D.G. Matei, H. Muzik, A. Gölzhäuser, A. Turchanin, Structural Investigation of 1,1'-Biphenyl-4-thiol Self-Assembled Monolayers on Au(111) by Scanning Tunneling Microscopy and Low-Energy Electron Diffraction, *Langmuir* 28(39) (2012) 13905-13911.
- [94] W. Geyer, V. Stadler, W. Eck, M. Zharnikov, A. Gölzhäuser, M. Grunze, Electron-induced crosslinking of aromatic self-assembled monolayers: Negative resists for nanolithography, *Applied Physics Letters* 75(16) (1999) 2401-2403.
- [95] A. Turchanin, A. Gölzhäuser, Carbon nanomembranes from self-assembled monolayers: Functional surfaces without bulk, *Progress in Surface Science* 87(5) (2012) 108-162.
- [96] A. Turchanin, A. Beyer, C.T. Nottbohm, X. Zhang, R. Stosch, A. Sologubenko, J. Mayer, P. Hinze, T. Weimann, A. Gölzhäuser, One Nanometer Thin Carbon Nanosheets with Tunable Conductivity and Stiffness, *Advanced Materials* 21(12) (2009) 1233-1237.
- [97] C.T. Nottbohm, A. Turchanin, A. Beyer, R. Stosch, A. Gölzhäuser, Mechanically Stacked 1-nm-Thick Carbon Nanosheets: Ultrathin Layered Materials with Tunable Optical, Chemical, and Electrical Properties, *Small* 7(7) (2011) 874-883.
- [98] D. Rhinow, N.-E. Weber, A. Turchanin, Atmospheric Pressure, Temperature-Induced Conversion of Organic Monolayers into Nanocrystalline Graphene, *The Journal of Physical Chemistry C* 116(22) (2012) 12295-12303.
- [99] A.C. Ferrari, F. Bonaccorso, V. Fal'ko, K.S. Novoselov, S. Roche, P. Bøggild, S. Borini, F.H.L. Koppens, V. Palermo, N. Pugno, J.A. Garrido, R. Sordan, A. Bianco, L. Ballerini, M. Prato, E. Lidorikis, J. Kivioja, C. Marinelli, T. Ryhänen, A. Morpurgo, J.N. Coleman, V. Nicolosi, L. Colombo, A. Fert, M. Garcia-Hernandez, A. Bachtold, G.F. Schneider, F. Guinea, C. Dekker, M. Barbone, Z. Sun, C. Gallois, A.N. Grigorenko, G. Konstantatos, A. Kis, M. Katsnelson, L. Vandersypen, A. Loiseau, V. Morandi, D. Neumaier, E. Treossi, V. Pellegrini, M. Polini, A. Tredicucci, G.M. Williams, B. Hee Hong, J.-H. Ahn, J. Min Kim, H. Zirath, B.J. van Wees, H. van der Zant, L. Occhipinti, A. Di Matteo, I.A. Kinloch, T. Seyller, E. Quesnel, X. Feng, K. Teo, N. Rupesinghe, P. Hakonen, S.R.T. Neil, Q. Tannock, T. Löfwander, J. Kinaret, Science and technology roadmap for graphene, related two-dimensional crystals, and hybrid systems, *Nanoscale* 7(11) (2015) 4598-4810.
- [100] F.a. Sullivan, Global Graphene Market, Forecast to 2025, Europe, 2017.
- [101] J. Ma, D. Alfè, A. Michaelides, E. Wang, Stone-Wales defects in graphene and other planar  $\$s\{p\}^2\$$ -bonded materials, *Physical Review B* 80(3) (2009) 033407.
- [102] L. Li, S. Reich, J. Robertson, Defect energies of graphite: Density-functional calculations, *Physical Review B* 72(18) (2005) 184109.
- [103] T. Xu, L. Sun, 5 - Structural defects in graphene, in: J. Stehr, I. Buyanova, W. Chen (Eds.), *Defects in Advanced Electronic Materials and Novel Low Dimensional Structures*, Woodhead Publishing2018, pp. 137-160.
- [104] J.C. Meyer, C. Kisielowski, R. Erni, M.D. Rossell, M.F. Crommie, A. Zettl, Topological Defects in Graphene MembranesDirect Imaging of Lattice Atoms and Nano Letters 8(11) (2008) 3582-3586.

- [105] H.A. Jahn, E. Teller, F.G. Donnan, Stability of polyatomic molecules in degenerate electronic states - I;Orbital degeneracy, Proceedings of the Royal Society of London. Series A - Mathematical and Physical Sciences 161(905) (1937) 220-235.
- [106] A.A. El-Barbary, R.H. Telling, C.P. Ewels, M.I. Heggie, P.R. Briddon, Structure and energetics of the vacancy in graphite, Physical Review B 68(14) (2003) 144107.
- [107] Ç.Ö. Girit, J.C. Meyer, R. Erni, M.D. Rossell, C. Kisielowski, L. Yang, C.-H. Park, M.F. Crommie, M.L. Cohen, S.G. Louie, A. Zettl, Graphene at the Edge: Stability and Dynamics, Science 323(5922) (2009) 1705-1708.
- [108] K. Nakada, A. Ishii, Migration of adatom adsorption on graphene using DFT calculation, Solid State Communications 151(1) (2011) 13-16.
- [109] A.V. Krasheninnikov, P.O. Lehtinen, A.S. Foster, P. Pyykkö, R.M. Nieminen, Embedding Transition-Metal Atoms in Graphene: Structure, Bonding, and Magnetism, Physical Review Letters 102(12) (2009) 126807.
- [110] B.W. Jeong, J. Ihm, G.-D. Lee, Stability of dislocation defect with two pentagon-heptagon pairs in graphene, Physical Review B 78(16) (2008) 165403.
- [111] J. Lahiri, Y. Lin, P. Bozkurt, I.I. Oleynik, M. Batzill, An extended defect in graphene as a metallic wire, Nature Nanotechnology 5(5) (2010) 326-329.
- [112] S. Kurasch, J. Kotakoski, O. Lehtinen, V. Skákalová, J. Smet, C.E. Krill, A.V. Krasheninnikov, U. Kaiser, Atom-by-Atom Observation of Grain Boundary Migration in Graphene, Nano Letters 12(6) (2012) 3168-3173.
- [113] S.N. Shirodkar, U.V. Waghmare, Electronic and vibrational signatures of Stone-Wales defects in graphene: First-principles analysis, Physical Review B 86(16) (2012) 165401.
- [114] M. Topsakal, E. Aktürk, H. Sevinçli, S. Ciraci, First-principles approach to monitoring the band gap and magnetic state of a graphene nanoribbon via its vacancies, Physical Review B 78(23) (2008) 235435.
- [115] F. Banhart, J. Kotakoski, A.V. Krasheninnikov, Structural Defects in Graphene, ACS Nano 5(1) (2011) 26-41.
- [116] D. Nika, Graphene Thermal Properties: Applications in Thermal Management and Energy Storage, Applied Sciences 4 (2014) 525.
- [117] S.E. Krasavin, V.A. Osipov, Effect of Stone–Wales defects on the thermal conductivity of graphene, Journal of Physics: Condensed Matter 27(42) (2015) 425302.
- [118] F. Hao, D. Fang, Z. Xu, Mechanical and thermal transport properties of graphene with defects, Applied Physics Letters 99(4) (2011) 041901.
- [119] B. Mortazavi, S. Ahzi, Thermal conductivity and tensile response of defective graphene: A molecular dynamics study, Carbon 63 (2013) 460-470.
- [120] M.M. Bernal, A. Di Pierro, C. Novara, F. Giorgis, B. Mortazavi, G. Saracco, A. Fina, Edge-Grafted Molecular Junctions between Graphene Nanoplatelets: Applied Chemistry to Enhance Heat Transfer in Nanomaterials, Advanced Functional Materials 28(18) (2018) 1706954.
- [121] M. Tortello, S. Colonna, M. Bernal, J. Gomez, M. Pavese, C. Novara, F. Giorgis, M. Maggio, G. Guerra, G. Saracco, R.S. Gonnelli, A. Fina, Effect of thermal annealing on the heat transfer properties of reduced graphite oxide flakes: A nanoscale characterization via scanning thermal microscopy, Carbon 109 (2016) 390-401.
- [122] S. Yadav, Z. Zhu, C.V. Singh, Defect engineering of graphene for effective hydrogen storage, International Journal of Hydrogen Energy 39(10) (2014) 4981-4995.

- [123] E.J. Duplock, M. Scheffler, P.J.D. Lindan, Hallmark of Perfect Graphene, *Physical Review Letters* 92(22) (2004) 225502.
- [124] D. Datta, J. Li, N. Koratkar, V.B. Shenoy, Enhanced lithiation in defective graphene, *Carbon* 80 (2014) 305-310.
- [125] D. Datta, J. Li, V.B. Shenoy, Defective Graphene as a High-Capacity Anode Material for Na- and Ca-Ion Batteries, *ACS Applied Materials & Interfaces* 6(3) (2014) 1788-1795.
- [126] V. Georgakilas, M. Otyepka, A.B. Bourlinos, V. Chandra, N. Kim, K.C. Kemp, P. Hobza, R. Zboril, K.S. Kim, Functionalization of Graphene: Covalent and Non-Covalent Approaches, Derivatives and Applications, *Chemical Reviews* 112(11) (2012) 6156-6214.
- [127] J.S. Bunch, S.S. Verbridge, J.S. Alden, A.M. van der Zande, J.M. Parpia, H.G. Craighead, P.L. McEuen, Impermeable Atomic Membranes from Graphene Sheets, *Nano Letters* 8(8) (2008) 2458-2462.
- [128] O. Leenaerts, B. Partoens, F.M. Peeters, Graphene: A perfect nanoballoon, *Applied Physics Letters* 93(19) (2008) 193107.
- [129] V. Berry, Impermeability of graphene and its applications, *Carbon* 62 (2013) 1-10.
- [130] L.M. Robeson, The upper bound revisited, *Journal of Membrane Science* 320(1) (2008) 390-400.
- [131] H. Suda, K. Haraya, Gas Permeation through Micropores of Carbon Molecular Sieve Membranes Derived from Kapton Polyimide, *The Journal of Physical Chemistry B* 101(20) (1997) 3988-3994.
- [132] N. Kirkland, T. Schiller, N. Medhekar, N. Birbilis, Exploring graphene as a corrosion protection barrier, *Corrosion Science* 56 (2012) 1-4.
- [133] D. Prasai, J.C. Tuberquia, R.R. Harl, G.K. Jennings, K.I. Bolotin, Graphene: Corrosion-Inhibiting Coating, *ACS Nano* 6(2) (2012) 1102-1108.
- [134] L. Nilsson, M. Andersen, R. Balog, E. Lægsgaard, P. Hofmann, F. Besenbacher, B. Hammer, I. Stensgaard, L. Hornekær, Graphene Coatings: Probing the Limits of the One Atom Thick Protection Layer, *ACS Nano* 6(11) (2012) 10258-10266.
- [135] S. Chen, L. Brown, M. Levendorf, W. Cai, S.-Y. Ju, J. Edgeworth, X. Li, C.W. Magnuson, A. Velamakanni, R.D. Piner, J. Kang, J. Park, R.S. Ruoff, Oxidation Resistance of Graphene-Coated Cu and Cu/Ni Alloy, *ACS Nano* 5(2) (2011) 1321-1327.
- [136] D. Kang, J.Y. Kwon, H. Cho, J.-H. Sim, H.S. Hwang, C.S. Kim, Y.J. Kim, R.S. Ruoff, H.S. Shin, Oxidation Resistance of Iron and Copper Foils Coated with Reduced Graphene Oxide Multilayers, *ACS Nano* 6(9) (2012) 7763-7769.
- [137] R.K. Singh Raman, P. Chakraborty Banerjee, D.E. Lobo, H. Gullapalli, M. Sumandasa, A. Kumar, L. Choudhary, R. Tkacz, P.M. Ajayan, M. Majumder, Protecting copper from electrochemical degradation by graphene coating, *Carbon* 50(11) (2012) 4040-4045.
- [138] D.-e. Jiang, V.R. Cooper, S. Dai, Porous Graphene as the Ultimate Membrane for Gas Separation, *Nano Letters* 9(12) (2009) 4019-4024.
- [139] I. Jung, M. Vaupel, M. Pelton, R. Piner, D.A. Dikin, S. Stankovich, J. An, R.S. Ruoff, Characterization of Thermally Reduced Graphene Oxide by Imaging Ellipsometry, *The Journal of Physical Chemistry C* 112(23) (2008) 8499-8506.
- [140] Z. Luo, Y. Lu, L.A. Somers, A.T.C. Johnson, High Yield Preparation of Macroscopic Graphene Oxide Membranes, *Journal of the American Chemical Society* 131(3) (2009) 898-899.

- [141] D.R. Paul, Creating New Types of Carbon-Based Membranes, *Science* 335(6067) (2012) 413-414.
- [142] N.V. Medhekar, A. Ramasubramaniam, R.S. Ruoff, V.B. Shenoy, Hydrogen Bond Networks in Graphene Oxide Composite Paper: Structure and Mechanical Properties, *ACS Nano* 4(4) (2010) 2300-2306.
- [143] S.N. Tripathi, G.S.S. Rao, A.B. Mathur, R. Jasra, Polyolefin/graphene nanocomposites: a review, *RSC Advances* 7(38) (2017) 23615-23632.
- [144] Y.S. Hu, V. Pratipati, S. Mehta, D.A. Schiraldi, A. Hiltner, E. Baer, Improving gas barrier of PET by blending with aromatic polyamides, *Polymer* 46(8) (2005) 2685-2698.
- [145] J. Lange, Y. Wyser, Recent innovations in barrier technologies for plastic packaging—a review, *Packaging Technology and Science* 16(4) (2003) 149-158.
- [146] T. Kuilla, S. Bhadra, D. Yao, N.H. Kim, S. Bose, J.H. Lee, Recent advances in graphene based polymer composites, *Progress in Polymer Science* 35(11) (2010) 1350-1375.
- [147] H. Kim, H. Thomas Hahn, L.M. Viculis, S. Gilje, R.B. Kaner, Electrical conductivity of graphite/polystyrene composites made from potassium intercalated graphite, *Carbon* 45(7) (2007) 1578-1582.
- [148] R. Sengupta, M. Bhattacharya, S. Bandyopadhyay, A.K. Bhowmick, A review on the mechanical and electrical properties of graphite and modified graphite reinforced polymer composites, *Progress in Polymer Science* 36(5) (2011) 638-670.
- [149] J. Du, H.-M. Cheng, The Fabrication, Properties, and Uses of Graphene/Polymer Composites, *Macromolecular Chemistry and Physics* 213(10-11) (2012) 1060-1077.
- [150] K.K. Sadasivuni, D. Ponnamma, S. Thomas, Y. Grohens, Evolution from graphite to graphene elastomer composites, *Progress in Polymer Science* 39(4) (2014) 749-780.
- [151] M.N. Ismail, A.I. Khalaf, Styrene–butadiene rubber/graphite powder composites: Rheometrical, physicomechanical, and morphological properties, *Journal of Applied Polymer Science* 120(1) (2011) 298-304.
- [152] J. Yang, M. Tian, Q.-X. Jia, L.-Q. Zhang, X.-L. Li, Influence of graphite particle size and shape on the properties of NBR, *Journal of Applied Polymer Science* 102(4) (2006) 4007-4015.
- [153] L.E. Nielsen, Models for the Permeability of Filled Polymer Systems, *Journal of Macromolecular Science: Part A - Chemistry* 1(5) (1967) 929-942.
- [154] H. Heller, R. Keren, Rheology of Na-Rich Montmorillonite Suspension as Affected by Electrolyte Concentration and Shear Rate, *Clays and Clay Minerals* 49(4) (2001) 286-291.
- [155] B.M. Yoo, H.J. Shin, H.W. Yoon, H.B. Park, Graphene and graphene oxide and their uses in barrier polymers, *Journal of Applied Polymer Science* 131(1) (2014).
- [156] K. Kalaitzidou, H. Fukushima, L.T. Drzal, Multifunctional polypropylene composites produced by incorporation of exfoliated graphite nanoplatelets, *Carbon* 45(7) (2007) 1446-1452.
- [157] A. Al-Jabareen, H. Al-Bustami, H. Harel, G. Marom, Improving the oxygen barrier properties of polyethylene terephthalate by graphite nanoplatelets, *Journal of Applied Polymer Science* 128(3) (2013) 1534-1539.
- [158] H.-D. Huang, P.-G. Ren, J. Chen, W.-Q. Zhang, X. Ji, Z.-M. Li, High barrier graphene oxide nanosheet/poly(vinyl alcohol) nanocomposite films, *Journal of Membrane Science* 409-410 (2012) 156-163.

- [159] S.H. Shim, K.T. Kim, J.U. Lee, W.H. Jo, Facile Method to Functionalize Graphene Oxide and Its Application to Poly(ethylene terephthalate)/Graphene Composite, *ACS Applied Materials & Interfaces* 4(8) (2012) 4184-4191.
- [160] S. Morimune, T. Nishino, T. Goto, Ecological Approach to Graphene Oxide Reinforced Poly (methyl methacrylate) Nanocomposites, *ACS Applied Materials & Interfaces* 4(7) (2012) 3596-3601.
- [161] K.-C. Chang, W.-F. Ji, M.-C. Lai, Y.-R. Hsiao, C.-H. Hsu, T.-L. Chuang, Y. Wei, J.-M. Yeh, W.-R. Liu, Synergistic effects of hydrophobicity and gas barrier properties on the anticorrosion property of PMMA nanocomposite coatings embedded with graphene nanosheets, *Polymer Chemistry* 5(3) (2014) 1049-1056.
- [162] J.-T. Chen, Y.-J. Fu, Q.-F. An, S.-C. Lo, Y.-Z. Zhong, C.-C. Hu, K.-R. Lee, J.-Y. Lai, Enhancing polymer/graphene oxide gas barrier film properties by introducing new crystals, *Carbon* 75 (2014) 443-451.
- [163] H.-D. Huang, P.-G. Ren, J.-Z. Xu, L. Xu, G.-J. Zhong, B.S. Hsiao, Z.-M. Li, Improved barrier properties of poly(lactic acid) with randomly dispersed graphene oxide nanosheets, *Journal of Membrane Science* 464 (2014) 110-118.
- [164] Y. Cui, S.I. Kundalwal, S. Kumar, Gas barrier performance of graphene/polymer nanocomposites, *Carbon* 98 (2016) 313-333.
- [165] H.M. Kim, J.K. Lee, H.S. Lee, Transparent and high gas barrier films based on poly(vinyl alcohol)/graphene oxide composites, *Thin Solid Films* 519(22) (2011) 7766-7771.
- [166] E.L. Cussler, S.E. Hughes, W.J. Ward, R. Aris, Barrier membranes, *Journal of Membrane Science* 38(2) (1988) 161-174.
- [167] S.K. Nemani, R.K. Annavarapu, B. Mohammadian, A. Raiyan, J. Heil, M.A. Haque, A. Abdelaal, H. Sojoudi, Surface Modification of Polymers: Methods and Applications, *Advanced Materials Interfaces* 5(24) (2018) 1801247.
- [168] D.Y. Ryu, K. Shin, E. Drockenmuller, C.J. Hawker, T.P. Russell, A Generalized Approach to the Modification of Solid Surfaces, *Science* 308(5719) (2005) 236-239.
- [169] S. Haar, M. El Gemayel, Y. Shin, G. Melinte, M.A. Squillaci, O. Ersen, C. Casiraghi, A. Ciesielski, P. Samori, Enhancing the Liquid-Phase Exfoliation of Graphene in Organic Solvents upon Addition of n-Octylbenzene, *Scientific Reports* 5(1) (2015) 16684.
- [170] T. Carey, C. Jones, F. Le Moal, D. Deganello, F. Torrisi, Spray-Coating Thin Films on Three-Dimensional Surfaces for a Semitransparent Capacitive-Touch Device, *ACS Applied Materials & Interfaces* 10(23) (2018) 19948-19956.
- [171] K. Norrman, A. Ghanbari-Siahkali, N.B. Larsen, Studies of spin-coated polymer films, *Annual Reports Section "C" (Physical Chemistry)* 101(0) (2005) 174-201.
- [172] M. Eredia, S. Bertolazzi, T. Leydecker, M. El Garah, I. Janica, G. Melinte, O. Ersen, A. Ciesielski, P. Samori, Morphology and Electronic Properties of Electrochemically Exfoliated Graphene, *The Journal of Physical Chemistry Letters* 8(14) (2017) 3347-3355.
- [173] J. Zasadzinski, R. Viswanathan, L. Madsen, J. Garnaes, D. Schwartz, Langmuir-Blodgett films, *Science* 263(5154) (1994) 1726-1733.
- [174] H. Kim, C. Mattevi, H.J. Kim, A. Mittal, K.A. Mkhoyan, R.E. Rimann, M. Chhowalla, Optoelectronic properties of graphene thin films deposited by a Langmuir-Blodgett assembly, *Nanoscale* 5(24) (2013) 12365-12374.
- [175] G.M. Whitesides, B. Grzybowski, Self-Assembly at All Scales, *Science* 295(5564) (2002) 2418-2421.

- [176] R.K. Iler, Multilayers of colloidal particles, *Journal of Colloid and Interface Science* 21(6) (1966) 569-594.
- [177] G. Decher, J.D. Hong, J. Schmitt, Buildup of ultrathin multilayer films by a self-assembly process: III. Consecutively alternating adsorption of anionic and cationic polyelectrolytes on charged surfaces, *Thin Solid Films* 210-211 (1992) 831-835.
- [178] P. Berndt, K. Kurihara, T. Kunitake, Adsorption of poly(styrenesulfonate) onto an ammonium monolayer on mica: a surface forces study, *Langmuir* 8(10) (1992) 2486-2490.
- [179] H.L. Tan, M.J. McMurdo, G. Pan, P.G. Van Patten, Temperature Dependence of Polyelectrolyte Multilayer Assembly, *Langmuir* 19(22) (2003) 9311-9314.
- [180] J.D. Mendelsohn, C.J. Barrett, V.V. Chan, A.J. Pal, A.M. Mayes, M.F. Rubner, Fabrication of Microporous Thin Films from Polyelectrolyte Multilayers, *Langmuir* 16(11) (2000) 5017-5023.
- [181] R.A. McAloney, M. Sinyor, V. Dudnik, M.C. Goh, Atomic Force Microscopy Studies of Salt Effects on Polyelectrolyte Multilayer Film Morphology, *Langmuir* 17(21) (2001) 6655-6663.
- [182] H. Zhang, J. Rühe, Interaction of Strong Polyelectrolytes with Surface-Attached Polyelectrolyte Brushes-Polymer Brushes as Substrates for the Layer-by-Layer Deposition of Polyelectrolytes, *Macromolecules* 36(17) (2003) 6593-6598.
- [183] J. Bravo, L. Zhai, Z. Wu, R.E. Cohen, M.F. Rubner, Transparent Superhydrophobic Films Based on Silica Nanoparticles, *Langmuir* 23(13) (2007) 7293-7298.
- [184] M.E. Buck, S.C. Schwartz, D.M. Lynn, Superhydrophobic Thin Films Fabricated by Reactive Layer-by-Layer Assembly of Azlactone-Functionalized Polymers, *Chemistry of Materials* 22(23) (2010) 6319-6327.
- [185] T. Soeno, K. Inokuchi, S. Shiratori, Ultra-water-repellent surface: fabrication of complicated structure of SiO<sub>2</sub> nanoparticles by electrostatic self-assembled films, *Applied Surface Science* 237(1) (2004) 539-543.
- [186] G. Decher, Fuzzy Nanoassemblies: Toward Layered Polymeric Multicomposites, *Science* 277(5330) (1997) 1232-1237.
- [187] K.C. Krogman, N.S. Zacharia, S. Schroeder, P.T. Hammond, Automated Process for Improved Uniformity and Versatility of Layer-by-Layer Deposition, *Langmuir* 23(6) (2007) 3137-3141.
- [188] X. Huang, Q. Bai, J. Hu, D. Hou, A Practical Model of Quartz Crystal Microbalance in Actual Applications, *Sensors* 17(8) (2017) 1785.
- [189] J.C. Dijt, M.A.C. Stuart, G.J. Fleer, Reflectometry as a tool for adsorption studies, *Advances in Colloid and Interface Science* 50 (1994) 79-101.
- [190] W.-S. Jang, I. Rawson, J.C. Grunlan, Layer-by-layer assembly of thin film oxygen barrier, *Thin Solid Films* 516(15) (2008) 4819-4825.
- [191] E.R. Kleinfeld, G.S. Ferguson, Stepwise Formation of Multilayered Nanostructural Films from Macromolecular Precursors, *Science* 265(5170) (1994) 370-373.
- [192] L. Yu, Y.-S. Lim, J.H. Han, K. Kim, J.Y. Kim, S.-Y. Choi, K. Shin, A graphene oxide oxygen barrier film deposited via a self-assembly coating method, *Synthetic Metals* 162(7) (2012) 710-714.
- [193] J.-T. Chen, Y.-J. Fu, Q.-F. An, S.-C. Lo, S.-H. Huang, W.-S. Hung, C.-C. Hu, K.-R. Lee, J.-Y. Lai, Tuning nanostructure of graphene oxide/polyelectrolyte

- LbL assemblies by controlling pH of GO suspension to fabricate transparent and super gas barrier films, *Nanoscale* 5(19) (2013) 9081-9088.
- [194] Y.-H. Yang, L. Bolling, M.A. Priolo, J.C. Grunlan, Super Gas Barrier and Selectivity of Graphene Oxide-Polymer Multilayer Thin Films, *Advanced Materials* 25(4) (2013) 503-508.
- [195] B. Stevens, E. Dessiatova, D.A. Hagen, A.D. Todd, C.W. Bielawski, J.C. Grunlan, Low-Temperature Thermal Reduction of Graphene Oxide Nanobrick Walls: Unique Combination of High Gas Barrier and Low Resistivity in Fully Organic Polyelectrolyte Multilayer Thin Films, *ACS Applied Materials & Interfaces* 6(13) (2014) 9942-9945.
- [196] H. Li, Z. Song, X. Zhang, Y. Huang, S. Li, Y. Mao, H.J. Ploehn, Y. Bao, M. Yu, Ultrathin, Molecular-Sieving Graphene Oxide Membranes for Selective Hydrogen Separation, *Science* 342(6154) (2013) 95-98.
- [197] C. Chi, X. Wang, Y. Peng, Y. Qian, Z. Hu, J. Dong, D. Zhao, Facile Preparation of Graphene Oxide Membranes for Gas Separation, *Chemistry of Materials* 28(9) (2016) 2921-2927.
- [198] D. Pierleoni, M. Minelli, S. Ligi, M. Christian, S. Funke, N. Reineking, V. Morandi, F. Doghieri, V. Palermo, Selective Gas Permeation in Graphene Oxide–Polymer Self-Assembled Multilayers, *ACS Applied Materials & Interfaces* 10(13) (2018) 11242-11250.
- [199] P.T.H.K.C.K.N.S. Zacharia, AUTOMATED LAYER BY LAYER SPRAY TECHNOLOGY 2009.
- [200] A.A. Dameron, S.D. Davidson, B.B. Burton, P.F. Garcia, R.S. McLean, S.M. George, Gas Diffusion Barriers on Polymers Using Multilayers Fabricated by Al<sub>2</sub>O<sub>3</sub> and Rapid SiO<sub>2</sub> Atomic Layer Deposition, *The Journal of Physical Chemistry C* 112(12) (2008) 4573-4580.
- [201] S.M. George, A.W. Ott, J.W. Klaus, Surface Chemistry for Atomic Layer Growth, *The Journal of Physical Chemistry* 100(31) (1996) 13121-13131.
- [202] S.M. George, B. Yoon, A.A. Dameron, Surface Chemistry for Molecular Layer Deposition of Organic and Hybrid Organic–Inorganic Polymers, *Accounts of Chemical Research* 42(4) (2009) 498-508.
- [203] T. Hirvikorpi, M. Vähä-Nissi, T. Mustonen, E. Iiskola, M. Karppinen, Atomic layer deposited aluminum oxide barrier coatings for packaging materials, *Thin Solid Films* 518(10) (2010) 2654-2658.
- [204] Z. Jia, M.B. Tucker, T. Li, Failure mechanics of organic–inorganic multilayer permeation barriers in flexible electronics, *Composites Science and Technology* 71(3) (2011) 365-372.
- [205] S. Qin, S. Xiang, B. Eberle, K. Xie, J.C. Grunlan, High Moisture Barrier with Synergistic Combination of SiO<sub>x</sub> and Polyelectrolyte Nanolayers, *Advanced Materials Interfaces* 6(16) (2019) 1900740.
- [206] J. Sun, Q. Chen, Y. Han, H. Zhou, A. Zhang, Emissions of selected brominated flame retardants from consumer materials: the effects of content, temperature, and timescale, *Environmental Science and Pollution Research* 25(24) (2018) 24201-24209.
- [207] K. English, Y. Chen, L.-M. Toms, P. Jagals, R.S. Ware, J.F. Mueller, P.D. Sly, Polybrominated diphenyl ether flame retardant concentrations in faeces from young children in Queensland, Australia and associations with environmental and behavioural factors, *Environmental Research* 158 (2017) 669-676.
- [208] G. Stieger, M. Scheringer, C.A. Ng, K. Hungerbühler, Assessing the persistence, bioaccumulation potential and toxicity of brominated flame

- retardants: Data availability and quality for 36 alternative brominated flame retardants, *Chemosphere* 116 (2014) 118-123.
- [209] W. Zhang, G. Camino, R. Yang, Polymer/polyhedral oligomeric silsesquioxane (POSS) nanocomposites: An overview of fire retardance, *Progress in Polymer Science* 67 (2017) 77-125.
- [210] L. Song, S. Xuan, X. Wang, Y. Hu, Flame retardancy and thermal degradation behaviors of phosphate in combination with POSS in polylactide composites, *Thermochimica Acta* 527 (2012) 1-7.
- [211] B. Yu, Y. Tao, L. Liu, Y. Shi, H. Yang, G. Jie, S. Lo, Q. Tai, L. Song, Y. Hu, Thermal and flame retardant properties of transparent UV-curing epoxy acrylate coatings with POSS-based phosphonate acrylate, *RSC Advances* 5(92) (2015) 75254-75262.
- [212] T. Kashiwagi, F. Du, J.F. Douglas, K.I. Winey, R.H. Harris, J.R. Shields, Nanoparticle networks reduce the flammability of polymer nanocomposites, *Nature Materials* 4(12) (2005) 928-933.
- [213] P.a. Song, L. Xu, Z. Guo, Y. Zhang, Z. Fang, Flame-retardant-wrapped carbon nanotubes for simultaneously improving the flame retardancy and mechanical properties of polypropylene, *Journal of Materials Chemistry* 18(42) (2008) 5083-5091.
- [214] P. Song, L. Zhao, Z. Cao, Z. Fang, Polypropylene nanocomposites based on C60-decorated carbon nanotubes: thermal properties, flammability, and mechanical properties, *Journal of Materials Chemistry* 21(21) (2011) 7782-7788.
- [215] A.A. Cain, C.R. Nolen, Y.-C. Li, R. Davis, J.C. Grunlan, Phosphorous-filled nanobrick wall multilayer thin film eliminates polyurethane melt dripping and reduces heat release associated with fire, *Polymer Degradation and Stability* 98(12) (2013) 2645-2652.
- [216] G. Laufer, C. Kirkland, A.A. Cain, J.C. Grunlan, Clay-Chitosan Nanobrick Walls: Completely Renewable Gas Barrier and Flame-Retardant Nanocoatings, *ACS Applied Materials & Interfaces* 4(3) (2012) 1643-1649.
- [217] X. Wang, E.N. Kalali, J.-T. Wan, D.-Y. Wang, Carbon-family materials for flame retardant polymeric materials, *Progress in Polymer Science* 69 (2017) 22-46.
- [218] M. Jimenez, S. Duquesne, S. Bourbigot, Intumescence fire protective coating: Toward a better understanding of their mechanism of action, *Thermochimica Acta* 449(1) (2006) 16-26.
- [219] J.H. Cho, V. Vasagar, K. Shanmuganathan, A.R. Jones, S. Nazarenko, C.J. Ellison, Bioinspired Catecholic Flame Retardant Nanocoating for Flexible Polyurethane Foams, *Chemistry of Materials* 27(19) (2015) 6784-6790.
- [220] D. Battegazzore, J. Alongi, A. Frache, L. Wågberg, F. Carosio, Layer by Layer-functionalized rice husk particles: A novel and sustainable solution for particleboard production, *Materials Today Communications* 13 (2017) 92-101.
- [221] F. Carosio, A. Di Blasio, F. Cuttica, J. Alongi, G. Malucelli, Self-assembled hybrid nanoarchitectures deposited on poly(urethane) foams capable of chemically adapting to extreme heat, *RSC Advances* 4(32) (2014) 16674-16680.
- [222] S. Bellayer, M. Jimenez, B. Prieur, B. Dewailly, A. Ramgobin, J. Sarazin, B. Revel, G. Tricot, S. Bourbigot, Fire retardant sol-gel coated polyurethane foam: Mechanism of action, *Polymer Degradation and Stability* 147 (2018) 159-167.
- [223] S. Bellayer, M. Jimenez, S. Barrau, S. Bourbigot, Fire retardant sol-gel coatings for flexible polyurethane foams, *RSC Advances* 6(34) (2016) 28543-28554.

- [224] Q. Wu, Q. Zhang, L. Zhao, S.-N. Li, L.-B. Wu, J.-X. Jiang, L.-C. Tang, A novel and facile strategy for highly flame retardant polymer foam composite materials: Transforming silicone resin coating into silica self-extinguishing layer, *Journal of Hazardous Materials* 336 (2017) 222-231.
- [225] Q. Wu, L.-X. Gong, Y. Li, C.-F. Cao, L.-C. Tang, L. Wu, L. Zhao, G.-D. Zhang, S.-N. Li, J. Gao, Y. Li, Y.-W. Mai, Efficient Flame Detection and Early Warning Sensors on Combustible Materials Using Hierarchical Graphene Oxide/Silicone Coatings, *ACS Nano* 12(1) (2018) 416-424.
- [226] S. Liang, N.M. Neisius, S. Gaan, Recent developments in flame retardant polymeric coatings, *Progress in Organic Coatings* 76(11) (2013) 1642-1665.
- [227] Y.-C. Li, J. Schulz, J.C. Grunlan, Polyelectrolyte/Nanosilicate Thin-Film Assemblies: Influence of pH on Growth, Mechanical Behavior, and Flammability, *ACS Applied Materials & Interfaces* 1(10) (2009) 2338-2347.
- [228] J. Alongi, F. Carosio, G. Malucelli, Current emerging techniques to impart flame retardancy to fabrics: An overview, *Polymer Degradation and Stability* 106 (2014) 138-149.
- [229] F. Laoutid, L. Bonnaud, M. Alexandre, J.M. Lopez-Cuesta, P. Dubois, New prospects in flame retardant polymer materials: From fundamentals to nanocomposites, *Materials Science and Engineering: R: Reports* 63(3) (2009) 100-125.
- [230] S. Bourbigot, S. Duquesne, Fire retardant polymers: recent developments and opportunities, *Journal of Materials Chemistry* 17(22) (2007) 2283-2300.
- [231] F. Jiang, J.L. de Ris, M.M. Khan, Absorption of thermal energy in PMMA by in-depth radiation, *Fire Safety Journal* 44(1) (2009) 106-112.
- [232] G. Linteris, M. Zammarrano, B. Wilthan, L. Hanssen, Absorption and reflection of infrared radiation by polymers in fire-like environments, *Fire and Materials* 36(7) (2012) 537-553.
- [233] B. Schartel, A. Weiß, Temperature inside burning polymer specimens: Pyrolysis zone and shielding, *Fire and Materials* 34(5) (2010) 217-235.
- [234] B. Sang, Z.-w. Li, X.-h. Li, L.-g. Yu, Z.-j. Zhang, Graphene-based flame retardants: a review, *Journal of Materials Science* 51(18) (2016) 8271-8295.
- [235] F. Kim, J. Luo, R. Cruz-Silva, L.J. Cote, K. Sohn, J. Huang, Self-Propagating Domino-like Reactions in Oxidized Graphite, *Advanced Functional Materials* 20(17) (2010) 2867-2873.
- [236] B. Dittrich, K.-A. Wartig, D. Hofmann, R. Mülhaupt, B. Schartel, The influence of layered, spherical, and tubular carbon nanomaterials' concentration on the flame retardancy of polypropylene, *Polymer Composites* 36(7) (2015) 1230-1241.
- [237] D. Hofmann, K.-A. Wartig, R. Thomann, B. Dittrich, B. Schartel, R. Mülhaupt, Functionalized Graphene and Carbon Materials as Additives for Melt-Extruded Flame Retardant Polypropylene, *Macromolecular Materials and Engineering* 298(12) (2013) 1322-1334.
- [238] C. Bao, L. Song, W. Xing, B. Yuan, C.A. Wilkie, J. Huang, Y. Guo, Y. Hu, Preparation of graphene by pressurized oxidation and multiplex reduction and its polymer nanocomposites by masterbatch-based melt blending, *Journal of Materials Chemistry* 22(13) (2012) 6088-6096.
- [239] Y. Han, Y. Wu, M. Shen, X. Huang, J. Zhu, X. Zhang, Preparation and properties of polystyrene nanocomposites with graphite oxide and graphene as flame retardants, *Journal of Materials Science* 48(12) (2013) 4214-4222.
- [240] G. Huang, S. Chen, P. Song, P. Lu, C. Wu, H. Liang, Combination effects of graphene and layered double hydroxides on intumescence flame-retardant

- poly(methyl methacrylate) nanocomposites, *Applied Clay Science* 88-89 (2014) 78-85.
- [241] M.M. Hirschler, Polyurethane foam and fire safety, *Polymers for Advanced Technologies* 19(6) (2008) 521-529.
- [242] S.T. McKenna, T.R. Hull, The fire toxicity of polyurethane foams, *Fire Science Reviews* 5(1) (2016) 3.
- [243] Y.S. Kim, R. Davis, A.A. Cain, J.C. Grunlan, Development of layer-by-layer assembled carbon nanofiber-filled coatings to reduce polyurethane foam flammability, *Polymer* 52(13) (2011) 2847-2855.
- [244] Y.-C. Li, Y.S. Kim, J. Shields, R. Davis, Controlling polyurethane foam flammability and mechanical behaviour by tailoring the composition of clay-based multilayer nanocoatings, *Journal of Materials Chemistry A* 1(41) (2013) 12987-12997.
- [245] H. Pan, Y. Pan, W. Wang, L. Song, Y. Hu, K.M. Liew, Synergistic Effect of Layer-by-Layer Assembled Thin Films Based on Clay and Carbon Nanotubes To Reduce the Flammability of Flexible Polyurethane Foam, *Industrial & Engineering Chemistry Research* 53(37) (2014) 14315-14321.
- [246] K.M. Holder, M.E. Huff, M.N. Cosio, J.C. Grunlan, Intumescing multilayer thin film deposited on clay-based nanobrick wall to produce self-extinguishing flame retardant polyurethane, *Journal of Materials Science* 50(6) (2015) 2451-2458.
- [247] D. Patra, P. Vangal, A.A. Cain, C. Cho, O. Regev, J.C. Grunlan, Inorganic Nanoparticle Thin Film that Suppresses Flammability of Polyurethane with only a Single Electrostatically-Assembled Bilayer, *ACS Applied Materials & Interfaces* 6(19) (2014) 16903-16908.
- [248] M. Montalti, G. Battistelli, A. Cantelli, D. Genovese, Photo-tunable multicolour fluorescence imaging based on self-assembled fluorogenic nanoparticles, *Chemical Communications* 50(40) (2014) 5326-5329.
- [249] F.C. A. Fina, G. Saracco, A method for superficially coating polymeric foams in order to improve their flame reaction and the related superficially coated flame resistant polymeric foams, 2018.
- [250] X. Qin, Q. Meng, Y. Feng, Y. Gao, Graphene with line defect as a membrane for gas separation: Design via a first-principles modeling, *Surface Science* 607 (2013) 153-158.
- [251] A. Lerf, H. He, M. Forster, J. Klinowski, Structure of Graphite Oxide Revisited, *The Journal of Physical Chemistry B* 102(23) (1998) 4477-4482.
- [252] R.J. Smith, M. Lotya, J.N. Coleman, The importance of repulsive potential barriers for the dispersion of graphene using surfactants, *New Journal of Physics* 12(12) (2010) 125008.
- [253] T. Kobayashi, J-Aggregates.
- [254] J. Lu, I. Do, H. Fukushima, I. Lee, L.T. Drzal, Stable Aqueous Suspension and Self-Assembly of Graphite Nanoplatelets Coated with Various Polyelectrolytes, *Journal of Nanomaterials* 2010 (2010) 11.
- [255] J.M. Englert, J. Röhrl, C.D. Schmidt, R. Graupner, M. Hundhausen, F. Hauke, A. Hirsch, Soluble Graphene: Generation of Aqueous Graphene Solutions Aided by a Perylenebisimide-Based Bolaamphiphile, *Advanced Materials* 21(42) (2009) 4265-4269.
- [256] C. Huang, S. Barlow, S.R. Marder, Perylene-3,4,9,10-tetracarboxylic Acid Diimides: Synthesis, Physical Properties, and Use in Organic Electronics, *The Journal of Organic Chemistry* 76(8) (2011) 2386-2407.

- [257] C. Backes, F. Hauke, A. Hirsch, The Potential of Perylene Bisimide Derivatives for the Solubilization of Carbon Nanotubes and Graphene, *Advanced Materials* 23(22-23) (2011) 2588-2601.
- [258] C. Backes, C.D. Schmidt, F. Hauke, C. Böttcher, A. Hirsch, High Population of Individualized SWCNTs through the Adsorption of Water-Soluble Perylenes, *Journal of the American Chemical Society* 131(6) (2009) 2172-2184.
- [259] D. Görl, X. Zhang, F. Würthner, Molecular Assemblies of Perylene Bisimide Dyes in Water, *Angewandte Chemie International Edition* 51(26) (2012) 6328-6348.
- [260] J. Zhang, J.K. Lee, Y. Wu, R.W. Murray, Photoluminescence and Electronic Interaction of Anthracene Derivatives Adsorbed on Sidewalls of Single-Walled Carbon Nanotubes, *Nano Letters* 3(3) (2003) 403-407.
- [261] S.M.R.W.X.F.K.D. J.; Spectrometric identification of organic compounds, seventh ed., John Wiley & Sons 2005.
- [262] J.R. Lackowicz, Principles of Fluorescence Spectroscopy, 3rd ed., Singapore, 2006.
- [263] G. Socrates, Infrared and Raman Characteristic Group Frequencies - Table and Charts, Wiley 2006.
- [264] J. Choi, M.F. Rubner, Influence of the Degree of Ionization on Weak Polyelectrolyte Multilayer Assembly, *Macromolecules* 38(1) (2005) 116-124.
- [265] Y.-H. Yang, M. Haile, Y.T. Park, F.A. Malek, J.C. Grunlan, Super Gas Barrier of All-Polymer Multilayer Thin Films, *Macromolecules* 44(6) (2011) 1450-1459.
- [266] A.F. Xie, S. Granick, Local Electrostatics within a Polyelectrolyte Multilayer with Embedded Weak Polyelectrolyte, *Macromolecules* 35(5) (2002) 1805-1813.
- [267] E. Kharlampieva, S.A. Sukhishvili, Ionization and pH Stability of Multilayers Formed by Self-Assembly of Weak Polyelectrolytes, *Langmuir* 19(4) (2003) 1235-1243.
- [268] G. Findenig, S. Leimgruber, R. Kargl, S. Spirk, K. Stana-Kleinschek, V. Ribitsch, Creating Water Vapor Barrier Coatings from Hydrophilic Components, *ACS Applied Materials & Interfaces* 4(6) (2012) 3199-3206.
- [269] Y. Song, E.L. Lugo, S. Powell, P. Tzeng, B.A. Wilhite, J.C. Grunlan, Highly selective multilayer polymer thin films for CO<sub>2</sub>/N<sub>2</sub> separation, *Journal of Polymer Science Part B: Polymer Physics* 55(23) (2017) 1730-1737.
- [270] P. Podsiadlo, M. Michel, J. Lee, E. Verploegen, N. Wong Shi Kam, V. Ball, J. Lee, Y. Qi, A.J. Hart, P.T. Hammond, N.A. Kotov, Exponential Growth of LBL Films with Incorporated Inorganic Sheets, *Nano Letters* 8(6) (2008) 1762-1770.
- [271] K. Tang, N.A.M. Besseling, Formation of polyelectrolyte multilayers: ionic strengths and growth regimes, *Soft Matter* 12(4) (2016) 1032-1040.
- [272] P. Bicker, M. Schönhoff, Linear and Exponential Growth Regimes of Multilayers of Weak Polyelectrolytes in Dependence on pH, *Macromolecules* 43(11) (2010) 5052-5059.
- [273] A. Baba, F. Kaneko, R.C. Advincula, Polyelectrolyte adsorption processes characterized *in situ* using the quartz crystal microbalance technique: alternate adsorption properties in ultrathin polymer films, *Colloids and Surfaces A: Physicochemical and Engineering Aspects* 173(1) (2000) 39-49.
- [274] M.A. Priolo, K.M. Holder, D. Gamboa, J.C. Grunlan, Influence of Clay Concentration on the Gas Barrier of Clay-Polymer Nanobrick Wall Thin Film Assemblies, *Langmuir* 27(19) (2011) 12106-12114.

- [275] B. Dittrich, K.-A. Wartig, D. Hofmann, R. Mülhaupt, B. Schartel, Flame retardancy through carbon nanomaterials: Carbon black, multiwall nanotubes, expanded graphite, multi-layer graphene and graphene in polypropylene, *Polymer Degradation and Stability* 98(8) (2013) 1495-1505.
- [276] J. Gu, C. Liang, X. Zhao, B. Gan, H. Qiu, Y. Guo, X. Yang, Q. Zhang, D.-Y. Wang, Highly thermally conductive flame-retardant epoxy nanocomposites with reduced ignitability and excellent electrical conductivities, *Composites Science and Technology* 139 (2017) 83-89.
- [277] X. Zhang, Q. Shen, X. Zhang, H. Pan, Y. Lu, Graphene oxide-filled multilayer coating to improve flame-retardant and smoke suppression properties of flexible polyurethane foam, *Journal of Materials Science* 51(23) (2016) 10361-10374.
- [278] S.Y. Park, M.F. Rubner, A.M. Mayes, Free Energy Model for Layer-by-Layer Processing of Polyelectrolyte Multilayer Films, *Langmuir* 18(24) (2002) 9600-9604.
- [279] C. Negrell-Guirao, F. Carosio, B. Boutevin, H. Cottet, C. Loubat, Phosphonated oligoallylamine: Synthesis, characterization in water, and development of layer by layer assembly, *Journal of Polymer Science Part B: Polymer Physics* 51(16) (2013) 1244-1251.
- [280] H. Yang, B. Yu, P. Song, C. Maluk, H. Wang, Surface-coating engineering for flame retardant flexible polyurethane foams: A critical review, *Composites Part B: Engineering* 176 (2019) 107185.
- [281] M. Dash, F. Chiellini, R.M. Ottenbrite, E. Chiellini, Chitosan—A versatile semi-synthetic polymer in biomedical applications, *Progress in Polymer Science* 36(8) (2011) 981-1014.
- [282] M. Lavorgna, F. Piscitelli, P. Mangiacapra, G.G. Buonocore, Study of the combined effect of both clay and glycerol plasticizer on the properties of chitosan films, *Carbohydrate Polymers* 82(2) (2010) 291-298.
- [283] F. Chivrac, E. Pollet, L. Avérous, Progress in nano-biocomposites based on polysaccharides and nanoclays, *Materials Science and Engineering: R: Reports* 67(1) (2009) 1-17.
- [284] F. Carosio, J. Alongi, G. Malucelli, Layer by Layer ammonium polyphosphate-based coatings for flame retardancy of polyester–cotton blends, *Carbohydrate Polymers* 88(4) (2012) 1460-1469.
- [285] C.R.C.B. M.L. Silva Suedina, Marcus V.L. Fook, Claudia M.O. Raposo, Laura H. Carvalho, Eduardo L. Canedo, Application of Infrared Spectroscopy to Analysis of Chitosan/Clay Nanocomposites, *Infrared Spectroscopy*, 2012.
- [286] Y. Si, E.T. Samulski, Synthesis of Water Soluble Graphene, *Nano Letters* 8(6) (2008) 1679-1682.
- [287] B. Schartel, T.R. Hull, Development of fire-retarded materials—Interpretation of cone calorimeter data, *Fire and Materials* 31(5) (2007) 327-354.
- [288] R.H. Krämer, M. Zammarano, G.T. Linteris, U.W. Gedde, J.W. Gilman, Heat release and structural collapse of flexible polyurethane foam, *Polymer Degradation and Stability* 95(6) (2010) 1115-1122.
- [289] O. Köklükaya, F. Carosio, L. Wågberg, Superior Flame-Resistant Cellulose Nanofibril Aerogels Modified with Hybrid Layer-by-Layer Coatings, *ACS Applied Materials & Interfaces* 9(34) (2017) 29082-29092.
- [290] F. Carosio, C. Negrell-Guirao, J. Alongi, G. David, G. Camino, All-polymer Layer by Layer coating as efficient solution to polyurethane foam flame retardancy, *European Polymer Journal* 70 (2015) 94-103.

- [291] A.A. Cain, M.G.B. Plummer, S.E. Murray, L. Bolling, O. Regev, J.C. Grunlan, Iron-containing, high aspect ratio clay as nanoarmor that imparts substantial thermal/flame protection to polyurethane with a single electrostatically-deposited bilayer, *Journal of Materials Chemistry A* 2(41) (2014) 17609-17617.
- [292] H. Pan, Q. Shen, Z. Zhang, B. Yu, Y. Lu, MoS<sub>2</sub>-filled coating on flexible polyurethane foam via layer-by-layer assembly technique: flame-retardant and smoke suppression properties, *Journal of Materials Science* 53(12) (2018) 9340-9349.
- [293] F. Carosio, M. Ghanadpour, J. Alongi, L. Wågberg, Layer-by-layer-assembled chitosan/phosphorylated cellulose nanofibrils as a bio-based and flame protecting nano-exoskeleton on PU foams, *Carbohydrate Polymers* 202 (2018) 479-487.
- [294] V.Y. Rudyak, S.L. Krasnolutskii, Dependence of the viscosity of nanofluids on nanoparticle size and material, *Physics Letters A* 378(26) (2014) 1845-1849.
- [295] M. Lotya, A. Rakovich, J.F. Donegan, J.N. Coleman, Measuring the lateral size of liquid-exfoliated nanosheets with dynamic light scattering, *Nanotechnology* 24(26) (2013) 265703.
- [296] Z. Wu, J. Walish, A. Nolte, L. Zhai, R.E. Cohen, M.F. Rubner, Deformable Antireflection Coatings from Polymer and Nanoparticle Multilayers, *Advanced Materials* 18(20) (2006) 2699-2702.
- [297] A. Richard Horrocks, S. Zhang, Enhancing polymer char formation by reaction with phosphorylated polyols. 1. Cellulose, *Polymer* 42(19) (2001) 8025-8033.
- [298] U. Braun, A.I. Balabanovich, B. Schartel, U. Knoll, J. Artner, M. Ciesielski, M. Döring, R. Perez, J.K.W. Sandler, V. Altstädt, T. Hoffmann, D. Pospiech, Influence of the oxidation state of phosphorus on the decomposition and fire behaviour of flame-retarded epoxy resin composites, *Polymer* 47(26) (2006) 8495-8508.
- [299] W. Sun, W.-l. Liu, Y.-h. Hu, FTIR analysis of adsorption of poly diallyl-dimethyl-ammonium chloride on kaolinite, *Journal of Central South University of Technology* 15(3) (2008) 373-377.
- [300] G. Socrates, Infrared and Raman Characteristic Group Frequencies - Table and Charts, third edition ed., Wiley2006.
- [301] K. Krogman, N. Zacharia, S. Schroeder, P. Hammond, Automated process for improved uniformity and versatility of layer-by-layer deposition, *Langmuir* 23(6) (2007) 3137-3141.
- [302] A.C. Ferrari, D.M. Basko, Raman spectroscopy as a versatile tool for studying the properties of graphene, *Nature nanotechnology* 8(4) (2013) 235-246.
- [303] K. Kishore, K. Mohandas, Mechanistic studies on the action of ammonium phosphate on polymer fire retardancy, *Combust Flame* 43 (1981) 145-153.
- [304] M. Ghanadpour, B. Wicklein, F. Carosio, L. Wågberg, All-natural and highly flame-resistant freeze-cast foams based on phosphorylated cellulose nanofibrils, *Nanoscale* 10(8) (2018) 4085-4095.
- [305] J.M. Hughes, D. Aherne, J.N. Coleman, Generalizing solubility parameter theory to apply to one- and two-dimensional solutes and to incorporate dipolar interactions, *Journal of Applied Polymer Science* 127(6) (2013) 4483-4491.
- [306] T.J. Ohlemiller, Modeling of smoldering combustion propagation, *Progress in Energy and Combustion Science* 11(4) (1985) 277-310.
- [307] M. Zammarano, S. Matko, R.H. Krämer, R.D. Davis, J.W. Gilman, L.P. Sung, D.M. Fox, S. Mehta, Smoldering in Flexible Polyurethane Foams: The

Effect of Foam Morphology, Fire and Polymers VI: New Advances in Flame Retardant Chemistry and Science, American Chemical Society2012, pp. 459-479.  
[308] SFPE Handbook of Fire Protection Engineering, third edition ed.2002.